OXIDATIVE POTENTIAL OF URBAN HAZE IN A COATAL AREA: CHEMICAL CHARACTERISATION, SOURCE IDENTIFICATION AND LUNG DEPOSITION

Ke CHEN

(B.Eng. Chongqing Technology and Business University, P.R. China

M.Sc. University of Bristol, UK)

A THESIS SUBMITTED FOR THE DEGREE OF DOCTOR OF PHILOSOPHY

FACULTY OF CHEMICAL AND ENVIRONMENTAL ENGINEERING

UNIVERSITY OF NOTTINGHAM

2022

Acknowledgements

This thesis arose out of years of research since I came to Prof. Jun He's research group. During the research period, I worked with a lot of great people who helped and supported me in various ways for the research and deserved special mention.

First and foremost, I would like to express my most sincere gratitude and appreciation to Prof. Jun He, for his hands-on guidance and continuous encouragement. His enthusiasm for atmospheric science and his rigorous attitude towards science have really inspired me. He gave me enough trust and freedom to explore my research interests and become an independent and confident researcher. His high expectation on me is the essential motivation that keeps me moving forward. Above all and the most needed, he cultivated me the ability of how to learn systematically in such an environment full of fragmented information. I would like to extend my heartfelt gratitude to Prof. Sarah E. Metcalfe, for her generous support and supervision, when I studied in the UK campus. I am grateful to Dr. Yu-Ting Tang and Dr. Bencan Tang for their professional advice and assistance. I would also like to thank to Dr. Jingsha Xu, from whom I learnt important experimental and statistical approaches.

This thesis is also made with the technical support from Ms. Jane Zhang, Mr. Julian Zhu, Ms. Helen Xu, Ms. Karey Shan in the campus, and Dr. Honghui Xu, Mr. Rongguang Du, Mr. Bing Qi in Hangzhou, and Dr. Lei Tong and Mr. Junyi Zhao in Beilun. In addition, my special thanks go to my colleagues and friends, Dr. Chaohui Wei, Dr. Xiaotong Guo, Ms. Lulu Wang, Ms. Manxuan Xiao, Ms. Yueying Zheng, Mr. Jiayuan Xu, Mr. Lord Famiyeh, Mr. Lucen Li, who created a pleasant and nice studying and researching environment for me.

Words fail me to express my gratitude to my parents for their unconditional love, caring

and dedication for educating and preparing me for my future. My mother, Jian-Min HE, is the one who gives me the endless love and patience to encourage me through all the difficulties, and taught me to delay gratification since I was a child. My father, Tie-Jun CHEN, who is always by my side and understanding me, past and present.

Last but not the least, I would like to thank my husband, Dr. Zihao YE, the love of my life who stayed with me, in China and UK, through all up and downs for the past five years. My thanks also go to a special family member, a kitten named Nailao (Cheese), who gives me spiritual companionship when I sank into depression and stress.

Table of Contents

Abstract

Ambient aerosols, one of the components to deteriorate air quality, have been associated with chronic and acute effects on human health. The oxidative potential (OP) of ambient particles has been applied as a new metric for aerosol toxicity rather than mass concentration. A comprehensive year-round field campaign was conducted in a coastal city of Ningbo, China to examine OP of $PM_{2.5}$ (particulate matter with aerodynamic diameter $\leqslant$ 2.5 μm) and size-fractioned PM, as well as their chemical characterisation, source contribution and respiratory deposition.

Using dithiothreitol (DTT) cell-free assay, OP of water-soluble component (OP^{ws}) and OP of methanol-soluble component (OP^{meth}) of $PM_{2.5}$-based samples were measured. Extrinsic (volume-normalised) OP^{meth} (OP_v^{meth}) exhibited stronger seasonal variability than that of OP^{ws} (OP_v^{ws}). Different seasonal trends were observed for OP_v^{ws} and OP_v^{meth}, with highest averaged levels in autumn (4.09 ± 2.02 nmol min^{-1} m^{-3}) and winter (11.51 ± 2.56 nmol min^{-1} m^{-3}), respectively, and lowest in summer (OP_v^{ws}: 3.24 ± 1.39 nmol min^{-1} m^{-3}, OP_v^{meth}: 0.79 ± 0.83 nmol min^{-1} m^{-3}). In contrast, the intrinsic (mass normalized) OP, OP_m^{ws} and OP_m^{meth} exhibited highest in summer, with 0.21 ± 0.16 and 0.17 ± 0.21 nmol min^{-1} μg^{-1}, respectively. The analysis of major chemical components of aerosol samples, including carbonaceous species (organic carbon (OC), elemental carbon (EC), water-soluble organic carbon (WSOC)), water-soluble inorganic ions (WSIIs), trace elements, polycyclic aromatic hydrocarbons (PAHs) and quinones, were used for source apportionment analysis via chemical mass balance (CMB) model. Seven emission sources of $PM_{2.5}$ mass were identified, including secondary aerosol (SA), coal combustion (CC), industry emission (IE), vehicle emission (VE), biomass burning

(BB), fugitive dust (FD), and sea salts (SS). Using multiple linear regression (MLR), the dominant contributions from IE and SS to OP_v^{ws} and IE, BB, and CC to OP_v^{meth} were identified. We believe this is the first study to report DTT oxidation for SS and the reason for that is also explained. VE and FD-derived OP_v exhibited non-linearity due to antagonistic and/or synergistic interactions with SS and CC sources. Based on spectra of chemical composition data obtained from CMB model, we further compared OP values among $PM_{2.5}$ of similar mass concentrations with ranges of 20-30 and 30-40 μg m^{-3}. For Ningbo itself, we observed that IE-emitted $PM_{2.5}$ presents the highest intrinsic OP, while SS aerosol is redox-active in the coastal area. Our results showed that aerosols of similar mass concentrations exhibited remarkably different OP values, depending on their chemical compositions and source contributions.

For size-resolved particles, both concentrations of PM and its related OP (OP_v^{ws} and OP_v^{meth}) were substantially higher during haze period (29.76-40.97μg m^{-3} and 0.50-3.22 nmol min^{-1} m^{-3} of OP_v^{ws} and 29.76-40.97μg m^{-3} and 0.40-2.43 nmol min^{-1} m^{-3} of OP_v^{meth}) than non-haze period (9.15-22.20 μg m^{-3} and 0.19-0.95 nmol min^{-1} m^{-3} of OP_v^{ws} and 9.15-22.20 μg m^{-3} and 0.21-0.88 nmol min^{-1} m^{-3}) for all size ranges. The maximum of OP_v^{ws} centred in ultrafine-mode PM while OP_v^{meth} centred in coarse mode. Ultrafine particles contributed increasingly to the OP_v^{ws} deposition when penetrating into deeper regions of the respiratory tract, from 1.22 nmol min^{-1} in head airway to 1.80 nmol min^{-1} in pulmonary region, however, the deposited doses of PM and their DTT oxidation in coarse- and accumulation-modes were highest in respective head and pulmonary regions during both periods. The OP_v^{ws} resided in ultrafine particles was driven by SS and Cu, deposited mainly in pulmonary region in the two scenarios. However, SNA and soluble transition metals of Fe and Cr dominated the OP_v^{ws} from coarse-mode

particles, which had largest depositions in head airway during the two periods. The OP_v^{meth} resided in coarse particles was driven by Acy and 1,2-NQ during haze period and Acy during non-haze period. Nap, BbF and Ind dominated the OP_v^{meth} of accumulation-mode PM in polluted days while Acy and Flt in clear days. The deposited OP_v^{ws} in TB region had a combined contribution from ultrafine (SS, Cu) and coarse particles (SNA, Fe, Cr) in polluted days, while deposited OP_v^{meth} level in the TB region was highest in coarse mode during haze period and ultrafine mode during non-haze period.

In conclusion, this study has demonstrated the temporal variations and potential sources of OP induced from ambient PM. Investigations have revealed that the health effects of atmospheric aerosols are associated with PM OP and deposition efficiency of OP in different respiratory tracts. Overall, this study, based on a combination of field studies, laboratory experiments and statistical models, has provided essential insights into the mechanisms about how PM impact respiratory health from the perspective of OP in Ningbo, China.

Keywords: Oxidative potential (OP), $PM_{2.5}$, size-fractionated PM, catalytic oxidiser, source apportionment, lung deposition.

List of Figures

List of Tables

List of Symbols

1,2-NQ	1,2-napthaquinone
1,4-AQ	1,4-anthraquinone
1,4-NQ	1,4-napthaquinone
Ace	Acenaphthene
Acy	Acenaphthylene
Ag	Silver
Al	Aluminum
Ant	Anthracene
As	Arsenic
Ba	Barium
BaA	Benzo[a]anthracene
BaP	Benzo[a]pyrene
BbF	Benzo[b]fluoranthene
Bi	Bismuth
BkF	Benzo[k]fluoranthene
Bpe	Benzo-[ghi]perylene
Br^-	Bromine
Ca	Calcium
Ca^{2+}	Calcium ion
Cd	Cadmium
Ce	Cerium
Chr	Chrysene
Cl^-	Chloride ion
Co	Cobalt
CO	Carbon monoxide
CO_2	Carbon dioxide
Cr	Chromium
Cu	Copper
DBA	Dibenzo[a,h]anthracene
F^-	Fluoride ion
Fe	Iron

Flt	Fluoranthene
Flu	Fluorene
H_2O_2	Hydrogen peroxide
HNO_3	Nitric acid
Ind	Indeno[1,2,3-cd]pyrene
K^+	Potassium ion
Li^+	Lithium ion
Mg^{2+}	Magnesium ion
Mn	Manganese
Na^+	Sodium ion
Na_2CO_3	Sodium carbonate
$NaHCO_3$	Sodium bicarbonate
Nap	Naphthalene
NH_4^+	Ammonium ion
Ni	Nickel
NO	Nitrogen monoxide
NO_2	Nitrogen dioxide
NO_3^-	Nitrate ion
NO_x	Nitrogen oxides
$O_2\cdot^-$	Superoxide radical
O_3	Ozone
$OH\cdot$	Hydroxide radical
Pb	Lead
Phe	Phenanthrene
Pyr	Pyrene
Sb	Stibium
SO_2	Sulphur dioxide
SO_4^{2-}	Sulphate ion
Sr	Strontium
V	Vanadium
Zn	Zinc

List of Abbreviations

AA	Ascorbate acid
ASE	Accelerate solvent extraction
BB	Biomass burning
BPEA-nit	9-(1,1,3,3,tetramethylisoindolin-2-yloxyl-5-ethynyl)-10-(phenylethynyl) anthracene
BTH	Beijing-Tianjin-Hebei district
CBD	Central business district
CC	Coal combustion
CE	Collision Energy
CEP	Collision Cell Entrance Potential
CMAQ	Community Multiscale Air Quality
CMB	Chemical mass balance model
COPD	Chronic obstructive pulmonary disease
CXP	Collision Cell Exit Potential
DCF	2',7'-dichlorofluorescin
DCFH-DA	2',7'-dichlorofluorescin diacetate
DCM	dichloromethane
DHBAs	dihydrobenzoates
DMPO-OH	2-hydroxy-5,5-dimethyl-1-pyrrolidinyloxy
DMSO	Dimethyl sulphoxide
DP	De-clustering Potential
DPPC	Dipalmitoylphosphatidylcholine
DTNB	5, 5'-dithiobis (2-nitrobenzoic acid)

DTT	Dithiothreitol
EC	Elemental carbon
EDTA	Ethylenediaminetetraacetic acid
ELF	Epithelial lining fluid
EPA	Environmental Protection Agency
EPFRs	Environmentally persistent free radicals
EPR	Electron paramagnetic resonance
ESI	Electrospray ionisation
ESR	Electron span resonance
FA	Formic acid
FD	Fugitive dust
GC-MSD	Gas chromatograph – mass selective detector
GDP	Gross domestic product
GIS	Geographic information system
GMD	Geometric mean diameter
GSH	Glutathione
He	Helium
HMW	Heavy molecular weight
HPLC-MS/MS	High Performance Liquid Chromatograph – tandem Mass Spectrometry
HULIS	Humic-like substances
HYSPLIT	Hybrid single particle lagrangian integrated trajectory
ICS	Ion chromatography Spectrophotometry
ICP-MS	Inductively Coupled Plasma – Mass Spectrophotometry

IE	Industry emission
LMW	Low molecular weight
LOD	Limit of detection
MeOH	Methanol
MLR	Multiple linear regression
MPPD	Multiple-path particle dosimetry
MRM	Multiple reaction monitoring
NAAQS	National Ambient Air Quality Standards
NOAA	National Oceanic and Atmospheric Administration
OC	Organic carbon
OM	Organic matter
OP	Oxidative potential
OP_m	Mass-normalised oxidative potential
OP_v	Volume-normalised oxidative potential
OP_m^{meth}	Mass-normalised oxidative potential from methanol-extracted fraction of ambient particles
$OP_m^{meth\text{-}BB}$	Mass-normalised oxidative potential from methanol-extracted fraction of biomass burning emitted particles
$OP_m^{meth\text{-}CC}$	Mass-normalised oxidative potential from methanol-extracted fraction of coal combustion emitted particles
$OP_m^{meth\text{-}IE}$	Mass-normalised oxidative potential from methanol-extracted fraction of industry emitted particles
$OP_v^{meth\text{-}BB}$	Volume-normalised oxidative potential from methanol-extracted fraction of biomass burning emitted particles
$OP_v^{meth\text{-}CC}$	Volume-normalised oxidative potential from methanol-extracted fraction of coal combustion emitted particles

$OP_v^{meth\text{-}IE}$	Volume-normalised oxidative potential from methanol-extracted fraction of industry emitted particles
OP_m^{ws}	Mass-normalised oxidative potential from water-extracted fraction of ambient particles
$OP_m^{ws\text{-}IE}$	Mass-normalised oxidative potential from water-extracted fraction of industry emitted particles
$OP_m^{ws\text{-}SS}$	Mass-normalised oxidative potential from water-extracted fraction of sea salt related particles
OP_v^{meth}	Volume-normalised oxidative potential from methanol-extracted fraction of ambient particles
OP_v^{ws}	Volume-normalised oxidative potential from water-extracted fraction of ambient particles
$OP_v^{ws\text{-}IE}$	Volume-normalised oxidative potential from water-extracted fraction of industry emitted particles
$OP_v^{ws\text{-}SS}$	Volume-normalised oxidative potential from water-extracted fraction of sea salt related particles
PAHs	Polycyclic aromatic hydrocarbons
PBL	Planetary boundary layer
PCA	Primary component analysis
PM	Particulate matter
PMF	Positive Matrix Factorisation
PQ	Phenanthrenequinone
PRD	Pearl River Delta
PTFE	Poly tetrafluoroethylene
RH	Relative humidity
ROS	Reactive oxygen species
SA	Secondary aerosol
SD	Standard deviation

SIA	Secondary inorganic aerosol
SIM	Selective ion monitoring
SNA	Sulphate-nitrate-ammonia
SOA	Secondary organic aerosol
SOC	Secondary organic carbon
SS	Sea salt
SVOCs	Semi-volatile organic compounds
TCA	Trichloroacetic acid
TE	Tris-base and ethylenediaminetetraacetic acid buffer
TNB	2-nitro-5-thiobenzoic acid
TOC	Total organic carbon
TSP	Total suspended particles
UNNC	University of Nottingham Ningbo China
UV	Ultra-violet
VE	Vehicle emission
VOC	Volatile organic compounds
WHO	World Health Organisation
WIOC	Water insoluble organic carbon
WRF	Weather Research and Forecasting
WSIIs	Water soluble inorganic ions
WSOC	Water-soluble organic carbon
YRD	Yangtze River Delta

Chapter 1 Introduction

1.1 Research Background

Poor air quality linked to high mass concentrations of ambient particles has posed one of the greatest health risks worldwide (Bates et al., 2019a, Fang et al., 2019, Gao et al., 2020a). As the world's largest developing country, China has experienced dramatic progress in economy over the past four decades and surpassed Japan, becoming the world's second largest economy in 2010 (Dong et al., 2019, Ma et al., 2020). In the meanwhile, severe environmental deterioration owing to the large consumption of energy fuels has been a serious challenge in China. The increase in the number of hazy days, the reduction in atmospheric visibility and increase in public health effects are major concerns for national policy makers (Ji et al., 2018, Wang et al., 2018b). It has shown that concentration levels of fine particles ($PM_{2.5}$) directly contribute to the formation of atmospheric haze (Behera et al., 2015, Shen et al., 2017, Xu et al., 2017, Zhang et al., 2018). Higher levels of fine particles ($PM_{2.5}$) emitted from primary sources and formed via secondary transformation have drawn the attention of scientific bodies, and local and central governments. Consequently, $PM_{2.5}$ was included as one of the criteria pollutants in the National Ambient Air Quality Standards (NAAQS, GB 3095-2012) in China, with the acceptable daily average mass concentration (Grade II NAAQS) $\leqslant$ 75 μg m^{-3} (You, 2014).

The atmospheric $PM_{2.5}$ was governed by various anthropogenic sources. Mounting studies in apportioning the $PM_{2.5}$ sources have been conducted in different areas of China, with investigations of source identification, as well as the temporal and spatial variations of source

contributions, especially in developed areas of China such as Beijing-Tianjin-Hebei area (BTH), Yangtze River Delta (YRD) area and Pearl River Delta (PRD). According to the current analytical results, coal combustion, vehicular exhausts, industrial activity, biomass burning and road dust have been identified as the major primary sources of $PM_{2.5}$ in China (Zhang et al., 2017, Zheng et al., 2016). Moreover, additional source of sea salt aerosol and ship emissions are included when the study site is in the coastal area or in vicinity of port (e.g., Guangzhou, Nanjing, Shanghai, Ningbo, Hong Kong). Source contributions to $PM_{2.5}$ mass concentration exhibit obvious spatial variations. The traffic emissions and secondary inorganic aerosols (SIA) were reported to higher contributions to $PM_{2.5}$ in the southern China, while coal combustion contributed more in the north (Yan et al., 2017). The $PM_{2.5}$ contribution from coal combustion also exhibited seasonal variations, with lower in spring and summer and higher in autumn and winter, owing to the heating supply in the northern China (Zhao et al., 2013). In addition, a significant amount of coal is also applied in industrial activity and power plant, as well as the residential area, particularly in rural areas of northern China. For biomass burning sources, the residential biomass burning used for heating and cooking purposes is dominant in the north of China during winter, while the agriculture open fires are densely distributed in the North China Plain, along with a few provinces of southern and northern China. In most cities of southern China, SIA is the predominant contributor to $PM_{2.5}$ mass, such as Chengdu (33-44%), Chongqing (24-52%), Wuhan (23-41%) and Haikou (11-26%), etc (Tao et al., 2017). For secondary aerosols, SIA is commonly identified through SNA (sulphate (SO_4^{2-}) – nitrate (NO_3^-) – ammonia (NH_4^+)), the chemical compounds of which are formed via atmospheric reactions involving the primary emissions of gaseous precursors, such as SO_2 and NO_x (NO, NO_2). The

spatial variation of SIA presents the trend of higher percentage of $PM_{2.5}$ in the south, but higher mass concentration in the north (Zheng et al., 2017). In contrast, aromatic compounds are characterised as the main precursors of secondary organic aerosols (SOA) in the urban areas of China.

Because of a rapid increase in industrialization, fast growth in vehicle numbers and accelerated economic growth in the YRD area, which is one of the most developed areas in China comprising of northern Zhejiang Province, Shanghai and southern Jiangsu Province, an undesirable rise in levels of $PM_{2.5}$ has occurred. Such an increase in $PM_{2.5}$ concentration links directly to an increase in the occurrence of haze episodes (He et al., 2018). For example, there were only 12 hazy days observed during 2001, however, the number of hazy days increased to 239 during 2013 (Wang et al., 2018a). Ningbo, a vice-provincial city located in the northeast of Zhejiang Province, is one of the famous economic and industrial centres of YRD regions. Ningbo is an important coastal city and possesses large industrial zones in Beilun and Zhenhai districts, being a major exporter of textiles, electrical products, food and industrial tools, as well as the Ningbo-Zhoushan port, handling highest throughput quantities of total cargo worldwide (Li et al., 2018, Wang et al., 2018b). Ningbo is densely populated in the urban residential areas, with 8 million people and 1.7 million vehicles, according to the China's National GDP report in 2015 (Li et al., 2018). Due to these urban characteristics, Ningbo is affected by complicated air pollution from combined local emissions (i.e., industrial activity, vehicular exhausts, road dust, maritime activity and sea salts) and long-range transport (i.e., secondary aerosols). Previous study reported an obviously annual decrease of $PM_{2.5}$ mass concentration in recent five years, from 49 to 39 μg m^{-3} in Ningbo, however, it was still

exceeding the air quality guideline (annual mean $PM_{2.5} \leq 10$ μg m^{-3}) of World Health Organisation (WHO). Severe episode of haze pollution frequently occurred during cold seasons (autumn and winter) in Ningbo. Wang et al. (2018b) and Xu et al. (2016) captured a serious haze episode in Ningbo during cold seasons and revealed that long-range transport of air parcels from northern China, with densely distributed fire spots and industrial zones, bringing about substantial pollutants from biomass burning and industry emissions to Ningbo. Cheng et al. (2014) carried out a joint observation in YRD and reported a dominant contribution of local biomass burning (37%) to the severe air pollution in Ningbo via the simulation of Weather Research and Forecasting and Community Multiscale Air Quality (WRF/CMAQ). Most studies of air pollution analysis in Ningbo focused on the chemical characterisation and source apportionment of $PM_{2.5}$, however, few evaluates their health effects to human by investigating the particle toxicity rather than mass concentration.

Epidemiological studies have linked long-term $PM_{2.5}$ exposure to detrimental heath endpoint, including asthma occurrences, cardiopulmonary diseases, lung cancer and chronic obstructive pulmonary disease (COPD), leading to increased morbidity and mortality. However, the pathogenesis of diseases associated with PM exposure remain unclear. Growing evidence proposed that the redox-active chemical components of $PM_{2.5}$ can stimulate the generation of excessive reactive oxygen species (ROS) and induce oxidative stress in the cell, eventually cause systemic inflammation. The ROS comprises of hydroxyl radical (OH·), superoxide ($O_2^{\cdot-}$), and hydrogen peroxide (H_2O_2) etc. The capacity of $PM_{2.5}$ to generate ROS by consuming antioxidants in human epithelial lining fluid (ELF) is known as oxidative potential (OP) (Campbell et al., 2021, Cheng et al., 2020, Lin and Yu, 2020). Extensive studies carried out in

China and developed countries in Northern America, Europe, explored specific PM species and their emission sources responsible for the OP initiation. Study in Los Angeles firstly applied OP measurement of PM via dithiothreitol (DTT) assay, pointing out the strong correlations between DTT oxidation and organic matters, including organic carbon (OC), polycyclic aromatic hydrocarbons (PAHs) and quinones (Cho et al., 2005). PAHs correlated well with DTT consumption, with correlation coefficient r^2 of 0.41 of total PAHs (between 0.32 of Ind (indeno[1,2,3-cd]pyrene) and 0.82 of BgP (benzo[g]perylene)), but are not redox active in DTT assay. Such correlations are attributed to the oxidation of PAHs to polar compounds (i.e., quinones, nitro-PAHs), which can directly induce DTT decay. Moreover, Cheng et al. (2021) also reported a DTT response to water-soluble humic-like substances (HULIS). Further studies reported that trace metals resided in PM can cause oxidative damage both in vivo and vitro. Charrier and Anastasio (2012c) conducted a laboratory measurement and denoted that particulate metals initiated approximately 80% of DTT consumption, with the most redox active metal ion of copper (Cu), followed by manganese (Mn), cobalt (Co), vanadium (V), nickel (Ni), lead (Pb), iron (Fe), zinc (Zn), cadmium (Cd) and chromium (Cr).

In this case, the vehicular exhausts marked by particulate organic fractions such as PAHs and quinones, and inorganic fractions of transition metals is strongly correlated with PM induced OP (Cho et al., 2004, Gasser et al., 2009). Trace elements like Cu, Mn and Fe released from industrial activity make it exhibiting high intrinsic oxidative potency, while HULIS contribute to the enhancement of biomass burning related OP (Liu et al., 2018a, Verma et al., 2015a). Cu and Fe are also abundant in tyre wear and road dust, leading to the great intrinsic generation ability of ROS (Liu et al., 2014a). The coastal areas also are affected by marine

sources, including diesel and petrol consumption within ship emissions, which can induce considerable oxidative capacities of ambient particles (Liu et al., 2018a). However, study in Atlanta observed that the OP induced from biogenic sources and crustal materials were relatively low (Verma et al., 2015a). In general, anthropogenic emissions have a higher oxidative potency per mass unit of the aerosol relative to biogenic emissions.

Since most studies in investigating OP of ambient aerosol focused more on fine particles ($PM_{2.5}$), due to its higher adverse health effects than PM with larger sizes to human. However, as the deposition of inhaled PM in human respiratory tracts is strongly size dependent, understanding the size distributions of ambient PM, characterisation of particulate catalytic oxidisers and particle-bound OP are essential. A substantial fraction of coarse-mode PM ($PM_{2.5-10}$, particles with aerodynamic diameter between 2.5 and 10 μm) components are hydrophobic, most of which are associated with tire and brake wear, construction activities and road dust in urban area. Organic oxidisers, such as quinones (1,2-napthaquinone (1,2-NQ), 1,4-napthaquinone (1,4-NQ), 1,4-anthraquinone (1,4-AQ)) adsorbed on solid particles can induce OP either via engulfment of cells or binding to a cell surface, or act as a carrier of toxic components such as PAHs (Schoonen et al., 2006). In contrast, the oxidative stress generated from organic fraction of PM with smaller sizes was dominantly affected by traffic emissions (i.e., tailpipe emissions, petroleum spills) (Saffari et al., 2014a, Shirmohammadi et al., 2016).

Coarse particles are inclined to deposit in the extra-thoracic airway, such as head airway and nasal areas. Although they are possibly restrained by rhinothrix through impaction processes, the metals resided in coarse particles can cross synapses in the olfactory bulb and traverse via secondary olfactory neurons to the distant nuclei of the brain, leading to the

olfactory deficits and brain lesions (Calderón-Garcidueñas et al., 2010a, Maher et al., 2016, Sunderman, 2001). In contrast, the fine particles are likely to penetrate into the deeper tract (tracheobronchial and pulmonary regions) and may contribute to the inflammation relevant to pulmonary and even systemic diseases (De Jong et al., 2008, Li et al., 2017). Prior studies manifested the higher toxic power and more harmful of small particles to human, owing to their difficulties in clearance but easy access to blood, especially the ultrafine particles, they can avoid phagocytosis via alveolar macrophages to enter the pulmonary interstitial sites and remain deposited for long periods, consequently introducing pulmonary inflammation (Lyu et al., 2018, Sioutas et al., 2005).

1.2 Research Objectives

In this study, to systematically explore the ROS generation capacity of ambient aerosol in Ningbo city, DTT assay will be applied to measure to PM-bound OP, as well as the analysis of chemical characterisation of redox-active species, source apportionment and contribution to OP and respiratory deposition of PM and OP. Regarding these, the specific objectives of this study are summarised as follow:

1) assessment of source dispersions of $PM_{2.5}$ and size-resolved PM and their OP in the study domain;
2) assessment of source profiles of $PM_{2.5}$ and estimation of source contributions to both $PM_{2.5}$-bound OP^{ws} and OP^{meth} in the study domain;
3) estimation of the respiratory deposited doses of size-fractioned PM and their OP^{ws} and OP^{meth};
4) identification of the dominant redox-active species of size-resolved PM to oxidative potency and compare their OP^{ws} and OP^{meth} contributions in haze and non-haze days;
5) finding scientific reasons on why OP increases non-linearly with the increased source contributions, and investigating the interaction within and between source-derived OP;
6) exploring the driving factors of OP^{ws} and OP^{meth} that are induced from $PM_{2.5}$ of similar mass concentrations;
7) exploring the driving factors of deposited OP^{ws} and OP^{meth} in different respiratory tracts.

Chapter 2 Literature Review

2.1 OP as a Toxicological Metric of Ambient Aerosols

Exposure to severe air pollution associated with higher level of particulate matter (PM) has posed a severe threat to the world population due to its adverse global health impacts on humans (Bates et al., 2019a, Cho et al., 2005, Gao et al., 2017, Gao et al., 2020a). Epidemiological and toxicological studies emphasised the cause-effect links between inhalation of ambient particles and a series of respiratory and cardiopulmonary diseases (Campbell et al., 2021, Daellenbach et al., 2020, Weber et al., 2021). However, pathogenesis of diseases associated with PM exposure through humans are not completely understood in the literature. Mounting evidence in human biomarker studies, rat models, and DNA methylation observations deciphered that PM exposure would induce oxidative stress in the body, providing a potential pathway of particulate toxicity (Abrams et al., 2017, Baulig et al., 2003, Liu et al., 2014a). Oxidative stress occurs due to generation of reactive oxygen species (ROS) such as hydroxyl radical (OH•), superoxide ($O_2^{\bullet -}$), hydrogen peroxide (H_2O_2), and many others in the human body to overwhelm natural antioxidant defences, thus giving rise to biochemical imbalance. The excessive ROS can also initiate inflammation and cytotoxicity in nose, lung and cardiovascular systems through chemical alterations of DNA, lipids, and proteins, leading to tissue and cell damages or ultimately death (Abrams et al., 2017, Bates et al., 2019a, Prahalad et al., 2001). The capacity of PM to generate ROS by consuming antioxidants in human epithelial lining fluid (ELF) is known as oxidative potential (OP) (Cheng et al., 2020, Lin and Yu, 2020).

2.2 Measurement of Particle-related OP

2.2.1 OP Measurement

Various approaches have been applied to measure the ROS generation. PM bound ROS can either be produced by particulate components in vivo or within the particles itself, chemically interacting in cells and fluids through particle inhalation. Current acellular assays estimate PM induced OP under simulated lung fluids and expressed in units of time rate-of-consumption of volume-normalised (% or nmol min^{-1} m^{-3}) or mass-normalised (% or nmol min^{-1} μg^{-1}) concentration. The volume-based OP is more associated with human exposure and mass-based OP is a useful metric to display the intrinsic oxidative stress of ambient PM. The common acellular assays, including dithiothreitol (DTT) assay, ascorbate acid (AA) assay and glutathione (GSH) assay, measure the consumption rates of the surrogates of cellular reductants (DTT) and/or antioxidants (AA and GSH), while electron span or paramagnetic resonance (ESR or EPR) measures the generation of OH•.

2.2.1.1 DTT Assay

DTT is a strong reductant, which forms of six membered ring and an internal disulphate bond under oxidative reaction. DTT is oxidised by PM redox reactive components to its disulphate form, during which DTT donates an electron to dissolved oxygen to generate superoxide, as presented in equation (2-1 to 2-5) (Cho et al., 2005):

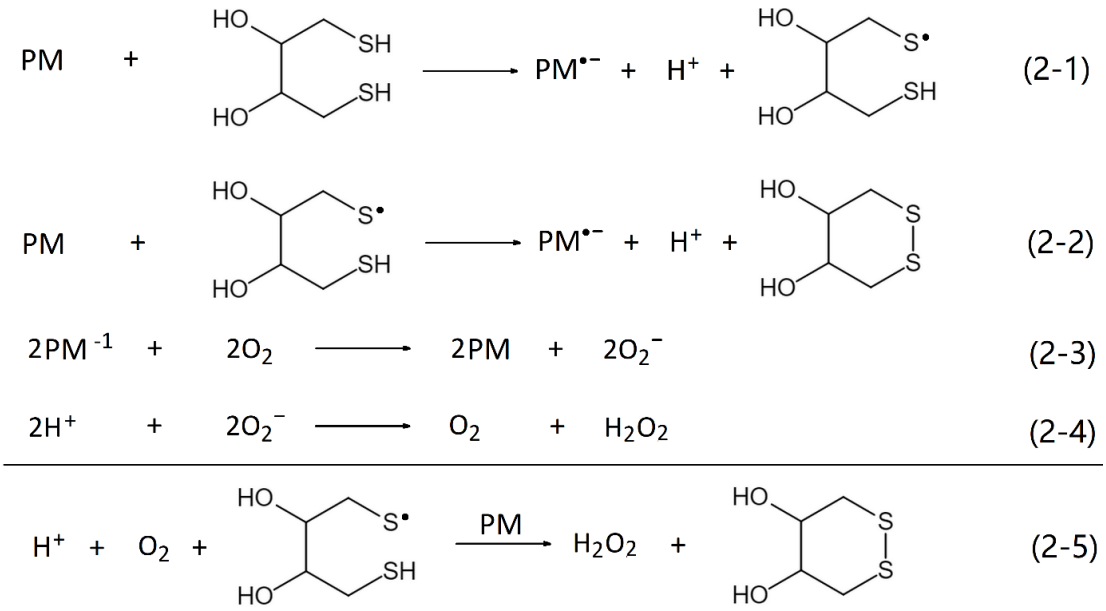

This acellular assay is one of the most commonly applied assays for quantifying PM-related OP, as well as in epidemiological analyses, due to its sensitivity to maximum kinds of catalytic oxidisers in ambient PM, including soluble trace elements, water-soluble inorganic ions (WSIIs), carbonaceous species and polycyclic aromatic species (Cho et al., 2005, Fang et al., 2015, Fang et al., 2017a, Gao et al., 2020b, Liu et al., 2014b, Shang et al., 2012). Therefore, this assay is selected for OP measurement in this study. Detailed procedures of DTT assay are described in Section 3.5.2.

2.2.1.2 AA Assay

Similar with the protocol of DTT assay, AA is a typical antioxidant and used to estimate the PM induced OP by reducing the redox-active species (i.e., transition metals), which finally forms OH•, as presented in following equations (2-6 to 2-11):

$$Asc + 2PM \longrightarrow Asc_{OX} + 2PM^{\bullet -} \quad (2\text{-}6)$$

$$2O_2 + 2PM^{\bullet -} \longrightarrow 2PM + 2O_2^{\bullet -} \quad (2\text{-}7)$$

$$2O_2^{\bullet -} \longrightarrow O_2 + H_2O_2 \quad (2\text{-}8)$$

$$2Fe^{3+} + Asc \longrightarrow 2Fe^{2+} + Asc_{OX} \quad (2\text{-}9)$$

$$2Fe^{2+} + H_2O_2 \longrightarrow {}^{\bullet}OH + Fe^{3+} + H_2O \quad (2\text{-}10)$$

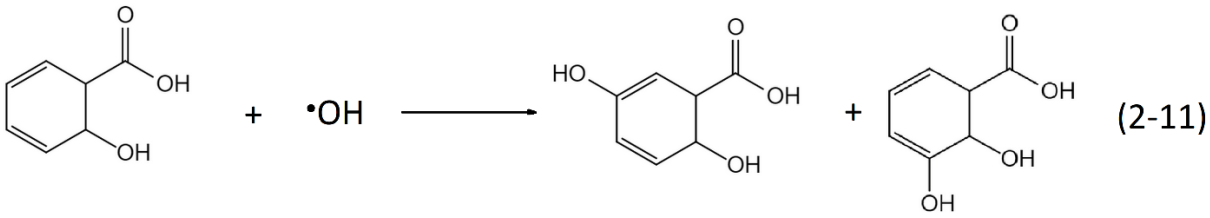

Salicylate 2,5-DHBA 2,3-DHBA (2-11)

The resultant reactive radicals can react with a substrate of salicylic acid to produce 2,5- and 2,3-dihydrobenzoates (DHBAs), which can be measured via liquid chromatography (LC) (DiStefano et al., 2009). The depletion rate of AA has strong correlation with water-soluble trace metals, especially copper (Cu), however, is insensitive to organic species (Fang et al., 2016).

2.2.1.3 ESR

ESR (or EPR) can measure the PM-bound persistent radical species directly (i.e., quinones) and $O_2^{\bullet -}$ and OH• indirectly via a spin trap (Khan et al., 2003). The ability of PM to generate ROS indicates as the electron paramagnetic resonance signals of spin trap 5,5-dimethyl-1-pyrroline-*N*-oxide byproduct 2-hydroxy-5,5-dimethyl-1-pyrrolidinyloxy (DMPO-OH) quartet as the average of overall amplitudes (Hellack et al., 2014, Shi et al., 2003). This method, however, is not suitable for real time ROS measurements, ascribing to that it can only detect the components with relatively long half-life (Khan et al., 2003).

2.2.2 Measurement of Particulate ROS

The ROS within ambient PM is measured via various fluorescence techniques, which is modified from intracellular assays. The principle of such measurements for quantifying PM bound ROS is to dilute particles in a prepared oxidant and measure the spectra of the resultant oxidation products (Bates et al., 2019a), including 2',7'-dichlorofluorescin diacetate (DCFH-DA) assay and 9-(1,1,3,3,tetramethylisoindolin-2-yloxyl-5-ethynyl)-10-(phenylethynyl) anthracene (BPEA-nit) assay, etc.

2.2.2.1 DCFH-DA Assay

One of the most commonly used probes for visualising the particulate ROS is 2',7'-dichlorofluorescin diacetate (DCFH-DA), which is not fluorescent originally, can convert to a fluorescent compound (2',7'-dichlorofluorescin, DCF) once being oxidised in the presence of ROS (Bates et al., 2019a). The proposed acellular mechanism of DCFH-DA is presented in following equation of 2-12 (Hedayat et al., 2015):

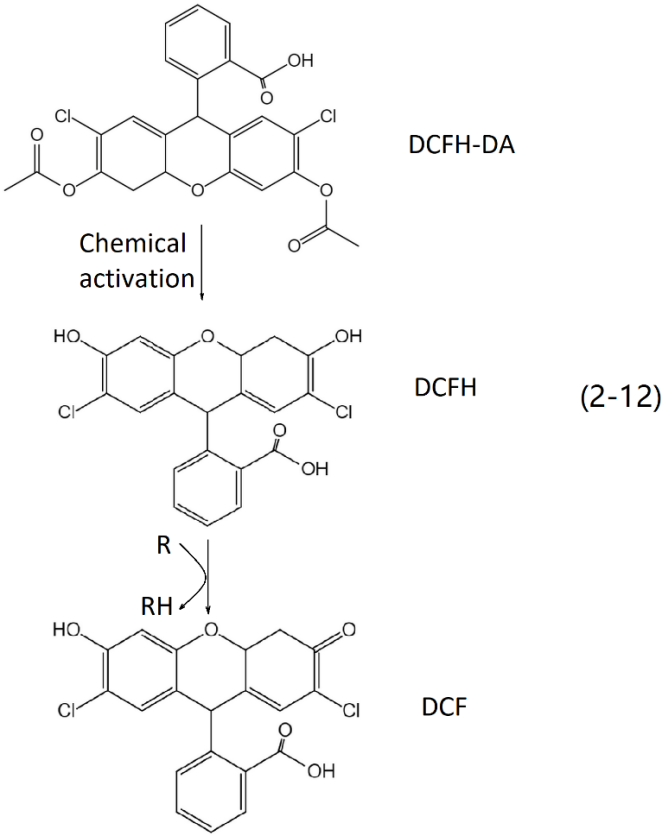

(2-12)

DCFH-DA probe is sensitive to multiple ROS, including OH•, H_2O_2, peroxyl radicals and peroxynitrite, owing to the ease of abstracting the hydrogen atom in the location of 9' position of DCFH molecule (Venkatachari and Hopke, 2008). Such properties of DCFH-DA make it extensively applied for measuring the particulate intrinsic OP of diesel engines (Chuang et al., 2011) and cigarette smoke derived ROS (Huang et al., 2005, Zhao and Hopke, 2012).

2.2.2.1 BPEA-nit Assay

BPEA-nit is the pro-fluorescent nitroxide probe to detect particle exerted ROS, which is formed from 9,10-bis-(phenylethynyl) anthracene (BPEA). BPEA-nit traps sulphur-centred and carbon-centred radicals, hydroxyl and peroxyl radicals under the dimethyl sulphoxide (DMSO) environment. The application of DMSO as a solvent in this assay displays as a

mediator during the reactions between BPEA-nit and different ROS. The detailed reaction produces of BPEA-nit and ROS are presented in Fig. 2.1. This probe has been utilised to quantify the ROS stemmed from combustion sources such as logwood stove and biomass burning (Miljevic et al., 2010b), diesel and biodiesel exhausts (Stevanovic et al., 2013, Surawski et al., 2012) and cigarette smoke (Miljevic et al., 2010a).

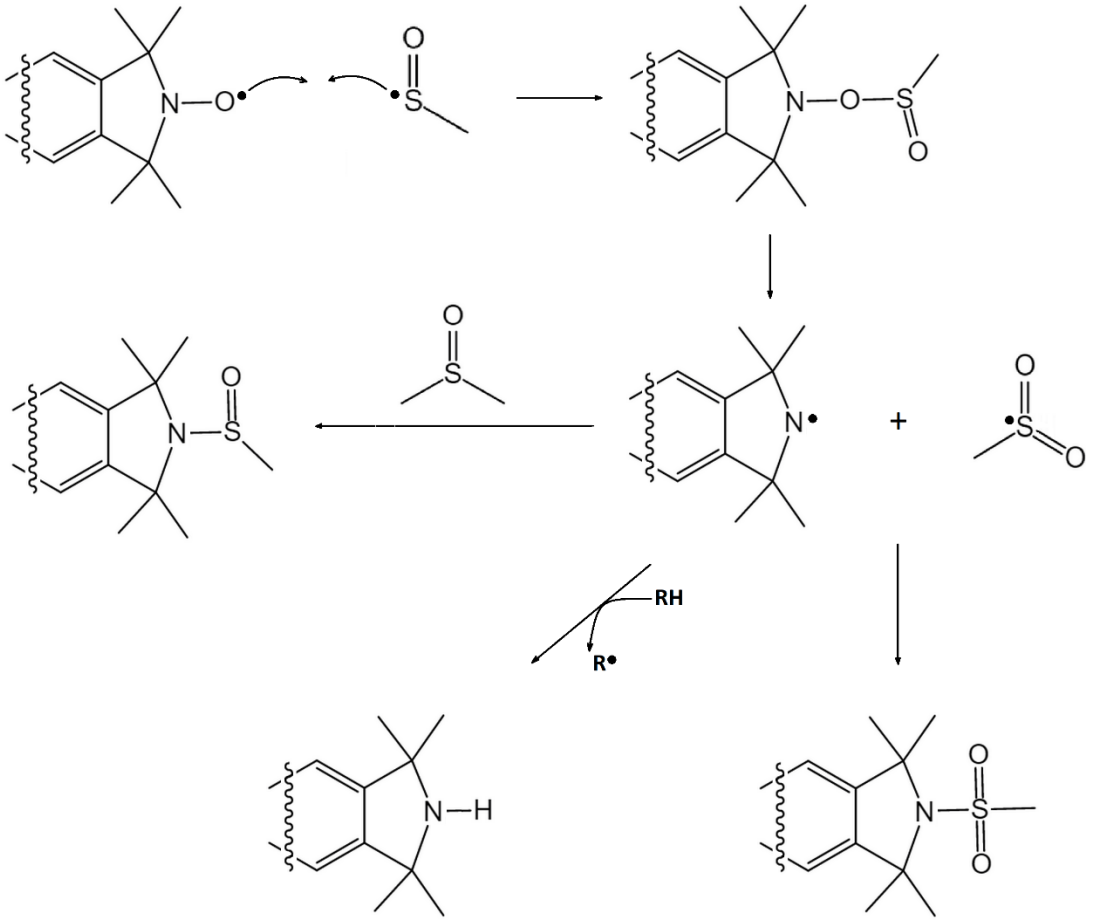

Figure 2.1 The reaction processes of BPEA-nit and ROS in the presence of DMSO

2.3 Effects, Mechanisms and Occurrences of PM Characteristics on OP

2.3.1 Transition Elements

Airborne trace elements exist in a variety of species and exhibit different physical and

chemical properties, having been reported to have diverse detrimental health outcomes on humans (Jin et al., 2019a, Zhao et al., 2021). One of the most widely acknowledged pathogenic mechanisms of trace metals related toxicity is addressing oxygen radical formation (Cho et al., 2005, Daellenbach et al., 2020). Trace elements occur in toxic source emissions, including industrial activities (Quitério et al., 2004), traffic emission (vehicular exhaust and tyre wear) (Lough et al., 2005) and road dust (Birmili et al., 2006) and ship engines (Moldanová et al., 2009), which are released majorly in an insoluble form. Only the soluble fractions of trace metals participate in redox reactions. The trace elements such as Cu, Fe, Zn, Mn, play essential roles in immune regulation and are indispensable for controlling inflammatory response, however, become the dominant species responsible for oxidative capacity generation of ambient aerosols when exposure to the polluted environment with abnormal trace metal accumulation (HaMai and Bondy, 2004, Liu et al., 2020b, Mattioli et al., 2019, Vignesh and Deepe, 2016). Excessive inhalation of these PM bound trace metals could disturb the original delicate homeostasis of body's trace metals, giving rise to an uncontrolled inflammatory response and injured ability to repair inflammatory damage (Liu et al., 2020b, Wallenborn et al., 2009).

Cu is the most redox active trace element in DTT oxidation, followed by Mn, Co, V, Ni, Pb and Fe (Charrier and Anastasio, 2012a). Both Cu and Mn appear non-linear dose-responses of Cu- and Mn- induced DTT depletions, respectively, while the concentration responses for others are linear (Charrier and Anastasio, 2012a, Charrier et al., 2016a). Unlike other metals having measurable DTT consumption rates, the intrinsic DTT oxidation by soluble Fe (II) and Fe (III) is substantially slow. Given that the ambient concentration of particulate Fe is relatively

high in urban areas, it is still significant for DTT loss and commonly considered as the dominant catalytic oxidiser of PM (Charrier et al., 2015, Xiong et al., 2017).

One of the most significant mechanisms of OP inducement from transition metals, including Cu, Mn, Co, Ni and V, is through the Fenton-like reaction, in which the metals are oxidised by H_2O_2 to form OH• radical (Quitério et al., 2004, Shi et al., 1999), as present in following equation:

$$metal^{n+} + H_2O_2 \rightarrow metal^{n+1} + OH\bullet + OH^- \quad (2.13)$$

Haber-Weiss reactions are another important mechanism for ROS generation from metals, involving Cu, Cr, Co and V. In these reactions, metals accept an electron from reductant (i.e., $O_2\cdot^-$), functioning as a catalyst, then donate an electron to dissolved oxygen (i.e., H_2O_2) to generate OH· radical (Shi et al., 1999, Shi and Dalal, 1993, Shi et al., 1998), as present in following equation:

$$metal^{n+1} + O_2^{\bullet-} \rightarrow metal^{n+} + O_2 \quad (2.14)$$

$$metal^{n+} + H_2O_2 \rightarrow metal^{n+1} + OH\bullet + OH^- \quad (2.15)$$

2.3.2 Inorganic Ions

Water-soluble inorganic ions (WSIIs), as the main constituents in ambient PM, account for more than 30% of annual $PM_{2.5}$ (particulate matters with aerodynamic diameter ≤ 2.5 μm) mass, which even increase to 50-60% during polluted days(Cao et al., 2012, Yang et al., 2020). Sulphate (SO_4^{2-}), nitrate (NO_3^-) and ammonium (NH_4^+) (SNA) are mostly treated as secondary inorganic aerosols (SIA), form through gas-to-particle conversion from chemical transformations of precursor gases including nitrogen oxides (NO_x), sulphur dioxide (SO_2) and

ammonia (NH_3) contribute significantly (20–48%) to $PM_{2.5}$ mass (Weijers et al., 2011). High level of SNA contributes to reducing atmospheric visibility and exacerbate the haze formation (Ji et al., 2020, Song et al., 2019). Other WSIIs including lithium (Li^+), sodium (Na^+), potassium (K^+), magnesium (Mg^{2+}), calcium (Ca^{2+}), fluoride (F^-), chloride (Cl^-), bromide (Br^-) and phosphate (PO_4^{3-}) have several significant roles in terms identifications of emission sources and catalytic effects on formation of SIA and secondary organic aerosol (SOA) because of several reasons including aerosol acidity and existing particle surfaces (Sun et al., 2013).

Chloride (Cl^-), a typical indicator of sea salt aerosol, is an essential trace reactant involved in the processes of oxidation chemistry in the mid-latitudes (Chi et al., 2015, Osthoff et al., 2008). For sea salt particles, active Cl^- instead of chloride bound in atmospheric particles is considered to be released through heterogeneous reaction with dinitrogen pentoxide (N_2O_5) at the surface of sea spray particle, which produces nitryl chloride ($ClNO_2$). For those aerosol particles that do not initially contain Cl^-, the yield of $ClNO_2$ is from gaseous Cl (mainly HCl) uptake by N_2O_5 through heterogeneous processes, where the HCl ultimately stems from SS particles through acid displacement (von Glasow, 2008). The reaction equation is shown as follow:

$$HCl_{(g)} + N_2O_{5\,(g)} \xrightarrow{het} ClNO_{2\,(g)} + HNO_{3\,(aq)} \quad (2.16)$$

$$ClNO_2 + \text{light}\ (\lambda < 840\ \text{nm}) \rightarrow Cl^- + NO_2 \quad (2.17)$$

Accumulation of $ClNO_2$ is stable at night-time, and photolysed rapidly to active chlorine radical and NO_2 after sunrise under deficiencies of other oxidant and radicals (e.g., OH•, NO_3). Reactive chlorine radical is the dominant oxidant and more reactive than OH• and NO_3, which oxidises volatile organic compounds (VOCs) that do not react with NO_3 directly (Osthoff et

al., 2008). This reaction produces peroxy radicals, which results to O_3 formation in the existence of NO_x.

Particulate SNA, while not redox active or directly produce ROS, are positively correlated with OP responses (Daellenbach et al., 2020, Fang et al., 2015, Longo et al., 2016). The SNA, especially SO_4^{2-}, can enhance the PM oxidative capacity through acidifying the ambient aerosols. There was a historical record of linkage between particle strong acidity of SO_4^{2-} and aerosol toxicity to detrimental health outcomes (Koutrakis et al., 1992, Koutrakis et al., 1988, Spengler et al., 1989). Since SNA are high hygroscopicity, they contributes to the formation of aqueous drops and provide H^+ to dissolve metals, facilitating the solubilities of metals and thus inducing an indirect influence on ROS generation (Fang et al., 2017a).

2.3.3 Organic Carbon

2.3.3.1 Carbonaceous Species

Organic carbon (OC) and elemental carbon (EC), known as carbonaceous aerosols having significant contributions (20–50%) to $PM_{2.5}$ mass are associated with many urban environmental impacts including local human health effects, reductions in atmospheric visibility and regional to global climate change (Tiwari et al., 2013). The emission of particulate EC occurs mostly from primary combustion processes of fossil fuels, whereas OC is generated through both primary combustion sources and secondary transformation (SOC, secondary organic carbon) through gas-to-particle conversion processes of organic precursor gases like volatile organic compounds (VOCs) (Wang et al., 2015).

Evidence shows significant positive correlations between OC, EC and/or water-soluble OC

(WSOC) and volume-normalised DTT oxidation (Liu et al., 2014b, Patel and Rastogi, 2018, Vreeland et al., 2017). The OP induced from OC and WSOC is mainly ascribed to their large fraction of water-soluble organic catalytic oxidisers, including the humic-like substances (HULIS) from biomass burning and secondary aerosol (Verma et al., 2009a, Verma et al., 2009b, Verma et al., 2012). Some studies also revealed the DTT decay from water insoluble OC (WIOC), such as quinones (Saffari et al., 2014a, Verma et al., 2015b). EC is redox inactive and primary in nature. Its positive correlation with OP of particles is often attributed to other chemicals adsorbed to its surface (Saffari et al., 2014a).

2.3.3.2 Polycyclic Aromatic Hydrocarbons (PAHs)

Particulate OC comprised of mostly organic compounds having substantial components of mutagens and/or carcinogens include polycyclic aromatic hydrocarbons (PAHs) and many other groups of chemical compounds (Chou et al., 2017). PAHs distribute widely in particles and are originated mainly from anthropogenic sources, including coal burning for domestic heating and cooking, industrial activities, biomass fuel burning, vehicle exhausts and road dust in urban environments (Han and Naeher, 2006, Kim et al., 2011, Maertens et al., 2004). Particulate PAHs are classified into two groups based on their molecular weight, i.e., LMW (low molecular weight) with two to three rings, and HMW (high molecular weight) with four to seven rings. LMW PAHs are normally gaseous in nature, whereas HMW PAHs are mostly in particulate phase due to their low water vapour pressure. From health implication point of view HMW PAHs have more potential to bio-accumulate in human body to cause serious implication and damages compared to that of LMW PAHs (Wei et al., 2015).

PAHs are not redox reactive for DTT oxidation. However, the concentrations of PAHs were found to be correlated with DTT consumption rate, the correlation coefficient of which was from medium ($r^2 = 0.32$) to strong ($r^2 = 0.82$), depending on the variability of emission sources (Charrier and Anastasio, 2012a, Cho et al., 2005). Such phenomena are explained by a variety of atmospheric reactions, transport and degradation after PAHs releasing, which then may produce polar components such as nitro-PAHs and quinones onto particles, which are redox active and more mutagenic and carcinogenic than parent PAHs (Cave et al., 2018). Nonetheless, PAHs play pivotal role in PM-related OP since they are the typical tracers for the common sources of organic components like quinones.

2.3.3.3 Quinones

Airborne quinones are the oxygenated derivatives of PAHs (Shang et al., 2014, Walgraeve et al., 2010). They are emitted from either incomplete combustion (i.e., vehicular exhausts, biomass fuel burning), or form through atmospheric photochemical transformation from parent PAHs. They can also be formed via enzymes in vivo (Walgraeve et al., 2010). Quinones and their reduction products, hydro-quinones and semi-quinones are of interests due to their overt toxicity to health endpoints, including formation of covalent bonds with tissue macromolecules (Cadenas et al., 1992, Henry and Wallace, 1996). The quinone-elicited OP measured by DTT assay has been well-documented by pioneer studies, including 1,2-naphthoquinone (1,2-NQ), 1,4-napthoquinone (1,4-NQ), phenanthrenequinone (PQ) and 1,4-anthraquinone (1,4-AQ), providing direct evidence that quinones can generate ROS by initiating redox cycling reactions (Li et al., 2012, Shang et al., 2012). Often the PQ was used as the positive control in DTT assay

(Cho et al., 2005, Fang et al., 2014, Saffari et al., 2014a). Although quinones exhibit high intrinsic OP values, the low concentrations of quinones (≤ 2 ng m^{-3}) in the ambient PM make emerges as the non-dominant drivers to induce PM oxidative burden (Charrier and Anastasio, 2012a).

2.3.4 Interactions between Particulate Compounds

Particle species such as transition metals (Cu, Fe, Mn, V, Ni), water-soluble organic carbon (WSOC), humic-like substances (HULIS) and quinones (1,2-naphthoquinone, 1,4-napthoquinone, phenanthrenequinone) have been typically examined and found to be responsible for OP activity by dithiothreitol (DTT) assay (Cho et al., 2004). Nonetheless, there is still debatable about whether or not a simple summation of relative contribution of chemical components could represent the overall OP of ambient PM.

Growing studies have confirmed the synergistic and/or antagonistic interactions among PM species and antioxidants which could alter the redox properties. The interaction effects among PM chemical species are varied via the measurements of different acellular. Lin and Yu (2020) found that Mn in PM exhibits synergistic and antagonistic effects in DTT oxidation when mixed with quinones and HULIS, respectively. The mixtures of Cu with 1,2-NQ or HULIS antagonistically oxidises DTT with a consumption rate lower than the sum of individual redox active species (Lin and Yu, 2020). Fe interacts additively with quinones and HULIS compounds in DTT consumption, but synergistically in OH· production (Charrier et al., 2015, Yu et al., 2018). In contrast, Wang et al. (2020a) and Guo et al. (2020) reported the antagonistic interactions in the mixtures of Mn-Cu, Mn-Fe and 1,4-NQ-PQ in both DTT assay and a Chinese

hamster ovary cells assay, while Fe and 1,2-NQ exhibited strongest synergistic interactions with other components (i.e., Cu, Mn, 1,4-NQ). Therefore, owing to a wide variety of complex interactions of PM species, it becomes a difficult and challenging task to deduce the key drivers of OP through focusing just on those generally recognized redox-active components.

2.4 Occurrence of PM-induced OP in China

The concentrations of OP induced from ambient particles in China have been reported in recent years, most of which are focused on the PM elicited OP in the urban areas (Liu et al., 2014b, Liu et al., 2018b, Lyu et al., 2018, Wang et al., 2015). The summary of field studies on PM-related OP, normalised in volume (OP_v, in unit of nmol min^{-1} m^{-3}) and mass (OP_m, in unit of nmol min^{-1} μg^{-1}), of various cities in China has been presented in Table 2.1.

There is growing evidence that PM-related OP, including OP_v and OP_m, exhibit distinctive temporal variations (Liu et al., 2020a, Yue et al., 2018). Wang et al. (2020b) reported a strong seasonality of OP in Xi'an, Shaanxi Province, with highest OP_v during winter (0.67 nmol min^{-1} m^{-3}), followed by spring (0.53 nmol min^{-1} m^{-3}), summer (0.50 nmol min^{-1} m^{-3}) and autumn (0.40 nmol min^{-1} m^{-3}). The OP_m, however, the was highest during summer (15. 67 nmol min^{-1} μg^{-1}). Similar observation of highest OP_m was also reported by another study in Beijing (Yu et al., 2019). Spatial variation of OP_v is also investigated by recent studies. The $PM_{2.5}$ eliciting OP_v is obviously high in urban area of Beijing and coastal areas of Bohai Sea, the yearly average of which is from 6.8 to 12.26 nmol min^{-1} m^{-3}, while the OP_v is much lower in Hangzhou (0.62 nmol min^{-1} m^{-3}) and Xi'an (0.53 nmol min^{-1} m^{-3}). Such differences are also explained by the different source types and chemical compositions. Liu et al. (2020a) compared the oxidative

capacities of $PM_{2.5}$ in urban site, industrial area and botanical garden in Wuhan, Hubei Province, and observed that the highest OP_v of $PM_{2.5}$ in summer was emitted from industrial activity (4.50 nmol min^{-1} m^{-3}), followed by botanical garden (2.20 nmol min^{-1} m^{-3}) and urban area (1.80 nmol min^{-1} m^{-3}).

All the studies mentioned above have been based on the OP induced from water-soluble fraction of ambient particles. Since particles contain a large variety of hydrophobic components (i.e., quinones, HULIS), most of which are organic and can contribute to the enhancement of oxidative burden of PM (Cao et al., 2021a). Therefore, more attention should be paid to exploring the measurements of OP induced from particulate organic fraction and redox-active organic species.

Table 2.1 Overview of field studies on OP of ambient particles via DTT assay from different areas of China

Location	Particle Size	[a] OP_v	[b] OP_m	Environment	Extraction solvent	Sampling Period	Study
Beijing	$PM_{2.5}$	12.26 ± 6.82	0.13 ± 0.10	Urban	Water	4 seasons, 2015-2016	(Yu et al., 2019)
Tianjin; Yantai; Jinzhou	$PM_{2.5}$	6.8 ± 3.4	1.70×10^{-3}-0.08	Urban	Water	4 seasons, 2015-2016	(Liu et al., 2018b)
Xi'an	$PM_{2.5}$	0.53	0.01	Urban	Water	4 seasons, 2017	(Wang et al., 2020b)
Wuhan	$PM_{2.5}$	1.80 ± 0.20	0.02 ± 0.00	Urban	Water	Summer, 2012	(Liu et al., 2020a)
Wuhan	$PM_{2.5}$	4.50-8.30	0.03-0.05	Industrial area	Water	Summer and spring, 2012	(Liu et al., 2020a)
Wuhan	$PM_{2.5}$	2.20-2.50	0.03-0.05	Botanical garden	Water	Summer and spring, 2012	(Liu et al., 2020a)
Shanghai	$PM_{0.056\text{-}18}$	0.07-0.19	0.04-0.06	Urban	Water	Winter, 2015; Spring, 2016	(Lyu et al., 2018)
Hangzhou	$PM_{2.5}$	0.62	6.39×10^{-3}	Urban	Water	4 seasons, 2016-2017	(Wang et al., 2019a)

[a] The unit for OP_v is nmol min^{-1} m^{-3};
[b] The unit for OP_m is nmol min^{-1} μg^{-1}.

2.5 Respiratory Deposition of Particle-induced OP

Numerous studies have revealed that the toxic metric of lung deposited dose is more relevant than ambient concentrations of PM (Fang et al., 2019, Schmid and Cassee, 2017). Coarse particles (i.e., PM_{10}) primarily deposit in the upper reaches of respiratory system (head or nasal airway), the fine particles ($PM_{2.5\text{-}3.2}$, PM with aerodynamic diameter ranged from 2.5 to 3.2 μm) are mainly retained in tracheobronchial region, and ultrafine particles ($PM_{0.18\text{-}1}$) can penetrate into deeper area of pulmonary region (Andrade et al., 2020, Falcon-Rodriguez et al., 2016). The oxidative stress generated in the extrathoracic airway would give rise to exacerbating the inflammation associated with neurodegenerative or nasal diseases, while those in deeper respiratory tracts would lead to systematic or pulmonary diseases (Fang et al., 2019, Schmid and Cassee, 2017). Particle size is associated with varied toxic effects. Some studies considered the PM with smaller sizes is considered to exhibit a stronger toxicity and pose a higher risk to health endpoint owing to their easier accessibility to deeper respiratory tracts compared to larger particles (Andrade et al., 2020, Kumar et al., 2014). Others, however, suggested that coarse particles are more potent in addressing DNA degradation, hemolysis and pro-inflammatory cytokines, and even have stronger effects in inhibiting cell proliferation than smaller particles (Hetland et al., 2004, Osornio-Vargas et al., 2011a). Those inflammation caused by inhalation of ambient PM are generally related to a cellular imbalance toward an excessive ROS production, the capability which is defined as OP of particles (Cho et al., 2005).

There is mounting evidence that chemical composition and their potential sources bear most responsibility for OP induced from ambient PM, which is size-dependent (Birmili et al., 2006, Fang et al., 2019, Verma, 2015, Wu et al., 2021a). Coarse particles tend to be emitted

from natural sources, including volcanic emission, sea salts and road dust resuspension, which may release substantial amount of the source tracers of Cu, Fe, Ba, Na^+, Cl^-, PAHs, and minerals (e.g., silicates, metal oxides, clay minerals or calcium carbonates), etc. Most of them are insoluble forms, leading to ROS generation through entering the cell by engulfment or binding to a cell surface (Fang et al., 2017a, Schoonen et al., 2006). Fine and ultrafine particles are produced from anthropogenic sources (i.e., biomass burning, traffic emission, industrial activities) and secondary processes. They are likely to penetrate into lower respiratory regions (i.e., pulmonary region). The ability to address OP from these PM is relevant to SNA, SOA (i.e., quinones) and transition metals (Cu, Fe, Mn, Zn, Ni, V) (Andrade et al., 2020, Gao et al., 2020c). Since the mutagenic activity and redox activity varied dependently with particle size, the deposited dose of OP induced from size-segregated PM may act as a pivotally determining factor in the respiratory deposited behaviour of PM-induced OP, which controls the toxicological mechanism from particulate redox active species (Guo et al., 2019, Wu et al., 2021a).

Currently, growing studies start to concern size-distributions of PM related OP and OP depositions in different respiratory regions (Andrade et al., 2020, Fang et al., 2019, Fang et al., 2017b, Guo et al., 2019, Wu et al., 2021a). However, few of them considered the potential source contributions to the OP, as well as the deposited doses of the dominant particulate catalytic oxidisers and their induced OP in different size modes. In this study, I will fill this research gap by estimating the size distributions of contributions from sources and specific redox cycling catalysts to OP of ambient particles.

2.6 Causal Links between Respiratory Health Effects and OP

Exposure to ambient particles is associated with adverse health endpoint (Andrade et al., 2020, Bates et al., 2019b, Charrier and Anastasio, 2012a, Fang et al., 2019, Guo et al., 2019, Liu et al., 2020b, Lyu et al., 2018). Previous studies have provided evidence that OP of ambient aerosols is a strong indicator to offer more information about health risks of PM beyond the risks captured by mass concentrations (Andrade et al., 2020, Bates et al., 2019b, He et al., 2021). The mechanism of PM related diseases is considered as the inflammation induced from cellular imbalance via excessive production of ROS.

Positive correlations between PM induced DTT oxidation and cardiorespiratory diseases have been reported. Hospital admissions, emergency department visits and mortality are considered most often outcomes for respiratory or cardiovascular causes (Gao et al., 2020c). A 14-year study conducted in Netherlands revealed that the DTT oxidation by $PM_{2.5}$ had strong correlations with respiratory health markers, including forced respiratory volume, rhinitis and asthma, which was estimated through land-use regression model (Yang et al., 2016). He et al. (2021) measured the lung function, airway mechanics, airway inflammation and asthma symptom score of 43 asthmatic children and concluded that the increase in personal daily exposure to OP of $PM_{2.5}$ have great influences on enhancements of total airway resistance and airway impedance, as well as the reduction of lung function and worsened scores of individual asthma symptoms and total symptoms. In addition, a cross-sectional study also suggested a relationship between DTT decay and diabetes prevalence (Gao et al., 2020c). However, the conclusions that can be drawn about the relationship between OP and health risk are still limited without considering the effect of lung deposition of OP to human health.

The deposited dose of particulate oxidative burden varies distinctively with different deposition efficiencies and particle sizes into different respiratory tracts (Guo et al., 2019, Lyu et al., 2018, Wu et al., 2021a). Coarse particles are likely to retain in head or nasal airways. A fraction of them is possibly hindered by rhinothrix through impaction processes and thus has a limited impact on health effect (Lyu et al., 2018). In contrast, the PM with smaller sizes, including fine and ultrafine particles, along with various particulate catalytic oxidisers, can penetrate into deeper regions of tracheobronchial region and pulmonary region. These particles are believed to be more harmful to human health since they commonly contain higher intrinsic oxidative capacities compared to coarse particles, especially for the ultrafine particles, the harmfulness of which is also due to their easy access to blood and difficult to eliminate via inhibiting the phagocytosis by alveolar macrophages and thus inducing pulmonary inflammation by entering the pulmonary interstitial sites (Sioutas et al., 2005). However, all studies mentioned above have been based on the overall and size distributions of PM-induced OP along with the chemical characterisation, limited effort has been devoted to exploring the dominant redox-active species or source contributions to size-dependent OP and their deposited doses in human lungs.

Chapter 3 Methodology

3.1 Location of Sampling Sites

Ningbo (28º51' – 30º33' N, 120º55' – 122º16' E), as a typical coastal city, lies in the south of Yangtze River Delta (YRD) and faces the East China Sea. The climate conditions in Ningbo are featured by the sub-tropical monsoon, with northwest and southeast winds prevailing during winter and summer. The annual average ambient temperature and relative humidity (RH) are 18.08 °C and 76%, respectively. The ambient temperature reaches its maximum in August (28.98 °C) and minimum in January (5.35 °C). Lower RH is usually observed in winter (73%) as well as spring (73%), due to the influences of cold dry air from Siberian in winter, while the higher occurs in summer and autumn (78% and 80%, respectively) is ascribed to dominant southeast winds and even typhoons bringing about humid warm air from the East China Sea. The annual mean wind speed (WS) is between 2 – 4 m s^{-1} in the study site.

In this project, aerosol samples were collected on the rooftop of Sir Peter Mansfield Building (PMB) in University of Nottingham Ningbo China (UNNC, 29.80º N, 121.56º E), which is about 10 m above the ground. The sampling site is located in the south of Ningbo city, approximately 10 km away from the central business district (CBD). As the sampling site is away from the immediate impacts of local sources (e.g. industrial emissions, traffic exhausts, coal combustions), it can be characterised as an intermediate transition zone that is affected by the mixed pollutions from both natural and anthropogenic sources. Our previous monitoring program showed small spatial variability of PM concentrations in this region, and thus UNNC can represent the overall air pollution level in Ningbo (Xu et al., 2019). The location of sampling site is shown in Fig. 3.1.

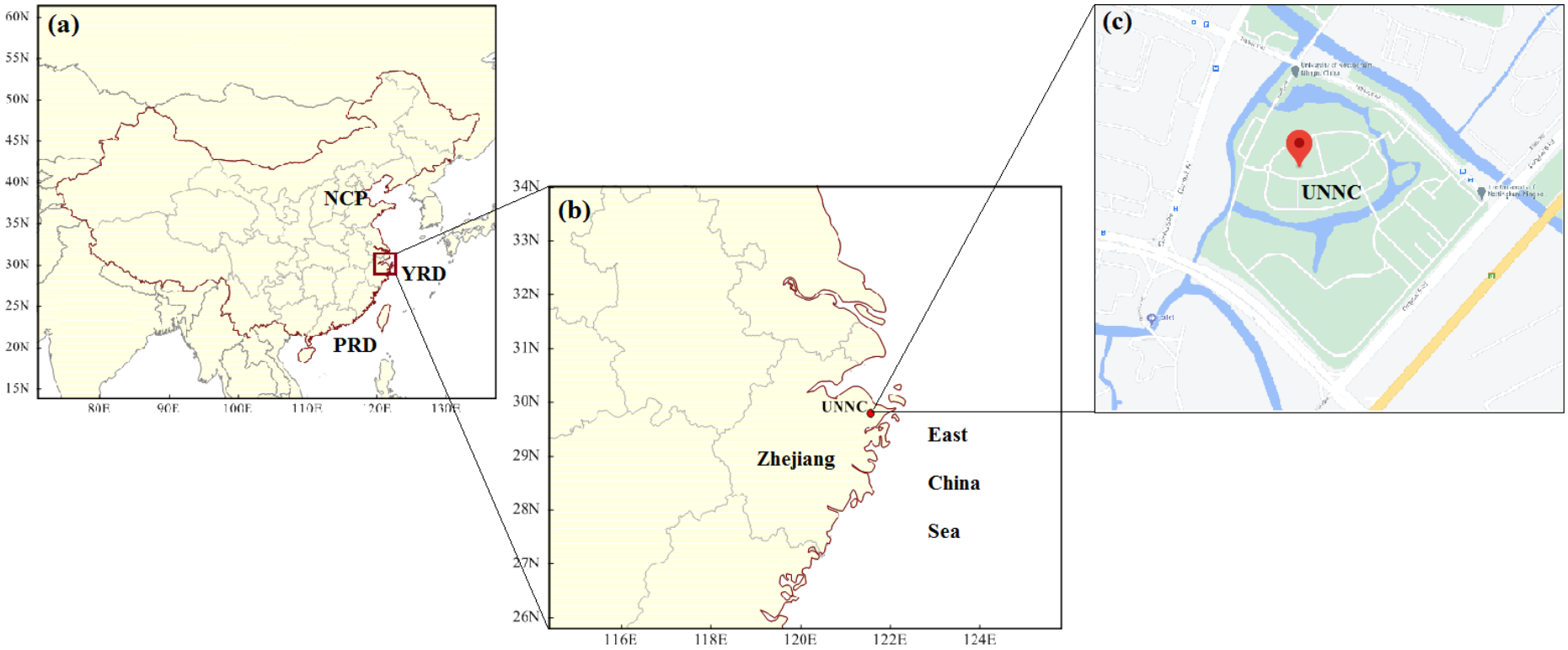

Figure 3.1 Location of sampling site: (a) China (NCP: North China Plain; YRD: Yangtze River Delta; PRD: Pearl River Delta); (b) Zhejiang Province; (c) UNNC

3.2 Sampling Instrument

Two instruments have been used for field sampling (Table 3.1).

Table 3.1 Summary of samplers used in this study

Instrumentation	Purpose
Universal Air Sampler	To collect $PM_{2.5}$ in the field by using pre-combusted quartz fibre filters.
Six-Stage High Volume Cascade Air Sampler	To collect TSP (total suspended particulate) with six different ranges of particle aerodynamic sizes (0.0 – 0.49, 0.49 – 0.95, 0.95 – 1.50, 1.50 – 3.00, 3.00 – 7.20, 7.20 - ∞).
Weather Station in Ningbo Meteorological Bureau	To record all the relevant meteorological parameters and online monitoring gaseous pollutants (air temperature, relative humidity (RH), wind speed, wind direction, solar radiation, sunshine duration; $PM_{2.5}$, SO_2, NO_2, CO, O_3) during sampling period.

3.2.1 Universal Air Sampler

The Model 310 Universal Air Sampler^{TM} (UAS^{TM}) is a general-purpose air sampler for atmospheric aerosol. Air is sampled at 285 L min^{-1} for $PM_{2.5}$ collection. The pre-combusted quartz filters (Pallflex Tissuquartz, Life Science, 8 × 10 inch) were placed on the clean gasket to capture atmospheric particles for 23 h. Field blank samples were obtained twice for each season. Fresh filters were pre-baked at 550 °C for 4 h to remove residual impurities and wrapped in the aluminium foil papers. Before and after sampling, the quartz filter was

equilibrated at temperature 25 ± 1 °C and RH of 30 ± 5% for 24 h, and weighed to obtain the particle mass. After sampling and weighing, filters were stored at -20 °C in the fridge until experimental analysis. The sampling period is listed in Table 3.2.

3.2.2 Six – Stage High Volume Cascade Air Sampler

The Six-Stage High Volume Cascade Air Sampler (Model: TE-230, Tisch Environmental, Inc. USA) was used for sampling the TSP with six different ranges of particle aerodynamic sizes (0.0 – 0.49, 0.49 – 0.95, 0.95 – 1.50, 1.50 – 3.00, 3.00 – 7.20, 7.20 - ∞). For each sampling, five of 5.6" × 5.4" and one of 8" × 10" quartz fibre filters (Pallflex Tissuquartz, Life Science) were used to capture ambient particles simultaneously at a flow rate of 1.03 m^3 min^{-1} and lasted for 23 h. Field blank filters were obtained twice for respective high and low pollution periods. Processes of pre-cleaning, weighing and storing filters were the same as the processes mentioned in Section 3.2.1.

Table 3.2 Sampling schedule of this study

Sampling Site	Sampling Period	Amount of Sample	Purpose
On the rooftop of PMB (UNNC)	Oct 2017 - Aug 2018	58 [a]	To obtain the $PM_{2.5}$ samples for seasonal variation analysis; To investigate the ROS generation induced from ambient $PM_{2.5}$;
On the rooftop of PMB (UNNC)	Oct 2017 - May 2018	138 [b]	To obtain the size-segregated TSP (6-stage); To compare the chemical species of TSP between different aerodynamic size ranges; To conduct the OP values of size-segregated particles for toxicological study;

[a] Sampling was conducted continuously for approximately 2 weeks for each season (Autumn: Sep-Nov; Winter: Dec-Feb; Spring: Mar-May; Summer: Jun-Aug), the sampling periods were selected randomly excluding the rainy days. No replicate sample was collected in this study.

[b] The sampling frequency for size-fractionated PM was the same as that for $PM_{2.5}$, however, the 20 sampling days with respective highest (N=10) and lowest (N=10) TSP concentrations were selected to better compare the PM differences in various aspects.

3.3 Materials

3.3.1 Reagents

All the chemical reagents used for DTT assay were from Sigma – Aldrich (Shanghai, China): DL-Dithiothreitol (DTT) (99.0%, CAS 3483-12-3), ethylenediaminetetraacetic acid (EDTA) (99.995%, CAS 60-00-4), 5, 5'-dithiobis (2-nitrobenzoic acid) (DTNB) (98.0%, CAS 69-78-3), trichloroacetic acid (TCA) (99.0%, CAS 76-03-9), Trizma® Base (Tris-Base) (99.9%, CAS 77-86-1), chelex resin 100 sodium form (chelex resin) (CAS 11139-85-8), potassium phosphate monobasic (KH_2PO_4) (99.0%, CAS 7778-77-0), potassium phosphate dibasic (K_2HPO_4) (99.0%, CAS 7758-11-4).

The authentic standards for water-soluble inorganic ions (WSII) including 6 cations (lithium (Li^+), sodium (Na^+), potassium (K^+), magnesium (Mg^{2+}), calcium (Ca^{2+}), ammonia (NH_4^+)) and 5 anions (fluorine (F^-), chloride (Cl^-), nitrate (NO_3^-), phosphate (PO_4^{3-}), sulphate (SO_4^{2-})), were obtained from Sigma – Aldrich (St. Louis, MO, USA). Eluent used for cation measurements was methanesulphonic acid (MSA) (99.0%, CAS 75-75-2, Sigma-Aldrich, Shanghai, China), and for anions was a mixture of sodium carbonate (Na_2CO_3) (99.0%, CAS 497-19-8, Sigma – Aldrich, Shanghai, China) and sodium bicarbonate ($NaHCO_3$) (99.7%, CAS 144-55-8, Sigma – Aldrich, Shanghai, China).

The standards for water soluble 18 trace elements were used as follow: copper (Cu), plumbum (Pb), ferrum (Fe), alumium (Al), manganese (Mn), vanadium (V), chromium (Cr), cerium (Ce), cadmium (Cd), zinc (Zn), cobalt (Co), nickel (Ni), silver (Ag), arsenic (As), strontium (Sr), bismuth (Bi), stibium (Sb), barium (Ba) (Sigma – Aldrich, St. Louis, MO, USA). Concentrated nitric acid (HNO_3) (65% GR grade, Sinopharm Chemical Reagent Co., Ltd.) was for acidifying the aqueous trace element samples that were extracted from PM samples.

The 0.2 mg mL^{-1} standard mixture USEPA 610 including 16 priority PAHs in dichloromethane (DCM): methanol (MeOH) (1:1) was obtained from AccuStandard (USA): naphthalene (Nap), acenaphthene (Ace), acenaphthylene (Acy), fluorene (Flu), phenanthrene (Phe), anthracene (Ant), fluoranthene (Flt), pyrene (Pyr), benzo[a]anthracene (BaA), chrysene (Chr), benzo[b]fluoranthene (BbF), benzo[k]fluoranthene (BkF), benzo[a]pyrene (BaP), indeno[1,2,3-cd]pyrene (Ind), dibenzo[a,h]anthracene (DBA) and benzo-[ghi]perylene (Bpe). Solvent used for extraction of PM related PAHs was CH_2Cl_2 (99.9% pesticide grade, CAS 75-09-2, ANPEL Laboratory Technologies (Shanghai) Inc.).

Standard for quinone measurement was 1, 2-naphthoquinone (1, 2-NQ) (95.0%, CAS 542-42-5, Tokyo Chemical Industry, Japan). Solvents used in these experiments were DCM (HPLC grade, CAS 75-09-2, ANPEL Laboratory Technologies (Shanghai) Inc.), MeOH (HPLC grade, CAS 67-56-1, ANPEL Laboratory Technologies (Shanghai) Inc.), ammonium acetate (NH_4COOCH_3) (99.0% HPLC, CAS 631-61-8, Macklin, Shanghai, China) and formic acid (HCOOH) (96.0%, CAS 64-18-6, Sigma – Aldrich, Shanghai, China).

3.3.2 Acquisition of Monitoring Online Data

The meteorological parameters (air temperature, RH, wind speed, wind direction, solar radiation and sunshine duration) and ambient concentrations of online monitoring gaseous pollutants (SO_2, NO_2, CO, O_3) and $PM_{2.5}$ applied in this study were obtained from Ningbo Meteorological Bureau (Wanli Monitoring Station), which is less than 500 m away from the sampling site.

3.4 Buffer Preparation and Treatment

3.4.1 Tris-Base and EDTA Buffer (TE-Buffer) Preparation

TE-buffer was used for DTNB solution preparation in this study. It contained 0.4 M Tris-base and 20 mM EDTA, with concentrated HCl adjusting the pH value of TE-buffer to 8.9.

3.4.2 Potassium Phosphate Buffer Preparation and Treatment

Potassium phosphate buffer solution (0.1 M) was prepared with 77.8 mM KH_2PO_4 and 22.2 mM K_2HPO_4 in de-ionised water, at a pH value of 7.4. Following Charrier and Anastasio

(2012b) and Holmén et al. (2017), the prepared potassium phosphate buffer was pre-cleaned with Chelex resin, which is a cation exchange resin, to eliminate trace metals and therefore reduce background oxidation. New Chelex resin was poured into an acid-rinsed glass chromatography column (3 cm diameter, 50 cm height) and washed with Milli-Q water until the pH value of the effluent is 7. Then the Chelex resin was first rinsed with one column volume of potassium phosphate buffer and discarded. The remaining potassium phosphate buffer was treated by the Chelex column at a rate of around one drop per second, and collected in an acid washed Teflon bottle.

3.5 Sample Preparation and Chemical Analysis

3.5.1 Filter Extraction and Preparation

Designated fractions of quartz filter sample were ultrasonically extracted by different solvents for various experimental analysis. We considered that the particles collected on the fraction of filter can represent the overall filter, since the aerosols collected by the samplers are evenly distributed on the filter.

3.5.1.1 Water Extraction

For the extraction of PM-related water-soluble fractions, all extractions were conducted using quartz fibre filters were extracted by 20 mL of deionised water and ultra-sonicated for 45 min. Aqueous $PM_{2.5}$ extracts were filtered using poly-tetrafluoroethylene (PTFE) 0.45 μm pore syringe filters and stored at 4 °C for further OP measurement via DTT assay, analysis of water-soluble inorganic ions (WSIIs), water soluble trace elements and water-soluble organic carbons (WSOC).

3.5.1.2 Methanol Extraction

Methanol extraction was applied for the analysis of organic components related OP, aerosol samples were ultra-sonically extracted using 20 mL of methanol for 45 min, filtered with PTFE 0.45 μm pore syringe filters. The extracts were collected in the sealed polypropylene bottles and stored at 4 °C for further concentration (Section 3.5.1.5).

3.5.1.3 Accelerated Solvent Extraction (ASE)

ASE (Dionex, Model ASE 350) was conducted for PAHs extraction from quartz filters. The filters were cut into pieces and well mixed with diatomaceous earth in 34 mL stainless steel cells of Dionex (ASE 350). The diatomaceous earth applied in this study had been pre-tested to make sure there was no PAHs contained. Extractions were performed with the increasing heat and pressure to 100 °C and 1500 psi within 5 min. The static extraction was held for 5 min, followed by the solvent rinsing with DCM (60% of rinse volume) and purging with nitrogen for 90s. All extractions were conducted in duplicates (2 cycles). The total extraction run time was approximately 25 min for each sample. All extracted analytes were collected in vessels for further concentration (Section 3.5.1.5).

3.5.1.4 Extraction of Quinones

Quinones were extracted from filters with a mixture of pure DCM and MeOH (v/v, 1:1) and ultra-sonicated for 1 h at 25 °C. After filtered with PTFE 0.45 μm pore syringe filters, the extracted analytes were collected in the sealed polypropylene bottles for further concentration

(Section 3.5.1.5).

3.5.1.5 Rotary Evaporator

The extracted analytes of PAHs, quinones and the organic fractions (for OP measurement) were concentrated by rotary evaporator (Biotage TurboVap II). For the measurements of PAHs and organic fractions, the extracts were blown by gentle nitrogen stream at 35 °C and reduced to 1 mL, then stored in sealed vials at -20 °C for analysis through gas chromatograph – mass selective detector (GC – MS) and DTT assay, respectively. As for the quinone measurement, after the extracts concentrated to near dryness under a gentle nitrogen gas at 35 °C, the residues were dissolved in 1 mL MeOH and transferred into a brown auto-sampler vial for further derivatisation reaction (Section 3.5.1.6).

3.5.1.6 MeOH Derivatisation

MeOH derivatisation was used for further quinone measurement by high performance liquid chromatograph – electrospray ionisation – tandem mass spectrometry (LC – ESI – MS/MS). The extracted analytes of quinones reconstituted in MeOH were subjected to air heating at 65 °C for 27 h, and kept at -20 °C.

3.5.2 DTT Assay

The consumption of 100 μM of DTT in 0.1 M potassium phosphate buffer (pH 7.4) was measured over time at 37 °C in water bath. An aliquot of the $PM_{2.5}$ extract (1 mL) was incubated along with 4.5 mL of potassium phosphate buffer in a brown polypropylene bottle at 37 °C for

5 min. Then at time zero, 0.5 mL, 1 mM of DTT solution that prepared in 0.1 M potassium phosphate buffer was added into the incubation mixture and shaken continuously in a water bath. After reacting for 10 min, 0.5 mL of the reaction mixture was removed and transferred into 0.5 mL of 10% (v/v) TCA to quench the redox reaction. Then 50 µL of 10 mM DTNB (prepared in 0.1 M potassium phosphate buffer) was added allowing to react for 5 min, 2 mL TE-buffer was added. It was noted that DTNB should be added before TE-buffer to ensure the redox reaction was quenched when DTNB reacted with remaining DTT. The concentration of formed 2-nitro-5-thiobenzoic acid (TNB) was quantified by its optical density absorption at 412 nm (EVOLUTION 201 UV-Visible Spectrophotometer, Thermofisher). In this study, a total of five standard DTT concentration gradients were prepared (0, 25, 50, 75, 100 µM). The linear regression line derived from DTT standard solutions was used for calculating DTT consumption in aerosol samples. Each sample extract was run in duplicate or triplicate with coefficient of variation (CV) less than 3.5%, blank samples were used for results correction.

3.5.2 Inorganic Ions

We totally characterised 5 anions and 6 cations, including F^-, Cl^-, Br^-, NO_3^-, SO_4^{2-}, Li^+, Na^+, K^+, NH_4^+, Ca^{2+}, Mg^{2+} through Ion Chromatography (ICS-1600, Dionex, US). The system consists of an autosampler (Dionex AS-DV), an analytical column (Dionex, IonPac™ AS23 for anions; Dionex, IonPac™ CS12A for cations), a guard column (Dionex, IonPac™ AG23 and IonPac™ CG12A for anions and cations, respectively) and a self-regenerating suppressor (Dionex, ASRS™ 300 and CSRS™ 300 for anions and cations, respectively). A constant eluent (4.5 mM Na_2CO_3 + 0.8 mM $NaHCO_3$ for anions, suppressor current: 25mA; 20 mM MSA,

suppressor current: 59mA) with flow rate of 1 mL min^{-1} was conducted for inorganic ions detection.

3.5.3 Trace Elements

Each filtered extract was acidified by adding nitric acid (2% w/v final solution, Sinopharm Chemical Reagent Co., Ltd.), and stored in fridge at 4°C before analysis. Measurements of 18 total metal concentrations (Cu, Pb, Fe, Al, Mn, V, Cr, Ce, Cd, Zn, Co, Ni, Ag, As, Sr, Bi, Sb, Ba) were then carried out by Inductively Coupled Plasma-Mass Spectrophotometry (ICP-MS, iCAP Q, Thermofisher).

3.5.4 Carbonaceous Species

The organic carbon (OC) and elemental carbon (EC) in ambient particles were analysed on a thermal/optical carbon analyser (Model 2001A, DRI) following the Interagency Monitoring of Protected Visual Environments-A (IMPROVE_A) temperature protocol (DRI, 2005). The thermal-optical reflectance correction scheme was used for the determination of optically detected pyrolysed carbon (OPC) (Watson et al., 2004). A 0.502 cm^2 filter punch was progressively heated from room temperature to 840 °C, and OC and EC fractions were determined based on their preferential oxidation at different temperatures in a pure helium (He) atmosphere and 2% of oxygen (O_2) contained He atmosphere, respectively. Due to the liberating time of the temperature, OC is volatised at the temperature at 140 °C (OC1), 280 °C (OC2), 480 °C (OC3) and 580 °C (OC4 + OPC). EC is not evolved until the introduction of O_2 under higher temperatures at 580 °C (EC1 – OPC), 740 °C (EC2) and 840 °C (EC3). OPC is

generated in an inert environment during heating when 2% O_2 is introduced and a laser monitors the surface reflectance and transmittance of a filter during thermal analysis. The concentrations of OC and EC were calculated as OC = OC1 + OC2 + OC3 + OC4 + OPC and EC = EC1 + EC2 + EC3 – OPC, respectively, and total carbon was reported as the sum of OC and EC concentrations. Water-soluble organic carbon (WSOC) was measured using a total organic carbon (TOC) analyser (Vario TOC Cube, Elementar, Germany).

3.5.6 Polycyclic Aromatic Hydrocarbons (PAHs)

In this study, 16 EPA priority PAHs were investigated, including Nap, Ace, Acy, Flu, Phe, Ant, Flt, Pyr, BaA, Chr, BbF, BkF, BaP, Ind, BDA and Bpe. The analysis of PAHs was conducted using a GC (Agilent Technologies 7890B) – MS (Agilent Technologies 5977A) equipped with a capillary column (HP – 5MS, film thickness 0.25 μm, 30 m × 0.25 mm i.d., Agilent J&W.) with carrier gas of He. 1 μL of sample was injected into the GC-MS in split-less mode with 5.5 min of solvent delay and the 250 °C of injector temperature. PAHs standards as well as extracted samples were analysed in selective ion monitoring (SIM) mode. The most abundant ions were regarded as the reference ions for confirmation of each analyte. 16 reference ions were selected and identified based on their specific m/z at different retention time. To obtain the maximum sensitivity, the 16 reference ions were divided into 7 groups, only those ions selected in same group were monitored during the specific interval of retention time. GC temperature program and MS monitoring ions for target PAHs were shown in Table 3.3.

3.5.7 Quinones

The advanced instrument applied for 1,2-NQ, 1,4-NQ and 1,4-AQ derivative (1,2-NQ-OCH_3, 1,4-NQ-OCH_3, 1,4-AQ-OCH_3) measurement in this study was High Performance Liquid Chromatograph (Shimadzu 30A) – tandem Mass Spectrometry (ABsciex 3200 Q trap) (HPLC-MS/MS) equipped with Electrospray Ionisation (ESI). The LC system consists of a binary pump and an auto-sampler with an analytical column (Zorbax RRHD Eclipse Plus 95A C18, 2.1 × 50 mm, 1.8 µm; Agilent Technologies, USA) and a guard column (UHPLC Grd, Ecl. Plus C18, 2.1 mm, 1.8 µm; Agilent Technologies, USA) used for LC separation at 35 °C. The programs of mobile phase was set as follow: initially 30% of A (MeOH) and 70% of B (5 mmol L^{-1} ammonium acetate and 0.1% FA in de-ionised water), followed by a linear gradient to 90% of A in 3 min, then kept isocratic for 2.5 min, and finally back to 30% of A for 0.5 min (Pei et al., 2018). The tandem MS was operated in the positive ionisation mode with multiple reaction monitoring (MRM). The quinone derivatives and optimised ionisation source parameters were presented in Table 3.4.

Table 3.3 GC temperature program and MS monitoring ions for analysis of PAHs

Time Interval min	Ion Group	Ion Amount	Reference Ions m/z	Target PAHs	GC Temperature °C
5.5	Group 1	1	128	Nap	70 °C for 2 min; 15 °C min^{-1} to 200 °C for 4 min; 5 °C min^{-1} to 220 °C for 5 min; 2 °C min^{-1} to 250 °C for 5 min; 2 °C min^{-1} to 270 °C for 5 min
9.0	Group 2	3	152, 153, 166	Ace, Acy, Flu	
12.0	Group 3	2	176, 178	Phe, Ant	
15.6	Group 4	2	200, 202	Flt, Pyr	
23.5	Group 5	3	226, 228, 234	BaA, Chr	
32.0	Group 6	2	250, 252	BbF, BkF, BaP	
46.0	Group 7	2	276, 278	Ind, DBA, Bpe	

Table 3.4 Conditions of MRM mode used for HPLC-MS/MS analysis of quinone derivatives

Quinone	Quinone Derivative	Parent Ion	Product Ion	De-clustering Potential (DP)	EP	Collision Cell Entrance Potential (CEP)	Collision Energy (CE)	Collision Cell Exit Potential (CXP)
				V	V	V	V	V
1,2-NQ	1,2-NQ-OCH_3	189*	77*	55.4	8.8	16.144	45.6	2.3
		189	161	55.4	8.8	16.144	45.6	2.3
1,4-NQ	1,4-NQ-OCH_3	189	77	55.0	8.8	16.144	45.6	2.3
		189	161	55.0	8.8	16.144	45.6	2.3
1,4-AQ	1,4-AQ-OCH_3	239	211	55.0	8.8	18.203	45.6	2.3
		239	127	55.0	8.8	18.203	45.6	2.3

* The labelled ion pairs were selected for quantifying the compound.

Chapter 4 OP of Water-soluble Fraction of Ambient $PM_{2.5}$: Chemical Characterisation, Seasonal Variation and Source Apportionment

4.1 Introduction

The correlation of OP and water-soluble chemical constituents of PM in urban cities has been widely investigated by many studies (Charrier et al., 2016b, Cho et al., 2005). Accordingly, the particle species such as soluble transition metals (Cu, Fe, Mn, V, Ni), water-soluble inorganic ions (WSIIs), water-soluble organic carbon (WSOC), and water-soluble humic-like substances (HULIS) have been typically examined and found to be responsible for OP activity by dithiothreitol (DTT) assay (Cho et al., 2004). Nonetheless, such findings are still debatable about whether or not a simple summation of relative contribution of chemical components could represent the overall OP of ambient PM. A very limited studies in the literature investigated synergistic and/or antagonistic interactions among PM species and antioxidants which could alter the redox properties. For example, Mn in PM exhibits synergistic and antagonistic effects in DTT oxidation when mixed with quinones and HULIS, respectively (Lin and Yu, 2020). The mixtures of Cu with quinones or HULIS antagonistically oxidise DTT with a consumption rate lower than the sum of individual redox active species (Lin and Yu, 2020). Fe interacts additively with quinones and HULIS compounds in DTT consumption, but synergistically in OH· production (Charrier and Anastasio, 2015, Yu et al., 2018). Therefore, owing to a wide variety of complex interactions of PM species, it becomes a difficult and challenging task to deduce the key drivers of OP through focusing just on those generally recognized redox-active components.

Several studies quantified source-specific contributions to PM-induced OP by applying receptor models such as Chemical Mass Balance (CMB), Positive Matrix Factorisation (PMF), and Principal Component Analysis (PCA) coupled with Multiple Linear Regression (MLR) (Bates et al., 2015, Weber et al., 2018, Yu et al., 2019). Cheng et al. (2021) observed that the metal-related factor dominated the source contribution to OP while marine vessels exhibited the highest intrinsic oxidative activity in Hong Kong. However, due to various factors affecting OP and potential non-linear increase of OP induced from source-specific PM, the traditional analytical methods without considering synergistic and/or antagonistic effects from multi-sources and multi-species could be limited to some extent in previous reported literature.

Knowing the scientific facts that PM redox activity can be induced from water-soluble, the analysis of source contributions to OP^{ws} can well represent the toxicity of ambient $PM_{2.5}$ to human health owing to its more bioavailability. However, biased OP contribution can be estimated by directly using linear regression model of individual particulate catalytic oxidisers generated due to potential interactions among PM species. To provide more clarity in understanding on characterization of OP, its driving factors and apportionment of responsible sources, this unique study has aimed to achieve the following objectives: 1) a thorough investigations on seasonal variations of ambient concentrations of $PM_{2.5}$ mass and its chemical constituents along with the overall OP^{ws} value ; 2) assessment of source profiles of $PM_{2.5}$ and its OP^{ws} in the study domain; 3) estimation of source contributions to OP^{ws}; 4) finding scientific reasons on why OP increases non-linearly with the increased source contributions, and investigating the interaction within and between source-derived OP; 5) exploring the driving factors of OP^{ws} that are induced from $PM_{2.5}$ of similar mass concentrations.

4.2 Methods

4.2.1 Sampling

The ambient $PM_{2.5}$ was captured by quartz filters using the Model 310 Universal Air Sampler^{TM} (UAS^{TM}) at PMB (Sir Peter Mansfield Building) of UNNC (University of Nottingham Ningbo China) between October 2017 and August 2018. The protocol of sampling procedure has been described in Section 3.2.1. After sampling, all filters were stored at -20 °C in the fridge until experimental analysis.

4.2.2 Sample Analysis

For individual aerosol sample preparation, a fraction of filter was extracted ultrasonically by 20 mL Milli-Q water for 45 min at room temperature, as described in Section 3.5.1.1. All the aqueous extracts were stored in sealed PTFE bottles at 4 °C prior to analysis. The analysis of WSIIs and WSOC were conducted by using IC (ICS-1600, Dionex, US) and TOC analyser (Vario TOC Cube, Elementar, Germany), respectively. For analysis of water-soluble trace elements, the aqueous extracts were acidified by nitric acid (2% w/v final solution) before measurement in ICP-MS (iCAP Q, Thermofisher). The OP was measured by DTT assay. Detailed descriptions of WSIIs, trace elements, WSOC analysis and DTT assay are presented in Section 3.5.2 – 3.5.4. The OP measured from water and methanol extracts are expressed as OP^{ws} and OP^{meth}, respectively. Both of the OP indicators were normalised by volume (OP_v^{ws}, OP_v^{meth}) and mass of $PM_{2.5}$ (OP_m^{ws}, OP_m^{meth}), where the volumetric OP is considered to be more relevant to human exposure, while the mass-normalised OP is a useful metric that displays the intrinsic ROS generation ability. Methanol is less polar than water and dissolves a

large proportion of water-insoluble organic components in addition to some of the water-soluble species (Verma et al., 2012). Although methanol and water may dissolve a few same components, it is reasonable to assume that components in methanol extracts and water extracts are mutually exclusive. OP^{ws} and OP^{meth} were then measured using the DTT assay (Cho et al., 2005, Verma et al., 2012). Measuring OP from both water and methanol extracts can provide more complete ROS generation ability of $PM_{2.5}$."

4.2.3 Quality Control

The analytical quality of the measured data was determined by recovery and linearity and limit of detection (LOD). The concentrations of WSIIs and trace elements were estimated via the external calibration, the linearity of calibration standards calculated through linear regression with values between 0.99 and 1.00 (r^2) for all ions and trace elements. The mean recoveries obtained were greater than 96.70%. The detection limits for WSIIs ranged from 0.02 ng m^{-3} of NO_3^- to 25.65 ng m^{-3} of SO_4^{2-}, for WSOC is 0.02 µg C m^{-3}, and for water-soluble trace elements ranged from 0.09 pg m^{-3} of Bi to 351.42 pg m^{-3} of Mg.

4.2.4 Analysis of Air Mass Backward Trajectory

Model of air mass backward trajectories was conducted to identify the impact of pollutants originating from medium and long-range transport of aerosols rather than local emissions, via Hybrid Single-Particle Lagrangian Integrated Trajectory model version 4.9 (HYSPLIT 4.9) from the National Oceanic and Atmospheric Administration (NOAA) Air Resources Laboratory from Oct 2017 to May 2018 (Draxler and Rolph, 2013). The air masses were traced

back 48 h to assess the trajectories, which arrived at the sampling site every 6 h over the whole sampling period at 500 m height above ground level. This atmospheric level is frequently used in previous studies (Chen et al., 2021, Xu et al., 2016, Xu et al., 2019), as it ensures that the trajectory starts within the limits of atmospheric boundary layer. All the calculated trajectories were subject to cluster analysis through an assessment tool, Trajstat 1.2.1.0, a geographic information system (GIS) based technique used for estimating the pollutant pathway from a large number of trajectories with high measurement (Chen et al., 2021, Wang et al., 2009). Euclidean distance model was applied for both distance and direction analysis in this study.

4.2.5 Graphical Analysis of Source Dispersion

To determine the seasonal variations of geographical origins and dispersion characteristics of $PM_{2.5}$-induced OP_v and local source contributions to OP_v, bivariate polar plots (BPPs) were applied in this study. The plots illustrate variation trends of OP_v values (OP_v^{ws} and OP_v^{meth}) versus hourly wind speed and wind direction in polar coordinates. The detailed description of BPPs construction can be found elsewhere (Carslaw and Beevers, 2013, Chen et al., 2021). Briefly, wind speed, wind direction and concentrations of OP_v values were partitioned into wind speed-direction 'bins' with calculated mean concentration for each bin. The wind direction intervals at 10° and wind speed of 30 m s^{-1} were set, respectively. For each $PM_{2.5}$ sample, the parameters obtained for 23 h sampling were distributed in previous 23 corresponding hourly wind direction and wind speed (Moufarrej et al., 2020). This model was made in computational tool of Rstudio 'openair' package, which is available at www.openair-project.org.

4.2.6 Chemical Mass Balance (CMB) Model

Considering the limited number of samples collected per season, chemical mass balance model (US EPA CMB8.2) was applied in this study to apportion emission sources of $PM_{2.5}$ during four seasons of this sampling campaign. In this model, the sample concentrations and source profile abundances with corresponding estimated uncertainties were used as input data. To obtain reliable fitting statistics, the essential criteria to be met for acceptable CMB results including $R^2 > 0.85$, $Chi^2 < 4$, Tstat values > 2, and percent mass (% mass, ratio of the sum of model-calculated source contribution estimates to measured mass concentration) ranged from 80-120%. The source profiles applied herein were obtained from previous studies in China and it was believed to well represent the source characteristics including coal combustion (Bi et al., 2019), industry emission (Liu et al., 2018c), vehicle emission (Liu et al., 2018c), fugitive dust (Bi et al., 2019), biomass burning (Liu et al., 2018c), sea salts and secondary aerosol (Zhang et al., 2016). The fitting species should be the major components or indicators of sources, including OC, EC, sulphate nitrate and ammonium (SNA), K^+, Ca^{2+}, Na^+, Al, As, Ba, Cd, Cr, Co, Cu, Fe, Pb, Mn, Zn, Ni, V, Nap, Ace, Flu, Phe, BbF, BkF, DBA, Bpe, and their concentrations are provided in Table 4.1 and Table 5.1.

Table 4.1 Mass concentrations of $PM_{2.5}$ and its chemical components during the four seasons

Components[a]	Autumn	Winter	Spring	Summer
$PM_{2.5}$	43.87 ± 18.09[b]	87.60 ± 35.63	36.54 ± 25.55	28.60 ± 12.31
OC	10.22 ± 4.47	14.07 ± 5.59	6.38 ± 4.32	4.62 ± 2.30
EC	4.14 ± 1.69	9.51 ± 5.87	1.92 ± 2.27	0.99 ± 0.70
WSOC	3.01 ± 1.35	5.83 ± 3.26	1.91 ± 2.10	1.91 ± 1.18
NH_4^+	3.57 ± 1.22	8.58 ± 4.97	4.78 ± 2.97	3.11 ± 1.75
NO_3^-	7.71 ± 4.34	33.31 ± 44.60	7.22 ± 7.35	2.33 ± 0.87
SO_4^{2-}	5.24 ± 1.72	14.60 ± 16.86	7.11 ± 3.59	8.42 ± 4.11
F^-	0.03 ± 0.05	0.73 ± 1.29	0.05 ± 0.04	0.61 ± 0.67
Cl^-	1.06 ± 0.76	3.52 ± 1.94	0.32 ± 0.22	0.17 ± 0.29
K^+	0.43 ± 0.20	0.83 ± 0.71	0.28 ± 0.22	0.16 ± 0.07
Ca^{2+}	0.19 ± 0.09	0.24 ± 0.24	0.18 ± 0.13	0.44 ± 0.41
Mg^{2+}	0.07 ± 0.03	0.05 ± 0.08	0.05 ± 0.02	0.05 ± 0.02
Na^+	0.25 ± 0.08	0.73 ± 0.65	0.24 ± 0.10	0.29 ± 0.12
Br^-	0.03 ± 0.03	0.19 ± 0.44	0.06 ± 0.04	0.05 ± 0.04
Al	1.42 ± 0.94	5.38 ± 11.81	12.21 ± 22.96	1.13 ± 0.93
As	0.20 ± 0.10	0.33 ± 0.31	0.29 ± 0.23	0.12 ± 0.07
Ba	0.60 ± 0.33	1.25 ± 1.75	0.65 ± 0.60	0.57 ± 0.85
Bi	0.07 ± 0.10	0.06 ± 0.10	0.04 ± 0.04	0.02 ± 0.02
Ca	9.85 ± 5.77	13.33 ± 13.44	16.34 ± 11.88	29.07 ± 21.61
Cd	0.11 ± 0.07	0.16 ± 0.16	0.13 ± 0.09	0.05 ± 0.03
Cr	0.28 ± 0.20	0.15 ± 0.11	0.73 ± 0.15	0.37 ± 0.59
Co	0.02 ± 0.01	0.18 ± 0.27	0.04 ± 0.02	0.02 ± 0.02

Cu	1.02 ± 0.41	0.99 ± 0.89	1.21 ± 0.81	1.57 ± 4.78
Fe	3.66 ± 2.08	4.92 ± 4.35	8.97 ± 7.97	3.51 ± 5.94
Pb	1.08 ± 0.57	2.24 ± 2.65	1.91 ± 2.03	0.65 ± 0.75
Sb	0.22 ± 0.25	0.31 ± 0.35	0.23 ± 0.23	0.10 ± 0.05
Mn	1.69 ± 0.68	3.80 ± 3.48	3.93 ± 2.36	2.66 ± 4.48
Ni	0.29 ± 0.16	10.01 ± 17.17	1.13 ± 1.21	0.47 ± 0.66
V	0.34 ± 0.25	0.27 ± 0.62	1.44 ± 1.63	0.55 ± 0.35
Zn	16.62 ± 12.47	19.30 ± 27.77	19.09 ± 12.34	10.88 ± 5.63
O_3	54.63 ± 26.04	30.72 ± 10.35	92.62 ± 27.11	62.32 ± 21.03

[a] The unit is μg m^{-3} for $PM_{2.5}$, OC, EC WSOC, WSIIs and O_3, and ng m^{-3} for water-soluble transition metals;
[b] Mean ± standard deviation (SD).

4.2.7 Multivariate Regression Models

The ROS generation potential from specific sources of $PM_{2.5}$ was estimated through a MLR analytical model (Bates et al., 2015). In this study, OP_v^{ws} was defined as the dependent variable and source contributions (SC) to $PM_{2.5}$ (SC_i, μg m^{-3}) as the independent variables, expressed in Eq. (1) (Daellenbach et al., 2020):

$$OP_v = \sum_i OP_m^{SC_i} \times SC_i + \varepsilon \quad (1)$$

where $OP_m^{SC_i}$ is the parameter of source contribution and represents DTT activity per mass of respective aerosol (nmol min^{-1} μg^{-1}) from the specific emission source. ε is the constant, representing OP_v induced from other sources. The overall sample size (N) is 55.

All the programming was conducted using SPSS (Statistics 23). The coefficients of emission sources with *F* statistics (*p* values) greater than 0.05 were removed. However, a

statistically significant negative value of intrinsic OP may be calculated for further analysis and interpretation. Based on the nature of mass based intrinsic OP, negative value was considered to be no geo-chemical sense as the air is known to be strong oxidant milieu (Weber et al., 2018). Therefore, a stepwise method was selected in this study. If the calculated intrinsic OP of the source is negative, then it was discarded, and the iteration was repeated until all intrinsic OP values were found to be greater than zero. The coefficients of the predicted source contribution values to OP_v^{ws} are summarised in Table 4.2. Source of secondary inorganic aerosol, SIA (NH_4^+, NO_3^-, SO_4^{2-}), was not included in this modelling as the source contribution to OP_v due to that these components cannot directly induce OP in ambient aerosol (Daellenbach et al., 2020, Zhou et al., 2018).

Table 4.2 Summary of the coefficients in the models of source contributions to OP_v^{ws}

Model	R^2	Adjusted R^2	Std. Error of the estimate	Durbin-Watson
$^{c}OP_v^{ws}$	0.22[a]	0.19	1.54	1.59

a. Predictors: (Constant), industrial emission, sea salt;

4.3 Results and Discussion

4.3.1 Seasonal Variation of $PM_{2.5}$ and OP Activity

Seasonal variations of $PM_{2.5}$ and OP induced by both water-soluble (hydrophilic) fractions (OP_v^{ws}, OP_m^{ws}) during the study period in Ningbo city are presented in Fig. 4.1. The averaged $PM_{2.5}$ mass concentration was highest (87.60 ± 35.63 μg m^{-3}) in winter (Dec 2017 to Feb 2018) and lowest (28.60 ± 12.31 μg m^{-3}) in summer (Jun to Aug 2018). During the marine monsoon, a subtropical climate, marked by a relatively warm humid summer and cold dry winter, prevails in Ningbo. During the sampling campaign, highest $PM_{2.5}$ levels occurred in the winter at a low wind speed (1.98 ± 1.01 m s^{-1}), low ambient temperature (7.83 ± 2.57 °C), and low relative humidity (RH, 67.57 ± 9.46%). Such synoptic conditions would depress the planetary boundary layer (PBL) and result in atmospheric inversion, then consequently the $PM_{2.5}$ levels increase. Lower levels of $PM_{2.5}$ in summer could be partially ascribed to the higher temperature (29.54 ± 0.99 °C) with the notable rainfall, which facilitate the dispersion and scavenging of aerosols (Xu et al., 2016).

The DTT consumption rate normalised by volume (OP_v^{ws}) is considered to be more relevant to human exposure, the seasonal variability of extrinsic OP_v in Ningbo city was presented in Fig. 4.1(b). In this study, we observed significant variability of than the OP_v^{ws} on the one-year basis. The annual average OP_v^{ws} was 3.65 ± 1.71 nmol min^{-1} m^{-3}, which was comparable to that in the Western Asian city of Tehran (2 ~10 nmol min^{-1} m^{-3}) (Al Hanai et al. (2019)), but slightly lower than those of other areas in China, such as the rural area in Inner Mongolia (5.32 nmol min^{-1} m^{-3}) (Secrest et al. (2016)), city centres of Tianjin (6.8 ± 3.4 nmol min^{-1} m^{-3}) (Liu et al. (2018a)) and Beijing (12.26 ± 6.82 nmol min^{-1} m^{-3}) (Yu et al. (2019)). The lower OP_v^{ws}

suggests a lower inhalation exposure risk of $PM_{2.5}$ in Ningbo. Previous studies have reported the highest averaged OP_v^{ws} in winter (heating season) and lowest in summer (non-heating season) (Daellenbach et al., 2020, Saffari et al., 2014b, Verma et al., 2014). However, in this study, there was no obvious seasonal variation of OP_v^{ws}, with slightly higher during autumn (median: 4.14 nmol min^{-1} m^{-3}, mean: 4.09 ± 2.02 nmol min^{-1} m^{-3}) than other seasons. This result embodied the availability of most abundant water-soluble catalytic $PM_{2.5}$ oxidisers (e.g., transition metals, WSOC) in the fine aerosols in Ningbo during autumn. As shown in Fig. 4.1(b), OP_v^{ws} was more variable during spring relative to winter, while the median of OP_v^{ws} was higher in winter (3.99 nmol min^{-1} m^{-3}) than spring (3.46 nmol min^{-1} m^{-3}). These phenomena signified that the OP_v^{ws} values hover around the higher median consistently in winter than spring, and further implies the relatively steady and strong ROS generation ability of ambient aerosols from water-soluble fractions during winter in Ningbo city.

The mass-normalised DTT activity (OP_m^{ws}) is a useful metric that displays the intrinsic ROS generation ability of ambient $PM_{2.5}$. The annual mean OP_m^{ws} (0.12 ± 0.12 nmol min^{-1} μg^{-1}) obtained in this study was comparable with the data reported in the city centre of Beijing (0.13 ± 0.10 nmol min^{-1} μg^{-1}, Yu et al. (2019)), slightly higher than the suburban area of Beijing (Huairou district, 0.09 nmol min^{-1} μg^{-1}, Wang et al. (2020c)) and cities of southeastern US (0.005-0.10 nmol min^{-1} μg^{-1}, (Verma et al., 2014)), but much higher than Hong Kong (0.022 ± 0.011 nmol min^{-1} μg^{-1}, Cheng et al. (2021)) and Bohai Sea area (0.002-0.084 nmol min^{-1} μg^{-1}, Liu et al. (2018a)) of China. The relatively high OP_m^{ws} suggested the greater intrinsic oxidative stress on the basis per $PM_{2.5}$ mass in Ningbo. The fine particles exhibited the highest mean OP_m^{ws} during summer, with 0.21 ± 0.16 nmol min^{-1} μg^{-1}, indicating that the highest oxidative

stress associated with water-soluble components per unit mass of ambient $PM_{2.5}$ in summer, although the $PM_{2.5}$ mass concentration is lowest.

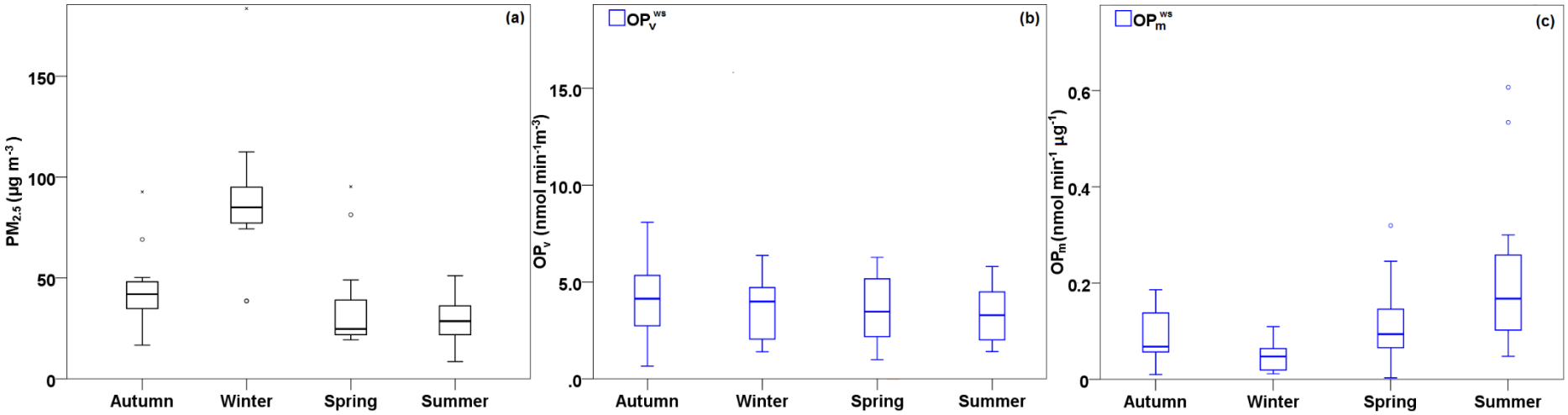

Figure 4.1 Seasonal variations of levels of (a) ambient $PM_{2.5}$ concentrations, (b) $PM_{2.5}$-induced OP_v^{ws} and (c) OP_m^{ws}

Table 4.3 Meteorological data and standard deviation (SD) of temperature (°C), relative humidity (%), wind speed (m s^{-1}), solar radiation (MJ m^{-2}) and sun duration (h) during autumn, winter, spring and summer seasons

	Temperature (°C)	RH (%)	Wind speed (m s^{-1})	Solar radiation (MJ m^{-2})	Sun duration (h)
Autumn	15.77 ± 2.34	74.01 ± 6.41	2.78 ± 1.47	0.12 ± 0.04	0.22 ± 0.13
Winter	7.83 ± 2.57	67.57 ± 9.46	1.98 ± 1.01	0.10 ± 0.01	0.23 ± 0.07
Spring	19.94 ± 1.90	65.59 ± 9.19	2.80 ± 0.76	0.22 ± 0.05	0.32 ± 0.12
Summer	29.54 ± 0.99	75.57 ± 4.14	2.40 ± 0.63	0.23 ± 0.06	0.37 ± 0.11

4.3.2 Graphical Analysis of Potential Sources of OP_v^{ws}

Bivariate polar plots of oxidative capacities and mass concentrations of $PM_{2.5,}$ as given in Fig. 4.2, for graphical comparisons of their potential sources. OP_v^{ws} and $PM_{2.5}$ exhibited considerably different temporal trends regarding the changes in wind speed and wind direction throughout the four seasons in Ningbo city. $PM_{2.5}$ showed no prevalent sector for autumn (Fig. 4.2(e)), with the highest contribution was from all wind directions at low wind speed (< 2 m s^{-1}) in the vicinity of the study site. Unlike $PM_{2.5}$, the maximum OP_v^{ws} was obtained when wind blow from the southeast (SE) during autumn, indicating the limited DTT oxidation induced from the highly concentrated ambient particles. As our study domain is surrounded by freeways, therefore we inferred that the high oxidative capacity (OP_v^{ws}) was dominant by traffic exhausts from freeway source, where the nearest freeway lies from SE to NE of the UNNC (Fig. 3.1(c)). The highest levels of $PM_{2.5}$ and OP_v^{ws} in winter were recorded when the wind came from the northwest (NW), and both increases with increasing the wind speed. Such a pattern of increase suggested a buoyant plume from a source like a chimney stack, from which the plumes are brought down to ground level under unstable atmospheric conditions with the increasing wind speed (Carslaw et al., 2006, Chen et al., 2021). According to the analysis of back trajectories (Fig. 4.3(b)), the aerosols from NW were significantly affected by the long-range transport of air masses, which more than 80% of the air parcels were from NW, originating from inland China with densely distributed fire spots in Anhui Province (37.3%) and passed through Hangzhou Bay before arriving the study domain. Thus, the aerosols from regional transport, bringing the pollutants from BB and sea salt particles, may aggravate the air quality and enhance the oxidative potency.

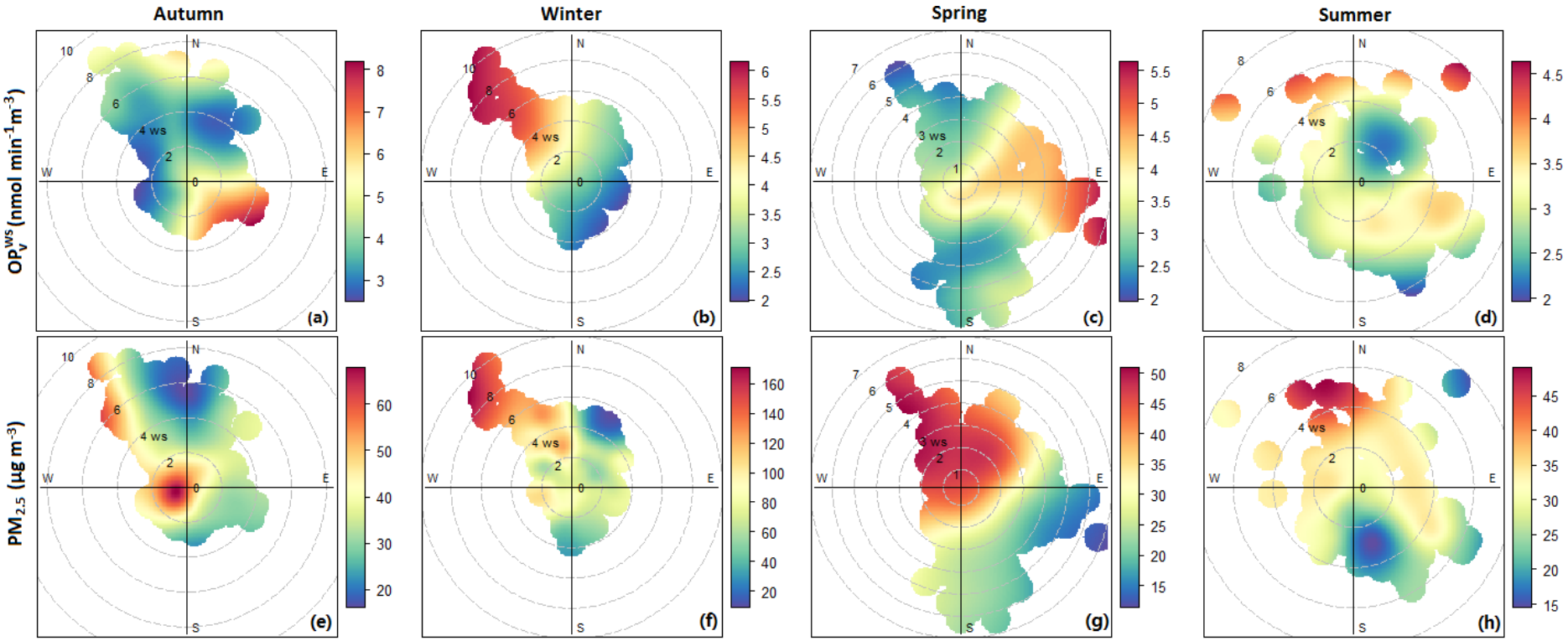

Figure 4.2 Bivariate polar plots of OP_v^{ws} (a-d) and $PM_{2.5}$ (e-h) predicted during autumn, winter, spring and summer

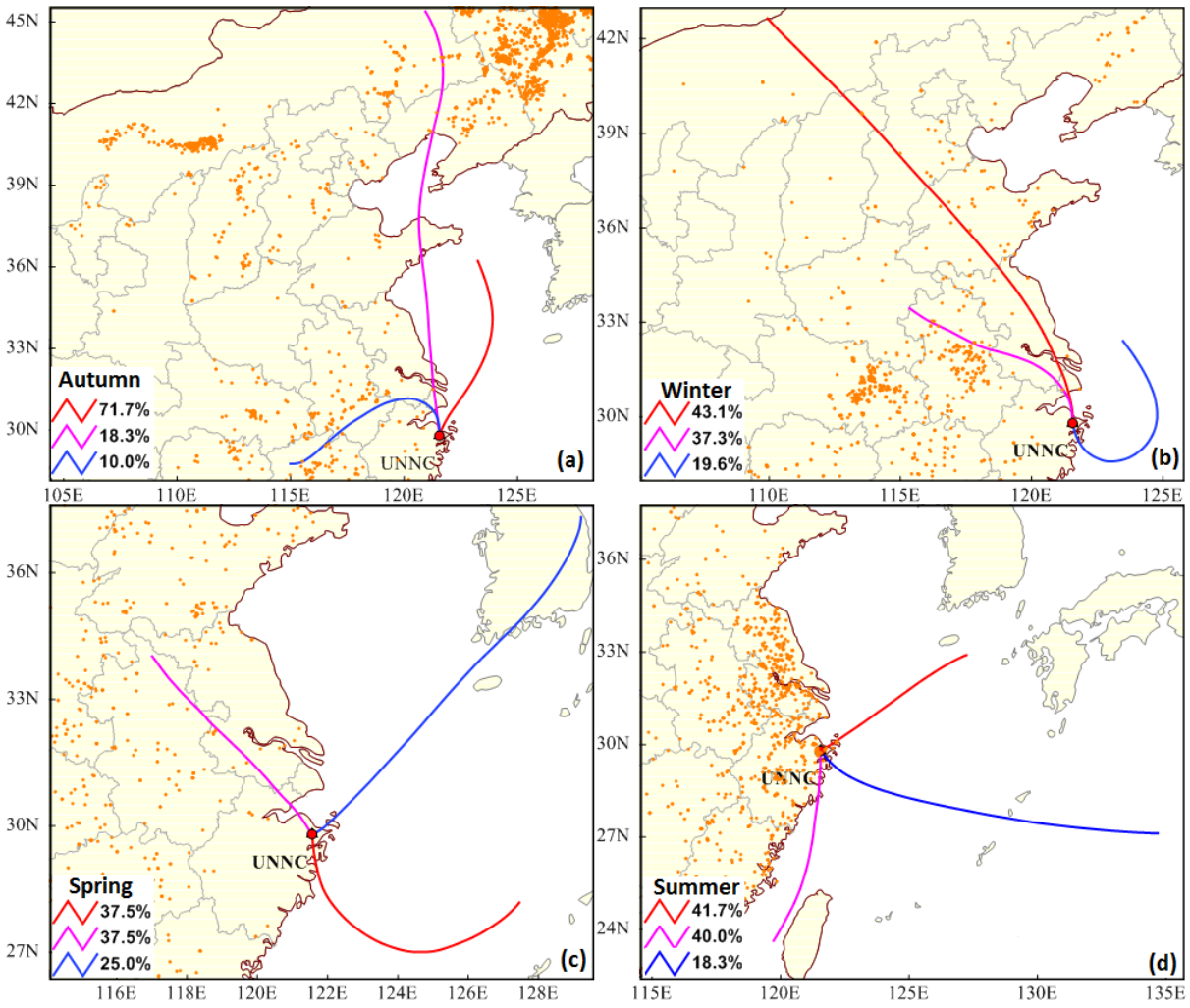

Figure 4.3 48-h back trajectories of air masses and distribution of fire spots during autumn (a), winter (b), spring (c) and Summer (d)

4.3.3 Source Contributions to OP_v^{ws}

4.3.3.1 Intrinsic OP_m^{ws} of $PM_{2.5}$ Source

We quantified the seasonal variations of source contributions to OP_v^{ws} based on a multiple linear regression (MLR) model. The modelled OP_v^{ws} was shown contributed by different emission sources with dissimilar intrinsic OP for the same source. The OP_v^{ws} activity substantially contributed from industry emission (IE) and sea salts (SS). As shown in Table 4.4

that IE exhibited a higher OP per mass unit of the aerosol ($OP_m^{ws\text{-}IE}$, in nmol min^{-1} μg^{-1}) than sea salt aerosol with 0.070 ± 0.021, suggesting the higher ROS generation ability of ambient $PM_{2.5}$ released from IE in Ningbo. For the water-soluble fractions of $PM_{2.5}$, we also observed the higher intrinsic OP induced from IE-related $PM_{2.5}$ in the northern cities of China (0.155 and 0.279 nmol min^{-1} μg^{-1} in Bohai Sea areas and Beijing, respectively), but lower in Hong Kong (0.038 nmol min^{-1} μg^{-1}) relative to Ningbo (Table. 4.5).

Sea salt aerosol ($OP_m^{ws\text{-}SS}$), considered redox inactive previously, was shown to have the intrinsic oxidative capacity but contributed substantially lower to overall DTT activity from water-soluble fractions (OP_v^{ws}) relative to $OP_m^{ws\text{-}IE}$, with 0.045 ± 0.022 nmol min^{-1} μg^{-1}. We infer such phenomenon would be due to the mixed sources of mineral dust and ship emissions within SS, explained partially by mineral-containing species with higher redox- active potency (e.g., Mg^{2+}, Fe, and Zn) (Cerro et al., 2020). Similarly, the observations of oxidative activity from mixed SS emitted PM aerosols with road dust and marine vessels were reported by previous studies in France (0.14 ± 0.03 nmol min^{-1} μg^{-1}) and Hong Kong (0.129 nmol min^{-1} μg^{-1}).

Table 4.4 Summary of regression coefficients (intrinsic OP_m, nmol min^{-1} μg^{-1}) of source contributions to OP_v^{ws} (nmol min^{-1} m^{-3})

	CC	IE	BB	SS	Intercept
OP_v^{ws}	N.A.*	0.070 ± 0.02 (0.002)#	N.A.	0.045 ± 0.022 (0.05)	2.23 ± 0.45 (< 0.001)

* N.A. refers to not applicable that includes the exclusion during the regression exercise.
# p value

4.3.3.2 Sea Salts (SS)

As depicted in Fig. 4.4, the source of OP_v^{ws} was dominated by SS during this field campaign and the highest average OP_v^{ws} induced from SS aerosol ($OP_v^{ws\text{-}SS}$) occurred during winter with a value of 0.26 ± 0.61 nmol min^{-1} m^{-3}. To the best of our knowledge, no study has yet reported the potential of toxicities of sea salt aerosol in China. To unravel the driving factors of such high $OP_v^{ws\text{-}SS}$ contribution, we plotted seasonal variations of chemical composition spectrum for sea salt emission in Fig. 4.5 (a). It was noted that chemical composition of sea salt aerosol was relatively constant, and high loadings of SO_4^{2-} (0.15 – 0.37 μg m^{-3}), Cl^- (0.13 – 0.32 μg m^{-3}), NO_3^- (0.11 – 0.28 μg m^{-3}), Ca (0.08 – 0.21 μg m^{-3}), Na (0.08 – 0.19 μg m^{-3}) and Fe (16.32 – 40.54 ng m^{-3}) were identified to SS-related particulates among four seasons during the study period. As widely reported, Cl^- is an essential trace reactant involved in the processes of oxidation chemistry in the mid-latitudes (Chi et al., 2015, Osthoff et al., 2008). For sea salt particles, active Cl^- instead of chloride bound in atmospheric particles is considered to be released through heterogeneous reaction with dinitrogen pentoxide (N_2O_5) at the surface of sea spray particle, which produces nitryl chloride ($ClNO_2$). For those aerosol particles that do not initially contain Cl^-, the yield of $ClNO_2$ is from gaseous Cl (mainly HCl) uptake by N_2O_5 through heterogeneous processes, where the HCl ultimately stems from SS particles through acid displacement (von Glasow, 2008). The reaction equation (Eq.2) is shown as follow:

$$HCl_{(g)} + N_2O_{5\,(g)} \xrightarrow{het} ClNO_{2\,(g)} + HNO_{3\,(aq)} \quad (2)$$

$$ClNO_2 + \text{light}\ (\lambda < 840\ \text{nm}) \rightarrow Cl^- + NO_2 \quad (3)$$

Accumulation of $ClNO_2$ is stable at night-time, and photolysed rapidly to active chlorine radical and NO_2 after sunrise under deficiencies of other oxidant and radicals (e.g., OH•, NO_3)

(Eq.3). As reported by earlier studies, reactive chlorine radical is the dominant oxidant and more reactive than OH• and NO_3, which oxidises volatile organic compounds (VOCs) that do not react with NO_3 directly (Osthoff et al., 2008). This reaction produces peroxy radicals, which results to O_3 formation in the existence of NO_x, implying that combination of anthropogenic emissions and sea salt led to enhancement of particulate ROS generation, especially in a VOC-rich area like Ningbo heavily affected by petrochemical industry and shipping emission. Air masses were transported from the East China Sea and passed through the Ningbo-Zhoushan port during four seasons (shown in Fig. 4.3). Such transportation routes of air mass might have made the sea salt particles more oxidizing before arriving at the study domain. Additionally, in N_2O_5 formation through the reaction of nitrogen dioxide (NO_2) and nitrate radical (NO_3), the presence of regional $ClNO_2$ is usually accompanied by a higher level of NO_2 (Osthoff et al., 2008). It explains that the highest contribution of $OP_v^{ws\text{-}SS}$ occurred during winter when NO_2 concentration (72.84 ± 9.47 μg m^{-3}) was significantly higher than other seasons, i.e., 49.05 ± 14.14 μg m^{-3}in autumn, 22.58 ± 9.75 μg m^{-3} in summer, and 49.05 ± 14.14 μg m^{-3} in spring.

Iron was one of the most abundant water-soluble metal ions in sea salt aerosol, with an average contribution of 2.40% during this sampling campaign. The higher level of Fe in sea salt aerosol would be due to either mixed sources from freight activities and/or vehicle exhausts in the Ningbo-Zhoushan port, or the atmospheric deposition of mineral dust from continental regions to the seawater (Paris and Desboeufs, 2013). Previous studies showed that Fe itself has low redox capacity, exhibiting weak and inconsistent relationship with PM catalysed DTT activity (Charrier and Anastasio, 2012c). However, the property of OP for Fe could be highly enhanced when complexed with organic compounds such as WSOC, abundant

in aromatic content with highly redox-activity as reported in recent studies (Charrier and Anastasio, 2011b, Xiong et al., 2017). Therefore, the co-existence of water-soluble Fe and water-soluble fraction of atmospheric organic species can cause the metal-organic complexation by forming a ligand with an organic species, possibly inducing a strong synergistic effect on ROS generation in a typical antioxidant environment (including DTT assay and surrogate lung fluid systems) (Cheng et al., 2020, Paciolla et al., 2002). Moreover, a synergistic effect of Fe also arises from Fenton reaction, where H_2O_2 generated by organic-catalysed (e.g., WSOC, quinones, HULIS) redox activity is converted to OH• more efficiently by Fe (II) (Yu et al., 2018), as shown in the following Eq. (4-7):

$$Fe(III) + Reductant \rightarrow Fe(II) + Reductant^{+1} \quad (4)$$

$$Fe\ (II) + O_2 \rightarrow Fe(III) + \bullet O_2^- \quad (5)$$

$$2\bullet O_2^- + 2H^+ \rightarrow O_2 + H_2O_2 \quad (6)$$

$$Fe(II) + H_2O_2 \rightarrow Fe(III) + OH^- + OH\bullet \quad (7)$$

As we observed a strong correlation between Fe and WSOC (Pearson's r = 0.79, Table 4.6) during winter, we inferred that the oxidative capacity could be induced through synergistic effects of Fe and WSOC with either Fe-WSOC complex or Fenton reaction under WSOC catalysis, which is more efficient in producing ROS than Fe alone. Besides, the highest concentration of SO_4^{2-} (0.37 μg m^{-3}) from sea salt source during winter could increase the aerosol acidity and facilitate Fe dissolution, indirectly impacting OP levels upward (Shahpoury et al., 2021). Therefore, the effect of Fe-WSOC mixture would be one of the principal drivers for DTT activity induced from sea-salt aerosol, and consequently the highest $OP_v^{ws\text{-}SS}$ during

winter.

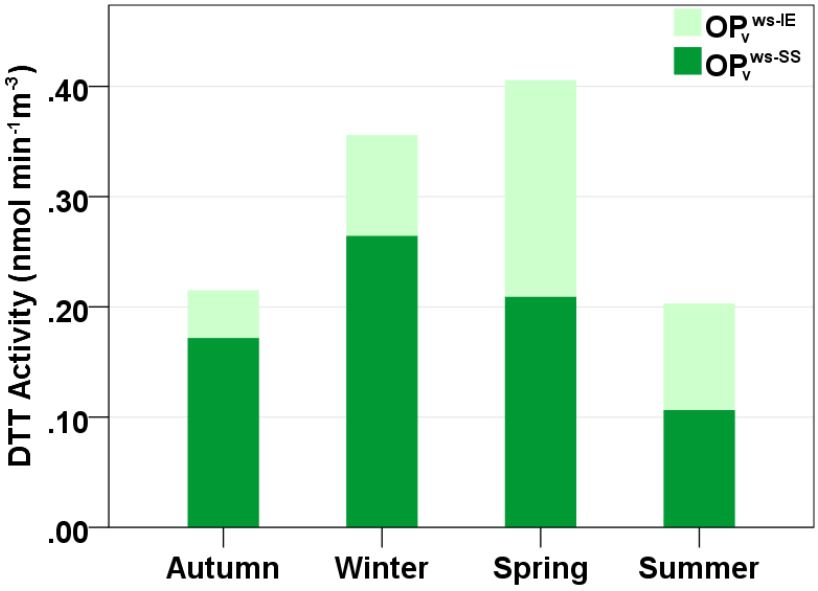

Figure 4.4 Seasonal variations of $PM_{2.5}$ source contributions to OP_v^{ws} in Ningbo

Table 4.5. Comparisons of intrinsic OP_m (nmol min^{-1} μg^{-1}) induced from specific source emitted PM from different regions in the world

	IE	CC	BB	VE	FD	SS	Marine vessel	Extraction solvent	Location	Location type	Reference
PM_{10}	--	--	0.07 ± 0.01	0.27 ± 0.03	0.14 ± 0.03	--	--	Gamble + DPPC*	Chamonix, France	City centre	Weber et al. (2018)
PM_{10}	--	--	0.13 ± 0.07	0.23 ± 0.09	0.12 ± 0.11	--	--	Gamble + DPPC	Alpine Valley, France	Urban area	Weber et al. (2021)
PM_{10}	0.52 ± 0.18	--	--	--	--	--	--	Gamble + DPPC	Grenoble, France	City centre	Borlaza et al. (2021)
PM_{10}	0.82 ± 0.24	--	--	--	--	--	--	Gamble + DPPC	Grenoble, France	Background station	Borlaza et al. (2021)
PM_{10}	0.44 ± 0.17	--	--	--	--	--	--	Gamble + DPPC	Grenoble, France	Suburban area	Borlaza et al. (2021)
$PM_{2.5}$	0.16	0.36	0.29	0.086	--	--	--	Water	Bohai Sea areas, China	Urban area	Liu et al. (2018a)
$PM_{2.5}$	0.28	0.24	--	0.48	0.21	--	--	Water	Beijing, China	Urban area	Yu et al. (2019)
$PM_{2.5}$	0.038	--	0.01	0.020	--	--	0.13	Water	Hong Kong, China	Urban area	Cheng et al. (2020)
$PM_{2.5}$	0.070 ± 0.02	--	--	--	--	0.045 ± 0.022	--	Water	Ningbo, China	Urban area	This study

Note: *DPPC: dipalmitoylphosphatidylcholine

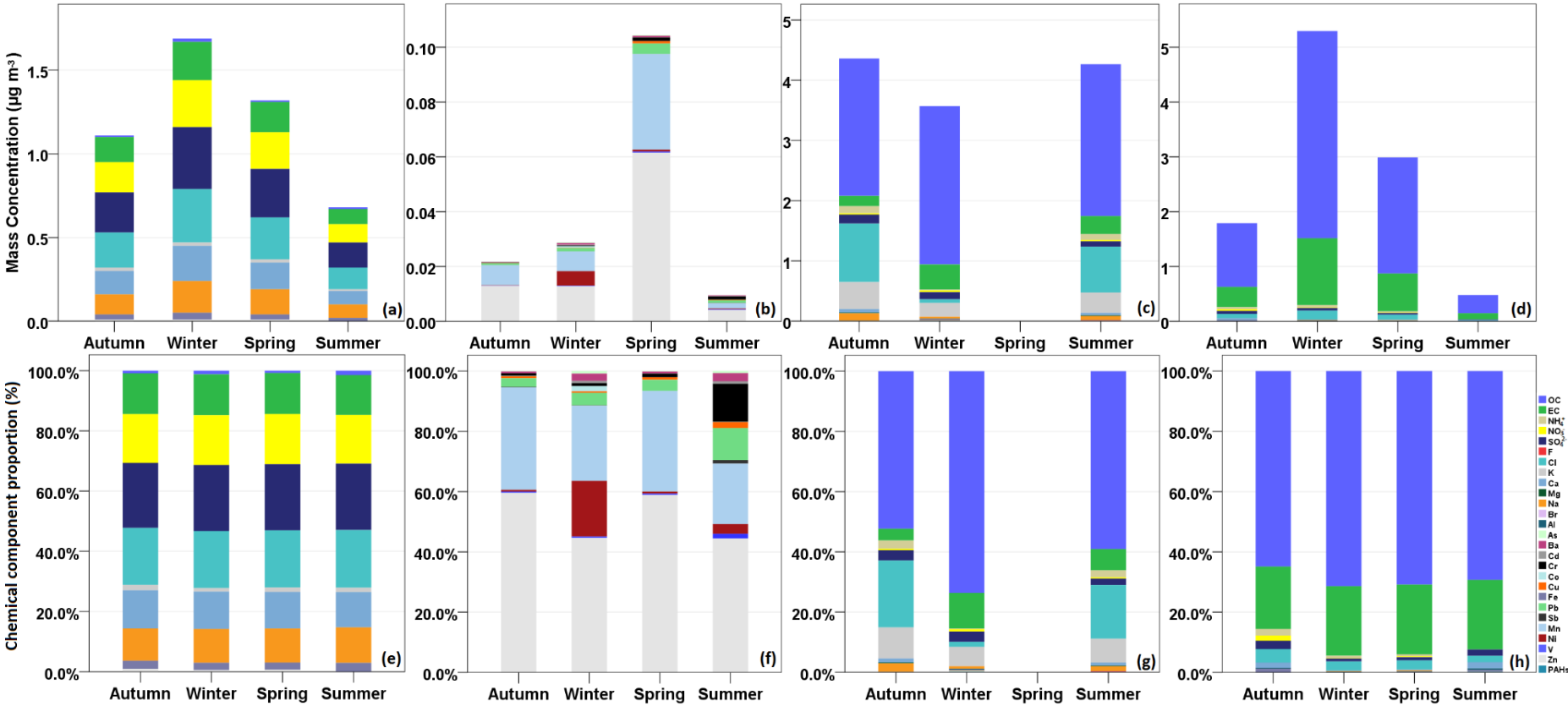

Figure 4.5. Chemical component spectrums and proportions of sea salt ((a) and (e)), industry emission ((b) and (f)), biomass burning ((c) and (g)) and coal combustion ((d) and (h)) during four seasons of sampling campaign via CMB model

Table 4.6 Pearson's correlation coefficient (r) between carbonaceous species and water-soluble trace elements

	OC	EC	WSOC	Al	As	Ba	Ca	Cd	Cr	Co	Cu	Fe	Pb	Sb	Mn	Ni	V	Zn
									Autumn									
OC	1.00																	
EC	0.91**	1.00																
WSOC	0.80**	0.77**	1.00															
Al	0.21	0.47	0.55**	1.00														
As	0.33	0.47	0.56**	0.72**	1.00	0.00												
Ba	0.29	0.13	0.40	0.21	0.00	1.00												
Ca	0.16	-0.12	0.11	-0.21	0.04	0.52	1.00											
Cd	0.89**	0.87**	0.65*	0.19	0.47	0.27	0.23	1.00										
Cr	-0.25	-0.38	-0.17	-0.10	0.21	-0.07	0.64*	-0.12	1.00									
Co	0.11	-0.11	0.24	0.07	0.21	0.40	0.69**	0.01	0.51*	1.00								
Cu	-0.13	-0.07	0.17	0.41	0.57*	0.05	0.34	0.04	0.56*	0.39	1.00							
Fe	0.37	0.15	0.48	0.10	0.24	0.61*	0.68**	0.29	0.47	0.78**	0.47	1.00						
Pb	0.50	0.44	0.72**	0.34	0.45	0.50	0.19	0.43	0.09	0.51	0.29	0.72**	1.00					
Sb	0.45	0.25	0.70**	0.07	0.23	0.12	0.15	0.20	0.15	0.34	0.09	0.45	0.60*	1.00				
Mn	0.55*	0.39	0.66**	0.21	0.39	0.59*	0.47	0.50	0.30	0.64*	0.23	0.82**	0.88**	0.54*	1.00			
Ni	-0.14	-0.26	-0.14	0.03	0.23	0.20	0.63*	-0.05	0.83**	0.70**	0.41	0.57*	0.26	0.00	0.42	1.00		
V	-0.11	-0.16	-0.20	-0.02	-0.16	0.11	0.26	-0.15	0.51	0.19	0.18	0.42	0.07	-0.08	0.11	0.64*	1.00	
Zn	0.71**	0.42	0.75**	-0.02	0.22	0.45	0.48	0.52	0.10	0.53*	0.07	0.66*	0.66*	0.82**	0.68**	0.13	-0.06	1.00

Winter

OC	1.00																
EC	0.92**	1.00															
WSOC	0.91**	0.93**	1.00														
Al	0.80**	0.86**	0.84**	1.00													
As	0.86**	0.86**	0.94**	0.88**	1.00												
Ba	0.73*	0.77**	0.81**	0.89**	0.82**	1.00											
Ca	0.84**	0.94**	0.78**	0.31	0.35	0.56	1.00										
Cd	0.94**	0.97**	0.96	0.27	0.37	0.77	0.89	1.00									
Cr	0.56	0.53	0.44	0.32	0.31	0.43	0.49	0.52	1.00								
Co	0.08	0.07	-0.03	0.18	-0.08	0.12	0.04	0.01	0.63*	1.00							
Cu	0.83**	0.83**	0.87**	0.15	0.17	0.90**	0.66*	0.86**	0.70*	0.20	1.00						
Fe	0.78**	0.80**	0.79**	0.16	0.17	0.89**	0.64*	0.78**	0.75**	0.39	0.95**	1.00					
Pb	0.79**	0.86**	0.85**	0.23	0.23	0.91**	0.72*	0.88**	0.59*	0.03	0.95**	0.87**	1.00				
Sb	0.91**	0.97**	0.93**	0.20	0.32	0.83**	0.88**	0.97**	0.51	-0.04	0.88**	0.82**	0.93**	1.00			
Mn	0.49	0.54	0.45	0.38	0.27	0.61*	0.46	0.53	0.82**	0.62*	0.70*	0.76**	0.70*	0.56	1.00		
Ni	0.03	0.02	-0.07	0.20	-0.08	0.08	0.00	-0.04	0.60	1.00**	0.15	0.35	-0.02	-0.09	0.59	1.00	
V	0.72**	0.79**	0.74**	0.05	0.18	0.83**	0.65*	0.80**	0.48	-0.11	0.86**	0.78**	0.94**	0.90**	0.61*	-0.16	1.00
Zn	0.80**	0.87**	0.78**	0.17	0.34	0.81**	0.76**	0.85**	0.56	0.01	0.85**	0.82**	0.92**	0.94**	0.68*	-0.04	0.96**

Spring

OC	1.00																	
EC	0.86**	1.00																
WSOC	0.84**	0.95**	1.00															
Al	-0.47	-0.57	-0.50	1.00														
As	-0.51	-0.56	-0.45	0.69	1.00													
Ba	0.40	0.31	0.38	-0.07	-0.33	1.00												
Ca	0.60*	0.34	0.46	-0.22	-0.11	0.18	1.00											
Cd	0.86**	0.92	0.84**	-0.50	-0.47	0.48	0.32	1.00										
Cr	0.65*	0.47	0.60*	0.05	-0.32	0.55	0.64*	0.40	1.00									
Co	0.37	0.27	0.39	0.07	0.04	0.62*	0.60	0.34	0.74**	1.00								
Cu	0.81**	0.75	0.84**	-0.01	-0.21	0.45	0.69*	0.68*	0.86**	0.64*	1.00							
Fe	0.87**	0.79	0.87**	-0.26	-0.36	0.57	0.69*	0.72**	0.86**	0.69**	0.93**	1.00						
Pb	0.87**	0.88	0.94**	-0.24	-0.43	0.43	0.55	0.76**	0.79**	0.48	0.94**	0.94**	1.00					
Sb	0.85**	0.92**	0.96**	-0.43	-0.50	0.29	0.49	0.79**	0.68*	0.39	0.88**	0.88**	0.94**	1.00				
Mn	0.73**	0.71	0.75**	-0.20	-0.55	0.41	0.59	0.56	0.80**	0.42	0.83**	0.83**	0.87**	0.74**	1.00			
Ni	0.69*	0.38	0.45	-0.11	-0.25	0.58*	0.71*	0.43	0.73**	0.59	0.67*	0.76**	0.64*	0.42	0.71*	1.00		
V	0.44	0.61	0.62*	-0.42	-0.49	0.60*	0.32	0.59*	0.40	0.48	0.51	0.62*	0.58*	0.46	0.66*	0.49	1.00	
Zn	0.83**	0.88	0.90**	-0.30	-0.40	0.50	0.57	0.79**	0.70*	0.53	0.88**	0.92**	0.94**	0.85**	0.89**	0.69*	0.78**	1.00

Summer

OC	1.00																	
EC	0.42	1.00																
WSOC	0.40	0.85**	1.00															
Al	0.31	0.58	0.61	1.00														
As	0.04	0.17	0.32	0.69	1.00													
Ba	-0.15	0.15	0.07	-0.11	-0.48	1.00												
Ca	0.34	0.45	0.41	0.53	0.45	0.20	1.00											
Cd	0.60*	0.52*	0.46	0.42	0.02	0.12	0.34	1.00										
Cr	0.31	0.36	0.45	0.48	0.24	0.03	0.36	0.07	1.00									
Co	0.11	0.31	0.42	0.14	0.14	0.13	0.38	-0.14	0.61*	1.00								
Cu	0.19	0.72**	0.72**	0.55	0.24	0.23	0.69**	0.21	0.64**	0.71**	1.00							
Fe	0.26	0.67**	0.70**	0.53	0.24	0.15	0.62*	0.16	0.84**	0.72**	0.95**	1.00						
Pb	0.20	0.39	0.28	0.67	0.19	0.15	-0.12	0.09	0.47	0.19	0.25	0.37	1.00					
Sb	0.63*	0.60*	0.54*	0.19	-0.14	0.14	0.16	0.21	0.26	0.30	0.30	0.36	0.22	1.00				
Mn	0.17	0.72**	0.68**	0.56	0.24	0.24	0.66**	0.18	0.64*	0.68**	0.99**	0.94**	0.33	0.27	1.00			
Ni	0.23	0.63*	0.63*	0.50	0.23	0.15	0.67**	0.15	0.80**	0.75**	0.94**	0.98**	0.35	0.25	0.94**	1.00		
V	0.27	-0.01	-0.14	0.13	-0.10	-0.30	-0.46	0.18	0.06	-0.28	-0.37	-0.25	0.51	-0.03	-0.32	-0.22	1.00	
Zn	0.58*	0.80**	0.81**	0.59	0.10	0.26	0.44	0.47	0.60*	0.37	0.73**	0.75**	0.47	0.56*	0.72**	0.69**	0.12	1.00

* At 0.05 level (two-tail), the correlation is significant.

** At 0.01 level (two-tail), the correlation is significant.

4.3.3.3 Industry Emissions (IE)

As a typical industrial city, Ningbo is comprised of intensive industrial zones in Zhenhai and Beilun districts in the north and northeast of our study domain, respectively, relating to a power plant, dye industry, metallurgy, smelting and petrochemical industry. Fig. 4.4 demonstrates that $OP_v^{ws\text{-}IE}$ (0.20 ± 0.12 nmol min^{-1} m^{-3}) was significantly higher during spring, which was twice as much as that in winter (0.09 ± 0.21 nmol min^{-1} m^{-3}) and summer (0.10 ± 0.15 nmol min^{-1} m^{-3}), and almost five times that in autumn (0.04 ± 0.05 nmol min^{-1} m^{-3}). As presented in Fig. 4.5(b), the highest loadings of IE-related transition metals were observed including Zn (61.54 ng m^{-3}), Mn (34.85 ng m^{-3}), Pb (3.84 ng m^{-3}), Cr (1.29 ng m^{-3}), Cu (0.85 ng m^{-3}) and V (0.45 ng m^{-3}) during spring. The elements such as Zn, Mn, Cr, and Cu are the main species featured in IE, indicating the responsible sources as smelters and metallurgical industries. As documented by the Ningbo Statistics Bureau (http://english.nbtjj.gov.cn), there are approximately 5,028 enterprises associated with metal smelting and processing in Ningbo (Wang et al., 2018b). Pb was almost three times higher during spring (3.8 ng m^{-3}) than other seasons (0.62 – 1.2 ng m^{-3}), and such a trend might be due to the abundance in particulate matter generated from steelmaking processes and power plant operations. Previous studies reported the declined emission of Pb from vehicle exhaust attributable to the widespread use of unleaded petrol, and thus IE has now became a dominant contributor for this element (Zhang et al., 2020). Pb is also considered as an indicator of dye sources, the higher level of which suggested a strong impact of textile mill and garment factory on the air quality in Ningbo. Pb and Zn can cause oxidative stress through electrophilic reaction pathways (Yu et al., 2019). Cu and Mn were reported as the most redox-active transition metals due to their highest DTT

consumption rates and induced OP through catalytic processes and ROS formation (Charrier and Anastasio, 2012c). The occurrence of V in the aerosol signified the mixed source of heavy oil combustion for cargo ships and diesel vehicles, which was reported as one of the most reactive metals with DTT assay (Charrier and Anastasio, 2012c). Therefore, ambient levels of $PM_{2.5}$ derived from metal industry and dye industry possess prominent oxidative potential compared to other industries, and became more significant for public health (Chung et al., 2021).

4.3.3.4 Non-linearity of OP_v^{ws} Induced from Other Sources

The contributions of vehicle emissions (VE) and fugitive dust (FD) to $PM_{2.5}$ were identified through source apportionment analysis in CMB model, but were excluded as the main contributors to OP_v by MLR analysis. Most regression analysis applied in estimating source-specific OP assumed that there were linear source contributions to the levels of OP with no obvious interaction between independent variables (multi-sources or multi-components). The exclusion of VE and FD might be attributed to the potential statistical limitations, including low annual contribution of FD (0.43%) to $PM_{2.5}$ mass or the small sample size for VE source, although the VE contribution was significant (21.07%). However, non-linear oxidising capacity induced from VE- and FD-emitted $PM_{2.5}$ could be considered as one of the dominant reasons for exclusions of VE and FD from MLR analysis. Such trend was in agreement with several previous studies, showing the synergistic or antagonistic effects on the OP activity between metal and organic compound interactions (Lin and Yu, 2020, Yu et al., 2018). The multi-source interactions confirmed from Pearson's correlation coefficient between OP activity

and emission sources (Fig. 4.6).

A significant positive correlation was observed between $OP_v^{ws\text{-}SS}$ and VE during spring, with correlation coefficient of *r* ($OP_v^{ws\text{-}SS}$/VE) = 0.709. Thus, such result signified either the additive or synergistic effects in ROS generation between SS and VE- related $PM_{2.5}$. Fe exhibited an additive effect in DTT consumption with quinones (Xiong et al., 2017). The abundant Fe content identified from SS sources (16.307 – 40.535 ng m^{-3}) mixed with VE emitted quinones would be one of the driving factors for additive interactions between SS and VE. Despite such trend, Mn content from VE sources was relatively higher during spring (0.150 ng m^{-3}) than autumn (0.015 ng m^{-3}) and winter (0.000 ng m^{-3}), while 1,2-NQ during spring (5.27 ± 1.75 ng m^{-3}) was higher than autumn (4.37 ± 2.51 ng m^{-3}) and summer (2.70 ± 1.78 ng m^{-3}). Based on observations of previous reported studies, the mixture of Mn + 1,2-NQ, appeared to have a largely synergistic effect in DTT oxidation, which could play a dominant role in causing the non-linear oxidising capacity induced from VE (Xiong et al., 2017, Yu et al., 2018). FD correlated well with DTT activities induced from SS-related $PM_{2.5}$ during summer, with *r* ($OP_v^{ws\text{-}SS}$/FD) = 0.564. The catalytic oxidiser of Mn (0.616 ng m^{-3}) offered the highest contributions from FD sources during spring. Therefore, we suggested that the combination effects of synergistic effect of Mn and HULIS interaction essentially contributed to non-linear increase of DTT oxidation induced from FD-related particulates. As discussed in Section 4.3.3.2, SO_4^{2-} plays an essential role in dissolving metal ions due to its higher hygroscopic nature. Although, SO_4^{2-} from FD and SS were not the most abundant during summer, the highest RH (75.57 ± 4.14%, Table 4.3) might have facilitated the refractory trace metal conversions such as Cu, Fe, and Mn. Hence, forming soluble metal sulphates and

possibly increasing the ROS generation ability of the redox metals in $PM_{2.5}$ (Fang et al., 2017a).

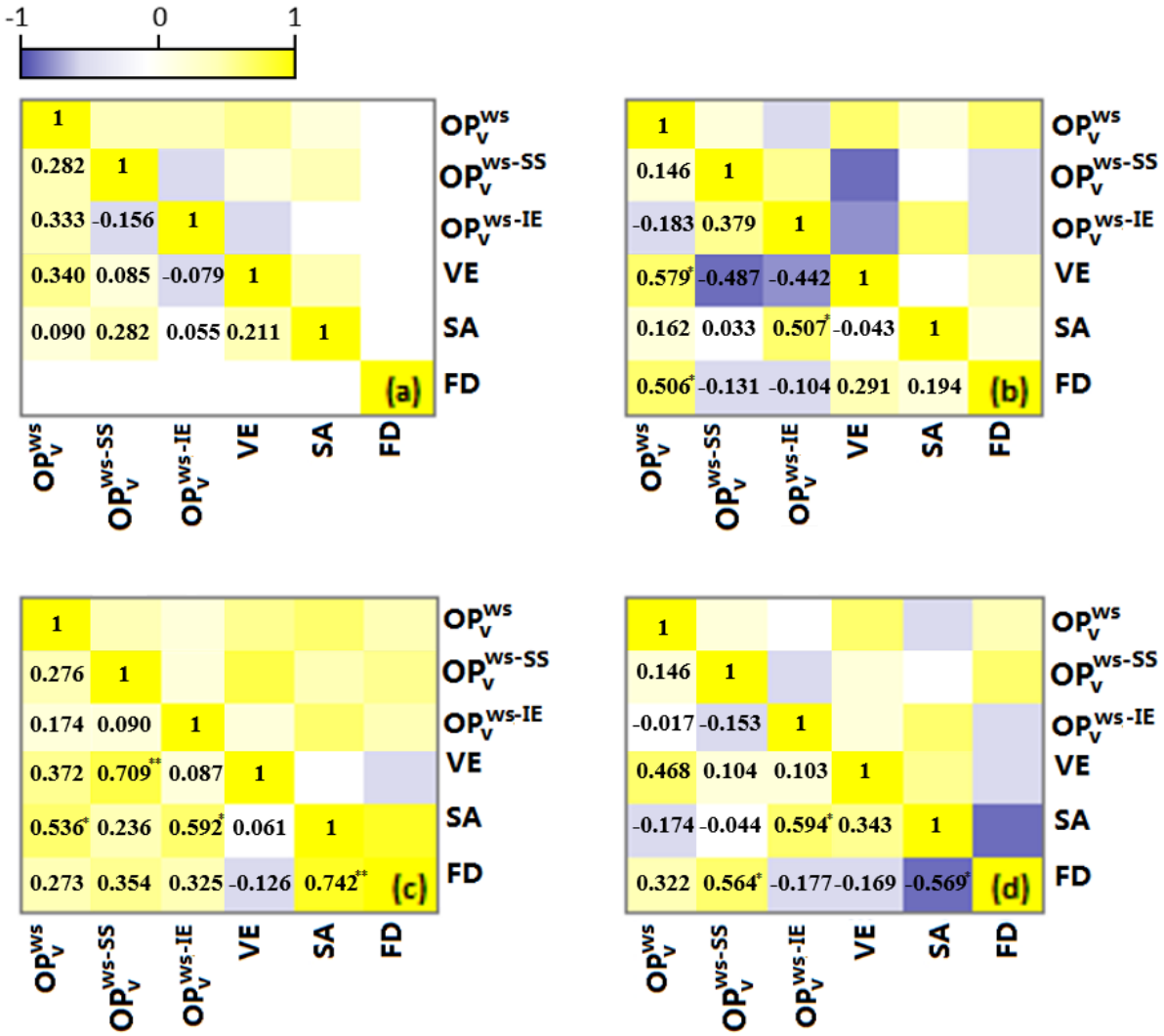

Figure 4.6 Pearson correlations among OP_v^{ws} source contributions OP_v (OP_v^{ws-SS}, OP_v^{ws-IE}) and source contributions of VE, SA, FD to $PM_{2.5}$ during autumn (a), winter (b), spring (c) and summer (d) (* At the 0.05 level (two-tail), the correlation is significant; ** At the 0.01 level (two-tail), the correlation is significant)

4.3.4 Comparison of Driving Factors of OP of $PM_{2.5}$ with Similar Concentrations

Since variation of OP values of ambient levels of $PM_{2.5}$ was due to a cascade of reasons, including different chemical composition, emission sources, and the

synergistic/antagonistic/additive interactions among various $PM_{2.5}$ components (e.g., metal – quinone, metal – HULIS, and metal – carboxylic acid mixtures), the particulates of similar mass concentrations exhibited a significant difference in generation ability of ROS (Cheng et al., 2020, Lin and Yu, 2020). In this study, the concentrations of most samples were centred between 20-40 μg m^{-3}. To investigate further about intrinsic OP of ambient $PM_{2.5}$, 21 out of 55 $PM_{2.5}$ samples with mass concentrations ranged from 20 to 40 μg m^{-3} (divided into 20 – 30 μg m^{-3} and 30 – 40 μg m^{-3}, named as group 20-30 and group 30-40, respectively) were selected, which was favourable for analysis and comparison of the representative drivers of particulate intrinsic OP. The OP_v^{ws} values ranged broadly from 0.99 to 6.10 nmol min^{-1} m^{-3} in group 20-30, while 1.40 to 6.37 nmol min^{-1} m^{-3} for OP_v^{ws} in group 30-40 (Fig. 4.7). Moreover, OP_v^{ws} also displayed insignificant correlation with $PM_{2.5}$ mass (R^2=0.037, p=0.66, Fig. 4.8). These results signified that different factors might interplay in driving OP_v and $PM_{2.5}$ mass concentrations. Therefore, the mitigation measures targeting to reduce particulate mass concentration alone could not be sufficient to decrease OP_v effectively.

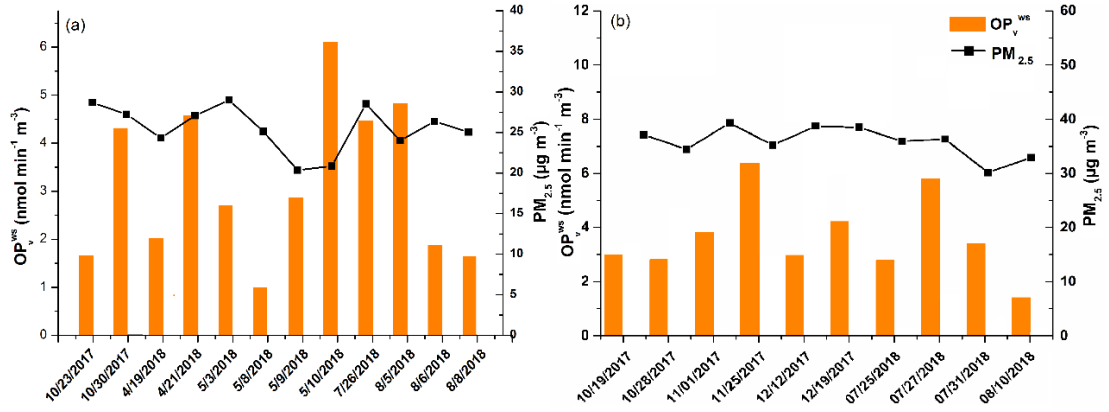

Figure 4.7 OP_v^{ws} of ambient levels of $PM_{2.5}$ with similar mass concentrations ranged from 20-30 μg m^{-3} (a) and 30-40 μg m^{-3} (b) in Ningbo during the sampling campaign

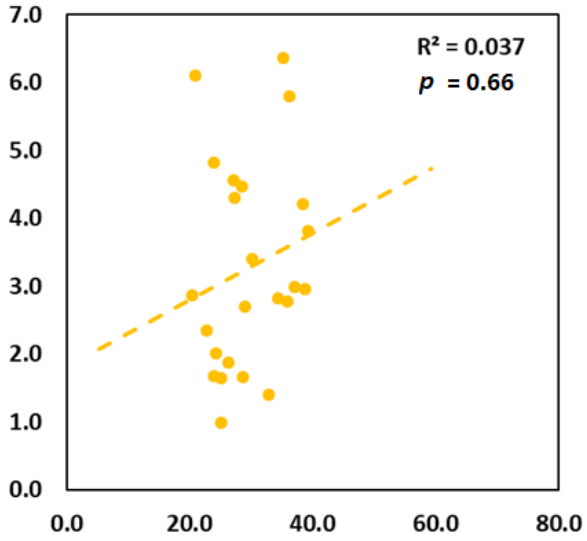

Figure 4.8 Correlation between OP_v^{ws} values and $PM_{2.5}$ mass concentrations with concentrations ranged from 20-40 μg m^{-3}

We observed higher levels of OP_v^{ws} on dates of 21 April (4.57 nmol min^{-1} m^{-3}), 10 May (6.10 nmol min^{-1} m^{-3}), 26 July (4.47 nmol min^{-1} m^{-3}), and 5 August 2018 (4.82 nmol min^{-1} m^{-3}) from group 20-30 Fig. 4.7(a)), implying the pivotal role of water-soluble fractions in inducing $PM_{2.5}$ oxidative capacities during these days. Regardless of SA including SNA which cannot directly produce OP response, $PM_{2.5}$ mass concentrations were governed by VE on 10 May and 26 Jul 2018, with source contributions of 41.50% and 61.31%, respectively (Fig. 4.9(b)). Given that traffic-emitted particulates tend to induce high DTT oxidation reported by previous studies, it is hypothesised that such high OP_v^{ws} values were mainly driven by VE (Daellenbach et al., 2020, Weber et al., 2018, Weber et al., 2021, Yu et al., 2019). To test such a hypothesis, the chemical component spectrums of PM contributed by VE and other sources (including CC, IE, FD, BB, SS) and their proportions were plotted for group 20-30 and group 30-40 (Fig. 4.10 & 4.12). Since particulate OC that was identified by CMB model contained

PAHs, the spectrums of PAH compositions contributed by CC and VE and their proportions were presented in Fig. 4.11 & 4.13 for group 20-30 and group 30-40, respectively. Fig. 4.10(c) & (c1) showed a significant difference in VE associated particulate compositions between dates of 10 May and 26 July, and the remaining days within group 20-30. We observed that VE related $PM_{2.5}$ was composed of transition metals, particularly samples on 10 May and 26 July, with particulate catalytic oxidisers of Cu (3.29 and 9.10 ng m^{-3}) and Mn (0.78 and 3.32 ng m^{-3}) being predominant, and contributed to the higher levels of OP_v^{ws} on these two days. However, only EC and OC with redox inactive PAHs were identified from VE sources during remaining days of group 20-30, which would have more impact on the OP induced from hydrophobic fractions. The $PM_{2.5}$ mass of sample on 21 April was mainly apportioned to IE (15.19%) and VE (10.62%). Considering the limited OP_v^{ws} induced from VE alone on 21 April, we inferred that IE would be the chief factor for OP_v^{ws} production, ascribing to its chemical composition of transition metals with higher loadings of Zn (112.65 ng m^{-3}) and Mn (63.86 ng m^{-3}) (Charrier and Anastasio, 2012c). The higher OP_v^{ws} value would also be due to the synergistic interaction between IE-related Mn and VE-derived quinones (e.g., 1,2-NQ), as discussed in Section 4.3.3.6. SS aerosol contributed distinctively to $PM_{2.5}$ mass concentration (18.06%) on 5 August together with IE (16.48%). The higher OP_v^{ws} observed during this day could be due to large loadings of Cl^- (0.23 μg m^{-3}), Fe (29.90 ng m^{-3}), Ni (1.73 ng m^{-3}), V (1.73 ng m^{-3}), and Zn (8.23 ng m^{-3}) from SS. The SS-related Cl^- was considered as more redox active than $OH^\cdot$ to oxidise VOCs emitted from IE sources, making the aerosols more oxidant, as discussed in Section 4.3.3.2.

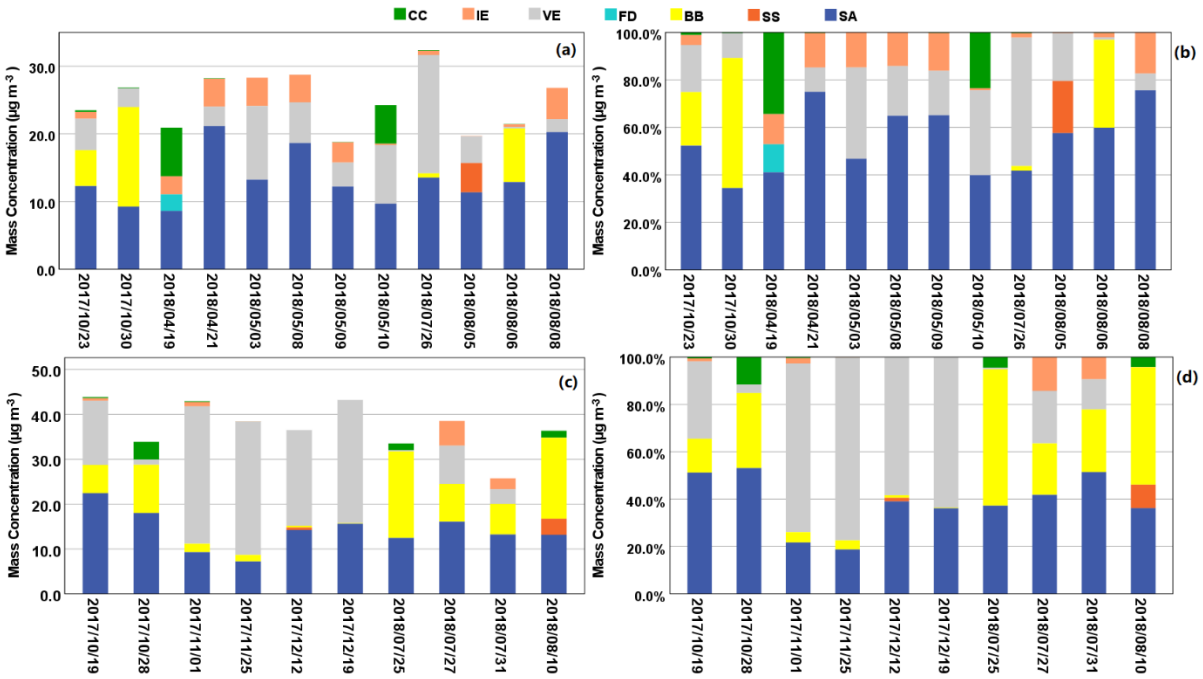

Figure 4.9 Source apportionment and proportions of source contributions to ambient $PM_{2.5}$ for group 20-30 (a-b) and group 30-40 (c-d)

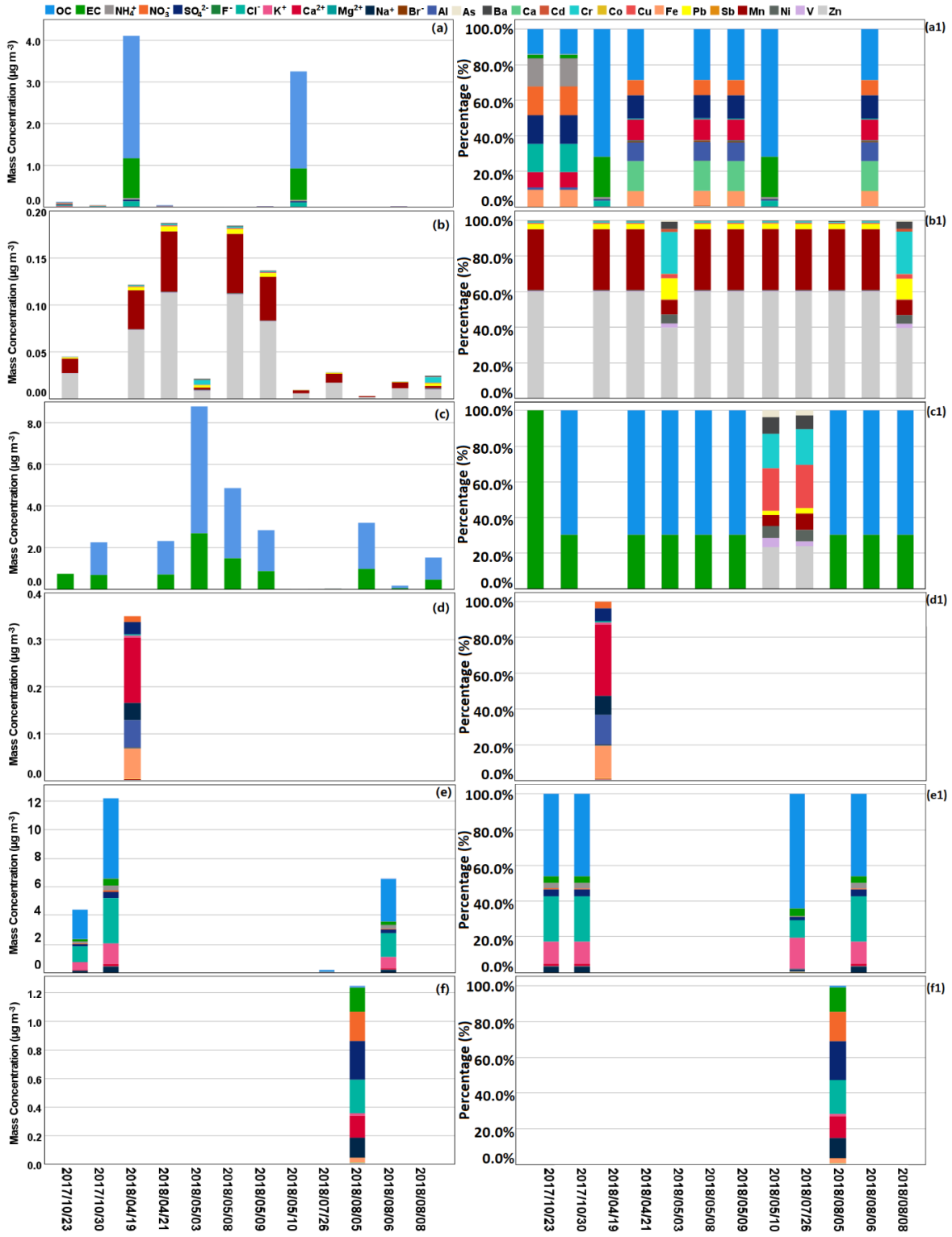

Figure 4.10 Chemical component spectrum of particles contributed by CC, IE, VE, FD, BB, SS (a-f) and their proportions (a1-f1) for group 20-30

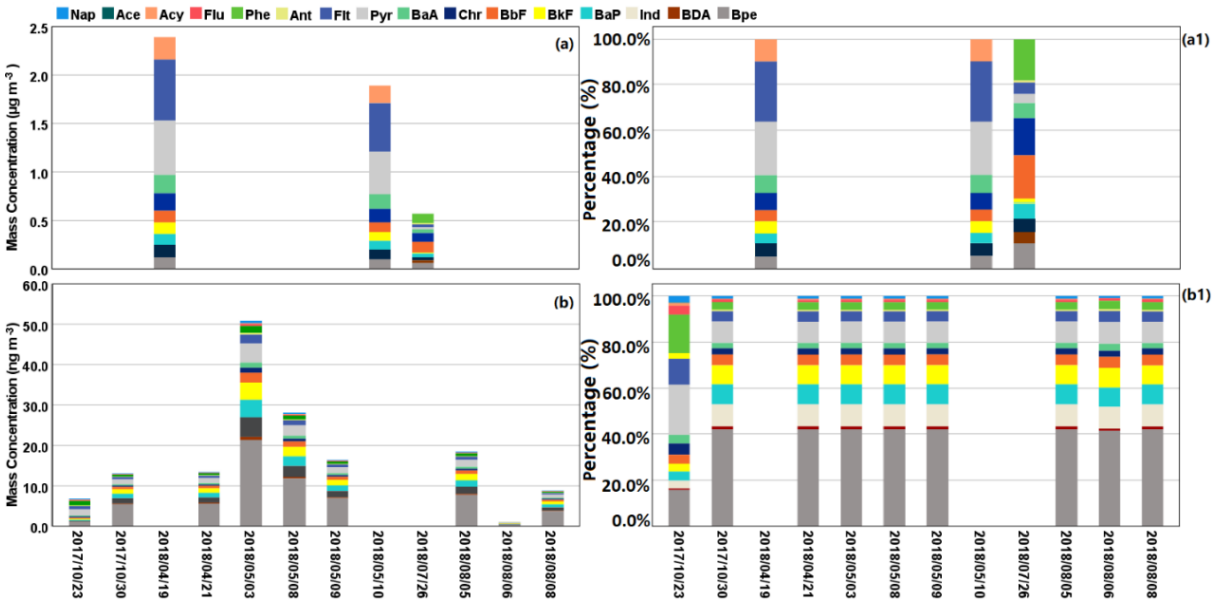

Figure 4.11 Spectrum of particulate PAHs components (contained in OC) contributed by CC and VE (a-b) and their proportions (a1-b1) for group 20-30

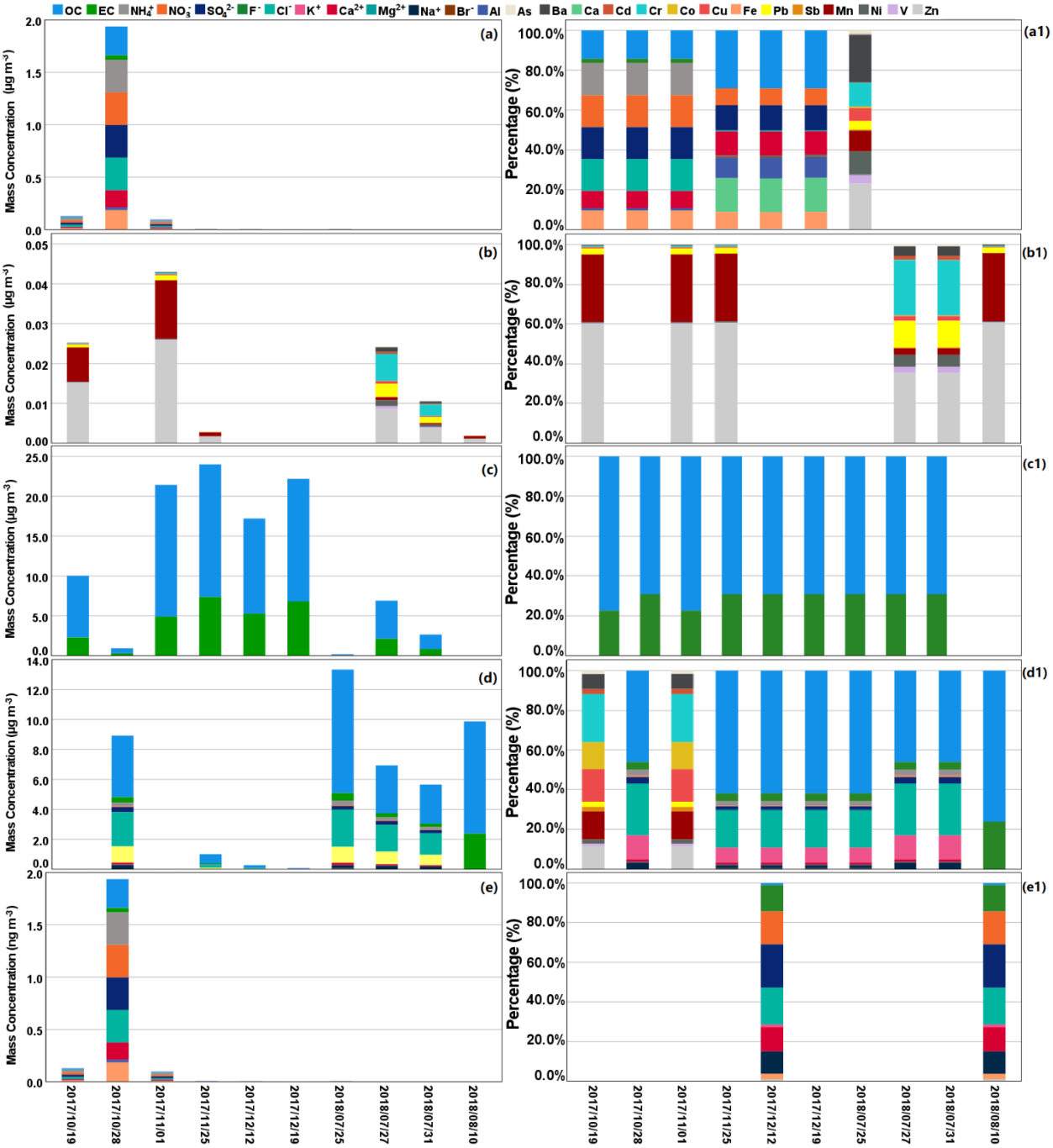

Figure 4.12 Chemical component spectrum of particles contributed by CC, IE, VE, BB, SS (a-e) and their proportions for group 30-40

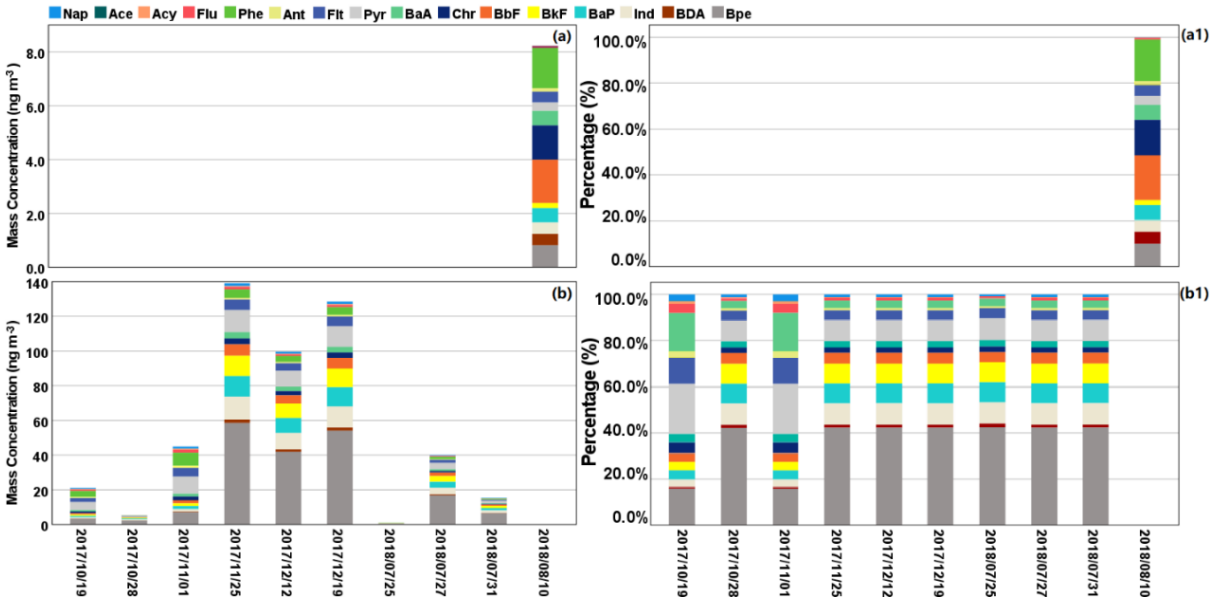

Figure 4.13 Spectrum of particulate PAHs components (contained in OC) contributed by CC and VE (a-b) and their proportions (a1-b1) for group 30-40

4.4 Conclusion

We successfully measured OP levels induced from water-soluble fraction of $PM_{2.5}$ collected in a coastal hotspot at Ningbo through application of DTT assay. Seasonal variation was observed for OP_v^{ws}, with the highest average values during autumn. There was a redistribution of source contributions to OP_v^{ws} compared to $PM_{2.5}$ mass. The higher contribution to OP_v^{ws} was derived from IE spring.

To the best of our knowledge, this is the first study to report the redox activity induced by SS aerosol. A significant contribution from SS aerosol to OP_v^{ws} was observed during winter, due to its higher content of Fe, predominantly from IE sources. More OP investigation might have to be conducted in the coastal cities of China to better understand the implications related to the oxidative stress of SS aerosols. There were non-linear increases between VE, FD derived

OP_v and $PM_{2.5}$ concentration, which can be ascribed to the prominent synergistic and/or antagonistic interactions among VE and FD sources and their chemical components.

In addition, it has been observed that the significantly different toxicities could occur to the PM of similar mass concentrations (in the range of 20 – 40 μg m^{-3}) due to their distinctly different chemical composition spectrums associated with varying emission sources. Therefore, the mitigation of $PM_{2.5}$ emission sources alone may not be sufficient in reducing OP activity. Thus, to decrease the $PM_{2.5}$ OP in this region, the emissions of $PM_{2.5}$ and its redox active components should be jointly controlled so as to reduce the $PM_{2.5}$ oxidative potential. In particular, as IE exhibited higher intrinsic OP contribution to OP_v^{ws} in Ningbo, a more stringent regulation of mitigating the industrial $PM_{2.5}$ and new technologies to lower the intrinsic OP^{ws} of IE-related $PM_{2.5}$ should be considered as a priority to improve the population health in Ningbo city. The methods and approaches developed and used in this study could be applicable in other regions to assess the discrepancy between $PM_{2.5}$ mass concentration and its oxidative potential in terms of inhalation toxicity so that more informed policies can be formulated for the mitigation of air pollution on local and regional scales.

Chapter 5 OP of Methanol-soluble Fraction of Ambient $PM_{2.5}$: Chemical Characterisation, Seasonal Variation and Source Apportionment

5.1 Introduction

Growing studies were focused on the correlation of OP and water-soluble fractions of PM because of the readily bioavailability of the chemical compositions compared to water-insoluble fractions (Charrier and Anastasio, 2012c, Cheng et al., 2021, Fang et al., 2016, Gao et al., 2020b, Verma et al., 2014). In fact, considerable field and laboratory measurements have denoted that the insoluble fractions of PM may also play an essential role in manifesting the oxidative activity (Cao et al., 2021b, Gao et al., 2020b, Li et al., 2021, Wong et al., 2019). Accordingly, the particle species such as polycyclic aromatic hydrocarbons (PAHs), humic-like substances (HULIS) and quinones (1,2-naphthoquinone, 1,4-napthoquinone, phenanthrenequinone) have been typically examined to be correlated with OP activity by dithiothreitol (DTT) assay (Cho et al., 2004, Cho et al., 2005, Dou et al., 2015, Gao et al., 2017, Gao et al., 2020b, Paciolla et al., 2002, Wong et al., 2019).

As reported by prior studies, organic catalytic oxidisers resided in the ambient PM, including HULIS and quinones, may participate in the synergistic and/or antagonistic interactions with other PM species and antioxidants, which could alter the redox properties. For example, mixtures of Cu with quinones or HULIS antagonistically oxidise DTT with a DTT consumption rate lower than the sum of individual redox

active species (Lin and Yu, 2020). Mn in PM exhibits synergistic and antagonistic effects in DTT oxidation when mixed with quinones and HULIS, respectively. Fe interacts additively with quinones and HULIS compounds in DTT consumption, but synergistically in OH· production (Charrier and Anastasio, 2015, Yu et al., 2018). Therefore, it is difficult to deduce the key drivers of OP by just focusing on the redox-active components.

A few studies estimated the source-specific contributions to PM-induced OP by applying the receptor models such as Positive Matrix Factorisation (PMF), Chemical Mass Balance (CMB) and Principal Component Analysis (PCA) coupled with Multivariate Regression (Bates et al., 2015, Fang et al., 2016, Verma et al., 2014, Weber et al., 2018, Yu et al., 2019). Across Europe, the OP level is more affected by residential biomass burning (BB) and vehicular non-exhaust emissions (Borlaza et al., 2021, Daellenbach et al., 2020). Similarly, in Atlanta, the anthropogenic source of BB was one of the key contributors to OP from water-soluble $PM_{2.5}$ fractions (Verma et al., 2014). Liu et al. (2018a) reported a considerable intrinsic OP of coal combustion (CC) derived OP in northern China. However, due to the interaction effects between multi-species and/or multi-sources, the traditional analytical methods considering the only linear increase of OP along with the increases of chemical components or source emissions could be to some extent limited.

As PM redox activity can be induced from water-insoluble fractions, analysis of source contributions to OP^{ws} alone cannot completely represent the toxicity of ambient $PM_{2.5}$. Besides, due to the potential interactions among PM species, biased OP

contribution would be estimated by directly using the linear regression model of individual particulate matter catalytic oxidisers. Therefore, in this study, we aim to: 1) analyse the seasonal variations of ambient $PM_{2.5}$ mass concentrations, and the overall OP^{meth} values ; 2) assess the spatial distributions of $PM_{2.5}$ and its OP^{meth} in the study domain; 3) estimate the source contributions to OP_v^{meth}; 4) explain the reason why OP increased non-linearly with the increased source contributions and investigate the interaction within and between the source-derived OP; 5) explore the driving factors of OP^{meth} that are induced from $PM_{2.5}$ with similar mass concentrations.

5.2 Methods

5.2.1 Sampling

The same sampling protocol for ambient $PM_{2.5}$ can be found in Section 4.2.1.

5.2.2 Sample Analysis

Collected filters were divided analyse through an array of experiments for quantifying organic species including carbonaceous species, PAHs and quinones. Organic carbon (OC) and elemental carbon (EC) were analysed using thermal/optical carbon analyser (Model 2001A, DRI), as described in Section 3.5.4. Filters used for measuring PAHs and quinones were extracted separately (as described in Section 3.5.1.3 and Section 3.5.1.4) and evaporated to 1 ml at 35 °C under gentle nitrogen stream (Section 3.5.1.5). Extracted analytes of quinones experienced derivatisation process before measurement (Section 3.5.1.6). All extracts for PAHs and quinone

measurements were then kept in sealed at -20 °C prior to respective GC-MS (Agilent Technologies 7890B)-MS (Agilent Technologies 5977A) and HPLC (Shimadzu 30A)-MS/MS (ABsciex 3200 Q trap) analysis, as described in Section 3.5.5 and Section 3.5.6, respectively.

5.2.3 Quality Control

The analytical quality of the measured data was determined by recovery and linearity and limit of detection (LOD). Blank filters were analysed to correct field aerosol samples for quality control and assurance. The concentrations of PAHs and quinones were estimated via the 5-point external standard calibration, ranged from 0.1 to 1000 ng mL^{-1}, the linearity of calibration standards calculated through linear regression with values between 0.99 and 1.00 (r^2) for all PAHs and quinones. The LOD was ranged from 0.23 ng m^{-3} of BaA to 8.79 ng m^{-3} of Acy for PAHs and 0.01 ng m^{-3} of 1,2-NQ, while the recovery ranged from 88.37% of Phe to 110.02% of BbF for PAHs and 95.77% of 1,2-NQ.

For OC and EC, known concentration of standard solution was used for calibration before each set of analysis, during which multipoint external calibration was conducted by analyser via dripping the sucrose solution onto a punch of pre-baked blank filter. The LOD was 0.65 µg m^{-3} of OC and 1.00 µg m^{-3} of EC, while recovery was 101.92% of OC and 89.02% of EC.

The concentrations of $PM_{2.5}$ and measured organic components are summarised in Table 5.1.

Table 5.1 Summary of mass concentrations of $PM_{2.5}$ and OC, EC, PAHs and quinones during four seasons

Components[a]	Autumn	Winter	Spring	Summer
$PM_{2.5}$	43.87 ± 18.09[b]	87.60 ± 35.63	36.54 ± 25.55	28.60 ± 12.31
OC	10.22 ± 4.47	14.07 ± 5.59	6.38 ± 4.32	4.62 ± 2.30
EC	4.14 ± 1.69	9.51 ± 5.87	1.92 ± 2.27	0.99 ± 0.70
Nap	0.63 ± 0.69	0.75 ± 0.58	0.20 ± 0.14	0.16 ± 0.10
Ace	0.33 ± 0.41	0.62 ± 0.61	0.09 ± 0.04	0.65 ± 1.19
Acy	0.39 ± 0.12	1.00 ± 0.95	0.14 ± 0.20	0.22 ± 0.18
Flu	0.10 ± 0.09	0.26 ± 0.36	0.04 ± 0.02	0.03 ± 0.05
Phe	1.50 ± 1.96	2.06 ± 2.68	0.02 ± 0.02	0.04 ± 0.09
Ant	0.17 ± 0.19	0.40 ± 0.32	0.03 ± 0.03	0.04 ± 0.08
Flt	2.77 ± 3.47	5.47 ± 7.02	0.56 ± 0.34	0.11 ± 0.10
Pyr	6.88 ± 7.92	9.38 ± 10.10	0.73 ± 0.50	0.30 ± 0.24
BaA	1.70 ± 2.79	4.25 ± 6.78	0.14 ± 0.12	0.04 ± 0.03
Chr	2.59 ± 4.60	7.56 ± 8.35	0.05 ± 0.04	0.02 ± 0.01
BbF	7.40 ± 9.07	13.47 ± 13.96	2.93 ± 3.61	0.77 ± 0.61
BkF	3.86 ± 5.27	7.80 ± 8.43	2.00 ± 5.88	0.25 ± 0.18
Bap	2.07 ± 3.80	5.37 ± 7.24	0.33 ± 0.38	0.11 ± 0.09
Ind	8.46 ± 13.35	16.73 ± 20.87	1.38 ± 2.03	0.43 ± 0.49
DBA	0.31 ± 0.37	1.04 ± 1.02	0.08 ± 0.04	0.06 ± 0.03
Bpe	5.31 ± 6.45	8.15 ± 9.14	1.35 ± 1.13	0.41 ± 0.39
1,2-NQ	4.74 ± 2.61	8.60 ± 3.23	5.27 ± 1.75	2.70 ± 1.78

a Concentration units for $PM_{2.5}$, OC, EC are μg m^{-3}, for PAHs and quinones are ng m^{-3}.

5.2.4 Analysis of Air Mass Backward Trajectory

The same protocol of modelling air mass back trajectory has been described in Section 4.2.4.

5.2.5 Graphical Analysis of Source Dispersion

Source dispersions of $PM_{2.5}$ mass concentration and $PM_{2.5}$ induced OP_v^{meth} were predicted via bivariate polar plots (BPPs). The detailed analysis procedures are the same as the description in Section 4.2.5.

5.2.6 CMB Model

The resultant source contributions to $PM_{2.5}$ share the same data with the CMB model applied in Chapter 4, and the detailed description of source apportionment analysis has been presented in Section 4.2.6.

5.2.7 Multiple Linear Regression (MLR)

The oxidative capacity from specific sources of $PM_{2.5}$ (N=55) was estimated through a MLR analytical model (Bates et al., 2015). In this study, OP_v^{meth} was defined as the dependent variable and source contributions (SC) to $PM_{2.5}$ (SC_i, μg m^{-3}) as the independent variables. All the programming was conducted using SPSS (Statistics 23). The detailed description of estimating source contributions to OP_v^{meth} has been presented in Section 4.2.7.

5.3 Results and Discussion

5.3.1 Seasonal Variation of $PM_{2.5}$ and OP Activity

Seasonal variations of $PM_{2.5}$ and OP induced by water-insoluble (hydrophobic) fractions (OP_v^{meth}, OP_m^{meth}) during this sampling campaign in Ningbo city are presented in Fig. 5.1. Detailed discussion in seasonal variation of $PM_{2.5}$ concentration has been described in Section 4.3.1. In this study, we observed significant variability of OP_v^{meth} on the basis of one-year observations. The annual OP_v^{meth} showed substantially high level of mean values (4.46 ± 4.62 nmol min^{-1} m^{-3}) but low level of median values (2.73 nmol min^{-1} m^{-3}), suggesting that OP_v^{meth} was more influenced by the extreme higher value occurring during winter. substantially higher OP_v^{meth} was observed during winter (median: 11.14 nmol min^{-1} m^{-3}, mean: 11.51 ± 2.56 nmol min^{-1} m^{-3}), followed by autumn (median: 3.41 nmol min^{-1} m^{-3}, mean: 3.83 ± 1.41 nmol min^{-1} m^{-3}), spring (median: 1.07 nmol min^{-1} m^{-3}, mean: 1.28 ± 1.28 nmol min^{-1} m^{-3}), and summer (median: 0.29 nmol min^{-1} m^{-3}, mean: 0.79 ± 0.83 nmol min^{-1} m^{-3}). Such seasonal trend was consistent with that of $PM_{2.5}$ mass concentrations, implying that those organic catalytic oxidisers were strongly associated with $PM_{2.5}$ mass accumulation. The median of our OP_v^{meth} was almost 10 times higher than the mean and median values reported in previous studies conducted in urban Atlanta, USA (0.32 ± 0.06 nmol min^{-1} m^{-3}) (Gao et al. (2017)) and mid-western USA (0.23 nmol min^{-1} m^{-3}) (Yu et al. (2021)), indicating the potentially more severe oxidative stress of ambient fine particles could be from organic fractions.

The mass-normalised DTT activity (OP_m^{meth}) was shown in Figure 5.1(c)). The annual median of OP_m^{meth} (0.12 ± 0.13 nmol min^{-1} μg^{-1}) was significantly higher than mid-western USA (0.021 nmol min^{-1} μg^{-1}) (Yu et al. (2021). The relatively higher OP_m^{meth} suggested that a greater intrinsic oxidative potential per unit mass of organic fraction of $PM_{2.5}$ could occur in Ningbo. The fine particles exhibited the highest mean OP_m^{meth} during summer, with 0.17 ± 0.21 nmol min^{-1} μg^{-1}, indicating that the highest intrinsic OP associated with water-insoluble components per unit mass of $PM_{2.5}$ despite the lowest $PM_{2.5}$ mass concentration in this season.

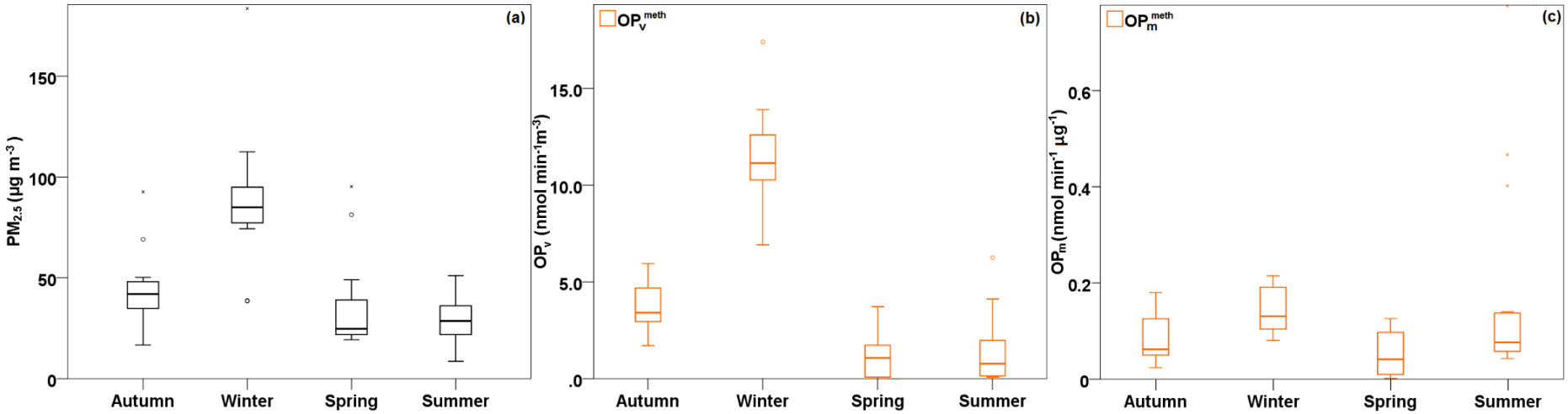

Figure 5.1 Seasonal variations of levels of (a) ambient $PM_{2.5}$ concentrations, (b) $PM_{2.5}$-induced OP_v^{meth} and (c) OP_m^{meth}

5.3.2 Graphical Analysis of Potential Source of OP_v^{meth}

Bivariate polar plots of OP_v^{meth} and mass concentrations of $PM_{2.5}$ are presented in Fig. 5.2, and these plots show the graphical comparisons of their potential sources. OP_v^{meth} and $PM_{2.5}$ exhibited considerably different temporal trends with respect to changes in wind speed and wind direction throughout four seasons in Ningbo. Detailed discussion of source dispersion of $PM_{2.5}$ concentrations has been presented in Section 4.3.2.

Fig. 5.2(c) and Fig. 5.2(d) showed the most abundant sources of $PM_{2.5}$ in the section between NW and NE, and the $PM_{2.5}$ concentrations could not reduce with the increase in wind speed during spring and summer, which were very possibly affected by the Zhenghai industry zone situated in the NE around 20 km away from the study site. The increased values of OP_v^{meth} during spring could also be attributed to those catalytic oxidisers on the particulate matter emitted from industrial activities (Fig. 5.2(g). This finding was in agreement with the reported study conducted in the northern France, showing that a higher oxidative capacity was induced from industrial sources related to PM (Moufarrej et al., 2020). The highest levels of OP_v^{meth} occurred when easterly wind dominated with speed higher than 7 m s^{-1} in spring (Fig. 5.2(g)). It signified the $PM_{2.5}$ contributed by those regional distant sources, such as the Beilun industry zone, Beilun port, and sea salt from the East China Sea, about 35 km away from the east of the study site, would have significant oxidative potency. In addition, the back trajectory analysis and fire spot distribution (Fig. 4.3(b)) show that over 80% of the air masses in winter were originated from the NW of the region and passed through Hangzhou Bay before

arriving at the study domain. Thus, aerosols from mid-range transport, bringing pollutants from regional BB might have aggravated the air pollution and enhanced the related oxidative potency. Further discussions on oxidative potentials of PM from industry and BB sources are presented in and Section 5.3.3.3 and Section 5.3.3.4.

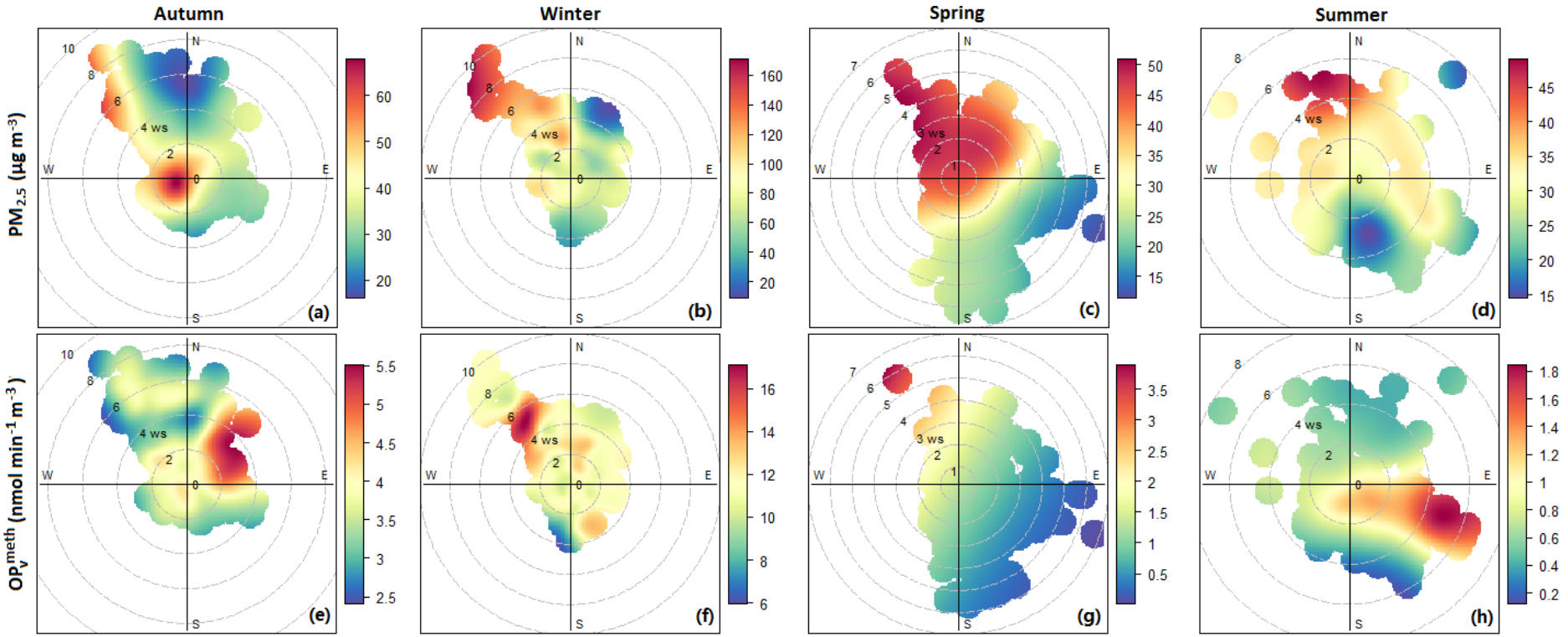

Figure 5.2 Bivariate polar plots of $PM_{2.5}$ (a-d) and OP_v^{meth} (e-h) predicted during autumn, winter, spring and summer

5.3.3 Source Contributions to OP_v^{meth}

5.3.3.1 Intrinsic OP_m^{meth} of $PM_{2.5}$ source

We estimated the seasonal variations of source contributions to OP_v^{meth} based on a multiple linear regression (MLR) model. The OP_v^{meth} from coal combustion (CC), IE, and biomass burning (BB). The highest $OP_m^{meth\text{-}IE}$, compared to other sources, possess greatest capacity for the generation of ROS, suggesting a highest ROS generation ability of per unit mass of $PM_{2.5}$ released from IE in the study site (Cao et al., 2021b). The intrinsic OP_m induced from BB ($OP_m^{meth\text{-}BB}$) was almost the same as that of CC ($OP_m^{meth\text{-}CC}$), with the following order of OP_v^{meth} as: $OP_m^{meth\text{-}IE}$ (0.38 ± 0.07 nmol min^{-1} μg^{-1}) > $OP_m^{meth\text{-}BB}$ (0.24 ± 0.06 nmol min^{-1} μg^{-1}) > $OP_m^{meth\text{-}CC}$ (0.24 ± 0.05 nmol min^{-1} μg^{-1}). However, Cao et al. (2021b) reported a lower intrinsic oxidative potency of primary BB smoke (3.8 pmol min^{-1} μg^{-1}), which suggests that the differences of particulate catalytic oxidisers in ambient aerosols could occur and implies the atmospheric aging processes of BB particles in this study. The higher $OP_m^{meth\text{-}BB}$ obtained in this study was possibly driven by the higher content of oxygenated secondary OC on $PM_{2.5}$, which could lead to stronger oxidative capacity as reported by Daellenbach et al. (2020). These findings are in general congruent with the previous studies showing that the anthropogenic sources may have higher intrinsic OP than crustal or biogenic sources (Liu et al., 2014a).

Table 5.2 Summary of regression coefficients (intrinsic OP_m, nmol min^{-1} μg^{-1}) of source contributions to OP_v^{meth} (nmol min^{-1} m^{-3}) and annual source contributions (%) to OP_v^{meth} and $PM_{2.5}$

	CC	IE	BB	SS	Intercept
OP_m^{meth}	0.24 ± 0.05 (< 0.001)	0.38 ± 0.07 (< 0.001)	0.24 ± 0.06 (0.001)	* N.A.	-3.30 ± 1.42 (0.03)
Contribution to OP_v^{meth}	24.01	12.51	29.36	* N.A.	* N.A.
Contribution to $PM_{2.5}$	9.52	3.11	11.54	8.68	* N.A.

* N.A. refers to not applicable that includes the exclusion during the regression exercise.
# p value

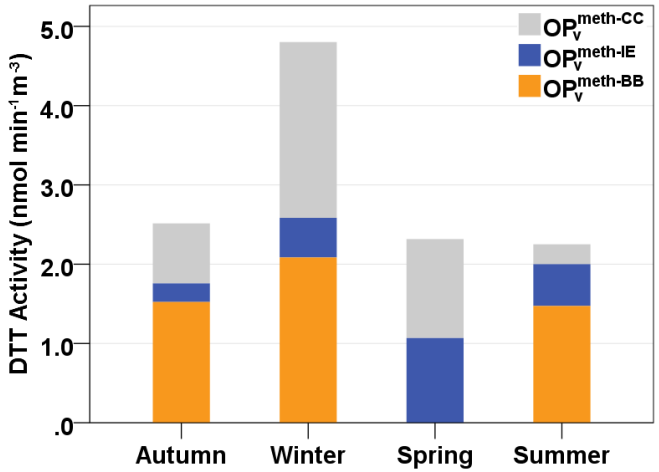

Figure 5.3 Seasonal variations of $PM_{2.5}$ source contributions to OP_v^{meth} in Ningbo

5.3.3.2 Industry Emissions (IE)

$OP_v^{meth\text{-}IE}$ had a distinctive seasonal variation, with the highest value in spring (1.07 ± 0.64 nmol min^{-1} m^{-3}), followed by summer (0.53 ± 0.82 nmol min^{-1} m^{-3}), winter (0.50 ± 1.13 nmol min^{-1} m^{-3}) and autumn (0.23 ± 0.30 nmol min^{-1} m^{-3}). These findings indicated that the organic fraction of ambient $PM_{2.5}$, including quinones, oxygenated PAHs (oxy-PAHs) and HULIS, had a greater impact on DTT responses than water-soluble fraction. However, heavy industries, such as petrochemical industry, steel plants, oil refineries, moulding machine industry, automobile industry and shipbuilding industry are intensely clustered in Zhenhai and Beilun industrial zones. Even one of the largest ethylene manufacturers in China is located in Zhenhai district. These industries could be the predominant sources responsible for emission or anthropogenic organic pollutants contributing to alkene-rich aerosols and VOCs (Guo et al., 2021; Fukusaki et al., 2021). Regardless of the limited impacts of quinones and oxy-PAHs on $OP_v^{meth\text{-}IE}$, it is speculated that such high OP values of $PM_{2.5}$ induced from IE-related organic species could be dominantly governed by DTT consumption of alkenes, since these IE sources released the shared redox-active species of alkenes. The ozonolysis of alkenes at night-time is capable of generating OH radicals under clean conditions or to some extent the mildly polluted conditions, contributing to enhancement of atmospheric oxidising ability (Guo et al., 2021). As the highest O_3 level was observed in spring (92.62 ± 27.11 μg m^{-3}) in this study, alkene ozonolysis would be one of the dominant drivers leading to the highest $OP_v^{meth\text{-}IE}$ during spring. Furthermore, it is hypothesized that a fraction of $OP_v^{meth\text{-}IE}$ was also accounted for by the electron-deficient alkenes

particularly as they are the significant non-catalytic oxidisers and can react with sulfhydryl group of DTT through a Michael addition, leading to the DTT consumption (Jiang and Jang, 2018). IE-related alkenes, whether in particle or gas phases, should be paid more attention to by investigating further their redox activity and public health implications.

5.3.3.3 Biomass Burning (BB)

The contribution of BB associated PM to OP ($OP_v^{meth\text{-}BB}$) was higher during in winter with the value of 2.09 ± 4.12 nmol min^{-1} m^{-3} than other seasons. The highest loadings of some transition metals were identified during winter that included Zn (7.50 ng m^{-3}), Pb (3.47 ng m^{-3}), Sb (2.43 ng m^{-3}), Cu (2.03 ng m^{-3}), Mn (1.87 ng m^{-3}), Fe (1.84 ng m^{-3}), Cd (0.18 ng m^{-3}), and V (0.06 ng m^{-3}). However, limited information pointed out the contributions of metal ions to OP_v^{meth}. As explained by Fang et al. (2017b), trace metals may remain bound to particles and the major contribution to OP_v^{meth} could possibly be from jointly adsorbed quinones. Such a higher contribution of $OP_v^{meth\text{-}BB}$ would not only be due to the primary aerosols emitted directly from local BB sources but also aged particles imported from regional transport. Based on recent reported studies, the capacity of ROS generation would increase with ageing processes during atmospheric transport at and beyond the regional scale (Daellenbach et al., 2020, Li et al., 2021). As shown in Fig. 4.3(b), more than 80% of air masses were originated from inland China, with approximately half of which passed through the densely distributed fire spots, very possibly bringing substantial aged aerosols emitted from BB to the study

domain.

The 16 EPA PAHs were distinctively identified in winter, but the weak correlations between the PAHs and $OP_v^{meth\text{-}BB}$ may imply the ageing of BB particles (Li et al., 2021). Based on correlation analysis (Fig. 5.4), measured Flu (r = 0.45), Pyr (r = 0.55) and Chr (r = 0.42) in ambient $PM_{2.5}$ exhibited moderate correlations with OP_v^{ws} during autumn, while in summer Flu (r = 0.40) and BaA (r = 0.36) correlated with OP_v^{ws}. Therefore, $PM_{2.5}$ captured in our study domain was from more fresh BB emission during autumn and summer, as Flu, Pyr, Chr and BaA are the four most abundant PAH congeners in freshly generated aerosols emitted from BB sources (Li et al., 2020). However, no significant correlation was observed between DTT response (OP_v^{ws} and OP_v^{meth}) and any measured BB tracer (K^+) or aromatic compounds (parent-PAHs) during winter, reflecting the impact of more aged BB aerosol during this period. Such results revealed that the relationship between $PM_{2.5}$ induced oxidative stress and BB related chemical compounds becomes more complicated after atmospheric oxidation ageing processes. Tuet et al. (2017) suggested that such as secondary organic aerosols (SOA) generated from photo-oxidation of anthropogenic precursors (isoprene, pentadecane, naphthalene, α-pinene, β-caryophyllene, etc.) have higher OP associated with higher levels of ROS production. Therefore, enhancement of BB particles related OP_v^{meth} in aged BB aerosols would be associated with the evolution of organic aerosols in atmospheric chemistry (Li et al., 2021).

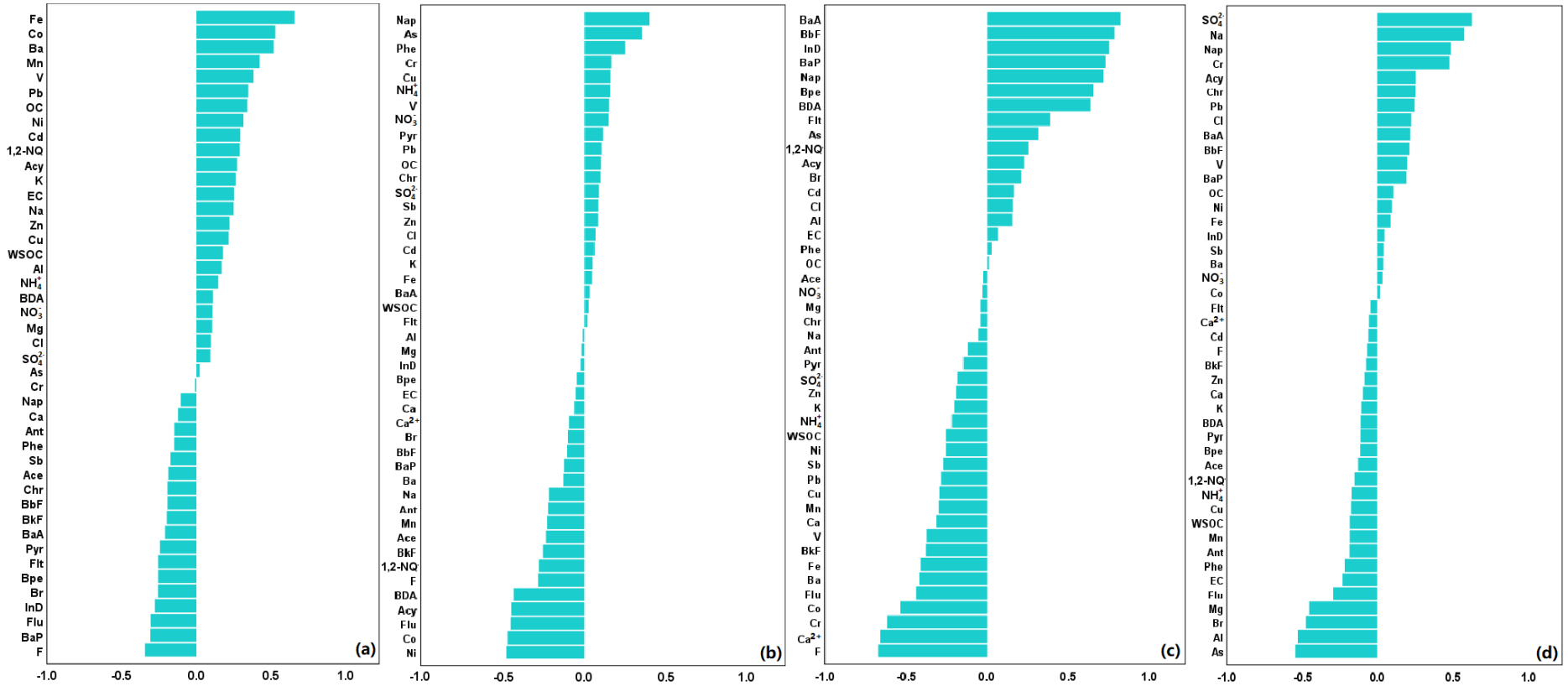

Figure 5.4 Pearson Correlations between the chemical components of $PM_{2.5}$ and OP_v^{meth} during autumn (a), winter (b), spring (c) and summer (d)

5.3.3.4 Coal Combustion (CC)

As shown in Fig. 5.3, the ROS generation capacity induced from CC emitted $PM_{2.5}$ ($OP_v^{meth\text{-}CC}$) exhibited seasonal variation, with the highest level during winter (2.22 ± 5.69 nmol min^{-1} m^{-3}), followed by spring (1.25 ± 1.87 nmol min^{-1} m^{-3}), autumn (0.76 ± 1.74 nmol min^{-1} m^{-3}) and summer (0.25 ± 0.51 nmol min^{-1} m^{-3}). It is noteworthy that higher loadings of carbonaceous species (OC and EC, 3.78 and 1.22 μg m^{-3}), secondary inorganic aerosols (SIA, NH_4^+ and SO_4^{2-}, 0.04 and 0.05 μg m^{-3}), PAHs (3.06 ng m^{-3}) and Cl^- (0.16 μg m^{-3}), and trace elements, such as As (0.006 ng m^{-3}), Ba (0.026 ng m^{-3}), Cu (0.004 ng m^{-3}), Pb (0.002 ng m^{-3}), Mn (0.023 ng m^{-3}), which were considered as catalytic oxidisers in particulate matter, were even minimum during winter. It can be inferred that a significant fraction of $OP_v^{meth\text{-}CC}$ was ascribed to organic components and SA from coal-related industry (e.g., power plants) and long-range transport from the northern China during heating period. The concentration of CC-emitted total PAHs during winter (3.06 ng m^{-3}) almost doubled that of spring (1.72 ng m^{-3}) and more than tripled relative to that in autumn (0.92 ng m^{-3}) and summer (0.86 ng m^{-3}) (Fig. 4.5(d)). Of sixteen PAH species investigated in this study, ten markers were identified with the highest loadings during winter, including Flt (0.811 ng m^{-3}) > Pyr (0.715 ng m^{-3}) > Acy (0.292 ng m^{-3}) > BaA (0.243 ng m^{-3}) > Chr (0.231 ng m^{-3}) > InP (0.167 ng m^{-3}) > BbF (0.157 ng m^{-3}) > Bpe (0.154 ng m^{-3}) > BkF (0.149 ng m^{-3}) > BaP (0.145 ng m^{-3}). The dominance of higher molecular weight (HMW) compounds (4-6 ring) of total PAHs from CC-emitted $PM_{2.5}$ demonstrated the influences of feed coal burning and fly ash in our study domain (Peng et al., 2016). Although PAHs studies have shown that PAHs do not produce ROS directly, they can be used as markers for identification of combustion sources of carbon containing organic compounds contributing

to OP, which were contributing to their redox reactivity after being oxidised to polar compounds, such as nitro-PAHs and quinones (Cho et al., 2005, Zhang et al., 2021). The highest SO_4^{2-} level during winter may also facilitate metal dissolution to induce an indirect OP response (Daellenbach et al., 2020, Fang et al., 2017a).

In contrast, CC was the dominant source contributing to PM oxidative potency, with 97.20% contribution to total OP_v^{meth} during spring. Concentrations of some trace elements from CC emission were greater during spring than those of winter, with higher levels of Ba (0.123 ng m^{-3}) > Mn (0.083 ng m^{-3}) > V (0.024 ng m^{-3}) > As (0.010 ng m^{-3}) > Cu (0.008 ng m^{-3}) > Pb (0.005 ng m^{-3}) > Co (0.004 ng m^{-3}). The total PAHs level was lower during spring than that of winter from CC sources, however, strong correlations (Fig. 5.4(c)) were observed between OP_v^{meth} with BaA (r = 0.83), BbF (r = 0.79), InP (r = 0.76), BaP (r = 0.73), Bpe (r = 0.66) and BDA (r = 0.64). Such findings revealed a combined effect of particulate trace metal compositions and poly-aromatic precursors on $OP_v^{meth\text{-}CC}$, suggesting more freshly emitted aerosols from primary CC sources during spring than those in winter. We also observed smaller proportions of SNA of CC-emitted $PM_{2.5}$ during winter (2.00%) and spring (2.10%) relative to those during autumn (6.85%) and summer (3.03%), which were in contrast to contributions of $OP_v^{meth\text{-}CC}$ (Fig. 4.5(h)). These results were consistent with previous studies in Europe by Daellenbach et al. (2020) , which reported the differences of source inventories between $PM_{2.5}$ oxidative potential and $PM_{2.5}$ mass concentrations. Thus, it implied that reducing specific anthropogenic emission (e.g., coal-related burning) would contribute to a substantial reduction of OP_v.

5.3.3.5 Non-linearity of OP_v^{meth} Induced from Other Sources

As demonstrated in Section 4.3.3.4, the contributions of vehicle emissions (VE) and fugitive dust (FD) to $PM_{2.5}$ were identified through source apportionment analysis in CMB model, but were excluded as the main contributors to OP_v by MLR analysis. Such results could be ascribed to synergistic or antagonistic effects on the OP activity between metal and organic compound interactions (Lin and Yu, 2020, Yu et al., 2018), and shown in Fig. 5.5.

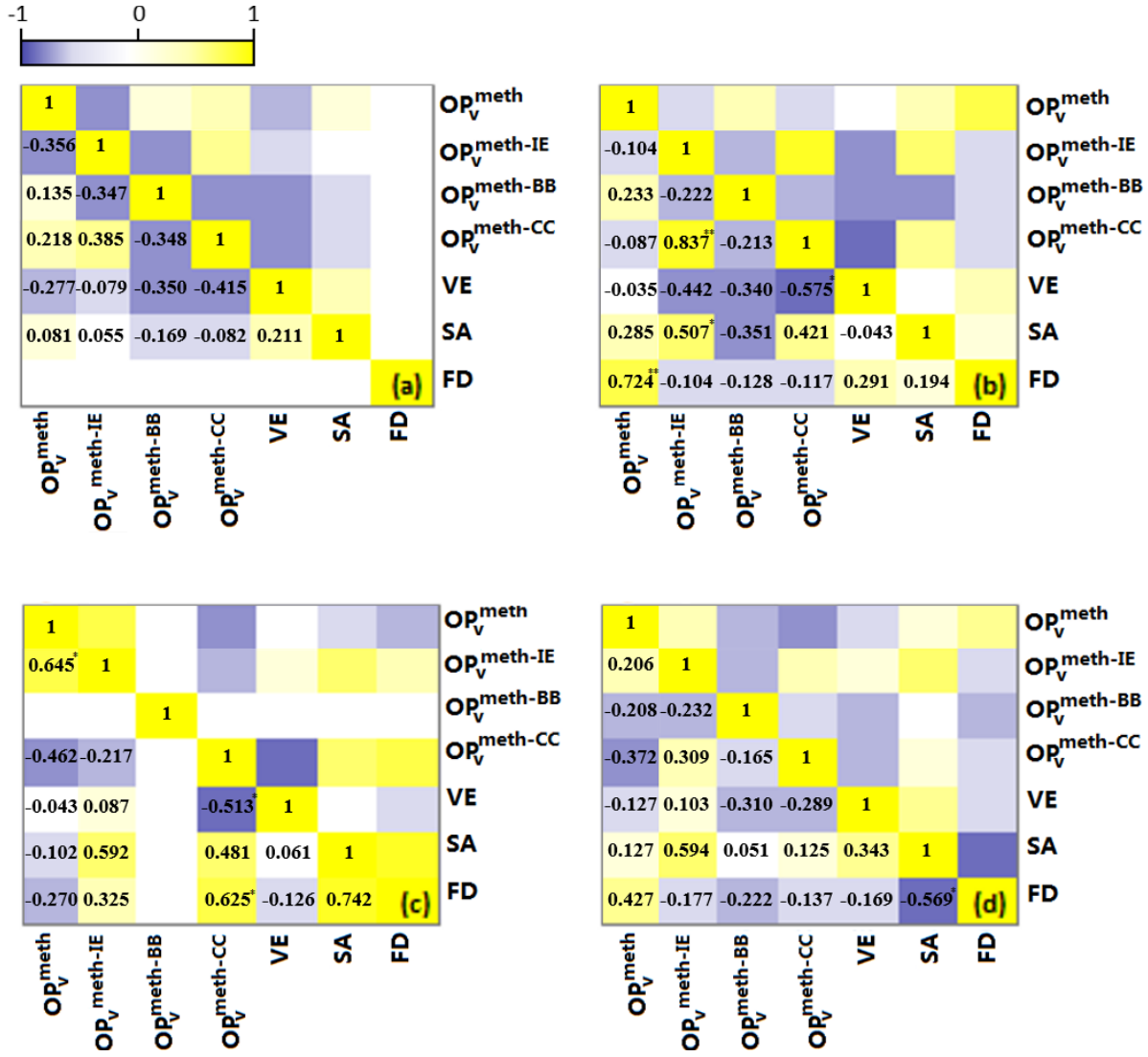

Figure 5.5 Pearson correlations among OP_v^{meth}, source contributions OP_v ($OP_v^{meth\text{-}IE}$, $OP_v^{meth\text{-}BB}$, $OP_v^{meth\text{-}CC}$), and source contributions of VE, SA, FD to $PM_{2.5}$ during autumn (a), winter (b), spring (c) and summer (d) (* At the 0.05 level (two-tail), the correlation is significant; ** At the 0.01 level (two-tail), the correlation is significant)

The negative correlations between $OP_v^{meth\text{-}CC}$ and VE observed during four seasons in Ningbo, with the strongest negative correlation (r ($OP_v^{meth\text{-}CC}$/VE) = -0.575) during winter, denoting the antagonistic interaction of DTT consumption between CC and VE emitted particles, especially during winter. The trace element, Cu contributing significant ability of ROS generation through DTT assay was reported to show an antagonistic effect with the existence of quinones in DTT oxidation (Xiong et al., 2017, Yu et al., 2018). VE was observed to one of the principal sources of quinones (e.g., 1,2-NQ) with CC being the predominant source of Cu loading throughout four seasons during sampling campaign (Fig. 5.3). Such antagonistic interaction between two sources could be attributed to the complexation of Cu with 1,2-NQ, which oxidises free DTT without generating any significant ROS. Hence, exhibiting a suppressing effect of ROS generation, but with high oxidative potential. As Cu was also identified from VE in most of the study period (autumn, spring, and summer), the antagonistic effect of Cu and coal emitted HULIS on DTT oxidation can also explain the counteractive effects between two oxidative species from two different sources.

5.3.4 Comparison of Driving Factors of OP of $PM_{2.5}$ with Similar Concentrations

As demonstrated in Fig. 5.6, the variations were prominent in oxidative capacity induced from hydrophobic fractions of $PM_{2.5}$ between ambient aerosols of similar mass concentrations, of which 21 out of 55 $PM_{2.5}$ samples were selected with mass concentrations ranged from 20 to 40 μg m^{-3} (divided into 20 – 30 μg m^{-3} and 30 – 40 μg m^{-3}, named as group 20-30 and group 30-40, respectively). The OP_v^{meth} values ranged broadly from 0.004 to 6.25 nmol min^{-1} m^{-3} for

OP_v^{meth} in group 20-30, while 0.08 to 11.00 nmol min^{-1} m^{-3} for OP_v^{meth} in group 30-40, respectively. Moreover, OP_v^{meth} also displayed relatively weak correlation with $PM_{2.5}$ mass (R^2=0.22, p = 0.03, Fig. 5.7).

OP_v^{meth} was significantly high from $PM_{2.5}$-derived organic fractions on 30 October 2017, 8 August 2018 within group 20-30 and 12th, 19th Dec 2017 within group 30-40, with 5.62, 6.25, 10.12, 11.00 nmol min^{-1} m^{-3} of OP_v^{meth}, respectively. Among anthropogenic sources, BB (53.98%) contributed substantially to $PM_{2.5}$ mass on 30 October, while IE (18.53%) contribution to $PM_{2.5}$ mass was considered as significant on 8 August 2017, with minor influences from VE (10.27% and 7.55%, respectively). The higher levels of OP_v^{meth} can be attributed to the individual organic catalytic oxidisers emitted from BB and VE, such as HULIS and quinones, and synergistic effects between IE-related transition metals and VE-related quinones. In contrast, VE dominated $PM_{2.5}$ mass on 12 and 19 December 2017, with contributions of 55.04% and 71.38%, respectively (Fig. 4.11 (d) and (d1)). Since OC was the major component from BB sources, we inferred that quinones might be the main contributor to higher levels of OP_v^{meth}. Even though BB played a minor role in $PM_{2.5}$ emission on both days (1.05% and 0.35%, respectively), BB-derived transition metals (Cu, Fe, Mn, Ni, Zn) and SNA might have facilitated ROS generation and further enhanced oxidative capacities of ambient aerosols. Our findings could imply that targeting the interactions of $PM_{2.5}$ sources rather than specific emission sources alone might become more critical for public health.

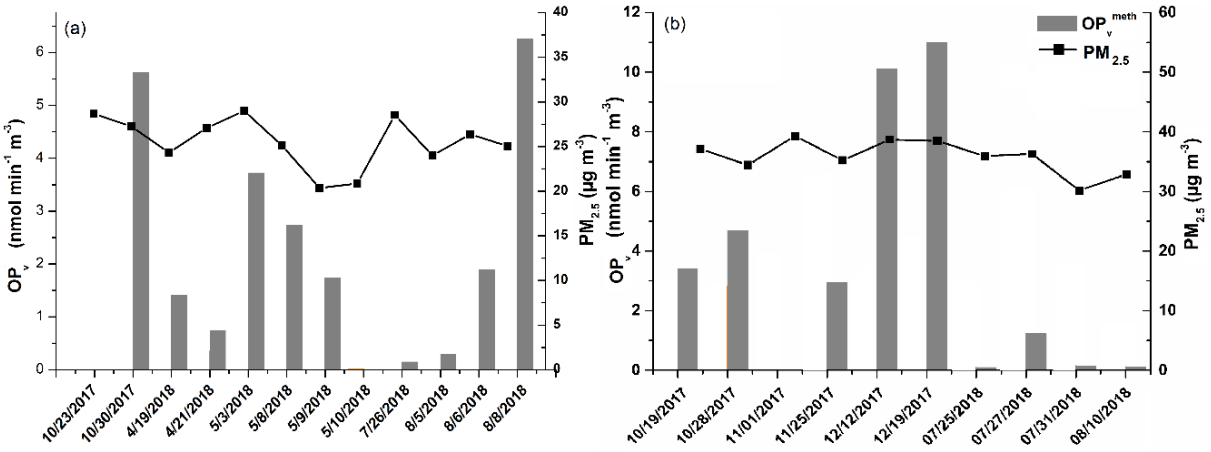

Figure 5.6 OP_v^{meth} of ambient levels of $PM_{2.5}$ with similar mass concentrations ranged from 20-30 µg m^{-3} (a) and 30-40 µg m^{-3} (b) in Ningbo during the sampling campaign

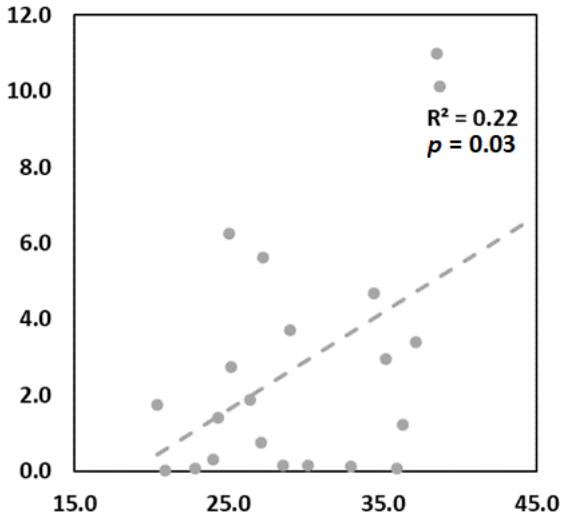

Figure 5.7 Correlation between OP_v^{meth} values and $PM_{2.5}$ mass concentrations with concentrations ranged from 20-40 µg m^{-3}

5.4 Conclusion

We successfully measured OP levels induced from methanol-soluble fractions of $PM_{2.5}$ collected in a coastal hotspot at Ningbo through application of DTT assay. Seasonal variations were observed for OP_v^{meth}, with the highest average values during winter. The highest

contributions to OP_v^{meth} were derived from CC and BB during winter, while IE contributed most to OP_v^{meth} during spring. There were non-linear increases between VE, FD derived OP_v and $PM_{2.5}$ concentration, which can be ascribed to the prominent synergistic and/or antagonistic interactions among VE and FD sources and their chemical components.

Significantly different oxidative capacities could occur to the PM of similar mass concentrations (in the range of 20 – 40 μg m^{-3}) due to their distinctly different chemical composition spectrums associated with varying emission sources. Thus, to decrease the $PM_{2.5}$ OP in this region, the emissions of $PM_{2.5}$ and its redox active components should be jointly controlled so as to reduce the $PM_{2.5}$ oxidative potential. In particular, as IE exhibited highest intrinsic OP contributions to OP_v^{meth} in Ningbo, a more stringent regulation and control actions of $PM_{2.5}$ and organic oxidative components emitted from industrial activities should be considered as a priority to improve the population health in Ningbo city.

Chapter 6 Particle Size Distributions of Oxidative Potential Induced from Water-Soluble PM Fractions and Their Lung Depositions during High and Low Pollution Periods

6.1 Introduction

Mounting evidence indicates the associations between exposure to ambient particulate matter (PM) and increased cardiorespiratory morbidity and mortality (Dominici et al., 2006, Hoek et al., 2013, Pope et al., 2004). One of the most commonly acknowledged pathophysiological mechanisms to interpret such relationship is the oxidative stress, as mediated by reactive oxygen species (ROS), including hydroxyl radicals ($OH^{\cdot}$), superoxide (O_2^{-}) and hydrogen peroxide (H_2O_2) (Cho et al., 2005). These ROS could either be bonded to the PM themselves or produce via interactions between particulate catalytic oxidisers and antioxidants (i.e., reduced glutathione, vitamin E, ascorbate and uric acid) or both (Lyu et al., 2018, Pöschl and Shiraiwa, 2015). Excessive ROS can give rise to the biochemical imbalance in oxidant redox-cycling reactions once the presence of ROS overwhelms the defences of antioxidant, and cause resultant cell and tissue injuries in the respiratory tract (Fang et al., 2019, Kumagai et al., 1997). The capability of PM to address ROS in vivo is defined as the oxidative potential (OP) of ambient particles, which has been considered as a more integrative health related measure of PM toxic power than its mass concentration. The ambient particles contain a mix of chemical compounds with highly redox activities, such as black carbon, water-soluble inorganic ions (WSIIs), water-soluble transition metals, water-soluble organic carbons (WSOC), humic-like substances (HULIS) and environmentally persistent free radicals (EPFRs)

(Charrier and Anastasio, 2012a, Cho et al., 2004, Khachatryan et al., 2011, Verma et al., 2015c). However, the oxidative stress elicited from water-soluble fraction of PM gain more attention as its more readily bioavailable than the water insoluble fraction (Charrier and Anastasio, 2012a, Gao et al., 2020b). The solubility of particle species is one of the essential factors in affecting the PM related OP.

Considerable field and laboratory measurements have been devoted to the investigation of particle deposition (Fang et al., 2017a, Fang et al., 2019, Gao et al., 2020a, Guo et al., 2019, Wu et al., 2021b). Coarse particles are inclined to deposit in the extra-thoracic airway, such as head airway and nasal areas. Although they are possibly restrained by rhinothrix through impaction processes, the metals resided in coarse particles can cross synapses in the olfactory bulb and traverse via secondary olfactory neurons to the distant nuclei of the brain, leading to the olfactory deficits and brain lesions (Calderón-Garcidueñas et al., 2010a, Maher et al., 2016, Sunderman, 2001). In contrast, the fine particles are likely to penetrate into the deeper tract (tracheobronchial and pulmonary regions) and may contribute to the inflammation relevant to pulmonary and even systemic diseases (De Jong et al., 2008, Li et al., 2017). Prior studies manifested the higher toxic power and more harmful of small particles to human, owing to their difficulties in clearance but easy access to blood, especially the ultrafine particles, they can avoid phagocytosis via alveolar macrophages to enter the pulmonary interstitial sites and remain deposited for long periods, consequently introducing pulmonary inflammation (Lyu et al., 2018, Sioutas et al., 2005).

Often the deposition of size-dependent OP can better reflect the detrimental effects of ambient aerosols. Accordingly, several studies modelled the respiratory deposition of OP via

multiple-path particle dosimetry (MPPD) (Liu et al., 2021b, Lyu et al., 2018, Wu et al., 2021b) or empirical expressions from human inhalation data (ICRP) (Andrade et al., 2021, Fang et al., 2019, Fang et al., 2017b), and estimated the correlations between OP and redox active species. Fang et al. (2017b) reported a peak of water-soluble OP (OP^{ws}) from the PM with size range between 1-2.5 μm in Atlanta, which was predominantly by transition metals in the upper respiratory regions while organic species (i.e., quinones) in the deeper lung. However, the oxidative stress of aerosols (OP^{ws}) in Shanghai and Santiago exhibited maximum centred in accumulation mode (0.18-3.2 μm). The accumulation-mode PM in Shanghai posed a more severe threat to the pulmonary region due to its abundance of metals (Cn and Mn), while the $PM_{3.2}$ dominated the OP lung deposition in different respiratory regions (Andrade et al., 2021, Lyu et al., 2018).

Given that the lung deposited OP varied with multiple factors, including the particulate catalytic oxidisers, emission sources, particle acidity (pH value), atmospheric aging processes and particle deposition efficiency, etc. Whereas, which respiratory region is more affected by the OP and which factor controls the concentration of OP that deposits in the specific respiratory region remain still unknow at present. Here, we aim to: 1) determine the size distribution of PM and its water-soluble fraction generated OP (OP^{ws}) via DTT assay during the haze and non-haze period; 2) assess the spatial dispersions of the size-fractioned PM and their OP^{ws} in the study domain; 3) estimate the respiratory deposited doses of PM and its OP^{ws} via MPPD model; 4) identify the governed PM redox-active species to oxidative potency and compare their OP^{ws} contributions in haze and non-haze days; 5) explore the driving factors of deposited OP^{ws} in different respiratory tracts.

6.2 Methods

6.2.1 Sampling

To compare the OP activities in different size range of PM in haze and non-haze periods, we selected 10 sets of size-fractionated PM samples collected in autumn and winter with highest mass concentrations, and 10 sets collected in summer with lowest concentrations, together with 2 sets of filter blanks for each group.

Size-segregated particulate matter was collected between October 2017 and May 2018 at PMB (Sir Peter Mansfield Building) of UNNC (University of Nottingham Ningbo China). The aerosol samples were captured using a 6-stage high volume cascade air sampler (Model: TE-230, Tisch Environmental, Inc. USA) at 1 m^3 min^{-1} by the same protocol as described in Section 3.2.2. After sampling, filters were stored at -20 °C in the fridge until experimental analysis.

6.2.2 Sample Analysis

The analysis of WSIIs and WSOC were conducted by using IC (ICS-1600, Dionex, US) and TOC analyser (Vario TOC Cube, Elementar, Germany), respectively. Water-soluble trace elements were measured by ICP-MS (iCAP Q, Thermofisher). The OP was measured by DTT assay. The same protocols of WSIIs, trace elements, WSOC analysis and DTT assay are presented in Section 4.2.2.

6.2.3 Quality Control

The analytical quality of the measured data was determined by reproducibility, recovery, linearity and limit of detection (LOD). For each set of samples, field blank samples were

included to correct the real-world samples by subtracting the mean blank values. The concentrations of WSIIs and trace elements were estimated via the external calibration, the linearity of calibration standards calculated through linear regression with values between 0.99 and 1.00 (r^2) for all ions and trace elements. The mean recoveries obtained were greater than 95.00%. The average LOD of reproducibility ranged from 0.07% of Li^+ to 5.33% of SO_4^{2-} for WSIIs, and from 0.00% of Ag to 5.73% of Mn for trace elements, while the LOD were between 0.00 μg m^{-3} of Li^+ and 0.56 μg m^{-3} of SO_4^{2-} for WSIIs and between 0.00 ng m^{-3} of Al and 3.53 ng m^{-3} of Ca for trace elements. The calibration of WSOC was conducted by using the standard solution of sucrose, the linearity of which was greater than 0.99 ($r^2 \geqslant 0.99$) for each set of samples. The recovery result of WSOC was 96.8%, with 2.53% and 0.14 μg m^{-3} for its repeatability and LOD, respectively. Concentrations of WSIIs, water-soluble trace elements and WSOC were summarised in Table 6.5. For OP analysis, duplicate or triplicate measurements of each sample extract were conducted with coefficient of variation (CV) less than 3.5%. The OP measured was blank corrected for quality control and assurance purposes.

6.2.4 Analysis of Air Mass Backward Trajectory

Model of air mass backward trajectories was conducted to identify the impact of pollutants originating from medium and long-range transport of aerosols rather than local emissions. Detailed description of modelling air mass back trajectory has been presented in Section 4.2.4.

6.2.5 Graphical Analysis of Source Dispersion

Bivariate polar plots (BPPs) were applied in this study to compare the geographical sources

and dispersion patterns of size-fractioned PM and their related OP from water-soluble fraction (OP_v^{ws} and OP_m^{ws}) during haze and non-haze period in Ningbo. Detailed description of BPPs construction can be found in Section 4.2.5.

6.2.6 Modelling Deposition in Human Respiratory System

The deposition efficiency represents the average probability that inhaled particles could be deposited into a specific region in the human respiratory tract. In this study, we conducted MPPD model (version 3.04, Applied Research Associates Inc., Arlington, VA, USA) to obtain the deposition fractions (DF) of size-fractioned PM in extrathoracic/head airway, tracheobronchial (TB) region and alveolar/pulmonary region. To be specific, we chose a stochastic lung model as it can better derive the realistic structure human lung than the symmetric structure (Lyu et al., 2018). The monodispersed particles with diameter ranged from 0.1 to 10.0 μm was selected as the deposition behaviour for an adult male at rest. The corresponding parameters and settings were summarised in Table 6.1. The depositions of PM and OP_v^{ws} were integrated over three particle modes: ultrafine (≤ 0.95 μm), accumulation (0.95-3.0 μm) and coarse (≥ 3.0 μm) (Andrade et al., 2021, Fang et al., 2017b). The deposited doses of 24-hour personal exposure to PM and its induced OP_v^{ws} in the human respiratory tract was further estimated by the following equation:

Deposited doses (μg or nmol min^{-1}) = DF × personal PM or OP_v concentration (μg m^{-3} or nmol min^{-1} m^{-3}) × TV (ml $time^{-1}$) × 10^{-6} × BF (time min^{-1}) × (24 × 60) min.

Table 6.1 The parameters in setting the respiratory deposition of monodispersed particles (0.1-10 μm) in the MPPD model (version 3.04)

Input categories	Parameters	Options/values
Airway morphometry		
	Species	Human
	Model	Stochastic lung model
	FRC (ml) *	3300.0
	URT volume (ml) *	50.0
Particle properties		
	Density (g cm^{-3})	1
	Aspect ratio	1
	Diameter	CMD *
	Distribution	Multiple particles (0.1-10 µm)
Exposure scenario		
	Acceleration of gravity (cm s^{-1})	981.0
	Body orientation	Upright
	Aerosol concentration (mg m^{-3})	Daily average PM_{10} during each period (sum of each staged PM)
	BF (time min^{-1}) *	12
	TV (ml) *	625.0
	Inspiratory fraction	0.5
	Pause fraction	0
	Breathing scenario	Nasal
Clearance settings		
	Tracheal mucous velocity (mm min^{-1})	5.5
	Fast human clearance rate (1 $days^{-1}$)	0.02
	Medium human clearance rate (1 $days^{-1}$)	0.001
	Slow human clearance rate (1 $days^{-1}$)	0.0001
	Lymph node human clearance rate (1 $days^{-1}$)	0.00002
	Number of hours per day	6

Number of days per week	5
Number of weeks	1
Max.post-exposure days	0

*Abbreviations: FRC, functional residual capacity; URT, upper respiratory tract; CMD, count median diameter; BF, breathing frequency; TV, tidal volume.

6.2.7 Multivariate Regression Models

The ROS generation ability from specific PM species was estimated by a multiple linear regression (MLR) analysis and performed on SPSS (Statistics 23). In this chapter, OP_v^{ws} was defined as the dependent variable while the OP induced from individual water-soluble chemical component or emission source as the independent variable. 10 samples were applied for MLR analysis for each PM size mode in each study period. Al and Ca were considered as the geographical minerals (Xu et al., 2021a), which were excluded from the MLR model as they are redox inactive. Sea salt particles were estimated as the sum of Cl^-, Na^+ and Mg^{2+} concentrations ($SS = Na^+ + Cl^- + Mg^{2+}$) (Hsu et al., 2010), while SNA referred to the sum of SO_4^{2-}, NO_3^- and NH_4^+. Detailed information for MLR analysis was described in Section 4.2.7.

6.2.8 pH Calculation

The thermodynamic modelling approach of E-AIM (Extended Aerosol Inorganics Model, http://www.aim.env.uea.ac.uk/aim.aim.php) was employed to estimate the characteristics of acidity of size-fractioned particles (Ding et al., 2017).

Temperature and relative humidity (RH) by E-AIM 4.

$$[H^+]_{Total} = 2 \times \frac{SO_4^{2-}}{96} + \frac{NO_3^-}{62} + \frac{Cl^-}{35.5} - \frac{NH_4^+}{18} - \frac{Na^+}{23}$$

Where the units for SO_4^{2-}, NO_3^-, Cl^-, NH_4^+ and Na^+ were μg m^{-3}. According to the model outputs, the in-situ particle pH value was estimated as follow:

$$pH = -\log(\gamma \times [H^+]_{Frac})$$

where γ is the activity coefficient based on mole fraction and $[H^+]_{Frac}$ is H^+ fraction in aqueous phase, thus $\gamma \times [H^+]_{Frac}$ represents the H^+ activity in aqueous phase.

6.3 Results and Discussion

6.3.1 Size Distribution of PM Concentration and OP^{ws}

We compared the size distributions of PM mass concentrations and OP induced from water-soluble fraction of PM (OP_v^{ws} and OP_m^{ws}) during the haze and non-haze periods (Fig. 6.1). Substantially higher concentration of PM was observed during haze period for all particle sizes compared with those during the non-haze period. The PM concentration exhibited an overall decreasing trend with the increase of particle size (Table 6.2, 40.94 ± 37.13 μg m^{-3} of $PM_{0.49}$ to 29.76 ± 14.08 μg m^{-3} of $PM_{7.2-10}$), with a small peak between 3.0 and 7.2 μm (37.67 ± 13.17 μg m^{-3}) during the haze episode, in stark contrast to the non-haze period, it had a bimodal distribution and was highest in the coarse mode of $PM_{3.0-7.2}$ (22.20 ± 6.38 μg m^{-3}). Both of them had concentration peaks in ultrafine and coarse modes, such trends were also detected by studies conducted in Beijing (concentration peaks in the diameter ranges of 0.56-1.0 μm and 3.2-5.6 μm) (Sun et al., 2015, Yue et al., 2018), and Chicago (concentration peaks in the diameter ranges of ≤ 1.0 μm and > 2.5 μm) (Zeng et al., 2021).

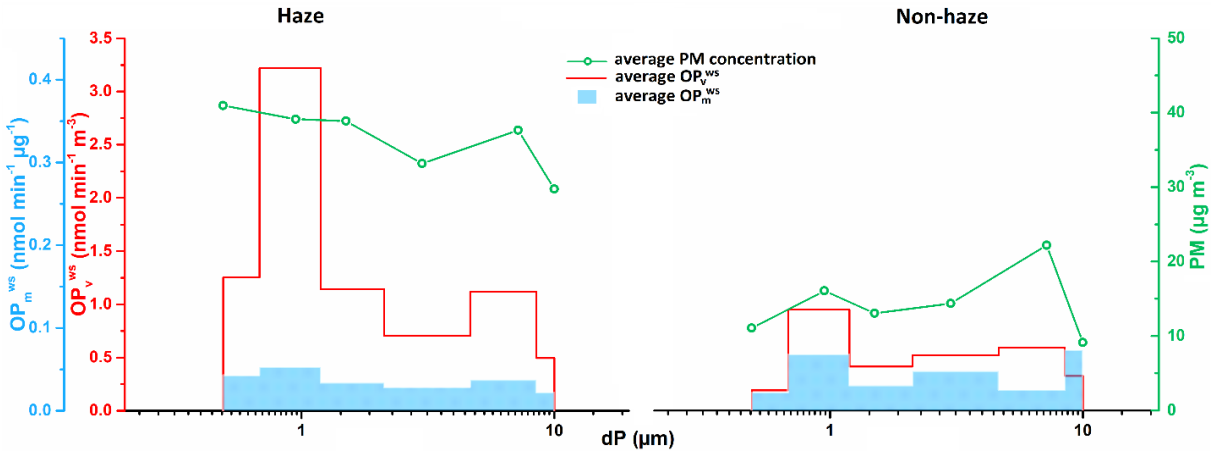

Figure 6.1 Size distribution of PM, OP_v^{ws} and OP_m^{ws} during haze and non-haze periods

Distribution of OP_v^{ws} varied analogously during the two periods, but the overall levels were higher during the haze period than non-haze period, both of which had bimodal distribution with the picks in ultrafine and coarse modes. The highest OP_v^{ws} during the two periods were induced from the PM with geometric mean diameter (GMD) ranged from 0.49 to 0.95 µm ($PM_{0.49\text{-}0.95}$), with 3.22 ± 0.94 and 0.95 ± 0.35 nmol min^{-1} m^{-3} during haze and non-haze periods, respectively. The predominance of ultrafine mode in the ROS activity (0.56-1.0 µm) was also reported by a previous study in Shanghai (Wu et al., 2021b). Such higher OP_v^{ws} signifies more oxidative stress induced from $PM_{0.49\text{-}0.95}$, and could be due to the higher concentrations of particulate catalytic oxidisers (e.g., Cu) or higher contributions from toxic emission sources (e.g., traffic emission) within $PM_{0.49\text{-}0.95}$ relative to other particle sizes, which will be discussed in Section 6.3.3-6.3.4.

The average intrinsic OP^{ws} (OP_m^{ws}) of all particle sizes was slightly higher during the non-haze period (0.044 ± 0.046 nmol min^{-1} μg^{-1}) than haze period (0.036 ± 0.026 nmol min^{-1} μg^{-1}). Distribution of OP_m^{ws} exhibited different variation trends between haze and non-haze periods.

Higher averaged OP_m^{ws} were observed from $PM_{0.49-0.95}$ (0.068 ± 0.033 nmol min^{-1} μg^{-1}), $PM_{1.5-3.0}$ (0.048 ± 0.033 nmol min^{-1} μg^{-1}) and $PM_{7.2-10}$ (0.073 ± 0.088 nmol min^{-1} μg^{-1}) in non-haze period than haze period (0.053 ± 0.031, 0.034 ± 0.018, 0.022 ± 0.015 nmol min^{-1} μg^{-1}, respectively), suggesting the greater intrinsic oxidative stress associated with water-soluble components per unit mass of ambient $PM_{0.49-0.95}$, $PM_{1.5-3.0}$ and $PM_{7.2-10}$ during warm season (20.38 ± 2.10 °C). We also noted that OP_m^{ws} generated from $PM_{0.49-0.95}$ (0.053 ± 0.031 nmol min^{-1} μg^{-1}) was lowest during haze period while highest from $PM_{7.2-10}$ (0.073 ± 0.088 nmol min^{-1} μg^{-1}) during non-haze period among the 6-stage size-resolved PM. Such findings denoted that the water-soluble catalytic oxidisers were inclined to accumulate on particles in ultrafine and coarse modes during haze and non-haze periods, respectively, suggesting the differences in the cumulative processes of ambient PM between the two periods. We infer that such phenomena could be due to the varied particle acidity, chemical composition and source contributions, detailed discussions are presented in Section 6.3.2 – 6.3.4.

Table 6.2 Summary of the size-segregated PM mass concentration, OP_v^{ws} and OP_m^{ws}

	Concentration ($\mu g\ m^{-3}$)		OP_v^{ws} (nmol min^{-1} m^{-3})		OP_m^{ws} (nmol min^{-1} μg^{-1})	
	Haze	Non-haze	Haze	Non-haze	Haze	Non-haze
$PM_{0.49}$	40.94 ± 37.13	11.06 ± 6.77	1.25 ± 0.31	0.19 ± 0.34	0.043 ± 0.028	0.022 ± 0.028
$PM_{0.49-0.95}$	39.14 ± 22.94	16.07 ± 8.75	3.22 ± 0.94	0.95 ± 0.35	0.053 ± 0.031	0.068 ± 0.033
$PM_{0.49-1.5}$	38.89 ± 20.67	13.05 ± 4.59	1.14 ± 0.63	0.41 ± 0.32	0.034 ± 0.018	0.030 ± 0.015
$PM_{1.5-3.0}$	33.18 ± 17.23	14.37 ± 6.54	0.71 ± 0.29	0.52 ± 0.16	0.028 ± 0.023	0.048 ± 0.033
$PM_{3.0-7.2}$	37.67 ± 13.17	22.20 ± 6.38	1.12 ± 0.10	0.59 ± 0.42	0.037 ± 0.027	0.025 ± 0.021
$PM_{7.2-10}$	29.76 ± 14.08	9.15 ± 5.86	0.50 ± 0.14	0.33 ± 0.09	0.022 ± 0.015	0.073 ± 0.088

6.3.2 Graphical Analysis of Size Distributions of Particulate OP^{ws}

To graphically compare the potential source characteristics between different size ranges, BPPs of PM mass concentrations, OP_v^{ws} and OP_m^{ws} during haze and non-haze periods were plotted, as given in Fig. 6.2 and 6.3, respectively. During haze period, the highest PM concentrations experienced with southerly winds when wind speeds were higher than 4 m s^{-1} (Fig. 6.2(b-f)), except $PM_{0.49}$ (Fig. 6.2(a)). The PM concentrations increased with the increasing wind speeds, which is an indicative pattern of buoyant plume such as road traffic sources (Chen et al., 2021). Therefore, a consideration of potential sources highlighted the traffic emissions from the freeway at approximately 600 m to the south of our study domain (Fig. 3.1). Since the traffic sources had a relatively constant influence on the PM mass concentrations (0.95-10 μm), we infer that it would emerged as one of the dominant sources in affecting the ambient particle accumulation and growth when the aerodynamic diameter larger than 0.49 μm during haze period. Unlike the particles with larger sizes, the highest level of $PM_{0.49}$ (Fig. 6.2(a)) was recorded when the wind is from the northwest (NW). The concentrations of $PM_{0.49}$ decreased with the increases of wind speeds from any directions, which would be regarded as a ground level source (Carslaw et al., 2006). This is entirely expected because of the sources of Wangchun industrial zone (12 km) and Ningbo Lishe airport (10 km) to the northwest of our study site.

The similar distributions between OP_v^{ws} and mass concentrations of PM were observed in ultrafine mode (Fig. 6.2(g-h)), suggesting their similar sources and further implying the strong toxicities of the ultrafine particles from the emissions of industries and transportation. In

contrast to the accumulation and coarse modes, the PM induced OP_v^{ws} (Fig 6.2(i-l)) exhibited significant differences compared to PM concentrations. For the PM with diameters of 1.5-3.0 ($PM_{1.5-3.0}$) and 3.0-7.2 μm ($PM_{3.0-7.2}$), the maximum OP_v^{ws} values of both $PM_{1.5-3.0}$ and $PM_{3.0-7.2}$ were obtained when wind blow from NW, where the PM levels were relatively low during haze period, denoting the limited DTT activities induced from the highly concentrated particles. According to the analysis of back trajectories (Fig. 6.4(a)) during haze period, 42.3% of the air parcels originated from NW in Hebei Province while 17.3% came from inland China and passed through Hangzhou Bay before arriving the study domain. Both of the clusters travelled through the areas with densely distributed fire spots, bringing the pollutants from biomass burning (BB) from the NW, may enhance the oxidative potency of ambient particles. Regardless, the industrial activities and airport emissions to the NW of our sampling site, as described above, could also be the major contributors to enhance the OP_v^{ws}. It further explains the highest values of OP_m^{ws} of PM to the NW and north in accumulation and coarse modes (Fig. 6.2(o-r)), as well as the west and north in ultrafine mode (Fig. 6.2(m-n)). We infer that such high intrinsic OP^{ws} values from these directions could be ascribing to the high concentrations of particulate catalytic oxidisers from BB, IE and airport emissions. Further discussions on OP^{ws} and PM redox-active species are presented in Section 6.3.3.

The dispersions of PM mass concentrations (Fig. 6.3(a-f)) in non-haze period exhibited greater variability between different size ranges relative to the haze period. Fig. 6.3(a-b) and Fig. 6.3(c-d) shown the presence of most abundant sources of PM to the NW and southeast (SE) in ultrafine and accumulation modes, respectively, the PM concentrations in both modes did not reduce with the wind speed increased. The NW sectors corresponded to the Wangchun

industrial zone and Ningbo Lishe airport, while in the SE direction is located the freeway. As a typically coastal city of Ningbo, we speculate that the marine sources, such as the marine vessels and sea salt (SS) aerosols, could also be another significant source to the accumulation-mode PM, especially for $PM_{1.5\text{-}3.0}$, as the Ningbo-Zhoushan Port, which is the busiest port and handles the largest cargo throughput in the world, is located away from 33 km to the east of our study domain. The coarse particles of $PM_{3.0\text{-}7.2}$ (Fig 6.3(e)) and $PM_{7.2\text{-}10}$ (Fig 6.3(f)) did not display exactly the same behaviour during non-haze period. Since the $PM_{3.0\text{-}7.2}$ distributed similarly with ultrafine-mode particles while $PM_{7.2\text{-}10}$ had similar dispersion with accumulation-mode PM, we inferred that the PM in coarse mode were affected by the emission sources of both industrial activities and traffic exhausts mixed with marine sources.

The dispersed patterns of OP_v^{ws} and OP_m^{ws} varied significantly compared to PM concentrations during non-haze period, in the meanwhile, similar distributions were observed between OP_v^{ws} and OP_m^{ws} induced from PM in accumulation mode and $PM_{3.0\text{-}7.2}$ in coarse mode. For the accumulation-mode particles, the both highest extrinsic (Fig. 6.3 (i-j)) and intrinsic OP^{ws} (Fig. 6.3 (o-p)) came from the NW and northeast (NE) for $PM_{0.95\text{-}1.5}$ and $PM_{1.5\text{-}3.0}$, respectively. It manifested that the PM from those directions may comprised of higher concentrations of the particulate catalytic oxidisers with stronger redox activities although the mass concentrations of it were not the highest. The analysis of back trajectories (Fig. 6.4(b)) depicted that the two clusters from northern direction were evenly distributed, with 28.6% for each during non-haze period. One of them (marked with pink) originated from Jiangsu Province and passed through the area with densely distributed fire spots, may bring substantial amount of BB pollutants before arriving Ningbo, another cluster (marked with blue)

transported from the East China Sea, Ningbo-Zhoushan port and Beilun industrial park in succession would possibly give rise to the stronger OP of PM during non-haze period. Therefore, we infer that the dominant sources contributing to the such oxidative potencies could be the BB source for $PM_{0.95\text{-}1.5}$ and marine vessels, SS aerosols and industry emissions (IE) or the mixtures involved in secondary processes for $PM_{1.5\text{-}3.0}$. The predominant air-mass trajectory (42.9%) travelled south-easterly from the sea and changed to southern direction before arriving Ningbo, would carried both marine or SS aerosols to our study domain, which would explain the dominant source contribution to the highest $PM_{3.0\text{-}7.2}$ induced OP^{ws} (Fig. 6.3(k) and Fig. 6.3(q)) of from the south. Similar distributions of OP_v^{ws} were found between $PM_{0.49}$ (Fig. 6.3(g)) and $PM_{7.2\text{-}10}$ (Fig. 6.3(l)), which had the highest concentrations from the southeast and decreased with the wind speed increased from any directions, signifying a distinctive ground level source such as vehicle emissions (VE). Consequently, the PM in both ultrafine and coarse modes were affected seriously by VE source and produced substantial VE-related OP owing to their high DTT activities during non-haze period.

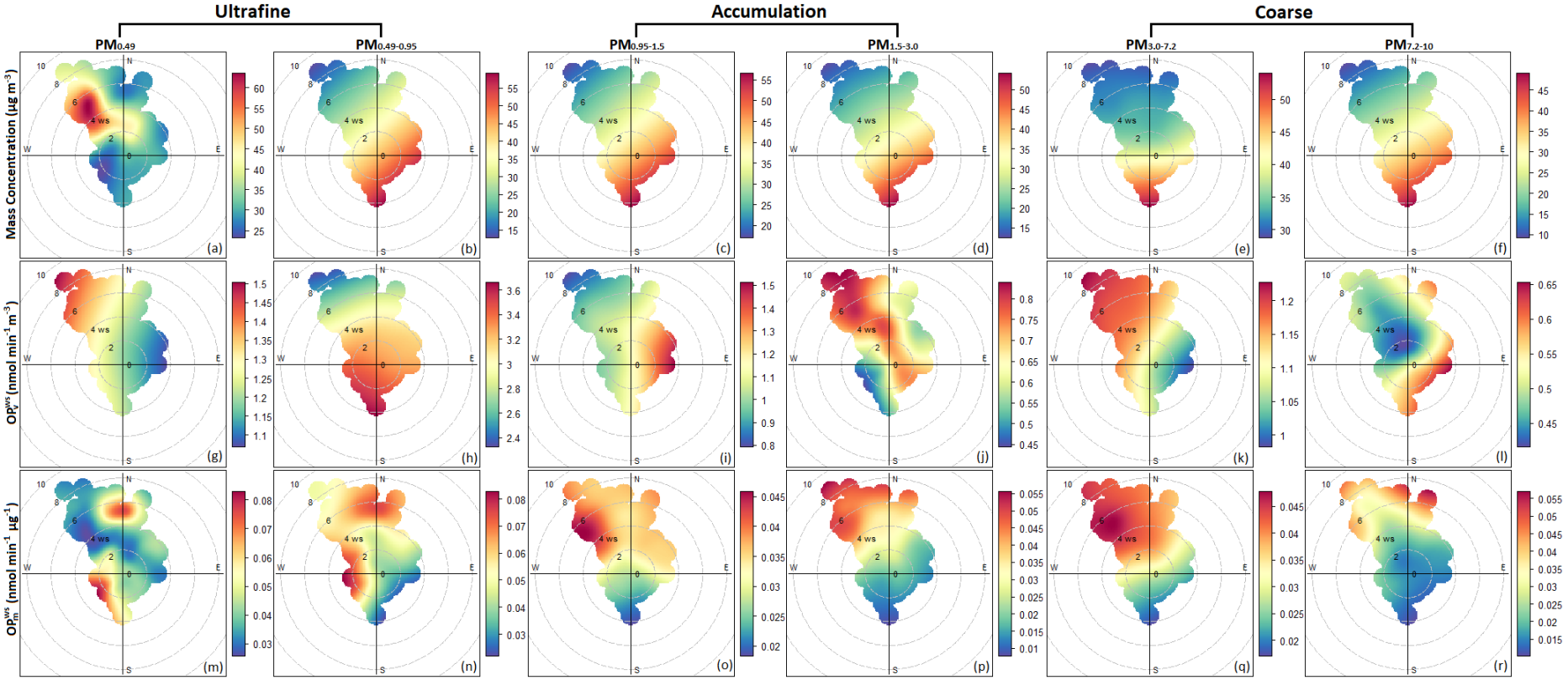

Figure 6.2 Bivariate polar plots of size-resolved PM concentration (a-f), OP_v^{ws} (g-l) and OP_m^{ws} (m-r) during the haze period

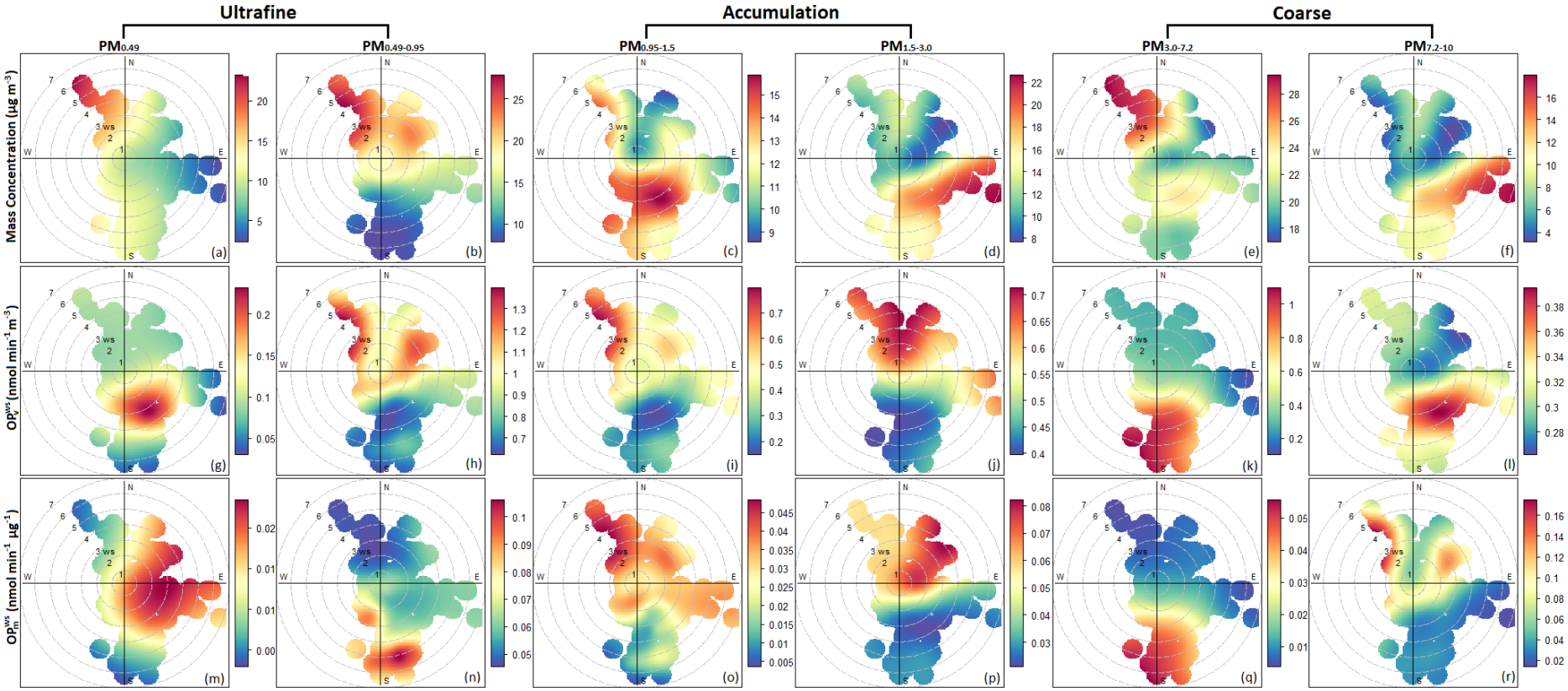

Figure 6.3 Bivariate polar plots of size-resolved PM concentration (a-f), OP_v^{ws} (g-l) and OP_m^{ws} (m-r) during the non-haze period

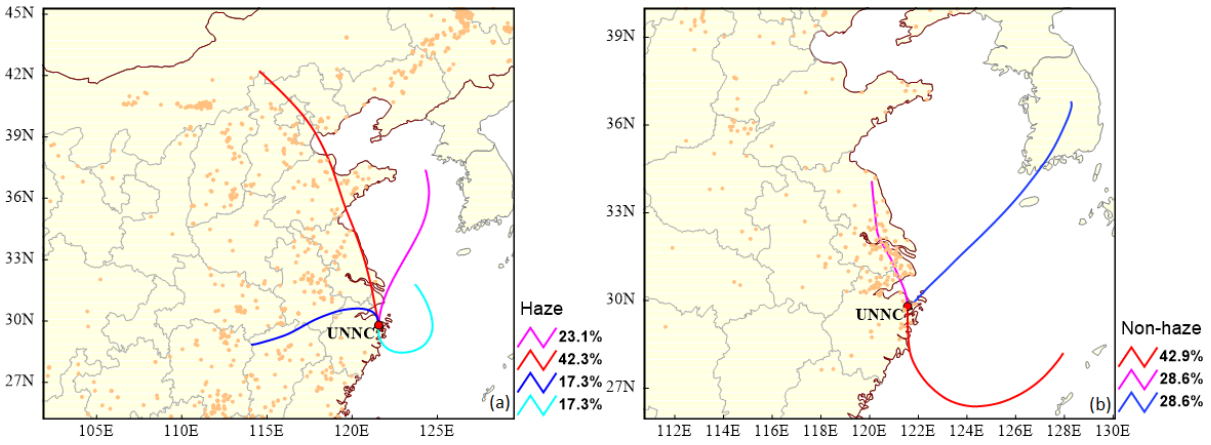

Figure 6.4 48-h back trajectories of air masses during the haze (a) and non-haze (b) periods

6.3.3 Comparison of Composition-dependent OP_v^{ws} in Different Size Mode

Given that the varied OP_v^{ws} between different particle size modes would be governed by different PM components, MLR analysis was conducted to identify the dominant particulate catalytic oxidisers that contributed to OP_v^{ws} and provide a comparison of them between the haze and non-haze periods. Geological minerals (Al, Ca) were not included as one of the predictors due to their natures of redox inactivity. Although the small sample size for each period may cause the potential uncertainty and limitation in regression analysis, the MLR model well captured the OP_v^{ws} variability as the coefficients of determination (R^2) between measured and modelled OP_v^{ws} were greater than 0.4 for all six sets of the data of ultrafine, accumulation and coarse PM modes during the two periods, indicating more than 40% of the variance in OP_v^{ws} could be explained by the chemical species included in the model (Gao et al., 2020a). The resulting linear relationships between OP_v^{ws} and chemical species are summarised in Table 6.3.

For the ultrafine-mode PM, SS aerosols (Na^+, Cl^-, Mg^{2+}) and Cu were identified to

contribute to OP_v^{ws} in both haze and non-haze periods, which was expected since Cl^- in SS aerosols and Cu have been found to be redox active (Charrier and Anastasio, 2012a, Cho et al., 2005, Osthoff et al., 2008, Yao and Zhang, 2012). Both SS and Cu exhibited bimodal distributions, with lower peaks in ultrafine mode during haze period (Fig. 6.5(a)) while accumulation mode during non-haze period (Fig. 6.5(d)). Such findings explain the noticeably higher oxidative potency of ultrafine particles during haze period relative to non-haze period, which was possibly contributed from the relative high concentrations of SS aerosols and Cu. As discussed in Section 4.3.2, Cl^- is a typical SS indicator as well as a significant trace reactant that involved in the processes of oxidant chemistry in the mid-latitudes, which is more reactive than hydroxyl radical ($OH^·$) to oxidise volatile organic compounds (VOCs) and consequently produces peroxy radicals (H_2O_2) (Osthoff et al., 2008, von Glasow, 2008). It signifies that the combination of SS and anthropogenic emissions might accelerate particulate ROS generation and thus aggravate the PM OP. As the close proximity to the freeway (~ 600 m) makes our study site a VOC-rich area, the high levels of VOCs released from vehicular exhausts mixed with SS aerosols would drove substantial OP_v^{ws} of ultrafine particles during haze and non-haze periods. Despite these, we noted that Ningbo was affected by the fresh SS particles (Na/Cl = 0.19) during haze period while aged SS aerosols (Na/Cl = 0.81) during non-haze period in terms of ultrafine-mode PM, according to the Na/Cl ratio of 0.6, which is the threshold to distinguish fresh and aged SS aerosols (Chen et al., 2021, Crilley et al., 2017). The aged SS particles in non-haze period would be classified into partially and fully aged SS. Partially aged SS aerosols are defined as the particles include NaCl core and coating with other redox active species on their surfaces when transported from sea to inland areas, and hence induce

significant DTT oxidation. In fully aged SS particles, the NaCl core was completely transformed into Na_2SO_4 and $NaNO_3$ via atmospheric heterogeneous chemical reactions with acidic gases (Chi et al., 2015). The increased particulate SO_4^{2-} and NO_3^- concentrations could indirectly produce an OP_v^{ws} response and exacerbate the ultrafine PM OP during non-haze period. Since the PM in ultrafine mode experienced strong secondary processes, which could lead to the alteration of the particle properties such as the pH, we then estimated the pH values of particles via E-AIM model and summarised in Table 6.4. The lower pH (1.62) resided in ultrafine PM during haze period would decipher its higher oxidative capacity due to the enhanced solubilities of transition metals relative to the non-haze period (pH = 2.46). The soluble Cu probably derived from industrial activities and non-exhaust VE such as tyre wear. The trend of Cu during haze period was in agreement with the previous study reported by Fang et al. (2017b), showing the peak Cu level in the small size of PM (~ 1 μm). The dominant contribution of Cu to OP_v^{ws} would be attributed to the highly acidic ultrafine aerosols, which facilitated the dissolution of Cu in insoluble form and thus induce an impact on OP_v^{ws} in ultrafine mode (Daellenbach et al., 2020, Fang et al., 2017b).

Table 6.3 Summary of regression Coefficients and major sources of OP_v^{ws} in ultrafine, accumulation and coarse mode

		Major sources	SS [a]	Cu	K	SNA	Cr	Fe	Zn	intercept	R^2 [d]
Haze	Ultrafine [b]	SS, industry, non-exhaust vehicle emission	1.523	1.240	-- [c]	--	--	--	--	0.409	0.500
	Accumulation	Biomass burning	--	--	0.025	--	--	--	--	0.589	0.456
	Coarse	Secondary aerosol, industry, vehicle	--	--	--	0.073	0.030	-0.005	--	0.446	0.713
Non-haze	Ultrafine	SS, industry, non-exhaust vehicle emission	1.182	1.363	--	--	--	--	--	0.057	0.744
	Accumulation	Secondary aerosols	--	--	--	0.047	--	--	--	0.304	0.437
	Coarse	SS, road dust	0.530	--	--	--	--	--	0.071	0.021	0.867

[a] The coefficient units of SS and SNA are nmol min^{-1} μg^{-1}, Cu, K, Cr, Fe and Zn are nmol min^{-1} ng^{-1};

[b] As an example, the linear equation of OP_v^{ws} induced from ultrafine-mode PM is as follow: OP_v^{ws} (ultrafine) = 1.523 × SS + 1.240 × Cu +0.409;

[c] Blank cells represent that the corresponding variable is not included in the equation.

[d] Coefficient of determination. R^2 is a statistical parameter of how close the data are to the fitted regression line.

Table 6.4 Summary of Na/Cl ratios and pH values of PM in ultrafine, accumulation and coarse modes during haze and non-haze period

	Ultrafine		Accumulation		Coarse	
	Haze	Non-haze	Haze	Non-haze	Haze	Non-haze
Na/Cl	0.19	0.81	0.51	1.84	0.71	1.49
pH	1.62	2.46	1.05	0.69	0.72	0.68

The regression model of OP_v^{ws} in accumulation mode captured the contributions from K and SNA during haze and non-haze periods, respectively (Table 6.3). Note that both K and SNA are not redox active components, the contributions to OP_v^{ws} may indicate their common emission sources such as BB and secondary processes, which also emit the water-soluble components responsible for DTT activity. Such findings further confirm our previous discussions in Section 6.3.2, suggesting that the OP_v^{ws} was dominated by BB source during haze period while secondary aerosols during non-haze period in accumulation mode. Both particulate K and SNA varied bimodally and reached a valley point in accumulation mode (Fig 6.5 (b) and Fig. 6.5 (e)), agreeing with the variations of OP_v^{ws}. During cold seasons, BB was a main source of oxidative potency, which contained a high abundance of humic-like substances (HULIS) and played an essential role in DTT decay and ROS production (e.g., O_2^-) (Fang et al., 2019). The study in Atlanta revealed that the catalytic oxidisers of quinones resided in HULIS could accounted for ~10% of water soluble DTT activity (Verma et al., 2015c). By considering that there was no fire spot in the northern Zhejiang Province during the haze period (Fig. 6.4(a)), the BB particles might travel from the remote areas of inland China in the NW and SW (as discussed in Section 6.3.2), and thus experienced the oxidation aging processes during atmospheric transport before arriving Ningbo. Prior study formulated the higher OP_v^{ws} induced from aged BB particle relative to freshly BB emitted PM, owing to the evaporation of non- or less redox active semi-volatile organic compounds (SVOCs) in aging processes, including fatty acids, fatty alcohols, n-alkanes and sterols (Wong et al., 2019). It implies that in this study the DTT response in accumulation mode was dominated by aged BB aerosols, which had enhanced capacity of ROS generation and cause a higher adverse effect on public

health during the haze period. By contrast, SNA contributed greater to the mass concentrations of accumulation-mode particles during the non-haze period (30.44%) relative to haze period (23.83%), whereas Cl^- showed an opposite trend, with lower contribution during the non-haze period (1.44%) than haze period (1.69%). Since the particulate Cl^- was replaced by the stronger acidic NO_3^- and SO_4^{2-} via atmospheric aging processes (Li et al., 2021), higher SNA levels indicated the stronger secondary formation in non-haze period compared with the haze period, during which the secondary aerosol from BB also affected Ningbo city. Higher levels of SNA contained in the secondary aerosols provided a highly acidic environment (pH = 0.69) to drive metals dissolution (e.g., Cu, Mn, Cr and Zn) and thus induced oxidative capacities during the non-haze period. Overall, the atmospheric aging processes played a crucial role in inducing DTT activities from accumulation-mode PM during both haze and non-haze periods.

OP_v^{ws} in the coarse mode was largely explained by SNA, Fe and Cr during haze period, denoting the sources of IE, VE and secondary aerosols predominated the oxidative burden. Particulate Fe and Cr exhibited similar bimodal patterns with peaks in the coarse mode (Fig. 6.5(c)). Interestingly, negative coefficient of Fe (-0.005 nmol min^{-1} ng^{-1}, Table 6.3) was estimated in the regression model, suggesting a suppressed effect of Fe on ROS generation. However, some of the previous studies documented a low intrinsic DTT oxidation of individual soluble Fe, while others revealed that Fe mixed with HULIS presented the additive effects in DTT oxidation and synergistic effects in $OH^{\cdot}$ generation (Charrier and Anastasio, 2012a, Yu et al., 2018, Yue et al., 2018). Considering that the actual effect of soluble Fe may not project itself in the antioxidant responses but generates $OH^{\cdot}$ via Fenton-like reactions from H_2O_2 in the surrogate lung fluid, the suppression in this study could be explained by that Fe in the PM water

extracts might complex with organic ligands, which alter its speciation and thus reduce the oxidative capacities (Charrier and Anastasio, 2011a, Shahpoury et al., 2021). Similar negative contribution to OP_v^{ws} from soluble Fe was also reported by Gao et al. (2020a) in Atlanta. Cr was treated as non-redox active transition metal as it cannot cause measurable DTT oxidation (Charrier and Anastasio, 2012a). However, Cr might be a surrogate measure of components co-emitted with Cr from IE and VE, which have been identified as the major sources of OP_v^{ws} in coarse mode in Section 6.3.2, comprised of a large amount of particulate catalytic oxidisers responsible for ROS formation. In contrast to the haze period, we noted that SS aerosols still had an impact on coarse particles related OP_v^{ws}, as well as the contribution from Zn during non-haze period. The coarse-mode SS aerosols, which had Na/Cl ratio of 1.49, would experience higher aging processes during the warmer period owing to its high photochemical activity. The aged SS particles become stronger acidic (pH = 0.68) and facilitate the transition metal dissolution, then induce more oxidative burden in an indirect way. Zn was considered to be emitted from tyre and road surface wear and resuspension of road dust. Such emission source could represent a relatively low risk factor due to their natures of dominant compounds (e.g., Fe, Zn, Mg, Al, Ca). The fugitive dust typically appears as coarse atmospheric particles and is known to have a relatively low deposition in the human lung. Similarly, the predominant contributions of DTT oxidation resided in super-micron particles (PM_{10}) from resuspended road dust was also observed in Canada (Shahpoury et al., 2021).

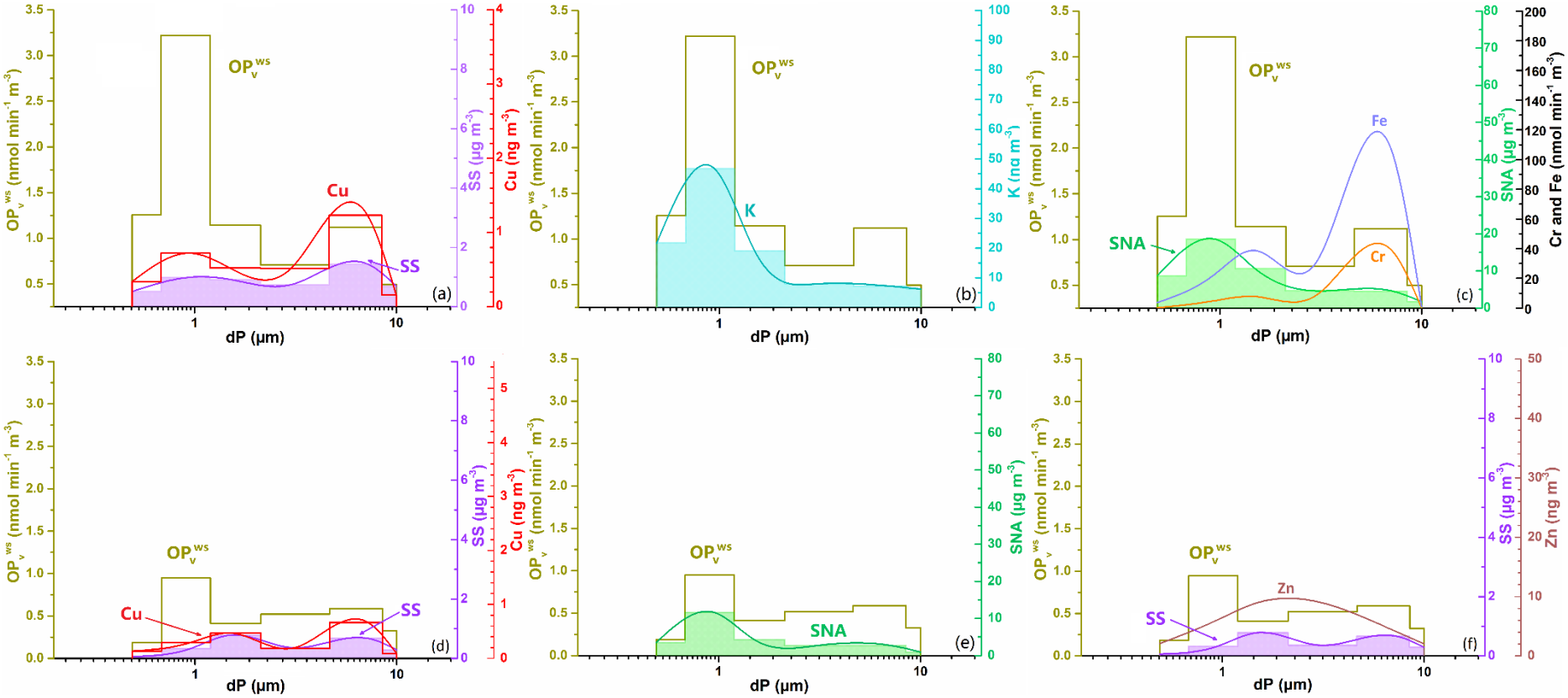

Figure 6.5 Size distributions of OP_v^{ws} and major catalytic oxidisers during the haze (a-c) and non-haze (d-f) periods in Ningbo

6.3.4 Respiratory Deposition and Driving Factors of OP_v^{ws}

The deposition patterns of particles in the respiratory system depends strongly on particle size. Therefore, we quantified the deposition doses of ambient particles and their OP_v^{ws} in head airway, TB and pulmonary regions for both polluted and clean days (Fig. 6.6). The overall PM and OP_v^{ws} depositions during haze period were higher than those during non-haze period. Similar patterns were observed for the PM and OP_v^{ws} deposited in head airways during haze and non-haze days, with the order of the size mode was: coarse > accumulation > ultrafine particles, which was in line with previous results (Liu et al., 2021b, Wang et al., 2019b, Wu et al., 2021b). Such comparison revealed the significance of coarse-mode particles in the deposition levels and their contributions to ROS generation. In TB region, the PM of three size modes was almost evenly deposited during the haze and non-haze days, as well as the OP_v^{ws} in non-haze days. Whereas, the TB region yielded noticeable higher OP_v^{ws} deposition dose that was induced from ultrafine PM (1.38 nmol min^{-1}), relative to coarse and accumulation PM (0.64 and 0.63 nmol min^{-1}, respectively) during haze period, suggesting that the smaller particles in PM would tend to carry more toxic components to drop deeper in to lung. The deposited OP_v^{ws} (49.81%, 2.18 nmol min^{-1}) from ultrafine PM was also dominated in pulmonary region during haze period, although the largest deposited dose of PM was in accumulation mode (45.24%, 57.34 μg). Therefore, coarse particles became the largest contributor to the total OP deposited dose in head airway in both periods, while ultrafine PM and accumulated PM induced OP_v^{ws} dominated pulmonary region in respective haze and non-haze periods. In TB region, however, ultrafine particles contributed most to OP_v^{ws} deposited dose in haze period, and no PM of three different size modes governed OP_v^{ws} deposition. Such

result was plausible as the PM in ultrafine mode would be affected by severe industrial emissions together with the atmospheric aging processes during haze period, as discussed in Section 6.3.3, which provided more highly redox active species (i.e., Cu) and led to their enrichment in ultrafine mode particles.

The varied deposited doses of PM and its OP_v^{ws} would be owing to the variations of size distribution of ambient particles and clearance patterns in different regions of respiratory system (Hussein et al., 2013, Kodros et al., 2018). Since the particulate catalytic oxidisers resided in PM varied with PM size, different chemical components induced OP_v^{ws} would be deposited in different regions (Fang et al., 2017b). However, it is still unknown which specific chemical components and/or emission sources in Ningbo were responsible for the deposited oxidative potency in different respiratory tracts. To unravel the size distributions of dominant OP_v^{ws} contributors in head airway, TB and pulmonary regions, we compared the OP_v^{ws} between measured and MLR modelled values and estimated the ROS generation rates of MLR variables, including SS, Cu, K, SNA, Cr, Fe and Zn, which were depicted in Fig. 6.7. In general, the deposited doses of the regression results for OP_v^{ws} better captured the diverse depositions of measured OP_v^{ws} via MPPD estimation in different respiratory tracts, as the correlation coefficient (r) between them was ranged from 0.58 to 0.96, thus the MLR variables could represent the dominant factors in driving the deposited oxidative capacities.

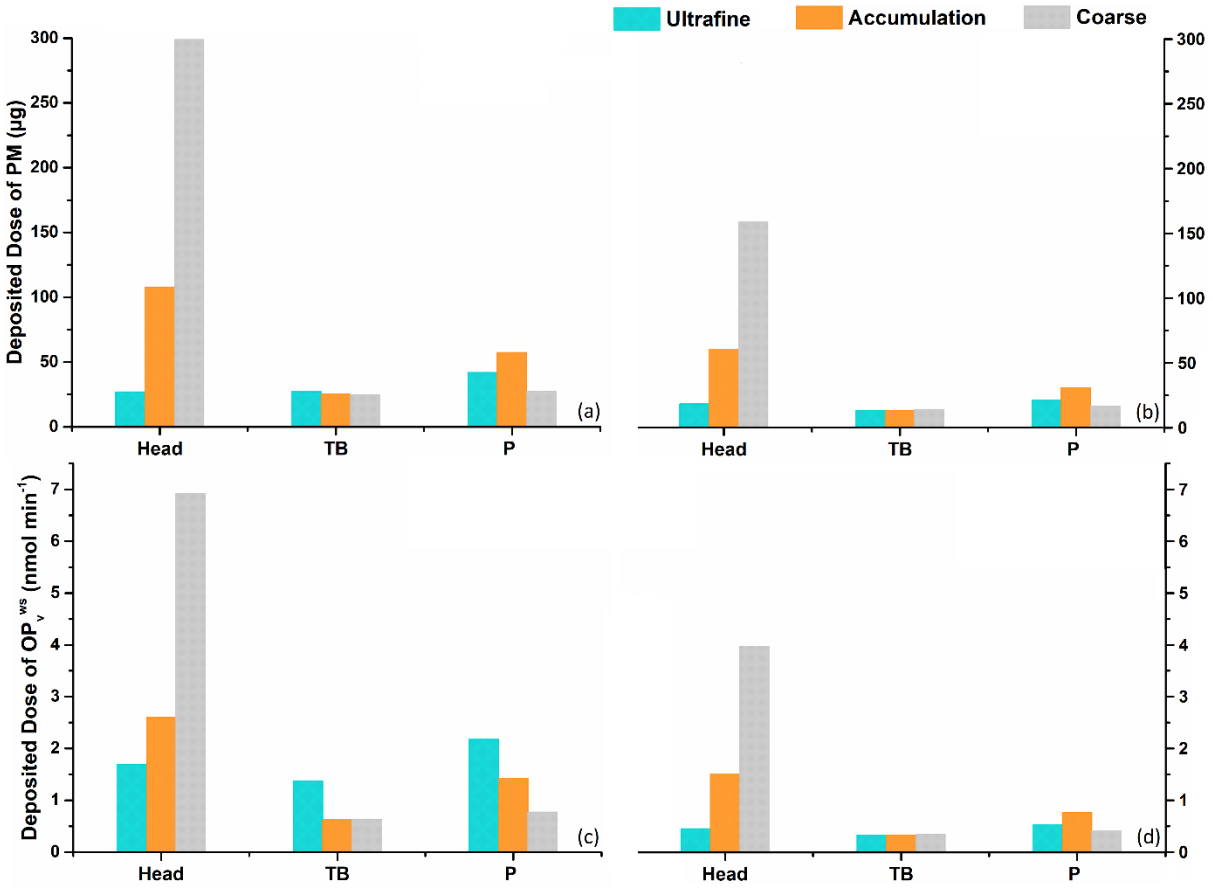

Figure 6.6 Deposited doses of PM (a-b) and OP_v^{ws} (c-d) of ultrafine, accumulation and coarse modes in head airway, tracheobronchial and pulmonary regions during the haze and non-haze periods

During the haze period, the coarse-mode PM generated OP_v^{ws} (4.82 nmol min^{-1}) made the largest contributions of the deposited doses in head airway, which was dominated by the ROS generations of SNA, Fe and Cr (Fig. 6.7(a)), denoting the detrimental effects from secondary aerosols, traffic emissions and industrial activities in the upper regions of respiratory tract. In contrast, the deposited OP_v^{ws} levels were almost the same in ultrafine and coarse modes in the TB region, but much higher than that in accumulation mode (Fig. 6.7(b)). The OP_v^{ws} of ultrafine particles was governed by SS and Cu while SNA, Fe and Cr drove the coarse PM related

oxidative capacity. It manifested that the ultrafine particles originated from SS aerosols, especially the aged SS aerosols as discussed in Section 6.3.3, industry and non-exhaust traffic emissions would produce the similar toxic power as the coarse-mode PM from secondary aerosols, road dust and industry emissions in the TB regions. Such similar deposited OP_v^{ws} doses between the two size modes could be attributed to the high redox activities of ultrafine particles and high deposition efficiency of coarse-mode particles. The deposited dose of OP_v^{ws} exhibited a bimodal pattern in pulmonary region, with a peak appearing in ultrafine mode (Fig. 6.7(c)) during haze period, indicating that the deposited OP_v^{ws} resided in ultrafine PM was predominantly affected by aged SS aerosols, industry and non-exhaust vehicle emissions. These results further elucidated that the particles in ultrafine mode contributed increasingly to the OP_v^{ws} deposition when penetrating into deeper regions of the respiratory tract, from 1.22 nmol min^{-1} in head airway to 1.80 nmol min^{-1} in pulmonary region, which is agreed with previous study in Santiago (Andrade et al., 2021). In the clean days, however, the deposited OP_v^{ws} in the different respiratory tracts had similar variations of bimodal trends, with peaks in the coarse mode. As depicted in Fig. 6.7(d-f), the deposited OP_v^{ws} of coarse PM in different respiratory regions were mainly driven from SS and Zn, demonstrating the essential roles in the redox properties of aged SS aerosols and road dust during non-haze period. Overall, the ultrafine PM released from SS and non-exhaust vehicle emission would be the main drivers in OP_v^{ws} enhancement in pulmonary region during both periods, while coarse PM from secondary aerosols and road dust was the largest contributor of OP_v^{ws} deposition in head airway.

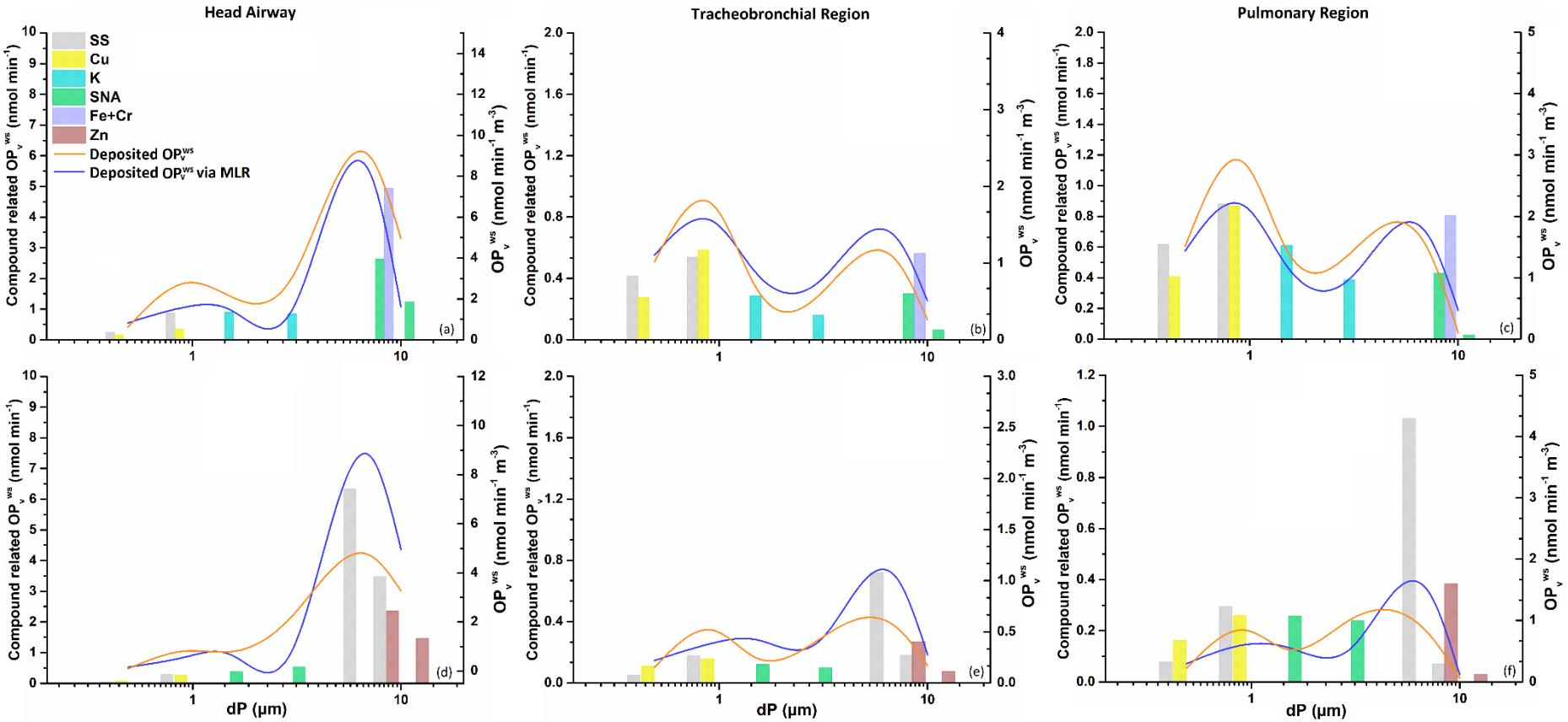

Figure 6.7 Average size distributions of deposited OP_v^{ws} (estimated from measured OP_v^{ws} and MLR modeled OP_v^{ws}) and chemical components related OP_v^{ws} in head airway, tracheobronchial and pulmonary regions during haze (a-c) and non-haze periods (d-f)

Table 6.5 Summary of mass concentrations of WSOC, WSIIs and water-soluble trace elements of size-resolved PM during haze and non-haze periods

	$PM_{0.49}$		$PM_{0.49-0.95}$		$PM_{0.95-1.5}$		$PM_{1.5-3.0}$		$PM_{3.0-7.2}$		$PM_{7.2+}$	
	Haze	Non-haze	Haze	Non-haze	Haze	Non-haze	Haze	Non-haze	Haze	Non-haze	Haze	Non-haze
Carbonaceous species (μg m^{-3})												
[a] WSOC	2.56 ± 1.00	1.62 ± 1.72	7.08 ± 3.82	3.61 ± 4.98	3.66 ± 3.50	1.49 ± 2.23	1.54 ± 0.75	0.98 ± 0.84	1.90 ± 1.11	1.08 ± 0.51	0.52 ± 0.58	0.23 ± 0.15
Water-soluble inorganic ions (μg m^{-3})												
Li^+	0.00 ± 0.00	0.00 ± 0.00	0.03 ± 0.00	0.00 ± 0.00	0.02 ± 0.03	0.02 ± 0.03	0.00 ± 0.00	0.00 ± 0.00	0.00 ± 0.00	0.00 ± 0.00	0.00 ± 0.00	0.00 ± 0.00
Na^+	0.07 ± 0.02	0.03 ± 0.01	0.16 ± 0.07	0.10 ± 0.07	0.23 ± 0.11	0.10 ± 0.02	0.27 ± 0.17	0.18 ± 0.15	0.55 ± 0.37	0.30 ± 0.21	0.24 ± 0.18	0.15 ± 0.10
K^+	0.19 ± 0.06	0.06 ± 0.04	0.40 ± 0.22	0.11 ± 0.13	0.19 ± 0.09	0.15 ± 0.22	0.06 ± 0.02	0.03 ± 0.02	0.07 ± 0.02	0.04 ± 0.01	0.04 ± 0.06	0.01 ± 0.01
Mg^{2+}	0.00 ± 0.00	0.00 ± 0.00	0.02 ± 0.01	0.01 ± 0.01	0.04 ± 0.01	0.39 ± 0.64	0.06 ± 0.02	0.05 ± 0.02	0.12 ± 0.05	0.07 ± 0.02	0.05 ± 0.02	0.02 ± 0.01
Ca^{2+}	0.02 ± 0.05	0.02 ± 0.01	0.05 ± 0.06	0.03 ± 0.01	0.24 ± 0.19	0.05 ± 0.04	0.46 ± 0.15	0.21 ± 0.11	1.33 ± 0.57	0.56 ± 0.27	0.65 ± 0.28	0.28 ± 0.23
F^-	0.02 ± 0.02	0.00 ± 0.01	0.01 ± 0.01	0.00 ± 0.00	0.04 ± 0.01	0.01 ± 0.01	0.01 ± 0.01	0.01 ± 0.01	0.05 ± 0.03	0.02 ± 0.02	0.02 ± 0.01	0.01 ± 0.01
Cl^-	0.44 ± 0.20	0.03 ± 0.01	0.82 ± 0.48	0.21 ± 0.17	0.65 ± 0.18	0.29 ± 0.16	0.42 ± 0.22	0.14 ± 0.10	0.78 ± 0.61	0.30 ± 0.25	0.41 ± 0.34	0.12 ± 0.08

Br^-	0.05 ± 0.06	0.01 ± 0.01	0.06 ± 0.10	0.01 ± 0.00	0.01 ± 0.02	0.01 ± 0.01	0.02 ± 0.01	0.02 ± 0.02	0.00 ± 0.00	0.01 ± 0.01	0.00 ± 0.00	0.00 ± 0.00
NH_4^+	2.81 ± 0.69	1.58 ± 0.80	4.94 ± 2.48	3.05 ± 2.56	1.97 ± 1.53	0.31 ± 0.29	0.70 ± 0.63	0.33 ± 0.37	0.30 ± 0.27	0.18 ± 0.19	0.16 ± 0.45	0.02 ± 0.03
NO_3^-	3.64 ± 1.66	1.19 ± 0.91	8.39 ± 6.15	3.89 ± 5.30	5.50 ± 4.60	2.25 ± 2.75	2.73 ± 1.53	1.72 ± 0.99	3.35 ± 1.66	2.28 ± 1.03	1.02 ± 0.54	0.76 ± 0.78
SO_4^{2-}	2.20 ± 0.54	0.76 ± 0.97	5.20 ± 3.41	4.68 ± 3.35	3.09 ± 2.56	1.72 ± 2.03	1.18 ± 0.87	0.57 ± 0.46	0.90 ± 0.36	0.21 ± 0.09	0.50 ± 0.42	0.15 ± 0.12
Water-soluble trace elements (ng m^{-3})												
Cu	0.34 ± 0.31	0.14 ± 0.16	0.72 ± 0.25	0.29 ± 0.28	0.52 ± 0.46	0.47 ± 0.85	0.52 ± 0.66	0.19 ± 0.20	1.24 ± 1.09	0.67 ± 0.42	0.16 ± 0.15	0.09 ± 0.06
Pb	0.75 ± 0.23	0.49 ± 0.37	1.33 ± 0.51	1.19 ± 0.79	0.83 ± 0.56	0.59 ± 0.68	0.13 ± 0.10	0.10 ± 0.11	0.10 ± 0.10	0.07 ± 0.04	0.10 ± 0.30	0.01 ± 0.02
Fe	3.64 ± 8.45	0.78 ± 1.03	23.03 ± 14.60	5.66 ± 5.09	38.74 ± 27.01	10.87 ± 11.58	30.66 ± 35.36	11.49 ± 12.90	103.83 ± 134.18	37.94 ± 31.45	1.04 ± 0.60	0.56 ± 0.50
Al	0.43 ± 0.17	0.38 ± 0.39	7.56 ± 3.86	2.48 ± 1.64	4.76 ± 5.50	2.65 ± 1.91	5.19 ± 5.59	1.10 ± 0.88	28.56 ± 67.43	6.87 ± 6.48	0.78 ± 0.64	0.36 ± 0.29
Mn	0.70 ± 0.39	0.45 ± 0.25	1.80 ± 0.79	1.46 ± 0.81	1.28 ± 1.00	1.02 ± 0.78	0.95 ± 1.03	0.43 ± 0.35	2.87 ± 2.75	2.88 ± 1.09	0.53 ± 0.15	0.32 ± 0.17
V	0.19 ± 0.14	0.32 ± 0.12	0.20 ± 0.12	0.38 ± 0.19	0.07 ± 0.05	0.05 ± 0.02	0.05 ± 0.04	0.02 ± 0.02	0.10 ± 0.12	0.06 ± 0.05	0.02 ± 0.01	0.01 ± 0.01
Cr	0.12 ± 0.04	0.06 ± 0.04	4.96 ± 3.34	0.98 ± 1.44	7.72 ± 5.67	3.12 ± 2.90	8.55 ± 8.48	0.94 ± 0.66	38.04 ± 27.33	7.10 ± 7.02	0.02 ± 0.02	0.05 ± 0.05
Ce	0.00 ± 0.00	0.00 ± 0.00	0.00 ± 0.00	0.00 ± 0.00	0.00 ± 0.00	0.00 ± 0.00	0.01 ± 0.01	0.00 ± 0.00	0.02 ± 0.02	0.02 ± 0.01	0.00 ± 0.01	0.00 ± 0.00
Cd	0.05 ± 0.02	0.02 ± 0.01	0.08 ± 0.05	0.04 ± 0.03	0.06 ± 0.03	0.03 ± 0.02	0.03 ± 0.02	0.02 ± 0.01	0.02 ± 0.02	0.01 ± 0.01	0.01 ± 0.02	0.00 ± 0.00

Zn	6.66 ± 3.35	2.07 ± 1.39	16.25 ± 11.13	6.09 ± 4.85	13.73 ± 7.48	8.98 ± 4.71	7.91 ± 3.73	9.09 ± 2.29	3.99 ± 2.75	4.17 ± 2.39	2.60 ± 4.38	2.05 ± 13.38
Co	0.01 ± 0.01	0.00 ± 0.01	0.06 ± 0.04	0.01 ± 0.01	0.10 ± 0.10	0.04 ± 0.02	0.07 ± 0.08	0.01 ± 0.02	0.24 ± 0.29	0.23 ± 0.07	0.01 ± 0.01	0.01 ± 0.01
Ni	0.14 ± 0.08	0.10 ± 0.04	3.13 ± 2.16	0.69 ± 0.77	4.28 ± 3.64	1.83 ± 1.42	4.42 ± 5.05	0.74 ± 0.48	27.30 ± 18.33	6.53 ± 7.51	0.03 ± 0.02	0.08 ± 0.07
Ag	0.00 ± 0.00	0.00 ± 0.00	0.00 ± 0.00	0.00 ± 0.00	0.00 ± 0.00	0.00 ± 0.00	0.01 ± 0.01	0.00 ± 0.00	0.02 ± 0.03	0.02 ± 0.01	0.00 ± 0.01	0.00 ± 0.00
As	0.12 ± 0.04	0.05 ± 0.04	0.23 ± 0.12	0.11 ± 0.12	0.12 ± 0.08	0.07 ± 0.08	0.04 ± 0.02	0.03 ± 0.03	0.07 ± 0.04	0.05 ± 0.02	0.02 ± 0.02	0.01 ± 0.00
Sr	0.05 ± 0.07	0.01 ± 0.01	0.20 ± 0.25	0.02 ± 0.02	0.22 ± 0.22	0.07 ± 0.04	0.26 ± 0.16	0.11 ± 0.08	0.88 ± 0.63	0.61 ± 0.24	0.22 ± 0.09	0.12 ± 0.06
Bi	0.01 ± 0.01	0.00 ± 0.00	0.05 ± 0.07	0.02 ± 0.03	0.03 ± 0.05	0.01 ± 0.02	0.01 ± 0.01	0.00 ± 0.00	0.03 ± 0.04	0.02 ± 0.01	0.04 ± 0.05	0.00 ± 0.00
Sb	0.21 ± 0.20	0.07 ± 0.07	0.26 ± 0.22	0.11 ± 0.15	0.12 ± 0.08	0.07 ± 0.08	0.04 ± 0.01	0.02 ± 0.02	0.06 ± 0.03	0.03 ± 0.01	0.03 ± 0.04	0.02 ± 0.03
Mg	6.18 ± 11.92	1.98 ± 3.90	2.09 ± 1.44	0.81 ± 0.71	4.15 ± 3.48	6.01 ± 7.68	7.41 ± 3.38	5.48 ± 2.33	16.10 ± 5.75	10.03 ± 6.73	6.32 ± 3.07	3.15 ± 1.41
Ca	1.91 ± 1.19	1.48 ± 1.29	7.98 ± 2.97	3.56 ± 1.64	20.03 ± 15.90	8.04 ± 2.67	32.68 ± 11.56	15.09 ± 9.16	95.80 ± 54.25	61.91 ± 16.59	48.58 ± 20.45	29.44 ± 14.59
K	21.69 ± 6.97	5.18 ± 4.54	46.68 ± 20.53	14.40 ± 15.15	19.09 ± 10.94	10.36 ± 9.14	7.91 ± 2.81	4.82 ± 2.08	7.13 ± 2.92	4.12 ± 2.52	6.24 ± 7.86	2.10 ± 1.00
Ba	0.54 ± 0.52	0.48 ± 0.45	0.40 ± 0.51	0.12 ± 0.07	0.62 ± 0.56	0.56 ± 0.66	0.67 ± 0.23	0.39 ± 0.30	0.68 ± 0.41	0.44 ± 0.29	0.72 ± 0.19	0.26 ± 0.10

[a] Concentration unit for WSOC and WSIIs are μg m^{-3} and for trace elements are ng m^{-3}.

6.4 Conclusion

This study presented the size distributions of PM and its water-soluble fraction generated OP, and estimated their respiratory deposition during the haze and non-haze period in Ningbo. The results showed that the concentrations of PM and its related OP_v^{ws} were substantially higher during haze period (29.76-40.97μg m^{-3} and 0.50-3.22 nmol min^{-1} m^{-3}) than non-haze period (9.15-22.20 μg m^{-3} and 0.19-0.95 nmol min^{-1} m^{-3}) for all size ranges, and maximum centred in ultrafine mode.

Ultrafine particles contributed increasingly to the OP_v^{ws} deposition when penetrating into deeper regions of the respiratory tract, from 1.22 nmol min^{-1} in head airway to 1.80 nmol min^{-1} in pulmonary region. The OP_v^{ws} resided in ultrafine particles was driven by SS and Cu, deposited mainly in pulmonary region in the two scenarios, implying the significance of SS aerosols, industrial activities and non-exhaust traffic emissions (road dust) in eliciting the ROS generation and thus causing pulmonary inflammation. However, SNA and soluble transition metals of Fe and Cr dominated the OP_v^{ws} from coarse-mode particles, which had largest depositions in head airway during the two periods. It can be attributed to the influences of secondary aerosols, industry emissions and road dust.

The deposited OP_v^{ws} in TB region had a combined contribution from ultrafine (SS, Cu) and coarse particles (SNA, Fe, Cr) in polluted days, while coarse-mode OP_v^{ws} (SNA, Fe, Cr) dominated the TB region in clean days. The similar OP_v^{ws} contributions between the two size modes during haze period were explained by the high redox activities of ultrafine particles and high deposition efficiency of coarse-mode particles. The PM in accumulation mode had less contribution to the deposited dose of OP_v^{ws}, compared to the other two size modes in different

respiratory regions during haze and non-haze periods.

Chapter 7 Comparison of Particle Size Distributions of OP Induced from Methanol-Soluble PM Fractions and Their Lung Depositions between High and Low Pollution Periods

7.1 Introduction

Exposure to ambient particulate matter (PM) is deemed to be a severe concern of public health, giving rise to the inflammation in respiratory tract and cardiovascular systems, yet the mechanisms of these actions are not completely understood (Gao et al., 2020b, Lin and Yu, 2021, Wong et al., 2019). Multiple factors are involved in toxicity of ambient PM, including individual and interactional inductions from active chemical components. One of the most acknowledged pathways to interpret casual links between PM exposure and health effects is addressing the oxidative stress via generation of reactive oxygen species (ROS) (Bates et al., 2019a, Xiong et al., 2017). The resultant oxidative stress can initiate a redox stage change in cells and further lead to cell necrosis or apoptosis, and consequently cause acute or chronic diseases (Bates et al., 2019a, Gao et al., 2020b). The ability of PM to produce ROS in vivo is considered as the oxidative potential (OP) of ambient particles (Cho et al., 2005).

Growing studies focused on water-soluble species of PM for OP characterisation, as they would be more readily available to interact with lung fluid owing to the water-soluble nature (Cheng et al., 2021, Fang et al., 2017a, Jin et al., 2019b, Lin and Yu, 2021). However, various water-insoluble particulate components have been demonstrated to be well-correlated with OP, such as polycyclic aromatic hydrocarbons (PAHs), quinones and humic-like substances (HULIS) (Kramer et al., 2021). PAHs, as semi-volatile organic compounds (SVOCs), are

commonly released from traffic emissions and incomplete combustion. Although PAHs are inactive in dithiothreitol (DTT) oxidation, they are treated as markers of the emission source for redox-active organic species (i.e., quinones) (Cho et al., 2004, Cho et al., 2005). Quinones are formed from PAHs through photochemical aging processes and can be bound to particle surfaces, and hence significantly increase the mass-normalised OP (OP_m) relative to fresh particles. Strong evidence also revealed the crucial role of secondary organic aerosols (SOA) in affecting OP responses, especially quinone-derived SOA and naphthalene SOA.

So far, efforts have been devoted to investigating the source contributions of size-dependent OP induced from water-insoluble fractions and their deposition efficiency. Focusing on different size modes, previous studies revealed that PM in coarse-mode is more inclined to exacerbate degradation of DNA and haemolysis relative to smaller size (Osornio-Vargas et al., 2011b). The ultrafine particles are commonly considered as strongly toxic, ascribing to its highly linked to biomarkers of systemic inflammation and enables penetration into deeper lung region, and transferred to other organs or cell membranes, causing mitochondria damage (Delfino et al., 2009, Li et al., 2003). Since the deposition of size-dependent OP can better reflect the detrimental effects of ambient aerosols, several studies modelled the respiratory deposition of OP via multiple-path particle dosimetry (MPPD) (Liu et al., 2021a, Lyu et al., 2018) or empirical expressions from human inhalation data (ICRP) (Fang et al., 2017b), and estimated the correlations between OP and redox active species. A substantial fraction of coarse-mode PM ($PM_{2.5\text{-}10}$, particles with aerodynamic diameter between 2.5 and 10 μm) components are hydrophobic, most of which are associated with tire and brake wear, construction activities and road dust in urban area. Organic oxidisers, such as quinones (1,2-

napthaquinone (1,2-NQ), 1,4-napthaquinone (1,4-NQ), 1,4-anthraquinone (1,4-AQ)) adsorbed on solid particles can induce OP either via engulfment of cells or binding to a cell surface, or act as a carrier of toxic components such as PAHs (Schoonen et al., 2006). In contrast, the oxidative stress generated from organic fraction of PM with smaller sizes was dominantly affected by traffic emissions (i.e., tailpipe emissions, petroleum spills) (Saffari et al., 2014a, Shirmohammadi et al., 2016).

Given that the lung deposited OP varied with multiple factors, including the particulate catalytic oxidisers, emission sources, mass loading of SOA, atmospheric aging processes and particle deposition efficiency, etc, which respiratory region is more affected by the OP and which factor controls the concentration of OP that deposits in the specific respiratory region remain still unknow at present. Here, we aim to: 1) determine the size distribution of PM and its methanol-soluble fraction generated OP (OP^{meth}) via DTT assay during the haze and non-haze period; 2) assess the spatial dispersions of the size-fractioned PM and their OP^{meth} in the study domain; 3) estimate the respiratory deposited doses of PM and its OP^{meth} via MPPD model; 4) identify the governed PM redox-active species to oxidative potency and compare their OP^{meth} contributions in haze and non-haze days; 5) explore the driving factors of deposited OP^{meth} in different respiratory tracts.

7.2 Methods

7.2.1 Sampling

The size-resolved aerosol samples used for the analysis of particulate organic components in this chapter shared the same samples of the study for water-soluble species in Chapter 6.

Detailed information for sampling procedures was presented in Section 6.2.1.

7.2.2 Sample Analysis

Collected filters were divided to analyse through an array of experiments for quantifying organic species including carbonaceous species (OC, EC and WSOC), PAHs and quinones. The same protocols for these organic species measurements have been described in Section 5.2.4.

7.2.3 Quality Control

The analytical quality of the measured data was determined by reproducibility, recovery, linearity and limit of detection (LOD). For each set of samples, field blank samples were included to correct the real-world samples by subtracting the mean blank values. The concentrations of PAHs and quinones were estimated via the 5-point external standard calibration, ranged from 0.1 to 1000 ng mL^{-1}, the linearity of calibration standards calculated through linear regression with values between 0.99 and 1.00 (r^2) for all PAHs and quinones. The LOD was ranged from 0.42 ng m^{-3} of Phe to 9.70 ng m^{-3} of Ace for PAHs and the between 0.00 ng m^{-3} of 1,2-AQ and 0.04 ng m^{-3} of 1,2-NQ, while the recovery ranged from 89.25% of Ant to 109.44% of BkF for PAHs and 92.13% of 1,4-NQ and 98.02% of 1,2-NQ for quinones. For OC and EC, known concentration of standard solution was used for calibration before each set of analysis, during which multipoint external calibration was conducted by analyser via dripping the sucrose solution onto a punch of pre-baked blank filter. The LOD was 0.70 µg m^{-3} of OC and 1.00 µg m^{-3} of EC, while recovery was 111.27% of OC and 86.91% of EC.

7.2.4 EC-tracer Method

The EC-tracer method was conducted to estimate the representative $(OC/EC)_{pri}$ during this sampling campaign, and the detailed approach of this method (Strader et al., 1999). EC is treated as a tracer for the prediction of concentration of OC_{pri} under the hypothesis that EC and OC_{pri} originate from the same sources, hence $(OC/EC)_{pri}$ can be estimated for a given region of study under consideration. With this hypothesis, it has been assumed that if measured ambient OC/EC values exceed estimated $(OC/EC)_{pri}$, the excess fraction of OC is believed to come from secondary sources and termed as OC_{sec}. The empirical expressions used in estimation of concentrations of OC_{sec} and secondary organic aerosol are given in the following equations,

$$OC_{pri} = EC \times (OC/EC)_{pri} \quad \text{Eq. (1)}$$

$$OC_{sec} = OC - OC_{pri} \quad \text{Eq. (2)}$$

$$SOA = f_{OM/OC} \times OC_{sec} \quad \text{Eq. (3)}$$

Based on previous reported studies, measured OC/EC values over 2.9 are treated as high and represent the upper value of the range of $(OC/EC)_{pri}$ (Conklin et al., 1981). Hence, we took 2.9 as the threshold value for ambient OC/EC and discarded samples with ambient OC/EC values exceeding 2.9. The remaining data were analysed with a least-square regression technique, and in this process, $(OC/EC)_{pri}$ of 1.29 was calculated. The improved regression coefficient (R^2 = 0.93) estimated through using the remaining data indicate reasonable confidence that 1.52 can represent $(OC/EC)_{pri}$, and values of mean mass concentrations of OC_{pri}, OC_{sec} and OC_{pri} percentage to total OC were estimated (Table 7.4). According to our previous study, SOA was estimated by multiplying 1.6 by OC_{sec} amount (Chen et al., 2021).

7.2.5 Analysis of Air Mass Backward Trajectory

Analysis of air mass backward trajectory was conducted for identifying the impact of pollutants originating from medium and long-range transport of aerosols rather than local emissions. Detailed information of analysing air mass backward trajectory was guaranteed by the same protocol as described in Section 6.2.4.

7.2.6 Graphical Analysis of Source Dispersion

Bivariate polar plots (BPPs) were applied in this study to compare the geographical sources and dispersion patterns of size-fractioned PM and their related OP from methanol-soluble fraction (OP_v^{meth} and OP_m^{meth}) during haze and non-haze period in Ningbo. Detailed description of BPPs construction can be found in Section 4.2.5.

7.2.7 Modelling Deposition in Human Respiratory System

MPPD model (version 3.04, Applied Research Associates Inc., Arlington, VA, USA) was conducted to obtain the deposition fractions (DF) of size-fractioned PM in extrathoracic/head airway, tracheobronchial (TB) region and alveolar/pulmonary region, which can reflect the ROS generation ability of size-dependent PM in human respiratory system. Detailed description of MPPD model application is presented in Section 6.2.6.

7.2.8 Multivariate Regression Models

A multiple linear regression (MLR) analysis was performed to estimate the OP_v^{meth}

contribution from individual hydrophobic PM component through SPSS (Statistics 23). 10 samples were applied for MLR analysis for each PM size mode in each study period. Detailed information for MLR analysis was described in Section 6.2.7.

7.3 Results and Discussion

7.3.1 Comparison of Size Distribution of PM and OP^{meth}

Figure 7.1 depicts the size distributions of OP normalised by air volume (OP_v^{meth}) and mass (OP_m^{meth}) elicited from methanol extracted PM fraction with ambient particle concentrations during the haze and non-haze periods. The OP_v^{meth} varied similarly during the two periods, which had trimodal trends with the highest peaks in the diameter range between 7.2 and 10.0 μm ($PM_{7.2-10}$, 2.43 ± 0.24 and 0.88 ± 0.77 nmol min^{-1} m^{-3} during haze and non-haze periods, respectively), but the overall levels were obviously higher during the haze period (0.40-2.43 nmol min^{-1} m^{-3}) relative to non-haze period (0.21-0.88 nmol min^{-1} m^{-3}). Analogous results were also reported by Fang et al. (2017b), showing that the substantially higher oxidative capacity induced from water insoluble fractions (extracted by methanol) of coarse particles (diameter > 3.2 μm, 3.62 ± 0.20 and 5.13 ± 0.52 nmol min^{-1} m^{-3}) relative to fine particles (≤ 3.2 μm, 0.22 ± 0.14 and 0.41 ± 0.07 nmol min^{-1} m^{-3}) at both road-site and urban area in Atlanta. It signifies the predominant role of coarse particles in addressing the oxidative stress from the hydrophobic components in the atmospheric aerosols. The greater OP_v^{meth} during haze period could be attributed to the higher concentrations of the particulate catalytic oxidisers (i.e., quinones). Although the other two peaks of oxidative potency occurred in $PM_{0.49}$ and $PM_{1.5-3.0}$ during the both periods, the OP_v^{meth} level in $PM_{1.5-3.0}$ (1.17 ± 0.27 nmol min^{-1} m^{-3}) was substantially higher

than that in $PM_{0.49}$ (0.73 ± 0.30 nmol min^{-1} m^{-3}) during haze period, in contrast to non-haze period, the OP_v^{meth} induced from the accumulation-mode particles of $PM_{1.5\text{-}3.0}$ (0.47 ± 0.38 nmol min^{-1} m^{-3}) showed slightly lower than it of $PM_{0.49}$ (0.57 ± 0.32 nmol min^{-1} m^{-3}). The difference of OP_v^{meth} trends between haze and non-haze periods reflects the different size distributions of redox-active species and varied toxic emission sources (i.e., vehicular exhaust), which will be discussed in Section 7.3.3.

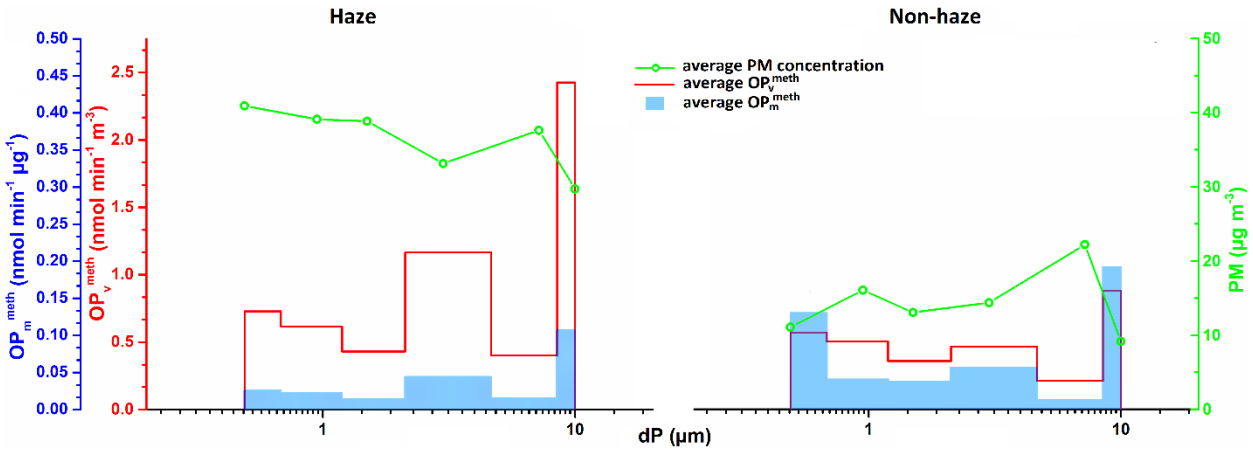

Figure 7.1 Size distribution of PM, OP_v^{meth} and OP_m^{meth} during haze and non-haze periods

By comparison, the overall intrinsic OP (OP_m^{meth}) of size-resolved PM was less than one half during the haze period (0.22 ± 0.11 nmol min^{-1} μg^{-1}) relative to the non-haze period (0.46 ± 0.38 nmol min^{-1} μg^{-1}). Such higher level of OP_m^{meth} in clean days was attributed to the higher averaged OP_m^{meth} of all particle sizes, except $PM_{3.0\text{-}7.2}$, suggesting the greater intrinsic oxidative stress related to the hydrophobic fractions of ambient particles with most PM sizes during warm season (20.38 ± 2.10 °C). We also noted that the OP_m^{meth} were pronouncedly higher from the coarsest (7.2-10.0 µm, 0.19 ± 0.23 nmol min^{-1} μg^{-1}) and finest PM (≤ 0.49 µm, 0.13 ± 0.23 nmol min^{-1} μg^{-1}) collected in this study than the PM with other sizes (0.01-0.06 nmol min^{-1} μg^{-}

^{1}) during non-haze period, while highest OP_m^{meth} was induced from coarse particle ($PM_{7.2-10}$, 0.11 ± 0.08 nmol min^{-1} μg^{-1}), followed by accumulation-mode PM ($PM_{1.5-3.0}$, 0.04 ± 0.02 nmol min^{-1} μg^{-1}) and ultrafine PM ($PM_{0.49}$, 0.03 ± 0.02 nmol min^{-1} μg^{-1}). Such results denoted that the hydrophobic redox-active compounds increased with the increase of particle size in polluted days, whereas they tend to accumulate to the finest and coarsest particles in clean days, insinuating the different cumulative processes of particulate catalytic oxidisers on the ambient particles in two periods. It is speculated that such difference would be ascribed to the atmospheric secondary processes, varied chemical composition and emission sources, detailed discussion is presented in Section 7.3.2-7.3.3.

Table 7.1 Summary of size-fractioned OP_v^{meth} and OP_m^{meth} during haze and non-haze periods

	OP_v^{meth} (nmol min^{-1} m^{-3})		OP_m^{meth} (nmol min^{-1} μg^{-1})	
	Haze	Non-haze	Haze	Non-haze
$PM_{0.49}$	0.73 ± 0.30	0.57 ± 0.32	0.03 ± 0.02	0.13 ± 0.23
$PM_{0.49-0.95}$	0.62 ± 0.26	0.50 ± 0.23	0.02 ± 0.02	0.04 ± 0.03
$PM_{0.49-1.5}$	0.43 ± 0.18	0.36 ± 0.20	0.01 ± 0.01	0.04 ± 0.02
$PM_{1.5-3.0}$	1.17 ± 0.27	0.47 ± 0.38	0.04 ± 0.02	0.06 ± 0.06
$PM_{3.0-7.2}$	0.40 ± 0.15	0.21 ± 0.15	0.02 ± 0.02	0.01 ± 0.01
$PM_{7.2-10}$	2.43 ± 0.24	0.88 ± 0.77	0.11 ± 0.08	0.19 ± 0.23
Σ PM	5.68 ± 0.71	2.92 ± 0.99	0.22 ± 0.11	0.46 ± 0.38

Table 7.2 Summary of size-resolved PAHs and quinones (average ± SD) during haze and non-haze periods

	$PM_{0.49}$		$PM_{0.49-0.95}$		$PM_{0.49-1.5}$		$PM_{1.5-3.0}$		$PM_{3.0-7.2}$		$PM_{7.2-10}$	
	Haze	Non-haze	Haze	Non-haze	Haze	Non-haze	Haze	Non-haze	Haze	Non-haze	Haze	Non-haze
PAHs (concentration in ng m^{-3})												
Nap	0.25 ± 0.17	0.26 ± 0.14	0.31 ± 0.07	0.24 ± 0.04	0.12 ± 0.03	0.13 ± 0.02	0.11 ± 0.04	0.09 ± 0.02	0.10 ± 0.06	0.06 ± 0.09	0.04 ± 0.02	0.05 ± 0.02
Ace	0.08 ± 0.06	0.03 ± 0.09	0.28 ± 0.03	0.11 ± 0.03	0.06 ± 0.02	0.04 ± 0.02	0.21 ± 0.06	0.06 ± 0.05	0.02 ± 0.00	0.01 ± 0.01	0.03 ± 0.01	0.02 ± 0.01
Acy	0.17 ± 0.02	0.05 ± 0.01	0.35 ± 0.02	0.11 ± 0.01	0.04 ± 0.01	0.02 ± 0.00	0.03 ± 0.02	0.02 ± 0.02	0.05 ± 0.03	0.02 ± 0.01	0.17 ± 0.15	0.03 ± 0.02
Flu	0.08 ± 0.02	0.03 ± 0.01	0.28 ± 0.05	0.10 ± 0.04	0.03 ± 0.01	0.01 ± 0.00	0.01 ± 0.01	0.01 ± 0.01	0.02 ± 0.01	0.01 ± 0.00	0.02 ± 0.01	0.00 ± 0.00
Phe	0.30 ± 0.08	0.14 ± 0.07	0.50 ± 0.09	0.28 ± 0.08	0.08 ± 0.02	0.04 ± 0.01	0.04 ± 0.03	0.04 ± 0.02	0.08 ± 0.02	0.02 ± 0.00	0.03 ± 0.01	0.02 ± 0.01
Ant	0.02 ± 0.02	0.01 ± 0.03	0.07 ± 0.01	0.03 ± 0.01	0.02 ± 0.00	0.01 ± 0.00	0.03 ± 0.02	0.00 ± 0.01	0.02 ± 0.01	0.01 ± 0.01	0.01 ± 0.01	0.00 ± 0.01
Flt	0.40 ± 0.16	0.32 ± 0.17	0.77 ± 0.08	0.31 ± 0.05	0.20 ± 0.01	0.15 ± 0.01	0.09 ± 0.04	0.07 ± 0.03	0.08 ± 0.03	0.01 ± 0.01	0.06 ± 0.03	0.04 ± 0.01
Pyr	1.44 ± 0.67	0.67 ± 0.42	2.38 ± 0.17	1.52 ± 0.08	0.33 ± 0.07	0.10 ± 0.06	0.16 ± 0.11	0.10 ± 0.09	0.23 ± 0.12	0.10 ± 0.04	0.23 ± 0.16	0.12 ± 0.02
BaA	0.39 ± 0.02	0.34 ± 0.02	0.99 ± 0.70	1.35 ± 0.88	0.12 ± 0.01	0.06 ± 0.01	0.05 ± 0.00	0.06 ± 0.00	0.02 ± 0.01	0.01 ± 0.01	0.03 ± 0.01	0.03 ± 0.00

Chr	0.81 0.51	±	0.08 0.05	±	0.90 0.55	±	0.06 0.08	±	0.26 0.16	±	0.02 0.03	±	0.12 0.07	±	0.02 0.01	±	0.06 0.03	±	0.01 0.00	±	0.03 0.06	±	0.01 0.00	±
BbF	1.29 0.96	±	0.15 0.12	±	1.49 0.85	±	0.31 0.35	±	0.59 0.38	±	0.06 0.08	±	0.23 0.11	±	0.02 0.08	±	0.04 0.06	±	0.03 0.01	±	0.05 0.08	±	0.03 0.02	±
BkF	1.61 1.03	±	0.18 0.23	±	1.50 1.12	±	0.16 0.20	±	0.16 0.06	±	0.03 0.02	±	0.06 0.04	±	0.04 0.01	±	0.07 0.01	±	0.04 0.01	±	0.07 0.05	±	0.04 0.02	±
BaP	1.08 1.02	±	0.14 0.06	±	1.39 0.94	±	0.07 0.11	±	0.22 0.15	±	0.04 0.02	±	0.09 0.04	±	0.02 0.01	±	0.04 0.01	±	0.01 0.01	±	0.07 0.11	±	0.03 ±0.01	
Ind	2.08 1.70	±	0.33 0.25	±	2.19 1.66	±	0.20 0.37	±	0.31 0.17	±	0.04 0.01	±	0.06 0.05	±	0.02 0.01	±	0.02 0.01	±	0.02 0.00	±	0.02 0.04	±	0.01 0.00	±
DBA	0.26 0.17	±	0.10 0.07	±	0.36 0.17	±	0.22 0.32	±	0.18 0.08	±	0.07 0.04	±	0.10 0.05	±	0.02 0.02	±	0.02 0.01	±	0.01 0.00	±	0.01 0.01	±	0.01 0.00	±
Bpe	1.66 1.16	±	0.30 0.23	±	1.36 0.08	±	0.14 0.26	±	0.25 0.13	±	0.05 0.01	±	0.08 0.04	±	0.01 0.01	±	0.02 0.02	±	0.01 0.00	±	0.04 0.10	±	0.01 0.00	±
ΣPAH	11.92 0.68	±	2.49 0.16	±	15.12 0.71	±	2.38 0.17	±	2.97 0.15	±	0.50 0.02	±	1.46 0.06	±	0.49 0.03	±	0.87 0.05	±	0.49 0.03	±	0.90 0.06	±	0.55 0.05	±

Quinones (concentration in ng m^{-3})

1,2-NQ	0.71 0.22	±	0.36 0.13	±	1.68 0.72	±	0.86 0.60	±	1.17 0.49	±	0.53 0.29	±	0.57 0.24	±	0.31 0.09	±	0.31 0.11	±	0.14 0.04	±	0.27 0.34	±	0.07 0.04	±
1,4-NQ	0.74 0.24	±	0.40 0.15	±	1.73 0.65	±	0.98 0.67	±	1.22 0.57	±	0.54 0.33	±	0.63 0.24	±	0.32 0.09	±	0.32 0.12	±	0.18 0.05	±	0.30 0.42	±	0.12 0.03	±
1,4-AQ	0.72 0.32	±	0.18 0.11	±	1.87 1.34	±	0.28 0.25	±	0.70 0.48	±	0.11 0.10	±	0.27 0.24	±	0.08 0.04	±	0.11 0.05	±	0.05 0.01	±	0.11 0.22	±	0.01 0.01	±

7.3.2 Graphical Analysis of OP^{meth} Induced from Size-resolved PM

To graphically compare the OP^{meth} dispersions from the potential sources in different PM size ranges, BPPs of OP_v^{meth} and OP_m^{meth} as well as PM mass concentrations during haze and non-haze periods were plotted, as given in Fig. 7.2 and 7.3, respectively. During the haze period, the highest level of $PM_{0.49}$ related OP_v^{meth} (Fig. 7.2(g)) was recorded when the wind blew from the west to the south. However, we observed the lower $PM_{0.49}$ mass concentration (Fig. 7.2(a)) from these directions but higher from the northwest (NW), which indicated the stronger DTT activities generated from the particles with limited mass concentration and further implied the toxic emission sources (i.e., vehicular exhausts) from the western to southern directions, releasing large number of redox-active organics. It also explains the highest value of intrinsic oxidative stress (Fig. 7.2(m)) induced from $PM_{0.49}$ to the southwest (SW). The OP_v^{meth} level increased with the increases of wind speed, which is an indicative trend of buoyant plume such as road traffic sources (Carslaw et al., 2006). This is entirely expected because of the source of ring expressway of Ningbo city is to the SW and south with approximately 2 km away from our study domain. Higher OP_v^{meth} from the southern direction was also found in $PM_{0.49\text{-}0.95}$ and accumulation-mode PM, thus we inferred that the traffic emission had a relatively constant impact on the ambient particle growth and particulate ROS generation, which could be considered as one of the dominant sources of both PM and its related OP_v^{meth}. In contrast to the OP_v^{meth} in ultrafine and accumulation modes having the common traffic source, the maximum OP_v^{meth} value of $PM_{3.0\text{-}7.2}$ (Fig. 7.2(k)) was obtained when wind blew from NW, while the $PM_{7.2\text{-}10}$ induced OP_v^{meth} (Fig. 7.2(l)) from the north. The $PM_{3.0\text{-}7.2}$ related OP_v^{meth} increased with the increasing wind speed. Therefore, a consideration of potential sources highlighted the

traffic emissions from Ningbo Lishe airport at around 10 km to the NW of our study site. According to the analysis of back trajectories (Fig. 6.4(a)) during haze period, almost half of the air masses originated from NW in Hebei Province while 17.3% came from the western areas of inland China and travelled through Hangzhou Bay before arriving in Ningbo. Both of the clusters passed through the areas with densely distributed fire spots, which may bring the contaminants from biomass burning from the NW and enhanced the oxidative stress of ambient aerosols. By contrast, the emission source of $PM_{7.2\text{-}10}$ induced OP_v^{meth} was regarded as a distinctive ground level source as the level of which decreased with the increase of wind speeds from any directions (Chen et al., 2021). Such results signified a mixed source from the central business district (CBD) of Ningbo, which is corresponded to the north sector with approximately 7.4 km away from our study domain, might comprise of the pollutants from traffic emission, secondary aerosols and long-range transport. Similar distributions of OP_m^{meth} were observed between the PM size ranged from 0.95 to 10 μm (Fig. 6.2 (n-r)), the maximum values of which were obtained from the NW. We infer that such high intrinsic OP^{meth} could be ascribing to their similar sources, including airport emission and biomass burning, emitting the high concentrations of particulate redox-active organics. Further discussions on OP^{meth} and redox-active organics are presented in Section 7.3.3.

The dispersed patterns of OP_v^{meth} and OP_m^{meth} varied significantly compared to PM concentrations in ultrafine mode during the non-haze period. The highest PM concentrations experienced with north-westerly winds when the wind speeds were higher than 5 m s^{-1} (Fig 7.3 (a-b)). Whereas, the maximum OP_v^{meth} and OP_m^{meth} resided in $PM_{0.49}$ and $PM_{0.49\text{-}0.95}$ were recorded from diverse wind sectors (Fig. 7.3(g-h) and (m-n)). Such phenomenon reflected the

contributions of mixed sources to both OP_v^{meth} and OP_m^{meth} of ultrafine particles. For the accumulation-mode particles, both highest extrinsic (Fig. 7.3(i-j)) and intrinsic oxidative potencies (Fig. 7.3(o-p)) came from the NW and northeast (NE) for $PM_{0.95\text{-}1.5}$ and $PM_{1.5\text{-}3.0}$, respectively, manifesting that the emission sources from those directions emitted higher concentrations of toxic PM, which was able to introduce stronger DTT activities. As the NW direction is located the Ningbo Lishe airport while NE sectors corresponded to the Ningbo-Zhoushan Port, we inferred that the dominant sources of OP^{meth} in accumulation mode would be the airport emission and marine source. The Ningbo-Zhoushan Port is currently the busiest port and possesses the largest cargo throughput in the world, which is located 33 km away to the east of our study site. It suggested a significant impact on our study site by releasing oil fly ash from marine vessels and exhausts from vehicle engines, as well as the mixed sea salt aerosols. On local days, the north-easterly winds brought those marine emissions from the East China Sea into Ningbo and thus enhanced the DTT activity (Cheng et al., 2021). For the coarse-mode particles, the OP_v^{meth} in $PM_{3.0\text{-}7.2}$ (Fig. 7.3(k)) and $PM_{7.2\text{-}10}$ (Fig. 7.3(l)) did not display exactly the same behaviour during the non-haze period, while the OP_m^{meth} patterns of them (Fig. 7.3(o-p)) shared similarities, with higher values recorded from the NE. The highest level of OP_v^{meth} resided in $PM_{3.0\text{-}7.2}$ was obtained from the NW and increased with the increasing in wind speed, demonstrating a potential source of traffic emissions from the Ningbo Lishe airport. By comparison, the OP_v^{meth} of $PM_{7.2\text{-}10}$ was maximum from the southeast (SE) to the south, the level of which decreased with increasing in wind speed from any directions, denoting a ground level source such as traffic emissions from the adjacent freeway (600 m). Highest OP_m^{meth} induced from $PM_{3.0\text{-}7.2}$ was observed from the NE while the OP_m^{meth} of $PM_{7.2\text{-}10}$ was affected

by the sources from both NE and NW. Regardless of the abovementioned emissions from Lishe airport, Ningbo-Zhoushan port, the analysis of back trajectories (Fig. 6.4(b)) depicted the same proportion (28.6%) of air parcels from the NE and NW, which were originated from the East China Sea and Jiangsu Province during the non-haze period. One of the clusters (in pink) passed through the densely distributed fire spots would carry substantial amount of pollutants from biomass burning before arriving Ningbo. The other cluster (in blue) travelled from the ocean would bring considerable sea salt aerosols. Therefore, the potential sources of traffic related emissions (i.e., freeway proximity, Lishe airport), Ningbo-Zhoushan port, biomass burning, and sea salt aerosols could be the dominant contributors giving rise to the enhancement of intrinsic oxidative stress in coarse mode PM.

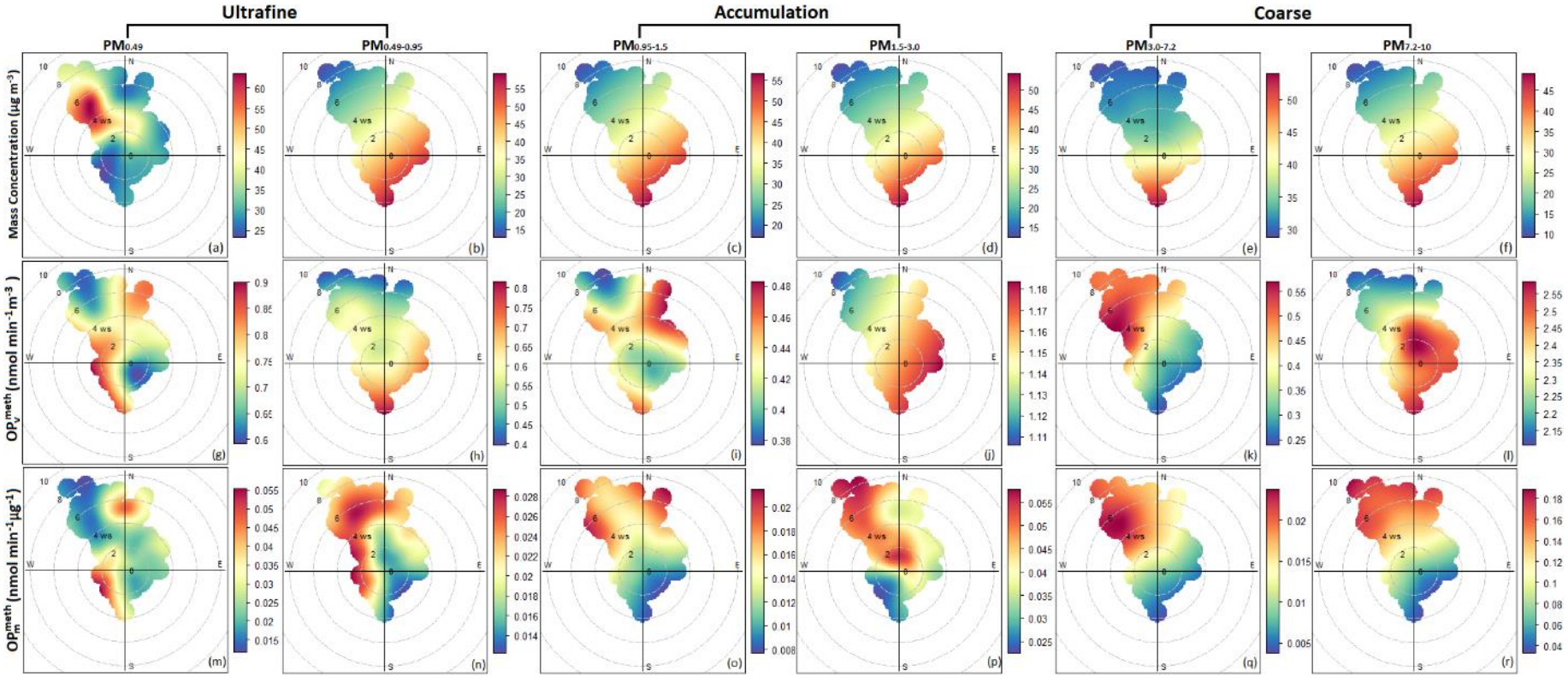

Figure 7.2 Bivariate polar plots of size-resolved PM concentration (a-f), OP_v^{meth} (g-l) and OP_m^{meth} (m-r) during the haze period

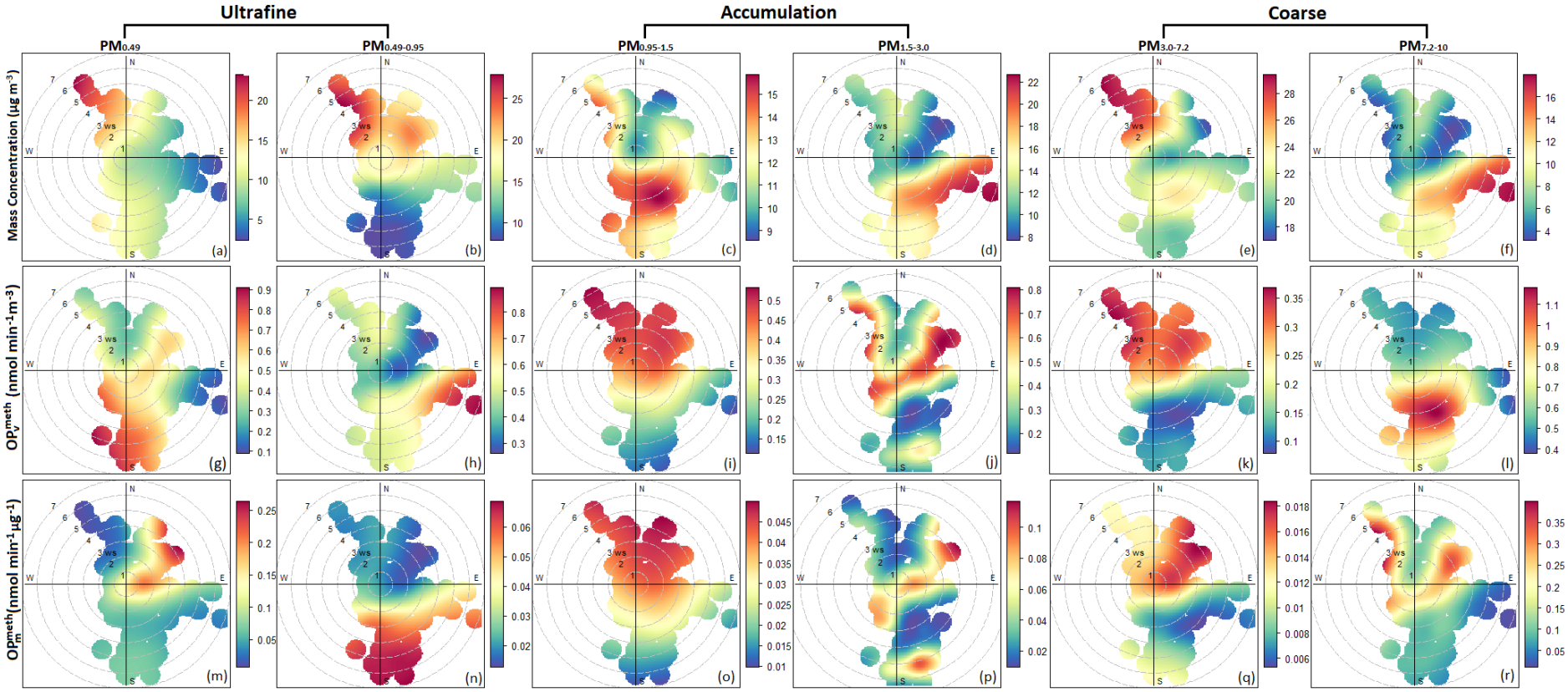

Figure 7.3 Bivariate polar plots of size-resolved PM concentration (a-f), OP_v^{meth} (g-l) and OP_m^{meth} (m-r) during the non-haze period

7.3.3 Comparison of Composition-dependent OP_v^{meth} in Different Size Mode

Since the OP_v^{meth} varied with the different particle sizes could be attributed to the varied PM components, multivariate analysis was conducted to identify the dominant redox-active organic species that governed OP_v^{meth} and compared their contributions between the haze and non-haze periods. In this model, quinones (1,2-NQ, 1,4-NQ, 1,4-AQ) and the PAHs that were positive correlated with OP_v^{meth} were considered as the predictors. The negative correlations of quinones were adopted due to their potential antagonistic interactions with other species (i.e., metal ions of Cu). The MLR model reliably reproduced the OP_v^{meth} as the coefficient of determination (R^2) between measured and modelled OP_v^{meth} was between 0.614 and 0.920 for the OP_v^{meth} in accumulation and coarse modes during the two periods. However, no predictor was estimated from the OP_v^{meth} in ultrafine mode during both haze and non-haze periods, demonstrating that there was no dominant redox-active component or source driving the OP_v^{meth} in ultrafine mode, and further implying a serious impact from the complex mixing of sources (i.e., secondary aerosols, traffic emission, industrial activities and marine source). The results of regression analysis between OP_v^{meth} and the chemical components are summarized in Table 7.3.

Table 7.3 Summary of regression coefficients of OP_v^{meth} in ultrafine, accumulation and coarse mode

		NaP [a]	Acy	Flt	BbF	Ind	1,4-NQ	Intercept	R^2
Haze	Ultrafine	-- [c]	--	--	--	--	--	--	--
	Accumulation[b]	1.405	--	--	2.128	-5.373	--	0.755	0.636
	Coarse	--	15.810	--	--	--	-1.079	0.076	0.904
Non-haze	Ultrafine	--	--	--	--	--	--	--	--
	Accumulation	--	-21.638	18.848	--	--	--	0.203	0.852
	Coarse	--	6.129	--	--	--	--	-0.001	0.614

[a] The units of coefficients are nmol min^{-1} ng^{-1};
[b] As an example, the linear equation of OP_v^{meth} induced from accumulation-mode PM is as follow: OP_v^{meth} (accumulation) = 1.405 × NaP + 2.128 × BbF – 5.373 × Ind + 0.755;
[c] Blank cells represent that the corresponding variable is not included in the equation.

OP_v^{meth} in accumulation mode was largely explained by Nap, BbF and Ind during haze period. Given that the PAHs themselves do not contain the functional groups capable of catalysing the DTT oxidation (Verma et al., 2009a), the positive contributions of the PAH compound to OP_v^{meth} may suggest the common sources of the specific PAH tracers and redox-active species. During the haze period, Nap had a bimodal variation and the lower peak appeared in accumulation modes (Fig. 7.4(a)). BbF exhibited a unimodal trend and peaked in ultrafine mode, the levels of which in accumulation mode took the subordinate position. Since Nap was considered as a tracer of asphalt surface pavement and BbF is highly indicative of exhausts from diesel and petrol vehicles (Zhang et al., 2019), the OP_v^{meth} resided in accumulation-mode PM would be governed by the traffic emissions from the freeways proximity, including vehicle exhausts and non-exhaust traffic emissions (road dusts). Although Ind is a typical indicator of heavy vehicle emission (Xu et al., 2021b), we noted that its contribution to OP_v^{meth} was negative. As Ind is one of the high-molecular-weight (HMW) PAHs with relatively low volatile pressure, the negative contributions could be explained by the photooxidative transformation of HMW PAHs. More explicitly, photooxidation of PAHs under strong solar radiation conditions may oxidise them into polar compounds, including oxy-PAHs, nitro-PAHs and quinones, and consequently address oxidative burden (Cho et al., 2005). In contrast to the haze period, Acy and Flt became the dominant contributors to OP_v^{meth} during non-haze period. Both Acy and Flt varied trimodally and peaked in all three particle size modes, in consistent with the variations of OP_v^{meth}. Since the Flt was probably derived from petroleum spills, the oxidative stress during non-haze period was still affected by vehicular exhaust, including the oil fly ash from marine vessels and traffic exhausts from Lishe airport and

adjacent freeway, as discussed in Section 7.3.2. Nevertheless, we observed that the measured Acy contributed negatively to OP_v^{meth} in this study. Unlike particulate Ind, such results were likely due to the relatively high volatility of Acy as it is classified as a low-molecular-weight (LMW) PAH, resulting in its decreased concentration in warm season (20.38 ± 2.10 °C) and thus limiting its contribution to DTT decay (Verma et al., 2009a).

The regression model of OP_v^{meth} in coarse mode captured the contributions from Acy during haze and non-haze periods (Table 7.3). Knowing that Acy was regarded as non-redox active component according to the earlier studies, it could be a surrogate measure of components co-emitted with Acy from biomass burning and road dust. Such findings further confirm our previous analysis of back trajectories in Section 7.3.2, showing the air masses in both polluted and clean days passed through the areas of densely distributed fire spots, which might bring considerable biomass burning related particulate reactive oxygen-bearing compounds (i.e., humic-like substances (HULIS), trace elements) and caused enhancement of oxidative burden. Acy was also utilized as an indicator of asphalt surface pavement (Wang et al., 2019c, Zhang et al., 2019), denoting the inevitable influence from road dust to OP_v^{meth} generation in coarse mode. However, negative contribution was also estimated between 1,2-NQ (-0.999 nmol min^{-1} μg^{-1}) and coarse-mode OP_v^{meth} during haze period. Quinones are released from either incomplete combustion or secondary processes such as oxidized derivatives of the parent PAH molecules (Layshock et al., 2010, McWhinney et al., 2013, Verma et al., 2015c). Therefore, the particulate 1,2-NQ could be produced from either diesel and petrol exhausts (McWhinney et al., 2013) or secondary oxidation from Nap (Bunce et al., 1997, Chan et al., 2009). In order to figure out the dominant generation process of 1,2-NQ, we quantified the mass concentrations

of size-fractioned secondary organic aerosols (SOA) via EC-tracer method and summarised in Table 7.4. The size-dependent SOA varied similarly with 1,2-NQ (correlation coefficient (r) = 0.73), both of which exhibited the highest levels in ultrafine mode (12.41 ± 8.14 μg m^{-3} and 1.68 ± 0.72 ng m^{-3}) during haze period. We inferred that the significant amount of 1,2-NQ in ultrafine particles could be contributed from the highest mass loadings of SOA for gas-particle partitioning and oxidation of Nap in ultrafine-mode (McWhinney et al., 2013). However, the lower supplies of SOA and parent PAH of Nap in coarse mode suggested a limited impact of secondary oxidation on 1,2-NQ generation, we inferred that the primary emission sources including traffic exhausts and resuspension of road dust might be dominated the 1,2-NQ production. Earlier studies also revealed that the pollutants from road dust or non-tailpipe traffic emissions tended to adsorb onto the coarse particles (Fang et al., 2017b, Shahpoury et al., 2021). The negative contribution of 1,2-NQ to coarse-mode particle related OP_v^{meth} signified a suppressed effect in generating the oxidative stress. Such result highlighted the antagonistic interaction between particulate copper (Cu) and 1,2-NQ in DTT oxidation, which was owing to the complex of Cu with 1,2-NQ can oxidise free DTT but does not generate significant ROS (Kachur et al., 1997, Xiong et al., 2017, Yu et al., 2018). Since Cu is a typical tracer of traffic-related emission (i.e., tyre wear, road dust) and might be jointly emitted with 1,2-NQ, it further confirmed the conjecture of the inhibition in DTT decay resulted from Cu and 1,2-NQ mixture. Overall, biomass burning and traffic related emissions played crucial roles in exerting ROS generation from coarse particles during both haze and non-haze periods.

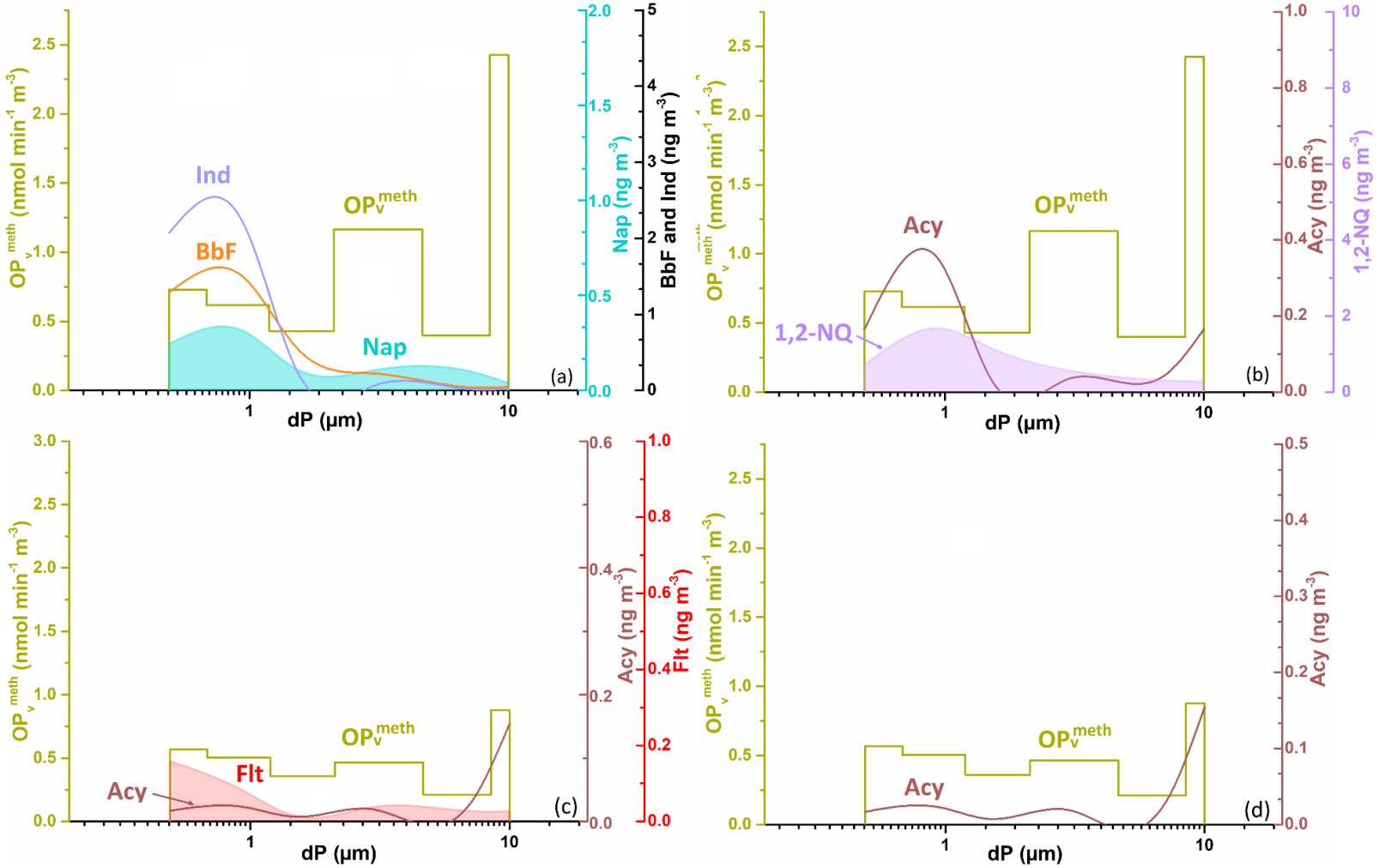

Figure 7.4 Size distributions of OP_v^{meth} and major OP contributors during the haze (a-b) and non-haze (c-d) periods in Ningbo

7.3.4 Respiratory Deposition and Driving Factors of OP_v^{meth}

Particle deposition patterns in the respiratory system depend strongly on the particle size. In this study, we estimated the deposited doses of atmospheric particles and their OP_v^{meth} in head airway, TB and pulmonary regions during haze and non-haze periods (Fig. 7.5). The overall deposited doses of PM and OP_v^{meth} in the whole respiratory tracts was 2.17 to 2.98 and 1.26 to 2.60 times higher in polluted days relative to the clean days among the three size modes, respectively, denoting the higher exposure to the ambient particles and oxidative potencies during haze period. Detailed discussions of PM deposition were presented in Section 6.3.4. Briefly, similar deposition patterns were observed for the PM in head airways and pulmonary region between both periods, with the orders of deposited level were: coarse > accumulation > ultrafine, and accumulation > ultrafine > coarse, respectively. The OP_v^{meth} followed such deposition trends, revealing the significances of coarse- and accumulation mode particles in deposited levels and their capabilities to generate ROS in respective head and pulmonary regions. Similar deposition patterns of oxidative burden induced from water insoluble PM fractions in these two respiratory regions were also reported by Fang et al. (2017b) in Atlanta, US. In the TB region, the PM of three size modes was almost evenly deposited during the haze and non-haze days, however, their induced OP_v^{meth} exhibited differently. During haze period, the TB region yielded highest OP_v^{meth} deposited dose that was generated from coarse PM (0.81 nmol min^{-1}), followed by accumulation (0.60 nmol min^{-1}) and ultrafine particles (0.46 nmol min^{-1}), implying that the coarse particles would carry the organic species with strong redox activities (i.e., quinones, HULIS and SOA), then giving rise to the resultant higher intrinsic oxidative potencies in deeper respiratory region. In contrast, the deposited OP_v^{meth} (0.37 nmol

min^{-1}) from ultrafine PM was dominated in TB region during non-haze period. Such finding was plausible as the PM in ultrafine mode along with various chemicals can penetrate into the lower regions of human respiratory tracts (Lyu et al., 2018). The smaller particles (ultrafine and accumulation modes) may lead to strong detrimental outcomes since they are difficult to clean and easy access to blood. Even the ultrafine particles can avoid phagocytosis via alveolar macrophages to enter the deep respiratory tracts. Thus, although in non-polluted days, the highest deposited does of OP_v^{meth} exerted by ultrafine particles would possibly induce inflammation in the TB region.

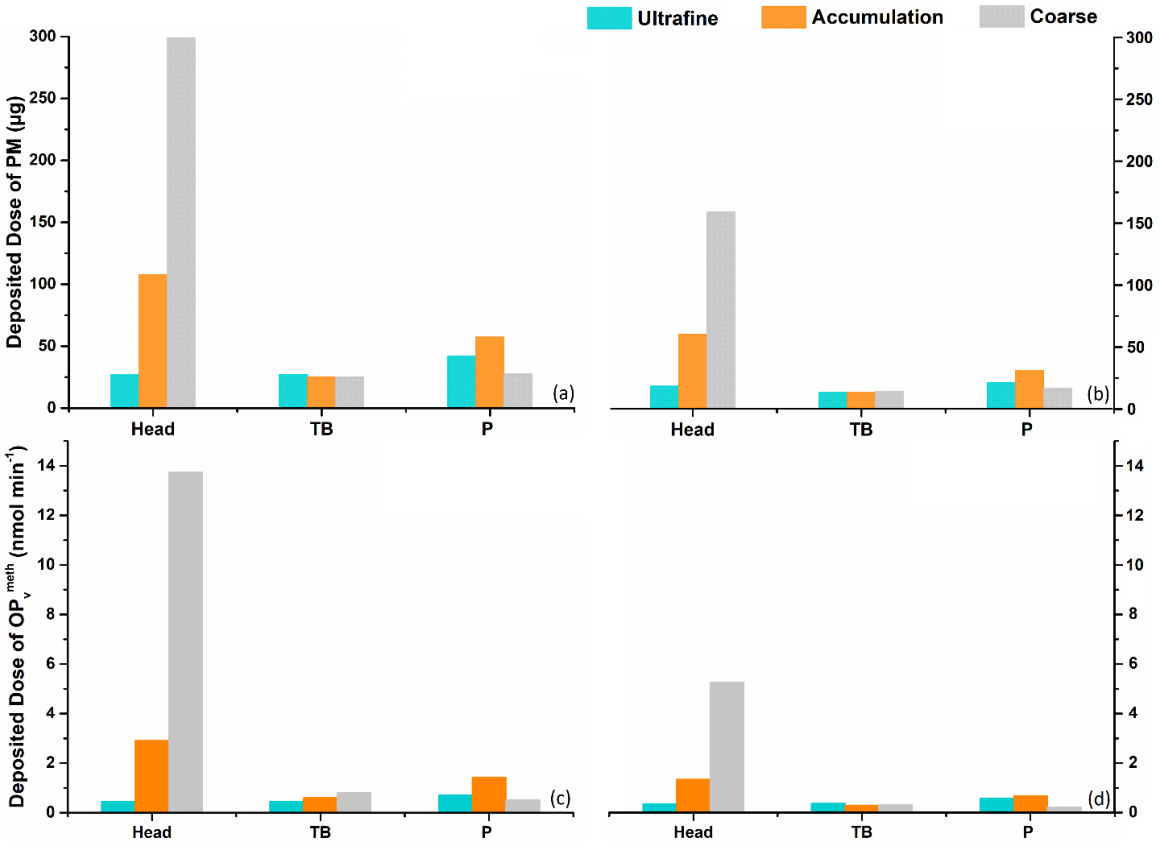

Figure 7.5 Deposited doses of PM (a-b) and OP_v^{meth} (c-d) of ultrafine, accumulation and coarse modes in head airway, tracheobronchial and pulmonary regions during the haze and non-haze period

By scaling the deposited dose of PM related OP_v^{meth} with the particulate catalytic oxidisers through MLR model, we identify the size distributions of dominant OP_v^{meth} contributors in head airway, TB and pulmonary regions for accumulation and coarse modes. However, no dominant component was estimated in the ultrafine mode for both haze and non-haze period (Fig. 7.6), suggesting that OP_v^{meth} resided in ultrafine particles might be affected by the effects of multi-contaminants or multi-sources. The deposited doses of regression results of OP_v^{meth} better captured the varied depositions of measured OP_v^{meth} by MPPD estimation in three respiratory tracts, with the correlation coefficients (*r*) ranged from 0.97 to 1.00. Therefore, we consider the MLR variables as the dominant factors responsible for driving the deposited oxidative potencies.

The coarse particles induced OP_v^{meth} made the largest contributions of the deposited does in head airway during haze (13.20 nmol min^{-1}) and non-haze periods (5.54 nmol min^{-1}), which was dominated by the positive contribution of Acy to ROS generation, denoting the toxicities from road dusts and biomass burning in the nasal regions of respiratory tracts (Fig 7.6(a) and (d)). Although more than 76% of the OP_v^{meth} in coarse mode deposited in head airways, it would be probably not as harmful as ultrafine particles due to the inhibition of impaction processes via rhinothrix (Calderón-Garcidueñas et al., 2010b). In contrast, deposited dose of OP_v^{meth} in TB region exhibited trimodal variations during the two periods, and the levels of three peaks were almost the same (Fig. 7.6(b) and (e)). The OP_v^{meth} in polluted days was governed by the positive contributions from Nap, BbF in accumulation mode and Acy in coarse mode, while Flt and Acy drove the respective accumulation- and coarse-mode OP_v^{meth} in clean

days. The negative contributions of Ind and Acy during respective polluted and non-polluted periods in accumulation mode indicated the fact that their mass concentrations decreased with the increases of OP_v^{meth}, which could be explained by the photooxidation of HMW PAHs and high volatility of LMW PAHs, as discussed in Section 7.3.3. The similar peak levels of OP_v^{meth} depositions were observed in TB region for accumulation- (0.81 and 0.36 nmol min^{-1}) and coarse-mode particles (0.86 and 0.34 nmol min^{-1}) during both periods, manifesting the similar toxic power of PM between releasing from vehicle exhausts in accumulation mode and road dusts in coarse mode. Such similarity between the two size modes could be attributed to the high redox activities of accumulation-mode particles and high deposition efficiency of coarse-mode particles. In pulmonary region, the deposited dose of OP_v^{meth} varied bimodally, with highest peaks appearing in accumulation mode during two periods (Fig. 7.6(c) and (f)), which were mainly induced from BbF and Ind during haze period while Acy and Flt during non-haze period. It elucidated that the highest deposited toxicities resided in accumulation-mode particles was governed by the traffic exhausts from diesel and petrol engines. Such highest deposition level of oxidative capacity induced from accumulated-mode PM was also observed in Atlanta (Fang et al., 2017b) and Shanghai (Lyu et al., 2018).

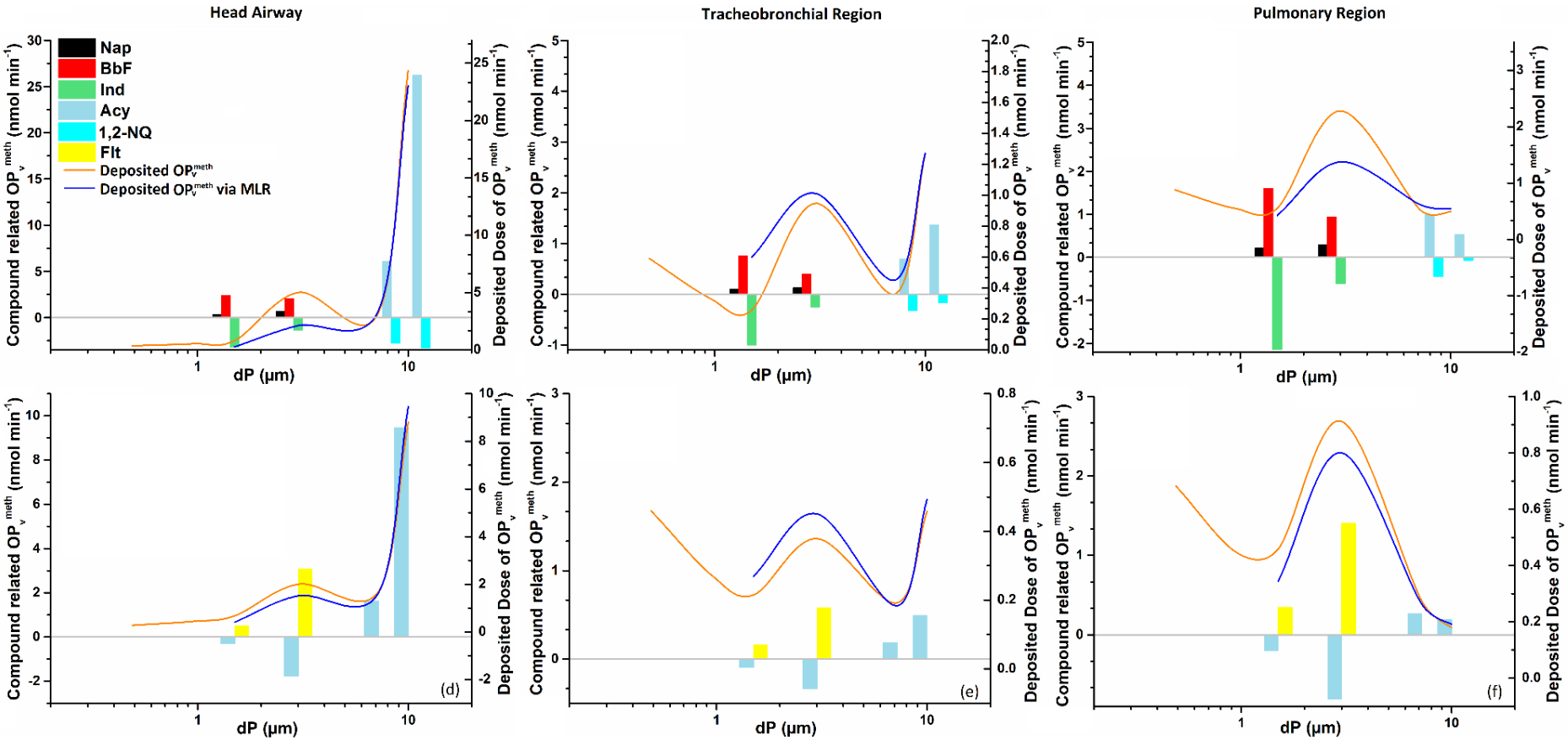

Figure 7.6 Average size distributions of deposited OP_v^{meth} (estimated from measured OP_v^{meth} and MLR modelled OP_v^{meth}) and chemical components related OP_v^{meth} in head airway, tracheobronchial and pulmonary regions during haze (a-c) and non-haze periods (d-f)

Table 7.4 Summary of mass concentrations (μg m^{-3}) of OC, EC, OCpri, OCsec and SOA resided in size-resolved PM during haze and non-haze periods

	$PM_{0.49}$		$PM_{0.49-0.95}$		$PM_{0.95-1.5}$		$PM_{1.5-3.0}$		$PM_{3.0-7.2}$		$PM_{7.2+}$	
	Haze	Non-haze	Haze	Non-haze	Haze	Non-haze	Haze	Non-haze	Haze	Non-haze	Haze	Non-haze
OC	7.79 ± 3.29	3.72 ± 0.74	9.11 ± 5.90	3.53 ± 2.34	5.12 ± 2.01	2.12 ± 2.05	2.79 ± 1.04	1.54 ± 1.02	4.64 ± 1.36	1.41 ± 0.89	3.07 ± 1.62	1.41 ± 0.66
EC	2.98 ± 1.64	1.03 ± 0.77	2.24 ± 1.69	0.85 ± 1.24	0.92 ± 0.47	0.31 ± 0.21	0.45 ± 0.16	0.32 ± 0.40	0.83 ± 0.38	0.42 ± 0.28	0.43 ± 0.12	0.17 ± 0.19
OC_{pri}	3.84 ± 2.11	1.33 ± 0.99	2.04 ± 1.54	0.77 ± 1.13	2.48 ± 1.28	0.00 ± 0.00	1.15 ± 0.40	0.00 ± 0.00	1.60 ± 0.73	0.80 ± 0.54	0.00 ± 0.00	0.00 ± 0.00
OC_{sec}	3.94 ± 2.48	2.39 ± 0.43	7.07 ± 5.46	2.76 ± 1.43	2.64 ± 1.84	2.12 ± 2.05	1.65 ± 1.03	1.54 ± 1.02	3.04 ± 1.46	0.61 ± 0.51	3.07 ± 1.62	1.41 ± 0.66
SOA	6.90 ± 3.50	3.83 ± 0.69	12.41 ± 8.14	4.41 ± 2.30	4.22 ± 2.94	3.39 ± 3.28	2.64 ± 1.65	2.46 ± 1.64	4.86 ± 2.34	0.98 ± 0.81	4.91 ± 2.59	2.26 ± 1.05

7.4 Conclusion

This study presented the size distributions of PM and its methanol-soluble fraction generated OP, and estimated their respiratory deposition during the haze and non-haze period in Ningbo. The results showed that the concentrations of PM and its related OP_v^{meth} were substantially higher during haze period (29.76-40.97μg m^{-3} and 0.40-2.43 nmol min^{-1} m^{-3}) than non-haze period (9.15-22.20 μg m^{-3} and 0.21-0.88 nmol min^{-1} m^{-3}) for all size ranges, and maximum centred in ultrafine mode for PM concentration and coarse-mode for OP_v^{meth}. The deposited doses of PM and their DTT oxidation in coarse- and accumulation-modes were highest in respective head and pulmonary regions during both periods. The OP_v^{meth} resided in coarse particles was driven by Acy and 1,2-NQ during haze period and Acy during non-haze period, implying the significance of road dust in the ROS generation and thus causing inflammation in head airway. Nap, BbF and Ind dominated the OP_v^{meth} of accumulation-mode PM in polluted days while Acy and Flt in clear days, elucidating the deposited toxicities resided in accumulation-mode particles was governed by the traffic exhausts from diesel and petrol engines. PM deposited in TB region was almost evenly distributed for three size mode, however, the deposited OP_v^{meth} level was highest in coarse mode during haze period and ultrafine mode during non-haze period. It can be attributed to the influence of traffic-related emissions on coarse PM and various sources on ultrafine particles.

Chapter 8 Conclusions and Future Work

8.1 Conclusions

A year-round field campaign was conducted in a coastal city of Ningbo, China, to study the driving factors of oxidative potential (OP) of fine particulates ($PM_{2.5}$) and 6-stage size-fractionated PM. Using dithiothreitol (DTT) cell-free assay, oxidative potential (OP) of water-soluble and methanol-soluble component of $PM_{2.5}$, represented as OP^{ws} and OP^{meth}, respectively, was measured.

There was a redistribution of source contributions to OP_v compared to $PM_{2.5}$ mass. The highest contributions to OP_v^{meth} were derived from CC and BB during winter, while IE contributed most to both OP_v^{ws} and OP_v^{meth} during spring. To the best of our knowledge, this is the first study to report the redox activity induced by SS aerosol. A significant contribution from SS aerosol to OP_v^{ws} was observed during winter, due to its higher content of Fe, predominantly from IE sources. More OP investigation might have to be conducted in the coastal cities of China to better understand the implications related to the toxicity of SS aerosols. There were non-linear increases between VE, FD derived OP_v and $PM_{2.5}$ concentration, which can be ascribed to the prominent synergistic and/or antagonistic interactions among VE and FD sources and their chemical components. In addition, it has been observed that the significantly different toxicities could occur to the PM of similar mass concentrations (in the range of 20 – 40 $\mu g\ m^{-3}$) due to their distinctly different chemical composition spectrums associated with varying emission sources. Therefore, the non-selective mitigation of PM2.5 emission sources may not have targeted the key sources that contain the highest (or higher) OP activities; the associated health risk may not be actually reduced. To decrease the $PM_{2.5}$ OP in

this region, the emissions of $PM_{2.5}$ and its redox active components should be jointly controlled so as to reduce the $PM_{2.5}$ oxidative stress. In particular, as IE exhibited higher intrinsic OP contributions to both OP_v^{ws} and OP_v^{meth} in Ningbo, and the VOCs released from IE source could also aggregate the oxidative stress of SS aerosols, a more stringent regulation and control actions of $PM_{2.5}$ and oxidative components emitted from industrial activities, as well as the Cl^- content in SS should be considered a priority to improve the population health in a coastal city like Ningbo. The methods and approaches developed and used in this study could be applicable in other regions to assess the discrepancy between $PM_{2.5}$ mass concentration and its oxidative potential in terms of inhalation toxicity so that more informed policies can be formulated for the mitigation of air pollution on local and regional scales.

Concentrations of PM and its related OP_v (OP_v^{ws}, OP_v^{meth}) were substantially higher during haze period (29.76-40.97μg m^{-3}, 0.50-3.22 nmol min^{-1} m^{-3}, 0.40-2.43 nmol min^{-1} m^{-3} for PM, OP_v^{ws} and OP_v^{meth}, respectively) than non-haze period (9.15-22.20 μg m^{-3}, 0.19-0.95 nmol min^{-1} m^{-3} and 0.21-0.88 nmol min^{-1} m^{-3}) for all size ranges. Both PM mass and OP_v^{ws} were maximum centred in ultrafine mode while OP_v^{meth} was highest in coarse mode. Ultrafine particles contributed increasingly to the OP_v^{ws} deposition when penetrating into deeper regions of the respiratory tract, from 1.22 nmol min^{-1} in head airway to 1.80 nmol min^{-1} in pulmonary region. In contrast, PM mass and OP_v^{meth} in coarse- and accumulation-modes deposited highest in respective head and pulmonary regions during both periods. The OP_v^{ws} resided in ultrafine particles was driven by SS and Cu, deposited mainly in pulmonary region in the two scenarios, implying the significance of SS aerosols, industrial activities and non-exhaust traffic emissions (road dust) in eliciting the ROS generation and thus causing pulmonary inflammation. However,

SNA and soluble transition metals of Fe and Cr dominated the OP_v^{ws} from coarse-mode particles, which had largest depositions in head airway during the two periods. It can be attributed to the influences of secondary aerosols, industry emissions and road dust. The OP_v^{meth} resided in coarse particles was driven by Acy and 1,2-NQ during haze period and Acy during non-haze period, implying the significance of road dust in the ROS generation and thus causing inflammation in head airway. Nap, BbF and Ind dominated the OP_v^{meth} of accumulation-mode PM in polluted days while Acy and Flt in clear days, elucidating the deposited toxicities resided in accumulation-mode particles was governed by the traffic exhausts from diesel and petrol engines. The deposited OP_v^{ws} in TB region had a combined contribution from ultrafine (SS, Cu) and coarse particles (SNA, Fe, Cr) in polluted days, while coarse-mode OP_v^{ws} (SNA, Fe, Cr) dominated the TB region in clean days. In contrast, PM deposited in TB region was almost evenly distributed for three size mode. However, the deposited OP_v^{meth} level was highest in coarse mode during haze period and ultrafine mode during non-haze period. The similar OP_v contributions between the two size modes during haze period were explained by the high redox activities of ultrafine particles for OP_v^{ws}, accumulation-mode particles for OP_v^{meth}, and high deposition efficiency of coarse-mode particles for both OP indicators. The PM in accumulation mode had less contribution to the deposited dose of OP_v^{ws}, compared to the other two size modes in different respiratory regions during haze and non-haze periods.

In summary, this work has achieved its objectives and provide new insight into the source contributions to $PM_{2.5}$ OP in coastal environment and the deposited doses of OP in different respiratory regions. These studies serve as a solid knowledge base for future work to further

the understanding of ambient aerosol toxicity, especially in coastal areas of China.

8.2 Future Work

Specific suggestions for future works include:

The measurements of particulate redox-active components are limited in this study, especially for organic components. A comprehensive measurement of organic catalytic oxidisers in ambient PM (e.g., hopanes, HULIS) should be investigated, which may provide different insight into the effects of chemical components and sources on aerosol OP. The gaseous pollutants are also relevant to DTT oxidation, including VOCs, alkenes, gas phase PAHs and the ROS of O_3, which were not fully investigated. A new field campaign should be designed to collect the gaseous pollutants and measure their capacities of ROS generation.

This study does not fully explore the synergistic and/or antagonistic effects of the PM components on overall OP. Further exploration regarding the synergistic and antagonistic effects on OP in ambient PM, the interactions between the water-soluble and methanol-soluble components, should be conducted to fully understand the ROS generation mechanisms among PM components. Since the particulate catalytic oxidisers have potentially non-linear contributions to PM OP increase, other statistical analysis (e.g., cluster analysis), rather than multiple linear regression analysis, which applied in this study, should be conducted to better elaborate the correlation between chemical components and PM-OP.

Other OP measurement, including AA assay, DCFH assay can be applied for analysing the same PM or gas samples to compare the sensitivity of redox active species among these assays, as this study is lack of other OP measurement to compare the results with DTT assay. Additionally, further environmental epidemiologic studies may be conducted to measure

personal exposure to $PM_{2.5}$ and respiratory health indicators (e.g., lung functions, oxidative stress), which allows the examination of whether OP is a better predictor of adverse respiratory outcomes and exploration of the underlying mechanisms.

Bibliography

Abrams, J. Y., Weber, R. J., Klein, M., Sarnat, S. E., Chang, H. H., Strickland, M. J., Verma, V., Fang, T., Bates, J. T., Mulholland, J. A., Russell, A. G. & Tolbert, P. E. 2017. Associations between Ambient Fine Particulate Oxidative Potential and Cardiorespiratory Emergency Department Visits. Environ Health Perspect, 125**,** 107008-107008. https://pubmed.ncbi.nlm.nih.gov/29084634

Al Hanai, A. H., Antkiewicz, D. S., Hemming, J. D. C., Shafer, M. M., Lai, A. M., Arhami, M., Hosseini, V. & Schauer, J. J. 2019. Seasonal variations in the oxidative stress and inflammatory potential of PM2.5 in Tehran using an alveolar macrophage model; The role of chemical composition and sources. Environment International, 123**,** 417-427. https://www.sciencedirect.com/science/article/pii/S0160412018320555.

Andrade, C., Molina, C., Sánchez, L. F., Manzano, C. A., R.Toro, A. & M.Leiva, G. 2020. Exploring the oxidative potential and respiratory deposition of size-segregated particulate matter at an urban site. Journal of South American Earth Sciences**,** 102957.

Andrade, C., Molina, C., Sánchez, L. F., Manzano, C. A., Toro A, R. & Leiva G, M. A. 2021. Exploring the oxidative potential and respiratory deposition of size-segregated particulate matter at an urban site. Journal of South American Earth Sciences, 105**,** 102957. https://www.sciencedirect.com/science/article/pii/S0895981120305009.

Bates, J. T., Fang, T., Verma, V., Zeng, L., Weber, R. J., Tolbert, P. E., Abrams, J. Y., Sarnat, S. E., Klein, M., Mulholland, J. A. & Russell, A. G. 2019a. Review of Acellular Assays of Ambient Particulate Matter Oxidative Potential: Methods and Relationships with Composition, Sources, and Health Effects. Environ Sci Technol, 53**,** 4003-4019.

Bates, J. T., Fang, T., Verma, V., Zeng, L., Weber, R. J., Tolbert, P. E., Abrams, J. Y., Sarnat, S. E., Klein, M., Mulholland, J. A. & Russell, A. G. 2019b. Review of Acellular Assays of Ambient Particulate Matter Oxidative Potential: Methods and Relationships with Composition, Sources, and Health Effects. Environmental Science & Technology, 53**,** 4003-4019. https://doi.org/10.1021/acs.est.8b03430.

Bates, J. T., Weber, R. J., Abrams, J., Verma, V., Fang, T., Klein, M., Strickland, M. J., Sarnat, S. E., Chang, H. H., Mulholland, J. A., Tolbert, P. E. & Russell, A. G. 2015. Reactive Oxygen Species Generation Linked to Sources of Atmospheric Particulate Matter and Cardiorespiratory Effects. Environ. Sci. Technol., 49**,** 13605.

Baulig, A., Garlatti, M., Bonvallot, V., Marchand, A., Barouki, R., Marano, F. & Baeza-Squiban, A. 2003. Involvement of reactive oxygen species in the metabolic pathways triggered by diesel exhaust particles in human airway epithelial cells. American Journal of Physiology-Lung Cellular and Molecular Physiology, 285**,** L671-L679. https://journals.physiology.org/doi/abs/10.1152/ajplung.00419.2002.

Behera, S. N., Cheng, J., Huang, X., Zhu, Q., Liu, P. & Balasubramanian, R. 2015. Chemical composition and acidity of size-fractionated inorganic aerosols of 2013-14 winter haze in Shanghai and associated health risk of toxic elements. Atmospheric Environment, 122**,** 259-271. http://www.sciencedirect.com/science/article/pii/S1352231015303952.

Bi, X., Dai, Q., Wu, J., Zhang, Q., Zhang, W., Luo, R., Cheng, Y., Zhang, J., Wang, L., Yu, Z., Zhang, Y., Tian, Y. & Feng, Y. 2019. Characteristics of the main primary source profiles of particulate matter across China from 1987 to 2017. Atmos. Chem. Phys., 19**,** 3223-3243. https://acp.copernicus.org/articles/19/3223/2019/.

Birmili, W., Allen, A. G., Bary, F. & Harrison, R. M. 2006. Trace Metal Concentrations and Water Solubility in Size-Fractionated Atmospheric Particles and Influence of Road Traffic. Environmental Science & Technology, 40**,** 1144-1153. https://doi.org/10.1021/es0486925.

Borlaza, L. J. S., Weber, S., Jaffrezo, J. L., Houdier, S., Slama, R., Rieux, C., Albinet, A., Micallef, S., Trébluchon, C. & Uzu, G. 2021. Disparities in particulate matter (PM10) origins and oxidative potential at a city-scale (Grenoble, France) – Part II: Sources of PM10 oxidative potential using multiple linear regression analysis and the predictive applicability of multilayer perceptron neural network analysis. Atmos. Chem. Phys. Discuss., 2021**,** 1-33. https://acp.copernicus.org/preprints/acp-2021-57/.

Bunce, N. J., Liu, L., Zhu, J. & Lane, D. A. 1997. Reaction of Naphthalene and Its Derivatives with Hydroxyl Radicals in the Gas Phase. Environmental Science & Technology, 31**,** 2252-2259. https://doi.org/10.1021/es960813g.

Cadenas, E., Hochstein, P. & Ernster, L. 1992. Pro- and antioxidant functions of quinones and quinone reductases in mammalian cells. Adv Enzymol Relat Areas Mol Biol, 65**,** 97-146.

Calderón-Garcidueñas, L., Franco-Lira, M., Henríquez-Roldán, C., Osnaya, N., González-Maciel, A., Reynoso-Robles, R., Villarreal-Calderon, R., Herritt, L., Brooks, D., Keefe, S., Palacios-Moreno, J., Villarreal-Calderon, R., Torres-Jardón, R., Medina-Cortina, H., Delgado-Chávez, R., Aiello-Mora, M., Maronpot, R. R. & Doty, R. L. 2010a. Urban air pollution: influences on olfactory function and pathology in exposed children and young adults. Exp Toxicol Pathol, 62**,** 91-102.

Calderón-Garcidueñas, L., Franco-Lira, M., Henríquez-Roldán, C., Osnaya, N., González-Maciel, A., Reynoso-Robles, R., Villarreal-Calderon, R., Herritt, L., Brooks, D., Keefe, S., Palacios-Moreno, J., Villarreal-Calderon, R., Torres-Jardón, R., Medina-Cortina, H., Delgado-Chávez, R., Aiello-Mora, M., Maronpot, R. R. & Doty, R. L. 2010b. Urban air pollution: Influences on olfactory function and pathology in exposed children and young adults. Experimental and Toxicologic Pathology, 62**,** 91-102. https://www.sciencedirect.com/science/article/pii/S0940299309001353.

Campbell, S. J., Wolfer, K., Utinger, B., Westwood, J., Zhang, Z. H., Bukowiecki, N., Steimer, S. S., Vu, T. V., Xu, J., Straw, N., Thomson, S., Elzein, A., Sun, Y., Liu, D., Li, L., Fu,

P., Lewis, A. C., Harrison, R. M., Bloss, W. J., Loh, M., Miller, M. R., Shi, Z. & Kalberer, M. 2021. Atmospheric conditions and composition that influence PM2.5 oxidative potential in Beijing, China. Atmos. Chem. Phys., 21**,** 5549-5573. https://acp.copernicus.org/articles/21/5549/2021/.

Cao, J. J., Shen, Z. X., Chow, J. C., Watson, J. G., Lee, S. C., Tie, X. X., Ho, K. F., Wang, G. H. & Han, Y. M. 2012. Winter and Summer PM2.5 Chemical Compositions in Fourteen Chinese Cities. Journal of the Air and Waste Management Association, 62**,** 1214-1226. https://www.scopus.com/inward/record.uri?eid=2-s2.0-84866769532&doi=10.1080%2f10962247.2012.701193&partnerID=40&md5=c0e0161dd65f4ab20c256c4d2b7cf663.

Cao, T., Li, M., Zou, C., Fan, X., Song, J., Jia, W., Yu, C., Yu, Z. & Peng, P. 2021a. Chemical composition, optical properties, and oxidative potential of water- and methanol-soluble organic compounds emitted from the combustion of biomass materials and coal. Atmos. Chem. Phys., 21**,** 13187-13205. https://acp.copernicus.org/articles/21/13187/2021/.

Cao, T., Li, M., Zou, C., Fan, X., Song, J., Jia, W., Yu, C., Yu, Z. & Peng, P. 2021b. Chemical composition, optical properties, and oxidative potential of water- and methanol-soluble organic compounds emitted from the combustion of biomass materials and coal. Atmos. Chem. Phys. Discuss., 2021**,** 1-47. https://acp.copernicus.org/preprints/acp-2021-159/.

Carslaw, D. C. & Beevers, S. D. 2013. Characterising and understanding emission sources using bivariate polar plots and k-means clustering. Environmental Modelling & Software, 40**,** 325-329. https://www.sciencedirect.com/science/article/pii/S136481521200237X.

Carslaw, D. C., Beevers, S. D., Ropkins, K. & Bell, M. C. 2006. Detecting and quantifying aircraft and other on-airport contributions to ambient nitrogen oxides in the vicinity of a large international airport. Atmospheric Environment, 40**,** 5424-5434. https://www.sciencedirect.com/science/article/pii/S1352231006004250.

Cave, M. R., Wragg, J., Beriro, D. J., Vane, C., Thomas, R., Riding, M. & Taylor, C. 2018. An overview of research and development themes in the measurement and occurrences of polyaromatic hydrocarbons in dusts and particulates. Journal of Hazardous Materials, 360**,** 373-390. https://www.sciencedirect.com/science/article/pii/S0304389418307167.

Cerro, J. C., Cerdà, V., Querol, X., Alastuey, A., Bujosa, C. & Pey, J. 2020. Variability of air pollutants, and PM composition and sources at a regional background site in the Balearic Islands: Review of western Mediterranean phenomenology from a 3-year study. Science of The Total Environment, 717**,** 137177. https://www.sciencedirect.com/science/article/pii/S0048969720306872.

Chan, A. W. H., Kautzman, K. E., Chhabra, P. S., Surratt, J. D., Chan, M. N., Crounse, J. D., Kürten, A., Wennberg, P. O., Flagan, R. C. & Seinfeld, J. H. 2009. Secondary organic aerosol formation from photooxidation of naphthalene and alkylnaphthalenes:

implications for oxidation of intermediate volatility organic compounds (IVOCs). Atmos. Chem. Phys., 9**,** 3049-3060. https://acp.copernicus.org/articles/9/3049/2009/.

Charrier, J. G. & Anastasio, C. 2011a. Impacts of Antioxidants on Hydroxyl Radical Production from Individual and Mixed Transition Metals in a Surrogate Lung Fluid. Atmos Environ (1994), 45**,** 7555-7562.

Charrier, J. G. & Anastasio, C. 2011b. Impacts of antioxidants on hydroxyl radical production from individual and mixed transition metals in a surrogate lung fluid. Atmos. Environ., 45**,** 7555.

Charrier, J. G. & Anastasio, C. 2012a. On dithiothreitol (DTT) as a measure of oxidative potential for ambient particles: evidence for the importance of soluble transition metals. Atmos Chem Phys, 12**,** 11317-11350.

Charrier, J. G. & Anastasio, C. 2012b. On dithiothreitol (DTT) as a measure of oxidative potential for ambient particles: evidence for the importance of soluble transition metals. Atmospheric Chemistry and Physics, 12**,** 9321-9333.

Charrier, J. G. & Anastasio, C. 2012c. On dithiothreitol (DTT) as a measure of oxidative potential for ambient particles: evidence for the importance of soluble transition metals. Atmos. Chem. Phys., 12**,** 9321.

Charrier, J. G. & Anastasio, C. 2015. Rates of Hydroxyl Radical Production from Transition Metals and Quinones in a Surrogate Lung Fluid. Environmental Science & Technology, 49**,** 9317-9325. https://doi.org/10.1021/acs.est.5b01606.

Charrier, J. G., McFall, A. S., Vu, K. K., Baroi, J., Olea, C., Hasson, A. & Anastasio, C. 2016a. A bias in the "mass-normalized" DTT response - an effect of non-linear concentration-response curves for copper and manganese. Atmos Environ (1994), 144**,** 325-334.

Charrier, J. G., McFall, A. S., Vu, K. K. T., Baroi, J., Olea, C., Hasson, A. & Anastasio, C. 2016b. A bias in the “mass-normalized” DTT response – An effect of non-linear concentration-response curves for copper and manganese. Atmospheric Environment, 144**,** 325-334. https://www.sciencedirect.com/science/article/pii/S1352231016306707.

Charrier, J. G., Richards-Henderson, N. K., Bein, K. J., McFall, A. S., Wexler, A. S. & Anastasio, C. 2015. Oxidant production from source-oriented particulate matter – Part 1: Oxidative potential using the dithiothreitol (DTT) assay. Atmos. Chem. Phys., 15**,** 2327-2340. https://acp.copernicus.org/articles/15/2327/2015/.

Chen, K., Metcalfe, S. E., Yu, H., Xu, J., Xu, H., Ji, D., Wang, C., Xiao, H. & He, J. 2021. Characteristics and source attribution of PM2.5 during 2016 G20 Summit in Hangzhou: Efficacy of radical measures to reduce source emissions. Journal of Environmental Sciences, 106**,** 47-65. https://www.sciencedirect.com/science/article/pii/S1001074221000139.

Cheng, Y., Ma, Y., Dong, B., Qiu, X. & Hu, D. 2020. Pollutants from primary sources dominate the oxidative potential of water-soluble PM2.5 in Hong Kong in terms of dithiothreitol (DTT) consumption and hydroxyl radical production. Journal of Hazardous Materials**,** 124218. http://www.sciencedirect.com/science/article/pii/S0304389420322081.

Cheng, Y., Ma, Y., Dong, B., Qiu, X. & Hu, D. 2021. Pollutants from primary sources dominate the oxidative potential of water-soluble PM2.5 in Hong Kong in terms of dithiothreitol (DTT) consumption and hydroxyl radical production. Journal of Hazardous Materials, 405**,** 124218. https://www.sciencedirect.com/science/article/pii/S0304389420322081.

Cheng, Z., Wang, S., Fu, X., Watson, J. G., Jiang, J., Fu, Q., Chen, C., Xu, B., Yu, J., Chow, J. C. & Hao, J. 2014. Impact of biomass burning on haze pollution in the Yangtze River delta, China: a case study in summer 2011. Atmos. Chem. Phys., 14**,** 4573-4585. https://acp.copernicus.org/articles/14/4573/2014/.

Chi, J. W., Li, W. J., Zhang, D. Z., Zhang, J. C., Lin, Y. T., Shen, X. J., Sun, J. Y., Chen, J. M., Zhang, X. Y., Zhang, Y. M. & Wang, W. X. 2015. Sea salt aerosols as a reactive surface for inorganic and organic acidic gases in the Arctic troposphere. Atmos. Chem. Phys., 15**,** 11341-11353. https://acp.copernicus.org/articles/15/11341/2015/.

Cho, A. K., Di Stefano, E., You, Y., Rodriguez, C. E., Schmitz, D. A., Kumagai, Y., Miguel, A. H., Eiguren-Fernandez, A., Kobayashi, T., Avol, E. & Froines, J. R. 2004. Determination of Four Quinones in Diesel Exhaust Particles, SRM 1649a, and Atmospheric PM2.5 Special Issue of Aerosol Science and Technology on Findings from the Fine Particulate Matter Supersites Program. Aerosol Science and Technology, 38**,** 68-81. https://doi.org/10.1080/02786820390229471.

Cho, A. K., Sioutas, C., Miguel, A. H., Kumagai, Y., Schmitz, D. A., Singh, M., Eiguren-Fernandez, A. & Froines, J. R. 2005. Redox activity of airborne particulate matter at different sites in the Los Angeles Basin. Environmental Research, 99**,** 40-47. http://www.sciencedirect.com/science/article/pii/S0013935105000058.

Chou, W. C., Hsu, C. Y., Ho, C. C., Hsieh, J. H., Chiang, H. C., Tsou, T. C., Chen, Y. C. & Lin, P. 2017. Development of an in Vitro-Based Risk Assessment Framework for Predicting Ambient Particulate Matter-Bound Polycyclic Aromatic Hydrocarbon-Activated Toxicity Pathways. Environ Sci Technol, 51**,** 14262-14272.

Chuang, H.-C., Jones, T. P., Lung, S.-C. C. & BéruBé, K. A. 2011. Soot-driven reactive oxygen species formation from incense burning. Sci Total Environ, 409**,** 4781-4787. http://europepmc.org/abstract/MED/21889784

Chung, C. Y., Yang, J., He, J., Yang, X., Hubbard, R. & Ji, D. 2021. An investigation into the impact of variations of ambient air pollution and meteorological factors on lung cancer mortality in Yangtze River Delta. Sci Total Environ, 779**,** 146427.

Conklin, M. H., Cass, G. R., Chu, L.-C. & Macias, E. S. 1981. Wintertime Carbonaceous Aerosols in Los Angeles: An Exploration of the Role of Elemental Carbon. In: MACIAS, E. S. & HOPKE, P. K. (eds.) Atmospheric aerosol: Source/Air Quality Relationships. Washington, DC: American Chemical Society.

Crilley, L. R., Lucarelli, F., Bloss, W. J., Harrison, R. M., Beddows, D. C., Calzolai, G., Nava, S., Valli, G., Bernardoni, V. & Vecchi, R. 2017. Source apportionment of fine and coarse particles at a roadside and urban background site in London during the 2012 summer ClearfLo campaign. Environmental Pollution, 220**,** 766-778. https://www.sciencedirect.com/science/article/pii/S0269749116304833.

Daellenbach, K. R., Uzu, G., Jiang, J., Cassagnes, L.-E., Leni, Z., Vlachou, A., Stefenelli, G., Canonaco, F., Weber, S., Segers, A., Kuenen, J. J. P., Schaap, M., Favez, O., Albinet, A., Aksoyoglu, S., Dommen, J., Baltensperger, U., Geiser, M., El Haddad, I., Jaffrezo, J.-L. & Prévôt, A. S. H. 2020. Sources of particulate-matter air pollution and its oxidative potential in Europe. Nature, 587**,** 414-419. https://doi.org/10.1038/s41586-020-2902-8.

De Jong, W. H., Hagens, W. I., Krystek, P., Burger, M. C., Sips, A. J. & Geertsma, R. E. 2008. Particle size-dependent organ distribution of gold nanoparticles after intravenous administration. Biomaterials, 29**,** 1912-9.

Delfino, R. J., Staimer, N., Tjoa, T., Gillen, D. L., Polidori, A., Arhami, M., Kleinman, M. T., Vaziri, N. D., Longhurst, J. & Sioutas, C. 2009. Air pollution exposures and circulating biomarkers of effect in a susceptible population: clues to potential causal component mixtures and mechanisms. Environ Health Perspect, 117**,** 1232-8.

Ding, X. X., Kong, L. D., Du, C. T., Zhanzakova, A., Fu, H. B., Tang, X. F., Wang, L., Yang, X., Chen, J. M. & Cheng, T. T. 2017. Characteristics of size-resolved atmospheric inorganic and carbonaceous aerosols in urban Shanghai. Atmospheric Environment, 167**,** 625-641. https://www.sciencedirect.com/science/article/pii/S1352231017305551.

DiStefano, E., Eiguren-Fernandez, A., Delfino, R. J., Sioutas, C., Froines, J. R. & Cho, A. K. 2009. Determination of metal-based hydroxyl radical generating capacity of ambient and diesel exhaust particles. Inhal Toxicol, 21**,** 731-8.

Dominici, F., Peng, R. D., Bell, M. L., Pham, L., McDermott, A., Zeger, S. L. & Samet, J. M. 2006. Fine particulate air pollution and hospital admission for cardiovascular and respiratory diseases. Jama, 295**,** 1127-34.

Dong, K., Hochman, G., Kong, X., Sun, R. & Wang, Z. 2019. Spatial econometric analysis of China's PM10 pollution and its influential factors: Evidence from the provincial level. Ecological Indicators, 96**,** 317-328. https://www.sciencedirect.com/science/article/pii/S1470160X18306897.

Dou, J., Lin, P., Kuang, B.-Y. & Yu, J. Z. 2015. Reactive Oxygen Species Production Mediated by Humic-like Substances in Atmospheric Aerosols: Enhancement Effects by Pyridine, Imidazole, and Their Derivatives. Environmental Science & Technology, 49**,** 6457-6465. https://doi.org/10.1021/es5059378.

Draxler, R. R. & Rolph, G. D. 2013. HYSPLIT (Hybrid Single-Particle Lagrangian Integrated Trajectory) model access via NOAA ARL READY [Online]. College Park: NOAA Air Resources Laboratory. Available: http://www.arl.noaa.gov/HYSPLIT.php. [Accessed].

DRI 2005. DRI Model 2001 Thermal/Optical Carbon Analysis (TOR/TOT) of Aerosol Filter Samples - Method IMPROVE_A. In: DESERT RESEARCH INSTITUTION, D. O. A. S. (ed.). 2215 Raggio Parkway Reno, NV 89506.

Falcon-Rodriguez, C. I., Osornio-Vargas, A. R., Sada-Ovalle, I. & Segura-Medina, P. 2016. Aeroparticles, Composition, and Lung Diseases. Front Immunol, 7**,** 3.

Fang, T., Guo, H., Verma, V., Peltier, R. E. & Weber, R. J. 2015. PM_{2.5} water-soluble elements in the southeastern United States: automated analytical method development, spatiotemporal distributions, source apportionment, and implications for heath studies. Atmos. Chem. Phys., 15**,** 11667-11682. https://acp.copernicus.org/articles/15/11667/2015/.

Fang, T., Guo, H., Zeng, L., Verma, V., Nenes, A. & Weber, R. J. 2017a. Highly Acidic Ambient Particles, Soluble Metals, and Oxidative Potential: A Link between Sulfate and Aerosol Toxicity. Environmental Science & Technology, 51**,** 2611-2620. https://doi.org/10.1021/acs.est.6b06151.

Fang, T., Lakey, P. S. J., Weber, R. J. & Shiraiwa, M. 2019. Oxidative Potential of Particulate Matter and Generation of Reactive Oxygen Species in Epithelial Lining Fluid. Environmental Science & Technology, 53**,** 12784-12792. https://doi.org/10.1021/acs.est.9b03823.

Fang, T., Verma, V., Bates, J. T., Abrams, J., Klein, M., Strickland, M. J., Sarnat, S. E., Chang, H. H., Mulholland, J. A., Tolbert, P. E., Russell, A. G. & Weber, R. J. 2016. Oxidative potential of ambient water-soluble PM2.5 in the southeastern United States: contrasts in sources and health associations between ascorbic acid (AA) and dithiothreitol (DTT) assays. Atmos. Chem. Phys., 16**,** 3865-3879. https://acp.copernicus.org/articles/16/3865/2016/.

Fang, T., Verma, V., Guo, H., King, L. E., Edgerton, E. S. & Weber, R. J. 2014. A semi-Automated system for quantifying the oxidative potential of ambient particles in aqueous extracts using the dithiothreitol (DTT) assay: Results from the Southeastern Center for Air Pollution and Epidemiology (SCAPE). Atmos. Meas. Tech. Discuss., 7**,** 7245-7279.

Fang, T., Zeng, L., Gao, D., Verma, V., Stefaniak, A. B. & Weber, R. J. 2017b. Ambient Size Distributions and Lung Deposition of Aerosol Dithiothreitol-Measured Oxidative Potential: Contrast between Soluble and Insoluble Particles. Environmental Science & Technology, 51**,** 6802-6811. https://doi.org/10.1021/acs.est.7b01536.

Gao, D., Fang, T., Verma, V., Zeng, L. & Weber, R. J. 2017. A method for measuring total aerosol oxidative potential (OP) with the dithiothreitol (DTT) assay and comparisons between an urban and roadside site of water-soluble and total OP. Atmos. Meas. Tech., 10**,** 2821-2835. https://amt.copernicus.org/articles/10/2821/2017/.

Gao, D., Godri Pollitt, K. J., Mulholland, J. A., Russell, A. G. & Weber, R. J. 2020a. Characterization and comparison of PM2.5 oxidative potential assessed by two acellular assays. Atmos. Chem. Phys., 20**,** 5197-5210. https://acp.copernicus.org/articles/20/5197/2020/.

Gao, D., Mulholland, J. A., Russell, A. G. & Weber, R. J. 2020b. Characterization of water-insoluble oxidative potential of PM2.5 using the dithiothreitol assay. Atmospheric Environment, 224**,** 117327. http://www.sciencedirect.com/science/article/pii/S1352231020300686.

Gao, D., Ripley, S., Weichenthal, S. & Pollitt, K. G. G. 2020c. Ambient particulate matter oxidative potential: Chemical determinants, associated health effects, and strategies for risk management. Free radical biology & medicine.

Gasser, M., Riediker, M., Mueller, L., Perrenoud, A., Blank, F., Gehr, P. & Rothen-Rutishauser, B. 2009. Toxic effects of brake wear particles on epithelial lung cells in vitro. Part Fibre Toxicol, 6**,** 30-30. https://pubmed.ncbi.nlm.nih.gov/19930544

Guo, H.-b., Li, M., Lyu, Y., Cheng, T.-t., Xv, J. j. & Li, X. 2019. Size-resolved particle oxidative potential in the office, laboratory, and home: Evidence for the importance of water-soluble transition metals. Environmental Pollution, 246**,** 704-709. https://www.sciencedirect.com/science/article/pii/S0269749118338855.

Guo, H., Fu, H., Jin, L., Huang, S. & Li, X. 2020. Quantification of synergistic, additive and antagonistic effects of aerosol components on total oxidative potential. Chemosphere, 252**,** 126573. https://www.sciencedirect.com/science/article/pii/S0045653520307669.

Guo, Y., Yan, C., Li, C., Ma, W., Feng, Z., Zhou, Y., Lin, Z., Dada, L., Stolzenburg, D., Yin, R., Kontkanen, J., Daellenbach, K. R., Kangasluoma, J., Yao, L., Chu, B., Wang, Y., Cai, R., Bianchi, F., Liu, Y. & Kulmala, M. 2021. Formation of nighttime sulfuric acid from the ozonolysis of alkenes in Beijing. Atmos. Chem. Phys., 21**,** 5499-5511. https://acp.copernicus.org/articles/21/5499/2021/.

HaMai, D. & Bondy, S. C. 2004. Pro- or anti-oxidant manganese: a suggested mechanism for reconciliation. Neurochemistry International, 44**,** 223-229. https://www.sciencedirect.com/science/article/pii/S0197018603001529.

Han, X. & Naeher, L. P. 2006. A review of traffic-related air pollution exposure assessment studies in the developing world. Environment International, 32**,** 106-120. https://www.sciencedirect.com/science/article/pii/S0160412005000905.

He, L., Norris, C., Cui, X., Li, Z., Barkjohn, K. K., Brehmer, C., Teng, Y., Fang, L., Lin, L., Wang, Q., Zhou, X., Hong, J., Li, F., Zhang, Y., Schauer, J. J., Black, M., Bergin, M. H. & Zhang, J. J. 2021. Personal Exposure to PM2.5 Oxidative Potential in Association with Pulmonary Pathophysiologic Outcomes in Children with Asthma. Environmental Science & Technology, 55**,** 3101-3111. https://doi.org/10.1021/acs.est.0c06114.

He, Q., Geng, F., Li, C., Yang, S., Wang, Y., Mu, H., Zhou, G., Liu, X., Gao, W., Cheng, T. & Wu, Z. 2018. Long-term characteristics of satellite-based PM2.5 over East China. Science of The Total Environment, 612**,** 1417-1423. http://www.sciencedirect.com/science/article/pii/S0048969717323690.

Hedayat, F., Stevanovic, S., Miljevic, B., Bottle, S. & Ristovski, Z. D. 2015. Review – Evaluating the molecular assays for measuring the oxidative potential of particulate matter. Chemical Industry and Chemical Engineering Quarterly, 21**,** 201-210. https://www.scopus.com/inward/record.uri?eid=2-s2.0-84928944611&doi=10.2298%2fCICEQ140228031H&partnerID=40&md5=6597365b6b0106f591b7ca5e907d9ec8.

Hellack, B., Yang, A., Cassee, F. R., Janssen, N. A. H., Schins, R. P. F. & Kuhlbusch, T. A. J. 2014. Intrinsic hydroxyl radical generation measurements directly from sampled filters as a metric for the oxidative potential of ambient particulate matter. Journal of Aerosol Science, 72**,** 47-55. https://www.sciencedirect.com/science/article/pii/S0021850214000391.

Henry, T. R. & Wallace, K. B. 1996. Differential mechanisms of cell killing by redox cycling and arylating quinones. Arch Toxicol, 70**,** 482-9.

Hetland, R. B., Cassee, F. R., Refsnes, M., Schwarze, P. E., Låg, M., Boere, A. J. & Dybing, E. 2004. Release of inflammatory cytokines, cell toxicity and apoptosis in epithelial lung cells after exposure to ambient air particles of different size fractions. Toxicol In Vitro, 18**,** 203-12.

Hoek, G., Krishnan, R. M., Beelen, R., Peters, A., Ostro, B., Brunekreef, B. & Kaufman, J. D. 2013. Long-term air pollution exposure and cardio- respiratory mortality: a review. Environmental Health, 12**,** 43. https://doi.org/10.1186/1476-069X-12-43.

Holmén, B. A., Rukavina, B., Kasumba, J. & Fukagawa, N. K. 2017. Reactive Oxidative Species and Speciated Particulate Light-Duty Engine Emissions from Diesel and Biodiesel Fuel Blends. Energy & Fuels, 31**,** 8171-8180.

Hsu, S. C., Liu, S. C., Tsai, F., Engling, G., Lin, I. I., Chou, C. K. C., Kao, S. J., Lung, S. C. C., Chan, C. Y., Lin, S. C., Huang, J. C., Chi, K. H., Chen, W. N., Lin, F. J., Huang, C.

H., Kuo, C. L., Wu, T. C. & Huang, Y. T. 2010. High wintertime particulate matter pollution over an offshore island (Kinmen) off southeastern China: An overview. Journal of Geophysical Research: Atmospheres, 115. https://agupubs.onlinelibrary.wiley.com/doi/abs/10.1029/2009JD013641.

Huang, M. F., Lin, W. L. & Ma, Y. C. 2005. A study of reactive oxygen species in mainstream of cigarette. Indoor Air, 15**,** 135-40.

Hussein, T., Löndahl, J., Paasonen, P., Koivisto, A. J., Petäjä, T., Hämeri, K. & Kulmala, M. 2013. Modeling regional deposited dose of submicron aerosol particles. Science of The Total Environment, 458-460**,** 140-149. https://www.sciencedirect.com/science/article/pii/S0048969713004439.

Ji, D., Cui, Y., Li, L., He, J., Wang, L., Zhang, H., Wang, W., Zhou, L., Maenhaut, W., Wen, T. & Wang, Y. 2018. Characterization and source identification of fine particulate matter in urban Beijing during the 2015 Spring Festival. Science of the Total Environment, 628-629**,** 430-440. https://www.scopus.com/inward/record.uri?eid=2-s2.0-85042118903&doi=10.1016%2fj.scitotenv.2018.01.304&partnerID=40&md5=cff37dc41c2c5b7023aeccb714132887.

Ji, Y., Li, Q., Ye, R., Tian, K. & Tian, X. 2020. The Impact of Water-Soluble Inorganic Ions in Particulate Matter (PM2.5) on Litter Decomposition in Chinese Subtropical Forests. Forests, 11**,** 238. https://www.mdpi.com/1999-4907/11/2/238.

Jiang, H. & Jang, M. 2018. Dynamic Oxidative Potential of Atmospheric Organic Aerosol under Ambient Sunlight. Environmental Science & Technology, 52**,** 7496-7504. https://doi.org/10.1021/acs.est.8b00148.

Jin, L., Xie, J., Wong, C. K. C., Chan, S. K. Y., Abbaszade, G., Schnelle-Kreis, J., Zimmermann, R., Li, J., Zhang, G., Fu, P. & Li, X. 2019a. Contributions of City-Specific Fine Particulate Matter (PM2.5) to Differential In Vitro Oxidative Stress and Toxicity Implications between Beijing and Guangzhou of China. Environmental Science & Technology, 53**,** 2881-2891. https://doi.org/10.1021/acs.est.9b00449.

Jin, L., Xie, J., Wong, C. K. C., Chan, S. K. Y., Abbaszade, G., Schnelle-Kreis, J., Zimmermann, R., Li, J., Zhang, G., Fu, P. & Li, X. 2019b. Contributions of City-Specific Fine Particulate Matter (PM(2.5)) to Differential In Vitro Oxidative Stress and Toxicity Implications between Beijing and Guangzhou of China. Environ Sci Technol, 53**,** 2881-2891.

Kachur, A. V., Held, K. D., Koch, C. J. & Biaglow, J. E. 1997. Mechanism of production of hydroxyl radicals in the copper-catalyzed oxidation of dithiothreitol. Radiat Res, 147**,** 409-15.

Khachatryan, L., Vejerano, E., Lomnicki, S. & Dellinger, B. 2011. Environmentally Persistent Free Radicals (EPFRs). 1. Generation of Reactive Oxygen Species in Aqueous Solutions. Environmental Science & Technology, 45**,** 8559-8566. https://doi.org/10.1021/es201309c.

Khan, N., Shen, J., Chang, T. Y., Chang, C. C., Fung, P. C. W., Grinberg, O., Demidenko, E. & Swartz, H. 2003. Plasma Membrane Cholesterol: A Possible Barrier to Intracellular Oxygen in Normal and Mutant CHO Cells Defective in Cholesterol Metabolism. Biochemistry, 42**,** 23-29. https://doi.org/10.1021/bi026039t.

Kim, K.-H., Jahan, S. A. & Kabir, E. 2011. A review of diseases associated with household air pollution due to the use of biomass fuels. Journal of Hazardous Materials, 192**,** 425-431. https://www.sciencedirect.com/science/article/pii/S0304389411007424.

Kodros, J. K., Volckens, J., Jathar, S. H. & Pierce, J. R. 2018. Ambient Particulate Matter Size Distributions Drive Regional and Global Variability in Particle Deposition in the Respiratory Tract. GeoHealth, 2**,** 298-312. https://agupubs.onlinelibrary.wiley.com/doi/abs/10.1029/2018GH000145.

Koutrakis, P., Thompson, K. M., Wolfson, J. M., Spengler, J. D., Keeler, G. J. & Slater, J. L. 1992. Determination of aerosol strong acidity losses due to interactions of collected particles: Results from laboratory and field studies. Atmospheric Environment. Part A. General Topics, 26**,** 987-995. https://www.sciencedirect.com/science/article/pii/096016869290030O.

Koutrakis, P., Wolfson, J. M. & Spengler, J. 1988. An improved method for measuring aerosol strong acidity: Results from a nine-month study in St Louis, Missouri and Kingston, Tennessee. Atmospheric Environment, 22**,** 157-162.

Kramer, A. L., Dorn, S., Perez, A., Roper, C., Titaley, I. A., Cayton, K., Cook, R. P., Cheong, P. H. Y. & Massey Simonich, S. L. 2021. Assessing the oxidative potential of PAHs in ambient PM2.5 using the DTT consumption assay. Environmental Pollution, 285**,** 117411. https://www.sciencedirect.com/science/article/pii/S0269749121009933.

Kumagai, Y., Arimoto, T., Shinyashiki, M., Shimojo, N., Nakai, Y., Yoshikawa, T. & Sagai, M. 1997. Generation of reactive oxygen species during interaction of diesel exhaust particle components with NADPH-cytochrome P450 reductase and involvement of the bioactivation in the DNA damage. Free Radic Biol Med, 22**,** 479-87.

Kumar, P., Morawska, L., Birmili, W., Paasonen, P., Hu, M., Kulmala, M., Harrison, R. M., Norford, L. & Britter, R. 2014. Ultrafine particles in cities. Environment International, 66**,** 1-10. https://www.sciencedirect.com/science/article/pii/S016041201400018X.

Layshock, J. A., Wilson, G. & Anderson, K. A. 2010. Ketone and quinone-substituted polycyclic aromatic hydrocarbons in mussel tissue, sediment, urban dust, and diesel

particulate matrices. Environ Toxicol Chem, 29, 2450-2460. https://pubmed.ncbi.nlm.nih.gov/20830751

Li, J., Li, J., Wang, G., Ho, K. F., Dai, W., Zhang, T., Wang, Q., Wu, C., Li, L., Li, L. & Zhang, Q. 2021. Effects of atmospheric aging processes on in vitro induced oxidative stress and chemical composition of biomass burning aerosols. Journal of Hazardous Materials, 401, 123750. https://www.sciencedirect.com/science/article/pii/S0304389420317398.

Li, J., Li, J., Wang, G., Zhang, T., Dai, W., Ho, K. F., Wang, Q., Shao, Y., Wu, C. & Li, L. 2020. Molecular characteristics of organic compositions in fresh and aged biomass burning aerosols. Science of The Total Environment, 741, 140247. https://www.sciencedirect.com/science/article/pii/S0048969720337682.

Li, M., Hu, M., Guo, Q., Tan, T., Du, B., Huang, X., He, L., Guo, S., Wang, W., Fan, Y. & Xu, D. 2018. Seasonal Source Apportionment of PM2.5 in Ningbo, a Coastal City in Southeast China. Aerosol and Air Quality Research, 18, 2741-2752. http://dx.doi.org/10.4209/aaqr.2018.01.0011.

Li, N., Sioutas, C., Cho, A., Schmitz, D., Misra, C., Sempf, J., Wang, M., Oberley, T., Froines, J. & Nel, A. 2003. Ultrafine particulate pollutants induce oxidative stress and mitochondrial damage. Environ Health Perspect, 111, 455-60.

Li, X. Y., Hao, L., Liu, Y. H., Chen, C. Y., Pai, V. J. & Kang, J. X. 2017. Protection against fine particle-induced pulmonary and systemic inflammation by omega-3 polyunsaturated fatty acids. Biochim Biophys Acta Gen Subj, 1861, 577-584.

Li, Y., Zhu, T., Zhao, J. & Xu, B. 2012. Interactive Enhancements of Ascorbic Acid and Iron in Hydroxyl Radical Generation in Quinone Redox Cycling. Environmental Science & Technology, 46, 10302-10309. https://doi.org/10.1021/es301834r.

Lin, M. & Yu, J. Z. 2020. Assessment of Interactions between Transition Metals and Atmospheric Organics: Ascorbic Acid Depletion and Hydroxyl Radical Formation in Organic-Metal Mixtures. Environmental Science & Technology, 54, 1431-1442. https://doi.org/10.1021/acs.est.9b07478.

Lin, M. & Yu, J. Z. 2021. Assessment of oxidative potential by hydrophilic and hydrophobic fractions of water-soluble PM2.5 and their mixture effects. Environmental Pollution, 275, 116616. https://www.sciencedirect.com/science/article/pii/S0269749121001949.

Liu, M., Guo, W., Zhao, L., Yang, H., Fang, Q., Li, M., Shu, J., Chen, S., Lai, X., Yang, L. & Zhang, X. 2021a. Association of personal fine particulate matter and its respiratory tract depositions with blood pressure in children: From two panel studies. J Hazard Mater, 416, 126120.

Liu, M., Guo, W., Zhao, L., Yang, H., Fang, Q., Li, M., Shu, J., Chen, S., Lai, X., Yang, L. & Zhang, X. 2021b. Association of personal fine particulate matter and its respiratory tract

depositions with blood pressure in children: From two panel studies. Journal of Hazardous Materials, 416, 126120. https://www.sciencedirect.com/science/article/pii/S0304389421010840.

Liu, Q., Baumgartner, J., Zhang, Y., Liu, Y., Sun, Y. & Zhang, M. 2014a. Oxidative Potential and Inflammatory Impacts of Source Apportioned Ambient Air Pollution in Beijing. Environmental Science & Technology, 48, 12920-12929. https://doi.org/10.1021/es5029876.

Liu, Q., Lu, Z., Xiong, Y., Huang, F., Zhou, J. & Schauer, J. J. 2020a. Oxidative potential of ambient PM(2.5) in Wuhan and its comparisons with eight areas of China. Sci Total Environ, 701, 134844.

Liu, Q., Zhang, Y., Liu, Y. & Zhang, M. 2014b. Characterization of springtime airborne particulate matter-bound reactive oxygen species in Beijing. Environ Sci Pollut Res Int, 21, 9325-33.

Liu, W., Xu, Y., Liu, W., Liu, Q., Yu, S., Liu, Y., Wang, X. & Tao, S. 2018a. Oxidative potential of ambient PM2.5 in the coastal cities of the Bohai Sea, northern China: Seasonal variation and source apportionment. Environmental Pollution, 236, 514-528. https://www.sciencedirect.com/science/article/pii/S0269749117339210.

Liu, W., Xu, Y., Liu, W., Liu, Q., Yu, S., Liu, Y., Wang, X. & Tao, S. 2018b. Oxidative potential of ambient PM(2.5) in the coastal cities of the Bohai Sea, northern China: Seasonal variation and source apportionment. Environ Pollut, 236, 514-528.

Liu, X., Wang, J., Zhou, M., Dai, Q. y., Wang, Q. g., Li, H. & Qian, X. 2020b. Particulate matter exposure disturbs inflammatory cytokine homeostasis associated with changes in trace metal levels in mouse organs. Science of The Total Environment, 727, 138377. https://www.sciencedirect.com/science/article/pii/S0048969720318908.

Liu, Y., Xing, J., Wang, S., Fu, X. & Zheng, H. 2018c. Source-specific speciation profiles of PM2.5 for heavy metals and their anthropogenic emissions in China. Environmental Pollution, 239, 544-553. https://www.sciencedirect.com/science/article/pii/S0269749118300526.

Longo, A. F., Vine, D. J., King, L. E., Oakes, M., Weber, R. J., Huey, L. G., Russell, A. G. & Ingall, E. D. 2016. Composition and oxidation state of sulfur in atmospheric particulate matter. Atmos. Chem. Phys., 16, 13389-13398. https://acp.copernicus.org/articles/16/13389/2016/.

Lough, G. C., Schauer, J. J., Park, J.-S., Shafer, M. M., DeMinter, J. T. & Weinstein, J. P. 2005. Emissions of Metals Associated with Motor Vehicle Roadways. Environmental Science & Technology, 39, 826-836. https://doi.org/10.1021/es048715f.

Lyu, Y., Guo, H., Cheng, T. & Li, X. 2018. Particle Size Distributions of Oxidative Potential of Lung-Deposited Particles: Assessing Contributions from Quinones and Water-Soluble Metals. Environmental Science & Technology, 52**,** 6592-6600. https://doi.org/10.1021/acs.est.7b06686.

Ma, M., Ma, X., Cai, W. & Cai, W. 2020. Low carbon roadmap of residential building sector in China: Historical mitigation and prospective peak. Applied Energy, 273**,** 115247. https://www.sciencedirect.com/science/article/pii/S0306261920307595.

Maertens, R. M., Bailey, J. & White, P. A. 2004. The mutagenic hazards of settled house dust: a review. Mutation Research/Reviews in Mutation Research, 567**,** 401-425. https://www.sciencedirect.com/science/article/pii/S1383574204000614.

Maher, B. A., Ahmed, I. A. M., Karloukovski, V., MacLaren, D. A., Foulds, P. G., Allsop, D., Mann, D. M. A., Torres-Jardón, R. & Calderon-Garciduenas, L. 2016. Magnetite pollution nanoparticles in the human brain. Proceedings of the National Academy of Sciences, 113**,** 10797. http://www.pnas.org/content/113/39/10797.abstract.

Mattioli, G. A., Rosa, D. E., Turic, E., Testa, J. A., Lizarraga, R. M. & Fazzio, L. E. 2019. Effect of Injectable Copper and Zinc Supplementation on Weight, Hematological Parameters, and Immune Response in Pre-weaning Beef Calves. Biol Trace Elem Res, 189**,** 456-462.

McWhinney, R. D., Zhou, S. & Abbatt, J. P. D. 2013. Naphthalene SOA: redox activity and naphthoquinone gas–particle partitioning. Atmos. Chem. Phys., 13**,** 9731-9744. https://acp.copernicus.org/articles/13/9731/2013/.

Miljevic, B., Fairfull-Smith, K. E., Bottle, S. E. & Ristovski, Z. D. 2010a. The application of profluorescent nitroxides to detect reactive oxygen species derived from combustion-generated particulate matter: Cigarette smoke – A case study. Atmospheric Environment, 44**,** 2224-2230. https://www.sciencedirect.com/science/article/pii/S1352231010001822.

Miljevic, B., Heringa, M. F., Keller, A., Meyer, N. K., Good, J., Lauber, A., DeCarlo, P. F., Fairfull-Smith, K. E., Nussbaumer, T., Burtscher, H., Prevot, A. S. H., Baltensperger, U., Bottle, S. E. & Ristovski, Z. D. 2010b. Oxidative Potential of Logwood and Pellet Burning Particles Assessed by a Novel Profluorescent Nitroxide Probe. Environmental Science & Technology, 44**,** 6601-6607. https://doi.org/10.1021/es100963y.

Moldanová, J., Fridell, E., Popovicheva, O., Demirdjian, B., Tishkova, V., Faccinetto, A. & Focsa, C. 2009. Characterisation of particulate matter and gaseous emissions from a large ship diesel engine. Atmospheric Environment, 43**,** 2632-2641. https://www.sciencedirect.com/science/article/pii/S1352231009001253.

Moufarrej, L., Courcot, D. & Ledoux, F. 2020. Assessment of the PM2.5 oxidative potential in a coastal industrial city in Northern France: Relationships with chemical composition,

local emissions and long range sources. Science of The Total Environment, 748, 141448. https://www.sciencedirect.com/science/article/pii/S0048969720349779.

Osornio-Vargas, A. R., Serrano, J., Rojas-Bracho, L., Miranda, J., García-Cuellar, C., Reyna, M. A., Flores, G., Zuk, M., Quintero, M., Vázquez, I., Sánchez-Pérez, Y., López, T. & Rosas, I. 2011a. In vitro biological effects of airborne PM2.5 and PM10 from a semi-desert city on the Mexico–US border. Chemosphere, 83, 618-626. https://www.sciencedirect.com/science/article/pii/S0045653510013810.

Osornio-Vargas, A. R., Serrano, J., Rojas-Bracho, L., Miranda, J., García-Cuellar, C., Reyna, M. A., Flores, G., Zuk, M., Quintero, M., Vázquez, I., Sánchez-Pérez, Y., López, T. & Rosas, I. 2011b. In vitro biological effects of airborne $PM_{2.5}$ and PM_{10} from a semi-desert city on the Mexico-US border. Chemosphere, 83, 618-26.

Osthoff, H. D., Roberts, J. M., Ravishankara, A. R., Williams, E. J., Lerner, B. M., Sommariva, R., Bates, T. S., Coffman, D., Quinn, P. K., Dibb, J. E., Stark, H., Burkholder, J. B., Talukdar, R. K., Meagher, J., Fehsenfeld, F. C. & Brown, S. S. 2008. High levels of nitryl chloride in the polluted subtropical marine boundary layer. Nature Geoscience, 1, 324-328. https://doi.org/10.1038/ngeo177.

Paciolla, M. D., Kolla, S. & Jansen, S. A. 2002. The reduction of dissolved iron species by humic acid and subsequent production of reactive oxygen species. Advances in Environmental Research, 7, 169-178. https://www.sciencedirect.com/science/article/pii/S1093019101001290.

Paris, R. & Desboeufs, K. V. 2013. Effect of atmospheric organic complexation on iron-bearing dust solubility. Atmos. Chem. Phys., 13, 4895-4905. https://acp.copernicus.org/articles/13/4895/2013/.

Patel, A. & Rastogi, N. 2018. Oxidative potential of ambient fine aerosol over a semi-urban site in the Indo-Gangetic Plain. Atmospheric Environment, 175, 127-134. https://www.sciencedirect.com/science/article/pii/S1352231017308282.

Pei, J., Wang, Y. & Yu, K. 2018. Sensitive Determination of Quinones by High-Performance Liquid Chromatography-Electrospray Ionization-Tandem Mass Spectrometry with Methanol Derivatization. Anal Sci, 34, 335-340.

Peng, N., Li, Y., Liu, Z., Liu, T. & Gai, C. 2016. Emission, distribution and toxicity of polycyclic aromatic hydrocarbons (PAHs) during municipal solid waste (MSW) and coal co-combustion. Science of The Total Environment, 565, 1201-1207. https://www.sciencedirect.com/science/article/pii/S0048969716311263.

Pope, C. A., 3rd, Burnett, R. T., Thurston, G. D., Thun, M. J., Calle, E. E., Krewski, D. & Godleski, J. J. 2004. Cardiovascular mortality and long-term exposure to particulate air pollution: epidemiological evidence of general pathophysiological pathways of disease. Circulation, 109, 71-7.

Pöschl, U. & Shiraiwa, M. 2015. Multiphase chemistry at the atmosphere-biosphere interface influencing climate and public health in the anthropocene. Chem Rev, 115**,** 4440-75.

Prahalad, A. K., Inmon, J., Dailey, L. A., Madden, M. C., Ghio, A. J. & Gallagher, J. E. 2001. Air Pollution Particles Mediated Oxidative DNA Base Damage in a Cell Free System and in Human Airway Epithelial Cells in Relation to Particulate Metal Content and Bioreactivity. Chemical Research in Toxicology, 14**,** 879-887. https://doi.org/10.1021/tx010022e.

Quitério, S. L., Silva, C. R. S. d., Arbilla, G. & Escaleira, V. 2004. Metals in airborne particulate matter in the industrial district of Santa Cruz, Rio de Janeiro, in an annual period. Atmospheric Environment, 38**,** 321-331.

Saffari, A., Daher, N., Shafer, M. M., Schauer, J. J. & Sioutas, C. 2014a. Seasonal and spatial variation in dithiothreitol (DTT) activity of quasi-ultrafine particles in the Los Angeles Basin and its association with chemical species. Journal of Environmental Science and Health, Part A, 49**,** 441-451. https://doi.org/10.1080/10934529.2014.854677.

Saffari, A., Daher, N., Shafer, M. M., Schauer, J. J. & Sioutas, C. 2014b. Seasonal and spatial variation in dithiothreitol (DTT) activity of quasi-ultrafine particles in the Los Angeles Basin and its association with chemical species. Journal of environmental science and health. Part A, Toxic/hazardous substances & environmental engineering, 49**,** 441-51.

Schmid, O. & Cassee, F. R. 2017. On the pivotal role of dose for particle toxicology and risk assessment: exposure is a poor surrogate for delivered dose. Part Fibre Toxicol, 14**,** 52-52. https://pubmed.ncbi.nlm.nih.gov/29216928

Schoonen, M. A. A., Cohn, C. A., Roemer, E., Laffers, R., Simon, S. R. & O'Riordan, T. 2006. Mineral-Induced Formation of Reactive Oxygen Species. Reviews in Mineralogy and Geochemistry, 64**,** 179-221. https://doi.org/10.2138/rmg.2006.64.7.

Secrest, M. H., Schauer, J. J., Carter, E. M., Lai, A. M., Wang, Y., Shan, M., Yang, X., Zhang, Y. & Baumgartner, J. 2016. The oxidative potential of PM2.5 exposures from indoor and outdoor sources in rural China. Science of The Total Environment, 571**,** 1477-1489. https://www.sciencedirect.com/science/article/pii/S0048969716314206.

Shahpoury, P., Zhang, Z. W., Arangio, A., Celo, V., Dabek-Zlotorzynska, E., Harner, T. & Nenes, A. 2021. The influence of chemical composition, aerosol acidity, and metal dissolution on the oxidative potential of fine particulate matter and redox potential of the lung lining fluid. Environment International, 148**,** 106343. https://www.sciencedirect.com/science/article/pii/S0160412020322984.

Shang, Y., Chen, C., Li, Y., Zhao, J. & Zhu, T. 2012. Hydroxyl Radical Generation Mechanism During the Redox Cycling Process of 1,4-Naphthoquinone. Environmental Science & Technology, 46**,** 2935-2942. https://doi.org/10.1021/es203032v.

Shang, Y., Zhang, L., Jiang, Y., Li, Y. & Lu, P. 2014. Airborne quinones induce cytotoxicity and DNA damage in human lung epithelial A549 cells: The role of reactive oxygen species. Chemosphere, 100**,** 42-49. https://www.sciencedirect.com/science/article/pii/S0045653514000162.

Shen, W., Ren, L., Zhao, Y., Zhou, L., Dai, L., Ge, X., Kong, S., Yan, Q., Xu, H., Jiang, Y., He, J., Chen, M. & Yu, H. 2017. C1-C2 alkyl aminiums in urban aerosols: Insights from ambient and fuel combustion emission measurements in the Yangtze River Delta region of China. Environmental Pollution, 230**,** 12-21. https://www.scopus.com/inward/record.uri?eid=2-s2.0-85020870223&doi=10.1016%2fj.envpol.2017.06.034&partnerID=40&md5=22d322f34555d59593c60150305d8b32.

Shi, T., Schins, R. P., Knaapen, A. M., Kuhlbusch, T., Pitz, M., Heinrich, J. & Borm, P. J. 2003. Hydroxyl radical generation by electron paramagnetic resonance as a new method to monitor ambient particulate matter composition. J Environ Monit, 5**,** 550-6.

Shi, X., Chiu, A., Chen, C. T., Halliwell, B., Castranova, V. & Vallyathan, V. 1999. Reduction of chromium(VI) and its relationship to carcinogenesis. J Toxicol Environ Health B Crit Rev, 2**,** 87-104.

Shi, X. & Dalal, N. S. 1993. Vanadate-mediated hydroxyl radical generation from superoxide radical in the presence of NADH: Haber-Weiss vs Fenton mechanism. Arch Biochem Biophys, 307**,** 336-41.

Shi, X., Leonard, S. S., Liu, K. J., Zang, L., Gannett, P. M., Rojanasakul, Y., Castranova, V. & Vallyathan, V. 1998. Cr(III)-mediated hydroxyl radical generation via Haber-Weiss cycle. Journal of Inorganic Biochemistry, 69**,** 263-268. https://www.sciencedirect.com/science/article/pii/S016201349710037X.

Shirmohammadi, F., Hasheminassab, S., Wang, D., Schauer, J. J., Shafer, M. M., Delfino, R. J. & Sioutas, C. 2016. The relative importance of tailpipe and non-tailpipe emissions on the oxidative potential of ambient particles in Los Angeles, CA. Faraday Discuss, 189**,** 361-80.

Sioutas, C., Delfino, R. J. & Singh, M. 2005. Exposure assessment for atmospheric ultrafine particles (UFPs) and implications in epidemiologic research. Environ Health Perspect, 113**,** 947-955. https://pubmed.ncbi.nlm.nih.gov/16079062

Song, X., Li, J., Shao, L., Zheng, Q. & Zhang, D. 2019. Inorganic ion chemistry of local particulate matter in a populated city of North China at light, medium, and severe pollution levels. Science of the Total Environment, 650**,** 566-574. https://www.scopus.com/inward/record.uri?eid=2-s2.0-85053059525&doi=10.1016%2fj.scitotenv.2018.09.033&partnerID=40&md5=b1207d89441222943fd7a9894a033627.

Spengler, J. D., Keeler, G. J., Koutrakis, P., Ryan, P. B., Raizenne, M. & Franklin, C. A. 1989. Exposures to acidic aerosols. Environ Health Perspect, 79**,** 43-51.

Stevanovic, S., Miljevic, B., Surawski, N. C., Fairfull-Smith, K. E., Bottle, S. E., Brown, R. & Ristovski, Z. D. 2013. Influence of oxygenated organic aerosols (OOAs) on the oxidative potential of diesel and biodiesel particulate matter. Environ Sci Technol, 47**,** 7655-62.

Strader, R., Lurmann, F. & Pandis, S. N. 1999. Evaluation of secondary organic aerosol formation in winter. Atmospheric Environment, 33**,** 4849-4863. http://www.sciencedirect.com/science/article/pii/S1352231099003106.

Sun, K., Liu, X., Gu, J., Li, Y., Qu, Y., An, J., Wang, J., Zhang, Y., Hu, M. & Zhang, F. 2015. Chemical characterization of size-resolved aerosols in four seasons and hazy days in the megacity Beijing of China. Journal of Environmental Sciences, 32**,** 155-167. https://www.sciencedirect.com/science/article/pii/S1001074215001333.

Sun, Y. L., Wang, Z. F., Fu, P. Q., Yang, T., Jiang, Q., Dong, H. B., Li, J. & Jia, J. J. 2013. Aerosol composition, sources and processes during wintertime in Beijing, China. Atmos. Chem. Phys., 13**,** 4577-4592. https://acp.copernicus.org/articles/13/4577/2013/.

Sunderman, F. W., Jr. 2001. Nasal toxicity, carcinogenicity, and olfactory uptake of metals. Ann Clin Lab Sci, 31**,** 3-24.

Surawski, N. C., Ristovski, Z. D., Brown, R. J. & Situ, R. 2012. Gaseous and particle emissions from an ethanol fumigated compression ignition engine. Energy Conversion and Management, 54**,** 145-151. https://www.sciencedirect.com/science/article/pii/S0196890411002767.

Tao, J., Zhang, L., Cao, J. & Zhang, R. 2017. A review of current knowledge concerning PM2. 5 chemical composition, aerosol optical properties and their relationships across China. Atmos. Chem. Phys., 17**,** 9485-9518. https://acp.copernicus.org/articles/17/9485/2017/.

Tiwari, S., Srivastava, A. K., Bisht, D. S., Safai, P. D. & Parmita, P. 2013. Assessment of carbonaceous aerosol over Delhi in the Indo-Gangetic Basin: characterization, sources and temporal variability. Natural Hazards, 65**,** 1745-1764. https://doi.org/10.1007/s11069-012-0449-1.

Tuet, W. Y., Chen, Y., Fok, S., Champion, J. A. & Ng, N. L. 2017. Inflammatory responses to secondary organic aerosols (SOA) generated from biogenic and anthropogenic precursors. Atmos. Chem. Phys., 17**,** 11423-11440. https://acp.copernicus.org/articles/17/11423/2017/.

Venkatachari, P. & Hopke, P. K. 2008. Development and Laboratory Testing of an Automated Monitor for the Measurement of Atmospheric Particle-Bound Reactive Oxygen Species

(ROS). Aerosol Science and Technology, 42**,** 629-635. https://doi.org/10.1080/02786820802227345.

Verma, S. K., Masto, R. E., Gautam, S., Choudhury, D. P., Ram, L. C., Maiti, S. K. & Maity, S. 2015a. Investigations on PAHs and trace elements in coal and its combustion residues from a power plant. Fuel, 162**,** 138-147. https://www.sciencedirect.com/science/article/pii/S0016236115008959.

Verma, V. 2015. Fractionating ambient humic-like substances (HULIS) for their reactive oxygen species activity – Assessing the importance of quinones and atmospheric aging. Atmospheric environment, v. 120**,** pp. 351-359-2015 v.120.

Verma, V., Fang, T., Guo, H., King, L., Bates, J. T., Peltier, R. E., Edgerton, E., Russell, A. G. & Weber, R. J. 2014. Reactive oxygen species associated with water-soluble $PM_{2.5}$ in the southeastern United States: spatiotemporal trends and source apportionment. Atmos. Chem. Phys., 14**,** 12915-12930. https://acp.copernicus.org/articles/14/12915/2014/.

Verma, V., Fang, T., Xu, L., Peltier, R. E., Russell, A. G., Ng, N. L. & Weber, R. J. 2015b. Organic Aerosols Associated with the Generation of Reactive Oxygen Species (ROS) by Water-Soluble PM2.5. Environmental Science & Technology, 49**,** 4646-4656. https://doi.org/10.1021/es505577w.

Verma, V., Ning, Z., Cho, A. K., Schauer, J. J., Shafer, M. M. & Sioutas, C. 2009a. Redox activity of urban quasi-ultrafine particles from primary and secondary sources. Atmospheric Environment, 43**,** 6360-6368. https://www.sciencedirect.com/science/article/pii/S1352231009007857.

Verma, V., Polidori, A., Schauer, J. J., Shafer, M. M., Cassee, F. R. & Sioutas, C. 2009b. Physicochemical and toxicological profiles of particulate matter in Los Angeles during the October 2007 Southern California wildfires. Environmental Science and Technology, 43**,** 954-960. https://www.scopus.com/inward/record.uri?eid=2-s2.0-63149179297&doi=10.1021%2fes8021667&partnerID=40&md5=f564e56fc03689655a06d1a1379d676b.

Verma, V., Rico-Martinez, R., Kotra, N., King, L., Liu, J., Snell, T. W. & Weber, R. J. 2012. Contribution of water-soluble and insoluble components and their hydrophobic/hydrophilic subfractions to the reactive oxygen species-generating potential of fine ambient aerosols. Environmental Science and Technology, 46**,** 11384-11392. https://www.scopus.com/inward/record.uri?eid=2-s2.0-84870014719&doi=10.1021%2fes302484r&partnerID=40&md5=ac04a840cc92896e661ebaed3c4c6667.

Verma, V., Wang, Y., El-Afifi, R., Fang, T., Rowland, J., Russell, A. G. & Weber, R. J. 2015c. Fractionating ambient humic-like substances (HULIS) for their reactive oxygen species activity – Assessing the importance of quinones and atmospheric aging. Atmospheric Environment, 120**,** 351-359. https://www.sciencedirect.com/science/article/pii/S1352231015303526.

Vignesh, K. S. & Deepe, G. 2016. Immunological orchestration of zinc homeostasis: The battle between host mechanisms and pathogen defenses. Archives of biochemistry and biophysics, 611**,** 66-78.

von Glasow, R. 2008. Pollution meets sea salt. Nature Geoscience, 1**,** 292-293. https://doi.org/10.1038/ngeo192.

Vreeland, H., Weber, R., Bergin, M., Greenwald, R., Golan, R., Russell, A. G., Verma, V. & Sarnat, J. A. 2017. Oxidative potential of PM2.5 during Atlanta rush hour: Measurements of in-vehicle dithiothreitol (DTT) activity. Atmospheric Environment, 165**,** 169-178. https://www.sciencedirect.com/science/article/pii/S1352231017304259.

Walgraeve, C., Demeestere, K., Dewulf, J., Zimmermann, R. & Van Langenhove, H. 2010. Oxygenated polycyclic aromatic hydrocarbons in atmospheric particulate matter: Molecular characterization and occurrence. Atmospheric Environment, 44**,** 1831-1846. https://www.sciencedirect.com/science/article/pii/S1352231009010140.

Wallenborn, J. G., Kovalcik, K. D., McGee, J. K., Landis, M. S. & Kodavanti, U. P. 2009. Systemic translocation of (70)zinc: kinetics following intratracheal instillation in rats. Toxicol Appl Pharmacol, 234**,** 25-32.

Wang, J., Lin, X., Lu, L., Wu, Y., Zhang, H., Lv, Q., Liu, W., Zhang, Y. & Zhuang, S. 2019a. Temporal variation of oxidative potential of water soluble components of ambient PM2.5 measured by dithiothreitol (DTT) assay. Science of The Total Environment, 649**,** 969-978. https://www.sciencedirect.com/science/article/pii/S0048969718333461.

Wang, M. W., Chen, J. & Cai, R. 2018a. Air quality and acute myocardial infarction in adults during the 2016 Hangzhou G20 summit. Environmental Science and Pollution Research, 25**,** 9949-9956.

Wang, P., Cao, J.-j., Shen, Z.-x., Han, Y.-m., Lee, S.-c., Huang, Y., Zhu, C.-s., Wang, Q.-y., Xu, H.-m. & Huang, R.-j. 2015. Spatial and seasonal variations of PM2.5 mass and species during 2010 in Xi'an, China. Science of The Total Environment, 508**,** 477-487. https://www.sciencedirect.com/science/article/pii/S0048969714015897.

Wang, S., Yan, Q., Zhang, R., Jiang, N., Yin, S. & Ye, H. 2019b. Size-fractionated particulate elements in an inland city of China: Deposition flux in human respiratory, health risks, source apportionment, and dry deposition. Environmental Pollution, 247**,** 515-523. https://www.sciencedirect.com/science/article/pii/S0269749118357798.

Wang, W., Yu, J., Cui, Y., He, J., Xue, P., Cao, W., Ying, H., Gao, W., Yan, Y., Hu, B., Xin, J., Wang, L., Liu, Z., Sun, Y., Ji, D. & Wang, Y. 2018b. Characteristics of fine particulate matter and its sources in an industrialized coastal city, Ningbo, Yangtze River Delta, China. Atmospheric Research, 203**,** 105-117. https://www.sciencedirect.com/science/article/pii/S016980951730889X.

Wang, Y., Puthussery, J. V., Yu, H. & Verma, V. 2020a. Synergistic and antagonistic interactions among organic and metallic components of the ambient particulate matter (PM) for the cytotoxicity measured by Chinese hamster ovary cells. Science of The Total Environment, 736**,** 139511. https://www.sciencedirect.com/science/article/pii/S004896972033028X.

Wang, Y., Wang, M., Li, S., Sun, H., Mu, Z., Zhang, L., Li, Y. & Chen, Q. 2020b. Study on the oxidation potential of the water-soluble components of ambient PM2.5 over Xi'an, China: Pollution levels, source apportionment and transport pathways. Environment International, 136**,** 105515. https://www.sciencedirect.com/science/article/pii/S0160412019337432.

Wang, Y., Zhang, Q., Zhang, Y., Zhao, H., Tan, F., Wu, X. & Chen, J. 2019c. Source apportionment of polycyclic aromatic hydrocarbons (PAHs) in the air of Dalian, China: Correlations with six criteria air pollutants and meteorological conditions. Chemosphere, 216**,** 516-523. https://www.sciencedirect.com/science/article/pii/S0045653518320551.

Wang, Y., Zhang, Y., Schauer, J. J., de Foy, B., Cai, T. & Zhang, Y. 2020c. Impacts of Sources on PM2.5 Oxidation Potential during and after the Asia-Pacific Economic Cooperation Conference in Huairou, Beijing. Environmental Science & Technology, 54**,** 2585-2594. https://doi.org/10.1021/acs.est.9b05468.

Wang, Y. Q., Zhang, X. Y. & Draxler, R. R. 2009. TrajStat: GIS-based software that uses various trajectory statistical analysis methods to identify potential sources from long-term air pollution measurement data. Environmental Modelling & Software, 24**,** 938-939. http://www.sciencedirect.com/science/article/pii/S1364815209000115.

Watson, J. G., Chow, J. C. & Chen, L. W. A. Summary of methods and comparison studies for organic and elemental carbon: Implications for visibility and global warming. Regional and Global Perspectives on Haze, 2004. 679-716.

Weber, S., Uzu, G., Calas, A., Chevrier, F., Besombes, J. L., Charron, A., Salameh, D., Ježek, I., Močnik, G. & Jaffrezo, J. L. 2018. An apportionment method for the oxidative potential of atmospheric particulate matter sources: application to a one-year study in Chamonix, France. Atmos. Chem. Phys., 18**,** 9617-9629. https://acp.copernicus.org/articles/18/9617/2018/.

Weber, S., Uzu, G., Favez, O., Borlaza, L. J., Calas, A., Salameh, D., Chevrier, F., Allard, J., Besombes, J. L., Albinet, A., Pontet, S., Mesbah, B., Gille, G., Zhang, S., Pallares, C., Leoz-Garziandia, E. & Jaffrezo, J. L. 2021. Source apportionment of atmospheric PM10 Oxidative Potential: synthesis of 15 year-round urban datasets in France. Atmos. Chem. Phys. Discuss., 2021**,** 1-38. https://acp.copernicus.org/preprints/acp-2021-77/.

Wei, C., Han, Y., Bandowe, B. A. M., Cao, J., Huang, R.-J., Ni, H., Tian, J. & Wilcke, W. 2015. Occurrence, gas/particle partitioning and carcinogenic risk of polycyclic aromatic hydrocarbons and their oxygen and nitrogen containing derivatives in Xi'an,

central China. Science of The Total Environment, 505, 814-822. https://www.sciencedirect.com/science/article/pii/S0048969714014995.

Weijers, E. P., Schaap, M., Nguyen, L., Matthijsen, J., Denier van der Gon, H. A. C., ten Brink, H. M. & Hoogerbrugge, R. 2011. Anthropogenic and natural constituents in particulate matter in the Netherlands. Atmos. Chem. Phys., 11, 2281-2294. https://acp.copernicus.org/articles/11/2281/2011/.

Wong, J. P. S., Tsagkaraki, M., Tsiodra, I., Mihalopoulos, N., Violaki, K., Kanakidou, M., Sciare, J., Nenes, A. & Weber, R. J. 2019. Effects of Atmospheric Processing on the Oxidative Potential of Biomass Burning Organic Aerosols. Environmental Science & Technology, 53, 6747-6756. https://doi.org/10.1021/acs.est.9b01034.

Wu, N., Lu, B., Chen, J. & Li, X. 2021a. Size distributions of particle-generated hydroxyl radical (·OH) in surrogate lung fluid (SLF) solution and their potential sources. Environ Pollut, 268, 115582.

Wu, N., Lu, B., Chen, J. & Li, X. 2021b. Size distributions of particle-generated hydroxyl radical (·OH) in surrogate lung fluid (SLF) solution and their potential sources. Environmental Pollution, 268, 115582. https://www.sciencedirect.com/science/article/pii/S0269749120362709.

Xiong, Q., Yu, H., Wang, R., Wei, J. & Verma, V. 2017. Rethinking Dithiothreitol-Based Particulate Matter Oxidative Potential: Measuring Dithiothreitol Consumption versus Reactive Oxygen Species Generation. Environmental Science & Technology, 51, 6507-6514. https://doi.org/10.1021/acs.est.7b01272.

Xu, J.-S., Xu, H.-H., Xiao, H., Tong, L., Snape, C. E., Wang, C.-J. & He, J. 2016. Aerosol composition and sources during high and low pollution periods in Ningbo, China. Atmospheric Research, 178-179, 559-569. https://www.sciencedirect.com/science/article/pii/S0169809516301132.

Xu, J.-S., Xu, M.-X., Snape, C., He, J., Behera, S. N., Xu, H.-H., Ji, D.-S., Wang, C.-J., Yu, H., Xiao, H., Jiang, Y.-J., Qi, B. & Du, R.-G. 2017. Temporal and spatial variation in major ion chemistry and source identification of secondary inorganic aerosols in Northern Zhejiang Province, China. Chemosphere, 179, 316-330. http://www.sciencedirect.com/science/article/pii/S0045653517305027.

Xu, J., Jia, C., He, J., Xu, H., Tang, Y.-T., Ji, D., Yu, H., Xiao, H. & Wang, C. 2019. Biomass burning and fungal spores as sources of fine aerosols in Yangtze River Delta, China – Using multiple organic tracers to understand variability, correlations and origins. Environmental Pollution, 251, 155-165. https://www.sciencedirect.com/science/article/pii/S0269749118355210.

Xu, J., Liu, D., Wu, X., Vu, T. V., Zhang, Y., Fu, P., Sun, Y., Xu, W., Zheng, B., Harrison, R. M. & Shi, Z. 2021a. Source apportionment of fine organic carbon at an urban site of

Beijing using a chemical mass balance model. Atmos. Chem. Phys., 21, 7321-7341. https://acp.copernicus.org/articles/21/7321/2021/.

Xu, Z., Wang, C., Li, H., Xu, S., Du, J., Chen, Y., Ma, C. & Tang, J. 2021b. Concentration, distribution, source apportionment, and risk assessment of surrounding soil PAHs in industrial and rural areas: A comparative study. Ecological Indicators, 125, 107513. https://www.sciencedirect.com/science/article/pii/S1470160X21001783.

Yan, C., Yu, J., Zhao, Y. & Zheng, M. 2017. Biomass Burning Sources in China. In: BOUARAR, I., WANG, X. & BRASSEUR, G. P. (eds.) Air Pollution in Eastern Asia: An Integrated Perspective. Cham: Springer International Publishing.

Yang, A., Janssen, N. A., Brunekreef, B., Cassee, F. R., Hoek, G. & Gehring, U. 2016. Children's respiratory health and oxidative potential of PM2.5: the PIAMA birth cohort study. Occup Environ Med, 73, 154-60.

Yang, L., Wang, S., Duan, S., Yan, Q., Jiang, N., Zhang, R. & Li, S. 2020. Characteristics and formation mechanisms of secondary inorganic ions in PM2.5 during winter in a central city of China: Based on a high time resolution data. Atmospheric Research, 233, 104696. https://www.sciencedirect.com/science/article/pii/S0169809518312651.

Yao, X. & Zhang, L. 2012. Chemical processes in sea-salt chloride depletion observed at a Canadian rural coastal site. Atmospheric Environment, 46, 189-194. https://www.sciencedirect.com/science/article/pii/S1352231011010442.

You, M. Q. 2014. Addition of PM2.5 into the National Ambient Air Quality Standards of China and the Contribution to Air Pollution Control: The Case Study of Wuhan, China. Scientific World Journal.

Yu, H., Puthussery, J. V., Wang, Y. & Verma, V. 2021. Spatiotemporal Variability in the Oxidative Potential of Ambient Fine Particulate Matter in Midwestern United States. Atmos. Chem. Phys. Discuss., 2021, 1-33. https://acp.copernicus.org/preprints/acp-2021-376/.

Yu, H., Wei, J., Cheng, Y., Subedi, K. & Verma, V. 2018. Synergistic and Antagonistic Interactions among the Particulate Matter Components in Generating Reactive Oxygen Species Based on the Dithiothreitol Assay. Environmental Science & Technology, 52, 2261-2270. https://doi.org/10.1021/acs.est.7b04261.

Yu, S., Liu, W., Xu, Y., Yi, K., Zhou, M., Tao, S. & Liu, W. 2019. Characteristics and oxidative potential of atmospheric PM2.5 in Beijing: Source apportionment and seasonal variation. Science of The Total Environment, 650, 277-287. https://www.sciencedirect.com/science/article/pii/S0048969718334399.

Yue, Y., Chen, H., Setyan, A., Elser, M., Dietrich, M., Li, J., Zhang, T., Zhang, X., Zheng, Y., Wang, J. & Yao, M. 2018. Size-Resolved Endotoxin and Oxidative Potential of

Ambient Particles in Beijing and Zürich. Environmental Science & Technology, 52**,** 6816-6824. https://doi.org/10.1021/acs.est.8b01167.

Zeng, Y., Yu, H., Zhao, H., Stephens, B. & Verma, V. 2021. Influence of environmental conditions on the dithiothreitol (DTT)-Based oxidative potential of size-resolved indoor particulate matter of ambient origin. Atmospheric Environment, 255**,** 118429. https://www.sciencedirect.com/science/article/pii/S135223102100248X.

Zhang, G., Ding, C., Jiang, X., Pan, G., Wei, X. & Sun, Y. 2020. Chemical Compositions and Sources Contribution of Atmospheric Particles at a Typical Steel Industrial Urban Site. Scientific Reports, 10**,** 7654. https://doi.org/10.1038/s41598-020-64519-x.

Zhang, J., Li, R., Zhang, X., Bai, Y., Cao, P. & Hua, P. 2019. Vehicular contribution of PAHs in size dependent road dust: A source apportionment by PCA-MLR, PMF, and Unmix receptor models. Science of The Total Environment, 649**,** 1314-1322. https://www.sciencedirect.com/science/article/pii/S0048969718333862.

Zhang, J., Tong, L., Peng, C., Zhang, H., Huang, Z., He, J. & Xiao, H. 2018. Temporal variability of visibility and its parameterizations in Ningbo, China. Journal of Environmental Sciences (China). https://www.scopus.com/inward/record.uri?eid=2-s2.0-85055729671&doi=10.1016%2fj.jes.2018.09.015&partnerID=40&md5=b5913bacb3a6e3f25c0a43b6b5cfe7f4.

Zhang, N., Zhuang, M., Tian, J., Tian, P., Zhang, J., Wang, Q., Zhou, Y., Huang, R., Zhu, C., Zhang, X. & Cao, J. 2016. Development of source profiles and their application in source apportionment of PM2.5 in Xiamen, China. Frontiers of Environmental Science & Engineering, 10**,** 17. https://doi.org/10.1007/s11783-016-0879-1.

Zhang, Y.-J., Huang, C., Lv, Y.-S., Ma, S.-X., Guo, Y. & Zeng, E. Y. 2021. Polycyclic aromatic hydrocarbon exposure, oxidative potential in dust, and their relationships to oxidative stress in human body: A case study in the indoor environment of Guangzhou, South China. Environment International, 149**,** 106405. https://www.sciencedirect.com/science/article/pii/S0160412021000295.

Zhang, Y., Cai, J., Wang, S., He, K. & Zheng, M. 2017. Review of receptor-based source apportionment research of fine particulate matter and its challenges in China. Science of The Total Environment, 586**,** 917-929. https://www.sciencedirect.com/science/article/pii/S0048969717303121.

Zhao, J. & Hopke, P. K. 2012. Concentration of Reactive Oxygen Species (ROS) in Mainstream and Sidestream Cigarette Smoke. Aerosol Science and Technology, 46**,** 191-197. https://doi.org/10.1080/02786826.2011.617795.

Zhao, P. S., Dong, F., He, D., Zhao, X. J., Zhang, X. L., Zhang, W. Z., Yao, Q. & Liu, H. Y. 2013. Characteristics of concentrations and chemical compositions for $PM_{2.5}$ in the

region of Beijing, Tianjin, and Hebei, China. Atmos. Chem. Phys., 13**,** 4631-4644. https://acp.copernicus.org/articles/13/4631/2013/.

Zhao, Z., Luo, X.-S., Jing, Y., Li, H., Pang, Y., Wu, L., Chen, Q. & Jin, L. 2021. In vitro assessments of bioaccessibility and bioavailability of PM2.5 trace metals in respiratory and digestive systems and their oxidative potential. Journal of Hazardous Materials, 409**,** 124638. https://www.sciencedirect.com/science/article/pii/S0304389420326285.

Zheng, M., Yan, C. & Li, X. 2016. PM2.5 Source Apportionment in China. Airborne Particulate Matter: Sources, Atmospheric Processes and Health. The Royal Society of Chemistry.

Zheng, M., Yan, C., Wang, S., He, K. & Zhang, Y. 2017. Understanding PM2.5 sources in China: challenges and perspectives. National Science Review, 4**,** 801-803. https://doi.org/10.1093/nsr/nwx129.

Zhou, J., Bruns, E. A., Zotter, P., Stefenelli, G., Prévôt, A. S. H., Baltensperger, U., El-Haddad, I. & Dommen, J. 2018. Development, characterization and first deployment of an improved online reactive oxygen species analyzer. Atmos. Meas. Tech., 11**,** 65-80. https://amt.copernicus.org/articles/11/65/2018/.

Appendix A: List of Publications

International journal articles

Ke Chen, Jingsha Xu, Lord Famiyeh, Zongshuang Wang, Yong Sun, Dongsheng Ji, Honghui Xu, Huan Yu, Sarah E. Metcalfe, Bencan Tang, Bing Qi, Sailesh N. Behara, Jun He. Characterizing chemical constituents and assessing season-specific driving factors and source apportionment of oxidative potentials in ambient $PM_{2.5}$ over the coastal city of Ningbo, China. *Journal of Hazardous Materials*, under review.

Ke Chen, Sarah E. Metcalfe, Huan Yu, Jingsha Xu, Honghui Xu, Dongsheng Ji, Chengjun Wang, Hang Xiao, Jun He. 2021. Characteristics and source attribution of $PM_{2.5}$ during 2016 G20 Summit in Hangzhou: Efficacy of radical measures to reduce source emissions. *Journal of Environmental Sciences*, 106**,** 47-65.

Lord Famiyeh, **Ke Chen**, Jingsha Xu, Yong Sun, Qingjun Guo, Chengjun Wang, Jungang Lv, Yu-Ting Tang, Huan Yu, Collin Snape, Jun He. 2021. A review on analysis methods, source identification, and cancer risk evaluation of atmospheric polycyclic aromatic hydrocarbons. *Science of The Total Environ*ment, 789, 147741.

Peer-reviewed conference papers

Ke Chen, Jun He. Season-specific driving factors and source apportionment of oxidative potentials in water-soluble fraction of ambient $PM_{2.5}$ over the coastal city of Ningbo, China. The 27th China Conference of Atmospheric Environment Science and Technology. November 2021, Beijing, China.

Ke Chen, Honghui Xu, Sailesh N, Behera, Jun He, Sarah Metcalfe, Bencan Tang. Chemical characterisation and source attribution of $PM_{2.5}$ during 2016 G20 Summit in Hangzhou: Examining efficacy of mitigation policies in reduction of source emissions. Air and Waste Management Association's (A&WMA) 112th Annual Conference and Exhibition. June 2019, Quebec, Canada.

Ke Chen, Honghui Xu, Jun He, Sarah E. Metcalfe, Bencan Tang. The effects of radical emission control on air quality during G20 Summit 2016 in Ningbo. The 12th Environmental Conference for Doctoral Students in Tsinghua University. October 2018, Beijing, China.

Book chapter

Jun He, **Ke Chen**, Jingsha Xu, 2017. Urban Air Pollution and Control. Reference Module in Earth Systems and Environmental Science. In Encyclopaedia of Sustainable Technologies, ed. M. Abraham, S. Silkdar, H. Jin, V. Strezov, S. Bandyopadhyay, W. Deng, J. M. Cawley, J. Zoeller. Elsevier.